

**A Numerical Study of the Axial Compressive Behavior of a
Hyperelastic Annular Seal Constrained in a Pipe**

by

Alix D. Bartel

A Thesis submitted to the Faculty of Graduate Studies of

The University of Manitoba

in partial fulfilment of the requirements of the degree of

MASTER OF SCIENCE

Department of Mechanical Engineering

University of Manitoba

Winnipeg, Manitoba, Canada

Abstract

Elastomer seals are used in a variety of industries that require flow isolation. The characterization of the behavior of these seals remains largely unexplored and hence, this study is focused on simulating and validating the axial-compressive behavior of an annular rubber seal constrained concentrically in a pipe. The elastomer material composing the seal, was experimentally characterized for its mechanical, frictional, and viscoelastic properties and modelled using models developed by Yeoh [1], Thirion [2], and Prony respectively. A 2D axisymmetric finite-element model was developed using ANSYS 16 and used alongside the material models to simulate an axial load versus displacement curve, a contact pressure distribution, and a pipe hoop strain gradient. The results for quasi-static loading and viscoelastic effects agreed within 7% and 18% of the experimental results [3], respectively. It was observed that pipe geometry, rubber chemistry, frictional properties, and viscoelastic effects have significant effect on the compressive behavior of the seal.

Acknowledgements

Thank you to my colleagues and co-workers for their guidance and encouragement:

- Thank you to my research partner Rony Shaha for his accompaniment and help throughout this project.
- Thank you to Anton Kuznetcov for his guidance, advice, and review of all the scripted FEA code.
- Thank you to Genadi Borisov for reviewing my thesis draft.
- Thank you to Dr. Paul Labossiere for offering consistent employment as a teaching assistant through the duration of this research project.

Thank you to our industrial partner:

- ProForma Engineering Ltd. for initiating and continuing this research and for generously assisting in any way required. This research would have otherwise not have been possible.

Thank you to NSERC, the Department of Mechanical Engineering, and the Faculties of Engineering and Graduate Studies at the University of Manitoba for their financial assistance.

Thank you to both my co-advisors Dr. Christine Wu and Dr. Raghavan Jayaraman for their guidance, support, advice, and review throughout the entire research process.

Special thanks to my friends and family for their support over the years.

Table of Contents

Abstract.....	i
Acknowledgements.....	ii
Table of Contents.....	iii
List of Tables.....	vii
List of Figures.....	viii
Chapter 1: Introduction.....	1
1.1 Background	1
1.2 Relevant Research	2
1.3 Knowledge Gap and Motivation	6
1.4 Thesis Objectives	7
1.5 Thesis Outline	7
Chapter 2: Background Information.....	9
2.1 Polymers	9
2.2 Elastomers & Rubber.....	10
2.3 NBR Rubber	11
2.4 Mechanical Properties of Elastomers.....	13
2.4.1 Rubber Elasticity	13
2.4.2 Hysteresis.....	20

2.4.3 Mullins Effect.....	21
2.5 Testing of Elastomers for Hyperelastic Modelling.....	22
2.5.1 Uniaxial Tensile Test	23
2.5.2 Planar Tension Test	25
2.5.3 Equibiaxial Extension Test	26
2.5.4 Volumetric Compression Test	28
2.6 Chemical Properties of Elastomers.....	29
2.6.1 Viscoelasticity	29
2.6.2 Linear Viscoelasticity	31
2.6.3 Creep.....	32
2.6.4 Stress Relaxation	34
2.6.5 Boltzmann Superposition Principle	36
2.6.6 Thermo-Rheological Simplicity.....	38
2.6.7 Aging.....	38
2.7 Testing of Elastomers for Viscoelastic Modelling.....	39
2.8 Elastomer Friction.....	40
2.9 Testing of Elastomers for Frictional Modelling.....	43
2.10 Material Models	46
2.10.1 Hyperelastic Models	47
2.10.2 Frictional Models.....	48
2.10.3 Viscoelastic Materials	50
2.11 Curve Fitting	51
Chapter 3: Methodology	55

3.1 Experiment	55
3.2 Hyperelastic Testing	60
3.3 Frictional Testing	63
3.4 Viscoelastic Testing.....	68
3.5 Finite-Element Model Setup.....	72
3.5.1 Finite-Element Code Selection	72
3.5.2 Geometry and Mesh.....	73
3.5.3 Elements	75
3.5.4 Solver Setup.....	79
3.5.5 Viscoelastic Time Approximation	81
3.5.6 Boundary Conditions	84
3.6 Methods of Experimental Comparison.....	86
3.7 Model Development Procedure	89
3.7.1 Linear Isotropic Model For Estimation	89
3.7.2 Hyperelastic Model Selection.....	90
3.7.3 Mesh Convergence Analysis	91
3.7.4 Implement Pipe and Mandrel.....	92
3.7.5 Mesh Convergence Analysis with Pipe	92
3.7.6 Parametric Study	93
3.7.7 Implementation of Final Friction and Hyperelastic Models	94
3.7.8 Viscoelastic Model Implementation.....	94
3.7.9 Final Model Optimization	94
3.7.10 FE Model Analysis.....	95

Chapter 4: Results	96
4.1 Hyperelastic Results	96
4.2 Frictional Testing Results.....	103
4.3 Linear Isotropic Approximation.....	109
4.4 Preliminary Hyperelastic Model Selection	111
4.5 Preliminary Mesh Sensitivity Analysis	116
4.6 Preliminary Attempt with Pipe.....	120
4.7 Final Mesh Sensitivity Analysis	126
4.8 Parametric Study	128
4.9 Final Hyperelastic Model	133
4.10 Viscoelastic Model.....	139
4.11 Final Simulation	143
4.12 Simulation Optimization.....	153
4.13 Final Results Analysis	164
4.14 Other Cases and Considerations	166
4.14.1 Chemistry Differences	168
4.14.2 Geometric Irregularities	173
4.14.3 Extrapolated Use of this Model	175
Chapter 5: Conclusion	176
References.....	179
Appendix A	A1
Appendix B	B1

List of Tables

Table 1: Case 2 Experimental Input.....	53
Table 2: Pipe-Seal Pairings.....	58
Table 3: Friction Testing Values.....	67
Table 4: Contact Element Setup	78
Table 5: Rough Comparison Results.....	113
Table 6: Lubricated Contact Comparison Results.....	114
Table 7: Preliminary Mesh Sensitivity Summary	117
Table 8: Final Results Summary for Quasi-Static Loading	159
Table 9: Final Results Summary for Viscoelastic Effects.....	159

List of Figures

Figure 1: NBR Uniaxial Tensile Test; 4 Previous Cycles at 100% Strain	14
Figure 2: Mullins Effect over 5 Trials during Uniaxial Tensile Test.....	14
Figure 3: Uniaxial Tensile Test.....	24
Figure 4: Planar Tension Test	24
Figure 5: Equibiaxial Extension Test	27
Figure 6: Volumetric Compression Test	27
Figure 7: Elastic, Viscous, and Viscoelastic Stress-Strain Behavior	30
Figure 8: Creep of a Linear Viscoelastic Polymer	33
Figure 9: Stress Relaxation of a Linear Viscoelastic Polymer	33
Figure 10: Time-Dependence of Creep Compliance.....	35
Figure 11: Time-Dependence of Relaxation Modulus.....	35
Figure 12: Boltzmann Superposition Principle	37
Figure 13: Sled Test for Frictional Testing	45
Figure 14: Axial-Torsion Test for Frictional Testing.....	45
Figure 15: Coulomb's Law in ANSYS	49
Figure 16: Velocity-Dependent Frictional Decay Model	49
Figure 17: Seals Tested	56
Figure 18: Experimental Jig Cross Section	56
Figure 19: Experimental Setup	58
Figure 20: Hyperelastic Test Specimens	62
Figure 21: Volumetric Compression	62

Figure 22: Rubber Friction Specimens.....	64
Figure 23: 102.5 mm Rough and Lubricated Data with 4" Sch. 10 Pipe.....	64
Figure 24: DMA Shear Sandwich	70
Figure 25: DMA Bulk Compression.....	70
Figure 26: 2D Axisymmetric Finite-Element Geometry.....	74
Figure 27: Manual Free Mesh; Smart-Size Free Mesh; Mapped Mesh	74
Figure 28: Contact Diagram.....	78
Figure 29: Material Strain Rate Dependency	82
Figure 30: Boundary Conditions	85
Figure 31: Results Collection Diagram.....	87
Figure 32: One Complete Trial for Each Hyperelastic Test Performed at a Strain Rate of 0.05 s^{-1}	97
Figure 33: Conditioned Stress-Strain Curves at 60% Hyperelastic and 6.6% Volumetric Strain	99
Figure 34: Comparison of 1 st and 5 th Cycles for each Hyperelastic Test at 60% Strain	99
Figure 35: 1 st Cycle Overlap for Uniaxial Tension	100
Figure 36: 5 th Cycle Comparison for Uniaxial Tension.....	100
Figure 37: Comparison of Strain Rates 0.05 s^{-1} and 0.00264 s^{-1}	102
Figure 38: Axial-Torsion Friction Testing	104
Figure 39: Single Axial-Torsion Test Tested at 3.4 MPa with Rough Surface	104
Figure 40: Static and Kinetic Friction Coefficient Results	105
Figure 41: Testing Difficulties for a Lubricated Surface at 0.5 MPa Normal Pressure	105
Figure 42: Thirion's Law Linear Regression	108
Figure 43: Thirion's Law Model	108
Figure 44: 1 st , 2 nd , 3 rd Principal Strains; Von-Mises Strain	110
Figure 45: Rough Contact Comparison: Top 4.....	113

Figure 46: Wet Comparison Top 4.....	114
Figure 47: Maximum (2 mm), Baseline (1 mm), Minimum (0.25 mm) Mesh Sizes.....	117
Figure 48: Mesh Sensitivity Analysis – Key Results	119
Figure 49: Localized Mesh Refinement Analysis	119
Figure 50: Rough Contact Radial Deformation Time-lapse	121
Figure 51: Lubricated Contact Radial Deformation Time-lapse	121
Figure 52: First Principal Element Strain for Rough Interface	123
Figure 53: First Principal Element Strain for Lubricated Interface	123
Figure 54: Third Principal Element Strain for Rough Interface.....	124
Figure 55: Third Principal Element Strain for Lubricated Interface.....	124
Figure 56: Preliminary Force-Displacement Results for Rough Interface	125
Figure 57: Preliminary Force-Displacement Results for Lubricated Interface	125
Figure 58: Final Mesh Sensitivity Analysis	127
Figure 59: Mesh Distortion Errors	127
Figure 60: Pipe Geometric Sensitivity	129
Figure 61: Axial Displacement Sensitivity with respect to Inner Pipe Diameter	129
Figure 62: Axial Force vs. Displacement as a Function of Friction Coefficient.....	132
Figure 63: Pipe Hoop strain as a Function of Friction Coefficient	132
Figure 64: 3 rd Order Yeoh Fit to the First Cycle of 100% Strain.....	134
Figure 65: 5 th Order Yeoh Fit to the First Cycle of 100% Strain	134
Figure 66: Superimposed 1 st Cycle Curve Generation.....	136
Figure 67: 3 rd Order Yeoh Fit to Superimposed 1 st Cycle Dataset	137
Figure 68: 5 th Order Yeoh Fit to Superimposed 1 st Cycle Dataset	137
Figure 69: 100% Strain Hyperelastic Model Comparison for Rough Contact.....	138

Figure 70: 100% Strain Hyperelastic Model Comparison for Lubricated Contact.....	138
Figure 71: DMA Shear Relaxation: 24 hours at 3.5% strain.....	140
Figure 72: DMA Bulk Relaxation: 24 hours at Various Strain Levels	140
Figure 73: Bulk Compression Re-Test using 250 kN Instron.....	142
Figure 74: Shear and Bulk Moduli Relaxation Fit to a 3-Term Prony Series.....	142
Figure 75: Rough Force-Displacement Curve	144
Figure 76: Lubricated Force-Displacement Curve	144
Figure 77: Rough Contact Pressure Gradient.....	146
Figure 78: Lubricated Contact Pressure Gradient	146
Figure 79: Rough Pipe Membrane Hoop Strain Gradient	147
Figure 80: Lubricated Pipe Membrane Hoop Strain Gradient.....	147
Figure 81: Rough Normalized Axial Force Relaxation.....	148
Figure 82: Lubricated Normalized Axial force Relaxation	148
Figure 83: Rough Maximum Pipe Membrane Hoop Strain Relaxation	149
Figure 84: Lubricated Maximum Pipe Membrane Hoop Strain Relaxation	149
Figure 85: Rough Axial Displacement Creep	151
Figure 86: Lubricated Axial Displacement Creep.....	151
Figure 87: Rough Maximum Pipe Hoop Strain Creep	152
Figure 88: Lubricated Maximum Pipe Hoop Strain Creep	152
Figure 89: Final Rough Force-Displacement Curve.....	155
Figure 90: Final Lubricated Force-Displacement Curve.....	155
Figure 91: Final Rough Pressure Gradient	156
Figure 92: Final Lubricated Pressure Gradient	156
Figure 93: Final Rough Pipe Hoop Strain Gradient	157

Figure 94: Final Lubricated Pipe Hoop Strain Gradient	157
Figure 95: Final Rough Normalized Axial Force Relaxation	160
Figure 96: Final Lubricated Normalized Axial Force Relaxation	160
Figure 97: Final Rough Hoop Strain Relaxation	161
Figure 98: Final Lubricated Hoop Strain Relaxation	161
Figure 99: Final Rough Axial-Displacement Creep.....	162
Figure 100: Final Lubricated Axial-Displacement Creep.....	162
Figure 101: Final Rough Pipe Hoop Strain Creep.....	163
Figure 102: Final Lubricated Pipe Hoop Strain Creep.....	163
Figure 103: Thin-Wall Pipe Strain Gradient Location Comparison.....	165
Figure 104: Thin-Wall Through-Thickness Pipe Hoop Strain at Location of Max. Strain.....	165
Figure 105: Thick-Wall Pipe Strain Gradient Location Comparison	167
Figure 106: Thick-Wall Through-Thickness Pipe Hoop strain Gradient at Location of Max. Strain ...	167
Figure 107: Seal Stress-Strain Compression Tests.....	169
Figure 108: 96.3 mm Force-Displacement Curve	171
Figure 109: 96.3 mm Pipe Membrane Hoop Strain Gradient	171
Figure 110: Force-Input for 96.3 mm Force-Displacement Curve.....	172
Figure 111: Force-Input for 96.3 mm Pipe Membrane Hoop Strain Gradient	172
Figure 112: 3D FE Model for Use with Irregular Geometry: View A	174
Figure 113: 3D FE Model for Use with Irregular Geometry: View B.....	174
Figure B1: Superposition of 1st Cycle Data for 0.00264 s^{-1}	B3
Figure B2: Curve-Fit for Superimposed Material Testing Dataset for 0.00264 s^{-1}	B3
Figure B3: Force-Displacement Comparison of Strain Rates.....	B4
Figure B4: Strain Gradient Comparison of Strain Rates	B4

Chapter 1: Introduction

The following chapter is an introduction describing the purpose and objectives of this research, the current pertaining research developments in the field of elastomer simulation, and how the expected results from this thesis satisfies a knowledge gap in the current understanding and development of rubber sealing applications.

1.1 Background

Elastomers and rubber compounds are widely used in a variety of engineering applications stretching across various industries. They are selected for their capability for sustaining large deformations while maintaining their physical integrity over a large range of operating environments, which makes them an ideal material for sealing applications. Predominantly selected for use in hydraulic systems, their use in isolating the flow of fluids over varying operating conditions is well documented.

At a small scale, elastomers compose o-rings, x-rings, t-rings, etc. for the localized sealing and isolation of hydraulic and pneumatic components. At a large scale, elastomers compose packers, remote isolators, gaskets, liners, etc. for the sealing of large pipe systems.

Knowledge of the use of elastomers in sealing applications is largely credited to the generation of empirical data through physical testing of the seals. Predicting the behavior of the seals using the properties of the elastomer composing the seals is inherently complex and not well documented. Empirical design data is often very specific to the application for which it is developed. In large-scale sealing applications or in novel forms of sealing, it is often unfeasible or expensive to generate empirical

data for design. Thus, it is beneficial to develop methods to predict the seal behavior using the material properties of elastomers

The large dependency of an elastomer's properties on time, temperature, and stress (the inherent non-linearity) imposes a higher degree of difficulty in conceiving an analytical solution. Hence, finite-element analysis may be a viable solution on many occasions.

1.2 Relevant Research

In general, non-linearity in structural simulations arises from the following:

- Material non-linearity
- Geometry
- Contact
- Friction
- Effect of environment on material properties

Rubber seals experience all of the listed conditions and as a result, simulations and experiments must be very specific to the design. As such, much of the current research in this area is dedicated to establishing specific solutions rather than developing generalized solutions.

Published studies on seals are very limited. In 1993, Gent [4] published a general solution to determine the apparent compressive modulus of solid and annular rubber blocks. The solution assumed small deformations, incompressibility, and complete bonding between the rubber block and the compression platens, using the elastic modulus of the rubber and the geometry (shape factor) of the block. This solution relates the compressive deformation to the superposition of unconstrained uniaxial deformation and shearing deformation due to the constraint applied by the compression platens. The

apparent compressive modulus was in sufficient agreement with the experimental modulus of the solid and annular rubber blocks predicting a significantly higher stiffness than the elastic modulus of the rubber but lower than its bulk modulus. The compressive modulus at higher shape factors, when hydrostatic compression is substantial, was obtained by an approximate relation combining the apparent compressive modulus and the bulk modulus.

In 2008, Gent *et al.* [5] extended the solution to the compression of rubber blocks between frictional surfaces. In their work, they related the pressure within the rubber acting normal to the contact surfaces to a Coulomb friction model. At a certain radius from its center, the block starts to slip relative to the compression platens, the magnitude of which increases to a maximum at the outer radius of the block. The pressure gradients for the slip and non-slip zones were integrated to forces, which were added to obtain the total force required to achieve a certain deformation and thus the overall apparent compressive modulus of a rubber block with frictional contacts. It was demonstrated that the apparent modulus of a block, for a given shape factor, decreased with a reduction in the friction coefficient; the proportionality of the reduction varied with the friction coefficient. These predictions were not experimentally verified and were attributed to very low strains in the linear region of the compressive rubber behavior.

One notable example of the finite-element modelling of pipe sealing using elastomer seals was published in 2010 by Alzebdeh *et al.* [6], where a finite-element model was created to simulate the compression of elastomer seals in open-hole liners for the control of water flow in open-hole wells. A solid expandable tubular (SET) is a deformable metal tube which is inserted concentrically into the opening of an open-well with diameter greater than the tube. Annular elastomer strips are placed between the SET and the open-well inner-diameter. A mandrel is used to plastically deform and expand the SET's diameter resulting in the compression of the elastomer strips against the well wall to form a

sealing surface. The analysis was aimed to approximate the contact pressure exerted by the elastomer seal on the well wall as a metric of sealing performance. The geometry was developed using low-order axisymmetric elements and the pipe and elastomer were modelled using an elasto-plastic model and an Arruda-Boyce hyperelastic model, respectively. Friction was briefly examined using a constant-coefficient Coulomb interfacial stress model. The analysis was not experimentally validated despite complex material models, friction, and boundary conditions. Furthermore the viscoelastic effects of the elastomer were not analyzed.

Continuing on the finite-element analysis of elastomer seals, rubber packers are widely used in the oil and gas industry as a means of remote isolation to control the flow of fluids. Fracking is a recent development relying heavily on the control of high-pressure fluids and gasses. Packers are essentially tubes or annuli composed of high-quality grades of vulcanized rubbers subject to axial compression [7]. The near-incompressible behavior of rubber translates axial compression into radial expansion, which forms a seal in a pipe by filling the asperities on the surface of the pipe's interior wall at high contact-pressure and preventing the flow of fluids past the pipe-rubber interface. The non-linear behavior, complex geometry, and contact interfaces require design through FEA and experimentation.

One analysis pertaining to the simulation of elastomer packers was performed by Feng *et al.* in 2010 [8] to analyze the relationship between the rubber packer's axial displacement and contact pressure with the inner pipe wall under different axial forces. The rubber packer was composed of high-stiffness rubber with a hardness of 94 SHORE A. The rubber compound was tested at 20 and 148°C and the stress-strain data was fit to a first-order Mooney-Rivlin model. Axisymmetric geometry was assumed and a mesh was generated with low-order quadrilateral plane elements for the rubber and 9-node quadrilateral plane elements for other geometry modelled with linear isotropic materials. The friction coefficient was measured experimentally to be 0.1 between the rubber and steel surfaces. The model

was able to predict sealing contact pressure and axial displacement as a function of axial load. Once more, there was no experimental validation performed despite complex material models, geometry, friction, and boundary conditions. Viscoelastic effects were not analyzed and neither were any changes in seal geometry or interfacial friction.

To examine the complexities of contact between rubber packers and a pipe or casing, Guo *et al.* [9] performed a study in 2012 using ANSYS to examine the relationship between contact-pair parameters and the frictional behavior of the packer-casing interface. A rubber packer was modelled using 3D 10 node tetrahedral hyperelastic elements and all other geometry modelled using 8-node brick elements. The steel casing and the rubber packer were modelled as linear isotropic materials. A parametric study was performed to determine the effect of contact stiffness and penetration of the rubber seal contacting the steel casing on the casing wall stresses. It was concluded that the contact stiffness and penetrations ratios for the contact element should be between 0.07-0.09 and 0.10-0.11 respectively. This analysis however did not model the rubber appropriately using a hyperelastic material model nor did it experimentally verify that the rubber could produce accurate results using a linear isotropic model.

The most recent analysis similar to this research was published in 2014 by Zhao *et al.* [10], which examined the analysis of contact stresses and strains in a pipe caused by the axial compression of a rubber seal. An annular nitrile rubber seal with a rectangular cross-section was held concentrically within a 4" nominal pipe size (NPS) steel pipe with intermediate wall thickness. Axial displacement on the seal was applied and the ensuing radial deflection developed contact pressure on the inner pipe wall, which resulted in a measurable pipe strain that was compared experimentally. The compressive behavior of the elastomer used in manufacturing the seal was modelled using a 1st order Mooney-Rivlin hyperelastic model. The effect of lubricated contact between the rubber annulus and steel was also examined. Lubricated contact interfaces were setup with a friction coefficient of 0.1 and rough contact

interfaces were setup using ‘rough’ formulation ($\mu \rightarrow \infty$). The model predictions compared with experimental results within an error range of approx. 40%. The large range of error was attributed to the absence of material and frictional testing in addition to experimental testing difficulties. Moreover, viscoelastic effects in the rubber were not analyzed leading to further inconsistency.

1.3 Knowledge Gap and Motivation

The finite-element analysis of rubber seals requires accurate and case-specific material models. In general, a rubber seal will exhibit differences in its compressive behavior dependent on its own non-linear mechanical, frictional, and viscoelastic properties all the while changing for different environmental conditions. Thus it is highly unlikely to achieve an accurate representation of the true compressive behavior of a rubber seal without experimental validation.

The common theme between the aforementioned analyses is the absence of experimental validation which cannot guarantee the validity of their results especially in the presence of significant non-linear material behavior. In an attempt for experimental validation, Zhao *et al.* [10] clearly demonstrated that the compressive behavior of the seal must be characterized very accurately in order to provide an accurate solution.

The creation of an accurate experimentally validated finite-element model of an axially-compressed elastomer seal constrained in a pipe will fulfil a significant knowledge gap in the understanding of the axial-compressive behavior of an elastomer seal.

The motivation for this research is thus to create a scalable and experimentally validated finite-element model in ANSYS capable of accurately simulating the sealing behavior of a rubber annulus. The framework for this model can subsequently be modified and improved to fit various sealing applications involving elastomers.

1.4 Thesis Objectives

The primary objective of this thesis is to study the axial-compressive behavior of an annular seal constrained within a pipe under quasi-static and static loading conditions. In order to realize this objective the following specific tasks have been pursued and completed:

- Comprehensively characterize the mechanical properties of the elastomer used in manufacturing the seal, under tensile, shear, biaxial, and hydrostatic compressive loading (both quasi-static and static).
- Characterize the friction between the elastomer and the compression rings.
- Characterize the short-term viscoelastic properties of the elastomer.
- Model the mechanical, frictional, and viscoelastic properties appropriately in ANSYS.
- Perform a parametric study to optimize the FE model to study the constrained behavior.
- Validate the FE model predictions using experimental data generated by Shaha [3], a fellow researcher in the research group.

1.5 Thesis Outline

The following thesis will be divided into four sections: Background Information, Methodology, Results, and Conclusion. The background information section will lay the foundation for the understanding of the behavior of rubber and identify key topics of the current knowledge of elastomers. Notably, elastomers will be characterized by discussing the physical, chemical and mechanical characteristics, the time and temperature dependent behavior, and the current methods of experimentally testing them and simulating their applications. For simulation, current modelling techniques will be discussed for use with ANSYS 16 APDL.

The research methodology will subsequently be established to organize the elements with which to experimentally characterize the rubber and create a simulation encompassing the procured experimental and material testing data. The methodology will be organized in a step-by-step fashion describing all steps required to proceed from research initialization to the final simulation.

The results will be shown in steps alongside the methodology to describe how the gradual addition of examined behavior is compiled to form the final simulation. All steps will be compared against experimental data to ensure each behavioral addition is successfully validated before proceeding to a subsequent behavior.

The thesis will end with the conclusion which will summarize the thesis scope and objectives and discuss the points of accomplishment. Additionally, appendices will provide supplementary information to the thesis.

Chapter 2: Background Information

The following chapter will provide a background and general understanding of the various theories describing the behavior of rubber and the corresponding creation of an FE model. Included are descriptions of elastomers and their behavioral characterizations, hyperelasticity, viscoelasticity and elastomer friction. In addition, many of the features and controls provided in ANSYS 16 APDL will be briefly described to provide an understanding of the selection and control process when using FE software in non-linear quasi-static analyses with large deformation.

2.1 Polymers

The innovation behind polymer science lies in the variety of engineering applications polymers can fulfill and in the advantages they introduce over standard isotropic metals and ceramics. The applications for the use of polymers range across many commercial sectors where the advantages of using polymers include weight-reduction, cost-reduction, high ductility, ease-of-manufacture, tailorability, and other unique properties. Polymers have the ability to fulfill a large variety of applications because of the variety of forms they can take.

Polymers are split into two types: Thermoplastic and Thermoset. Common thermoplastics can take the form of polyethylene, polyvinyl-chloride (PVC), polystyrene, etc. which are typically composed of linear or branched polymer molecules which have a tendency to soften and melt at high temperatures. Thermoset polymers exist as epoxies, urethanes, rubbers, resins, etc. which are composed of polymer molecules which are cross-linked which degrade at higher temperatures rather than melt. Polymers also have the ability to change their material behavior given their temperature dependency. Brittle and

glassy behavior is observed at temperatures below their glass transition point while rubbery, elastic, and liquid behavior can occur at or above the glass transition point.

As an engineering material however, polymers pose a challenge in that much of their behavior is non-linear and dependent on time, temperature, stress, and strain. Unlike metals, they do not exhibit a rapid response to load and temperature variations nor do they demonstrate a linear relationship between stress and strain prior to permanent deformation. For this, polymers exhibit viscoelastic behavior which is characterized as a combination of elastic behavior found in isotropic metals and viscous behavior found in viscous fluids such as oil which lends itself to hysteresis and thermal dissipation.

2.2 Elastomers & Rubber

Elastomers are a specialized group of polymers exhibiting low stiffness and a large capability for elastic deformation. In most cases, elastomers are thermoset polymers with amorphous structures composed of very long molecular chains with a low number of cross-links. To a lesser extent, thermoplastic elastomers exist where cross-linking is due to physical entanglement rather than chemical bonding. Examples of common elastomers include polyisoprene, polybutadiene, fluoroelastomers, and rubbers.

When subject to the addition of chemicals and fillers, most notably carbon black, and then subjected to a curing process known as vulcanization where the creation of chemical cross-links occurs, rubbers are formed. Rubbers are most widely used for their characteristically soft and highly elastic behavior in addition to their near-incompressibility and resistance to permanent deformation. Chemically, rubbers are essentially long hydrocarbon chains taking the form of carbon and hydrogen chains in their most

simple form with various molecular side-groups producing different chemical compounds. The most common repeat unit in a rubber compound is isoprene (C_5H_8) which is built up into a long chain.

When considering rubber-like elasticity, a rubber compound follows 3 general guidelines:

- Contains long-chain molecules with freely rotating links
- There are weak secondary forces between molecules
- Exhibits molecular interlocking in the form of cross-linking to form 3D networks

With cross-linking creating a 3D network, small-strain isotropic behavior is demonstrated due to the amorphous structure. Given the presence of very long molecular chains with weak inter-molecular forces, it is possible for a large amount of relative motion to occur with ease between the chains. Thus, rubbers are capable of large elastic deformation given that the large chains slip past, untangle, and align themselves in the direction of deformation where subsequent elastic retraction is caused by the 'memory' of cross-links.

However, when considering the performance of rubber at different temperatures, the structure of any rubber compound will transition to a glassy state at sufficiently low temperatures. While these temperatures are typically well below $0^{\circ}C$, most rubber applications operate at sufficiently high temperatures where glassy behavior does not occur.

2.3 NBR Rubber

One very common rubber compound is Nitrile Butadiene Rubber (NBR) which is commonly found in sealing applications such as o-rings and gaskets due to its excellent chemical resistance and long-term durability. NBR is an unsaturated copolymer formed with acrylonitrile (ACN) and butadiene (BD) molecules in addition to various other chemicals including fillers, plasticizers, protectants, and most

commonly carbon black producing a black appearance. The source behind the excellent chemical resistance of NBR and its common use in sealing application is the copolymerization of butadiene rubber with acrylonitrile which is a polar monomer. Hydrocarbons are normally non-polar which reduces the solubility of the rubber compound in an environment containing hydrocarbons.

Manufacturing is initiated using emulsion polymerization yielding coagulated polymer latex which can then be formed or extruded into various shapes and finally vulcanized for use. The curing characteristics and the balance of ACN and BD produce differences in the properties of the NBR. The ACN content is the first primary defining criteria with respect to the grade of NBR. With an increase in ACN, properties such as chemical resistance, processability, strength, and hardness are improved at the expense of lower flexibility, higher hysteretic losses, and higher compression set. The second criterion is the Mooney viscosity which relates to the processing of the material where higher ratings improve upon the extensibility in manufacturing. Lower ratings are suitable to injection molding while higher ratings are suitable to extrusion and compression molding.

Two general types of NBR exist provided the difference in curing characteristics. ‘Cold’ NB rubbers are polymerized at a temperature range of 5 to 15°C [11] depending on the ratio of linear to branched polymerization required which yields straighter polymer chains. The chemical composition for such NB rubbers varies greatly depending on the ACN content, the Mooney viscosity, and the desired additional properties resulting in a very broad variety of compositions.

‘Hot’ NB rubbers are processed at higher temperatures between 30 and 40°C [11] producing highly branched structures which are more suited to ‘tacky’ and adhesive applications also benefitted by an increase in tear-resistance. In addition, their higher resistance to flow makes them suitable for compression molding.

Various other types of NBR's exist provided the flexibility in the addition of chemical compounds which further tailors the properties to various applications. For the purpose of this research, the examined elastomer is Spareage NT-5A NBR developed for compression molding.

2.4 Mechanical Properties of Elastomers

For most applications, the most important aspect of rubber is its mechanical properties and how to design and analyze rubber components under a variety of operating conditions. The following section describes linear and non-linear rubber elasticity, hysteresis, Mullins effect, and the corresponding testing methodology for the characterization of rubber.

2.4.1 Rubber Elasticity

Rubbers display unique mechanical properties due the relative motion of large molecular chains and cross-links within the polymer and due to the amorphous random-coil structure. It is common that rubbers are capable of large strains in excess of 100% while being able to retain its original shape following deformation.

For NBR and similarly for most vulcanized rubbers, figure 1 shows the loading and unloading engineering stress-strain curves for a uniaxial tensile test which has been cyclically loaded over 5 cycles at a strain of 100%. Figure 2 displays the difference between the 1st and 5th loading cycles of a typical elastomer material test. For the loading curve, rubber displays 3 distinct regions of different stress-strain behavior separated by 2 points of inflection. The first region is the linear region which is a broadly defined zone where the stress-strain curve is approximately linear and the deformation is elastic and fully reversible due to the weak bonds within the rubber remaining intact after deformation.

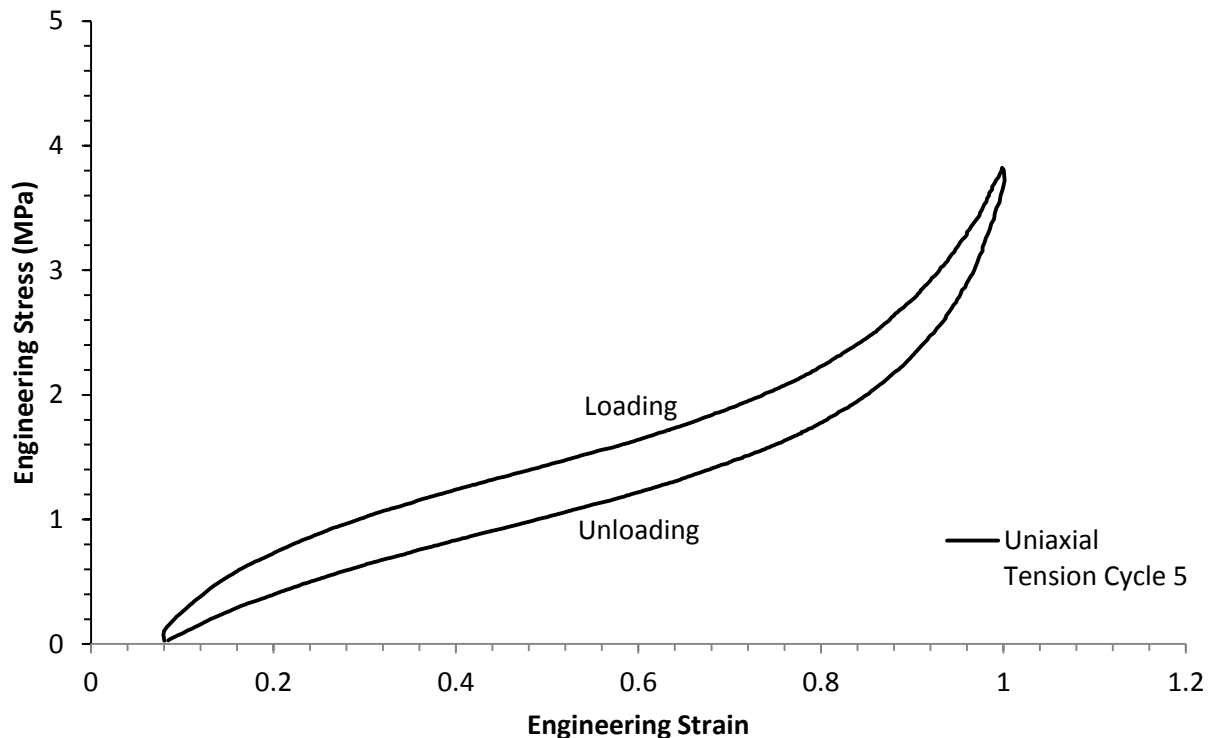


Figure 1: NBR Uniaxial Tensile Test; 4 Previous Cycles at 100% Strain

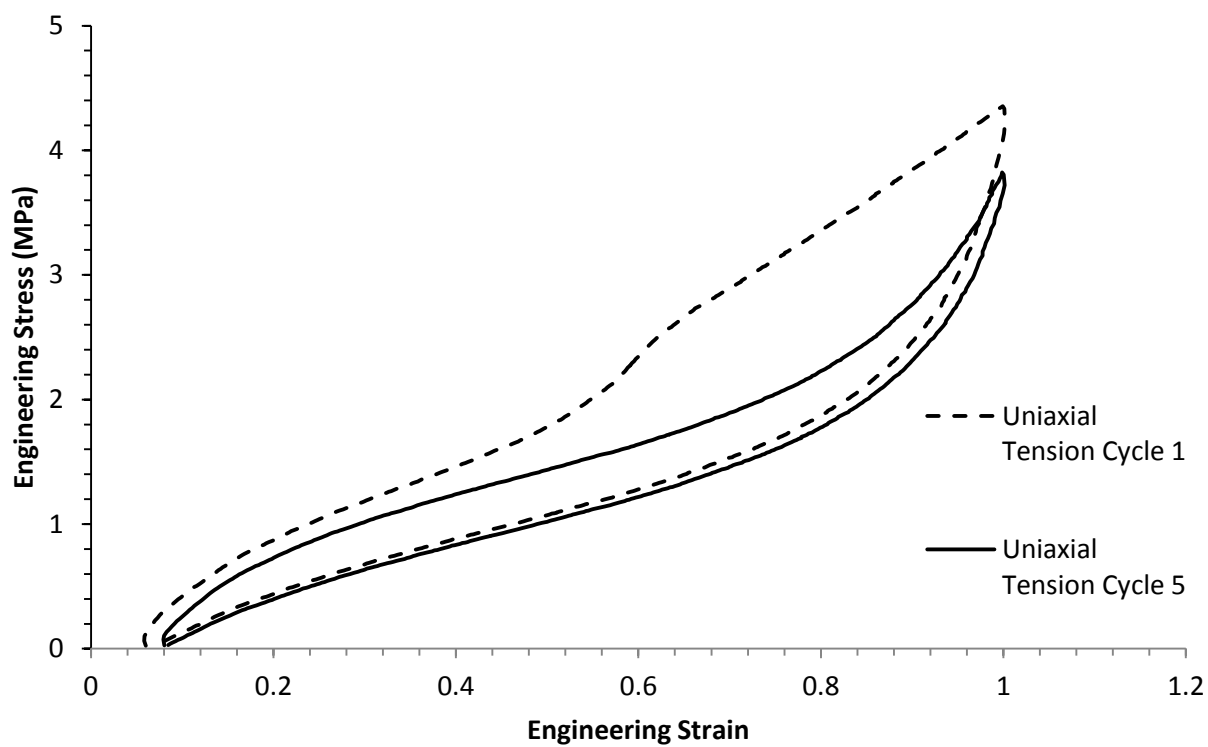


Figure 2: Mullins Effect over 5 Trials during Uniaxial Tensile Test

The second region displays a reduction in the stiffness of the material as weak bonds are being broken and large molecular motion occurs; this region is the strain-softening region. The third region displays a hardening stage where the limitations in chain extensibility in their aligned fully-stretched state display an increase in material stiffness. In this region, the elastomer strains due to the extension of much stronger aligned molecular chains. The specimen eventually ruptures when the subsequent scission of chains reaches instability.

At low strains, elastomers exhibit a certain range of linear stress-strain behavior similar to that of Hookean solids. For a stress-strain curve such as in figure 1, the elastic modulus E can be extracted from the early region of linearity with an end-point defined depending on the tolerance for error due to curvature in the measurement. Unlike metals in the elastic region however, the Poisson's ratio for elastomers range from 0.499 to 0.5 [12] in response to 'nearly-incompressible' behavior. Therefore, there is a higher presence of transverse deformation in the deformed cross-section as compared to most metals. It is thus, difficult to characterize the true stress-strain behavior of the rubber due to a continuously changing gaging area. Due to the difficult in testing, it is necessary to produce test data in several pure states of strain such as uniaxial tension, simple shear, simple compression, and volumetric compression followed by the use of correlations between the different moduli. For a Hookean solid, the shear modulus G and bulk modulus K are defined as follows in terms of both the Poisson's ratio and the Young's modulus. While it is difficult to measure the Poisson's ratio of an elastomer directly, its value is very near 0.5 indicating a bulk modulus roughly 1000 times higher than the elastic modulus. As such, it is recommended to experimentally measure 2 moduli and use correlations to determine the linear properties of an elastomer.

$$K = \frac{E}{3(1 - 2\nu)} \quad (1)$$

$$G = \frac{E}{2(1 + \nu)} \quad (2)$$

For the characterization of the stress-strain behavior beyond the linear region, non-linear models were developed. The earliest attempt at a phenomenological theory of large elastic deformations was developed in 1940 by Mooney [13] under the following assumptions:

- Elastomers are incompressible and isotropic in their unstrained state.
- Hooke's law is obeyed in simple shear.

The first assumption remains in close agreement to experiment while the second is known to approximate simple shear up to moderate strain. From these assumptions and the treatment of rubber as a continuum, large perfectly-elastic deformation was characterized in terms of a strain-energy function W in terms of the principal stretch ratios.

$$W = C_1 \left(\lambda_1^2 + \lambda_2^2 + \lambda_3^2 - 3 \right) + C_2 \left(\frac{1}{\lambda_1^2} + \frac{1}{\lambda_2^2} + \frac{1}{\lambda_3^2} - 3 \right) \quad (3)$$

$$\lambda_i = \frac{L}{L_o} = 1 + \epsilon_i^e \quad (4)$$

where C_1 and C_2 are elastic constants, λ_i is the principal stretch ratio in the i^{th} direction, and ϵ_i^e is the engineering strain in the i^{th} direction.

In an effort to generalize the strain-energy function in states of pure homogenous strain, Rivlin [14] expanded upon the work of Mooney in 1948 by taking the same basic assumptions that the material is incompressible and isotropic in the unstrained state. The condition of isotropy required that the strain-energy function was symmetrical with respect to the three principal stretch ratios λ_1 , λ_2 , and λ_3 . In addition, since strain-energy must remain unaltered by the sign of the principal stretch ratios, the strain-energy function was formed in terms of even powers of the principal stretch ratios. Thus, three strain invariants I_1 , I_2 , and I_3 described the generalized state of strain for the strain-energy function.

$$I_1 = \lambda_1^2 + \lambda_2^2 + \lambda_3^2$$

$$\begin{aligned} I_2 &= \lambda_1^2 \lambda_2^2 + \lambda_2^2 \lambda_3^2 + \lambda_3^2 \lambda_1^2 \\ I_3 &= \lambda_1^2 \lambda_2^2 \lambda_3^2 \end{aligned} \tag{5}$$

For any complex state of strain, the strain-energy function could now be used to derive stresses depending on any configuration of the principal stretch ratios. As an added simplification, for incompressibility, the third strain invariant can be simplified as follows:

$$I_3 = \lambda_1^2 \lambda_2^2 \lambda_3^2 = 1 \tag{6}$$

Following the contributions of Mooney and Rivlin, a generalized strain-energy function was developed for incompressible hyperelasticity; a term coined to describe incompressible solid materials capable of large elastic deformation.

$$W = \sum_{i=0, j=0}^{\infty} C_{ij} (I_1 - 3) \cdot (I_2 - 3) \tag{7}$$

where C_{ij} is a series of empirically derived constants curve-fit to experimental data. As an added possibility for a higher experimental conformance, the Mooney-Rivlin model could have any number of constants depending on the needs of its application.

Since the development of the Mooney-Rivlin hyperelastic model, several attempts were made to produce strain-energy function with different functionality and levels of accuracy. These models generally lie in one of three categories [15]:

- Phenomenological models derived from mathematical developments of W .
- Models determining dW/dI_1 and dW/dI_2 directly from experimental data.
- Physically motivation models based on polymer chain network and statistical interactions.

Phenomenological Models

The most commonly used hyperelastic models are phenomenological models. In addition to the Mooney and Mooney-Rivlin models, several models have been developed in the past. Notably in 1972, Ogden [16] expanded the strain-energy function through a series of real powers of λ_i .

$$W = \sum_{n=1}^N \frac{\mu_n}{\alpha_n} \cdot \left(\lambda_1^{\alpha_n} + \lambda_2^{\alpha_n} + \lambda_3^{\alpha_n} - 3 \right) \quad (8)$$

where μ_n and α_n are curve-fitting coefficients requiring the following condition to be met:

$$\mu_n \alpha_n > 0 \quad \forall n = 1, N$$

The Ogden model is well known and proven for its high accuracy in large-strain applications. Despite its strengths, it is computationally expensive and requires significant experimental data to accurately characterize using non-linear curve-fitting algorithms.

In 1993, Yeoh [1] performed further experiments with rubber and simplified Rivlin's general formulation under the assumption that the second strain invariant I_2 remains constant during stretch and contributes significantly less than the first strain invariant I_1 . Therefore, a strain-energy function was derived only in terms of the first and, if compressible, the third strain invariants.

$$W = \sum_{i=1}^N C_{i0} (I_1 - 3)^i \quad (9)$$

The Yeoh model has been demonstrated effective in its characterization of carbon-black filled vulcanized rubbers [17].

Experimentation of dW/dI₁ and dW/dI₂

To a lesser extent, various models have derived strain-energy function based on the direct determination of dW/dI_1 and dW/dI_2 . One such example is the Gent model [18] developed in 1996

which proposed to limit chain extensibility and to consider I_1 as a maximum denoted as I_m where E and I_m are experimentally measured parameters.

$$W = -\frac{E}{6} (I_m - 3) \ln \left(1 - \frac{I_1 - 3}{I_m - 3} \right) \quad (10)$$

Physically-based Models

Several derivations have been performed in an attempt to develop hyperelastic models based on the microscopic behavior of elastomer chains. Most differ significantly in their derivation due to their assumptions.

The simplest hyperelastic model for use with small but nonetheless non-linear strains is the Neo-Hookean model [19] developed in 1943 which was derived from molecular chain statistics assuming a Gaussian distribution to estimate the number of chain conformations of macromolecular chains assuming the elasticity of the network is due to changes in entropy.

$$W = \frac{1}{2} nkT (I_1 - 3) \quad (11)$$

where n is the chain density per unit-volume, k is the Boltzmann constant, and T is the absolute temperature. Another famous physical model is the Arruda-Boyce model [20] developed in 1993 which represented the stress-strain function by an 8-chain representation of the macromolecular structure of rubber:

$$W = G \left[\frac{1}{2} (I_1 - 3) + \frac{1}{20N} (I_1^2 - 9) + \frac{11}{1050N^2} (I_1^3 - 27) + \frac{19}{7000N^3} (I_1^4 - 81) + \frac{519}{673750N^4} (I_1^5 - 243) \right] \quad (12)$$

where G is equal to $nk\theta$, n is the chain density, k is the Boltzmann constant, N is the number of rigid links composing a single chain, and θ is the temperature.

Compressibility

If a particular application demands the modelling of the bulk compressive behavior of a hyperelastic material, it is possible to model it using an expanded version of the listed hyperelastic models where the addition of another term describes compressibility in terms of the third strain invariant I_3 and the volumetric ratio J .

$$J = \sqrt{I_3} = \lambda_1 \lambda_2 \lambda_3 = \frac{V}{V_0} \quad (13)$$

where the third strain invariant is less than 1 for bulk compressive behavior. Volumetric data is gathered using volumetric compression tests which are then curve-fit to produce coefficients for the compressive terms in a strain-energy function. For example, the Yeoh model shown below for use in ANSYS has the capability to combine equally as many volumetric compressive constants d_j as hyperelastic constants to accurately describe the volumetric change in the material.

$$W = \sum_{i=1}^N C_{i0} (I_1 - 3)^i + \sum_{j=1}^N \frac{1}{d_j} (J - 1)^{2j} \quad (14)$$

2.4.2 Hysteresis

If the cyclical stress-strain behavior of elastomers is examined, the hysteretic losses during loading cause the unloading curve to separate from the loading curve. An example for filled vulcanized rubber is shown in figure 1 where the separation of the loading and unloading curves indicates hysteresis during testing.

In elastomers, hysteresis is attributed to the thermodynamics of randomly arranged molecular chains in motion. During deformation, work is transferred onto the molecular chains which generate heat during deformation. As heat is dissipated, there is less energy present in the material during unloading than during loading. Hysteresis has a more significant effect for filled vulcanized rubbers due to a higher number of cross-links and the displacement of filler particles.

For quasi-static applications, hysteresis is of importance during material testing due to the heat generated during cyclical loading. If the strain rate is too high, an increase in temperature in the material may result in a change in material properties over the duration of the test. For practical purposes, as long as the strain rate is kept low enough and the specimens don't heat up considerably, prolonged cyclical loading may be used.

2.4.3 Mullins Effect

Mullins effect is a phenomenon characterized in 1969 by Mullins [21] where, during cyclical loading, subsequent loading cycles do not overlap and gradually 'soften'. For example, figure 2 compares the stress-strain curve for a uniaxial tensile test which was cyclically loaded at 100% strain for 5 cycles and another that was loaded at 100% strain for 1 cycle. The 5th cycle is shown to be considerably more uniform and 'softer'. Some notable observations in the cyclical testing of elastomers are [22]:

- The stress-strain curve for the first cycle is always unique and never repeated.
- The stress-strain curve will usually become repeatable after a sufficient number of pre-cycles.
- Following sufficient pre-cycling, testing at a higher level of strain will again change significantly between subsequent trials.
- Upon completing cyclical testing, the specimen will not immediately return to its initial dimensions.

While the physical explanation for Mullins effect is debated without any particularly accurate predictive models, most attribute the effect to the repeated scission and reformation of weak and strong chemical bonds within the rubber either between molecular chains or with filler particles. For practical applications and material testing, Mullins effect is mitigated by allowing sufficient pre-cycling

during a test at a constant stress or strain endpoint before accepting a final experimental stress-strain curve.

2.5 Testing of Elastomers for Hyperelastic Modelling

The complexity of modelling hyperelastic materials in a complex state of stress requires an expansive database of material test data. The characterization of hyperelastic coefficients is largely accredited to producing material test data in pure states of strain in an environment similar to the simulated application in such a way that it eliminates as much variability as possible. Some of the primary parameters requiring control are:

- Rate of loading or strain rate
- Temperature & humidity
- Overall level of extension
- Cyclical loading pattern
- Material composition & manufacturing method
- Material aging

Having control over these parameters improves the consistency of material testing results especially for the case of elastomers exhibiting prominent viscoelastic effects. While several elastomer tests exist in correspondence to several standards displaying variations of the same principals, most curve-fitters in commercial software require engineering stress and strain datasets to be as close as possible to the true stress and strain in pure states of strain. For a thorough collection of datasets for curve-fitting, the following tests should be performed at constant strain rate and temperature representing pure states of strain [23]:

- Uniaxial tensile

- Planar shear (Planar Tension)
- Equibiaxial extension
- Volumetric compression

As an added advantage, a complete package of hyperelastic tests allows the approximation of a polymer as a linear isotropic material because each pure state of strain allows the determination of any given modulus required for modelling at low strain levels (i.e., tensile, bulk and shear moduli). The following tests are based on experimental methodologies developed by Axel Products [24] for use with most ductile polymers.

2.5.1 Uniaxial Tensile Test

The simplest and most descriptive material test requires the material to be in a state of pure tensile strain provided by a uniaxial tensile test shown in figure 3. For a given strain rate and temperature, it is possible to produce an engineering stress-strain curve from which both a rubbery tensile modulus and hyperelastic coefficients can be determined. While several test standards exist describing the shape of the specimens to be in form of 'dog-bone', ring, or strip; there is no set specimen size requirement. Examples of standards include ASTM 412, ISO37, ISO527-2, and ISO527-3. However, experimental studies [17] suggest that the specimen shape does not matter so long as the gauge length is 10 times greater than the minimum width of the specimen to produce a primary elongation far greater than the thinning of the cross-section and also to mitigate the effect of the complex state of strain near the grips. Hence, the engineering stress and strain for a state of pure tensile deformation can be derived as follows:

$$\sigma_1 = \frac{F}{A_o} \quad \sigma_2 = \sigma_3 = 0 \quad (15)$$

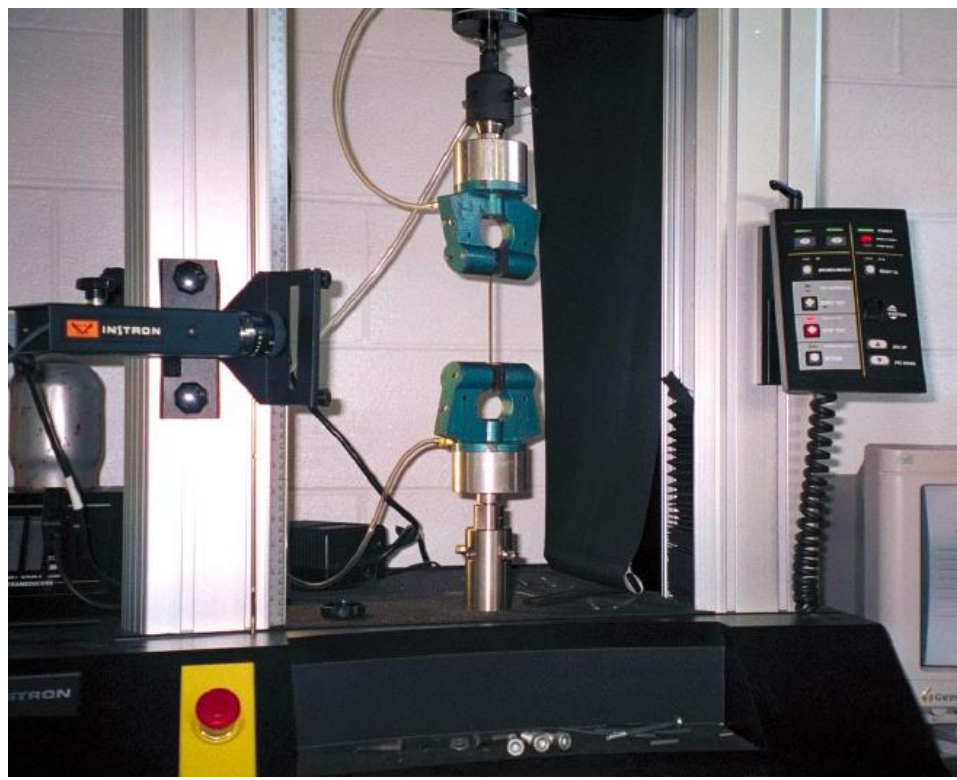


Figure 3: Uniaxial Tensile Test [22] (Used with Permission)



Figure 4: Planar Tension Test [22] (Used with Permission)

Engineering stress is derived by the use of load cell force divided by the initial gauge area.

$$\lambda_1 = \frac{L}{L_o} \quad \lambda_2 = \lambda_3 = \lambda_1^{-\frac{1}{2}} \quad (16)$$

Engineering strain is derived from the initial and final gauge length at an area near the center of the specimen through the preferable use of a non-contacting extensometer.

$$L_{sample} \geq 10 t_{min}$$

2.5.2 Planar Tension Test

The planar tension test shown in figure 4 is designed to simulate a state of pure shear while maintaining simplicity and control. Other tests exist such as dual and quadruple lap shear tests however they require the use of adhesives and other forms of constraint. The planar tension test is in essence a wide tensile test with a much shorter gauge length. As a parallel to tensile testing specimens, experimental studies [25] have determined that a specimen with a width at least 10 times larger than the gauge length can approximate a state of plane-strain through which the following equation describe the state of stress:

$$\sigma_1 = \frac{F}{A_o} = \frac{F}{w \cdot t} \quad \sigma_2 = 0 \quad \sigma_3 \neq 0 \quad (17)$$

Engineering stress is derived from the average normal stress as measured by the load cell over the cross-sectional area defined by width (w) and thickness (t).

$$\lambda_1 = \frac{L}{L_o} \quad \lambda_2 = \lambda_1^{-1} \quad \lambda_3 = 1 \quad (18)$$

Engineering strain is derived from a non-contacting measurement taken at the center of the specimen in terms of the deformed (L) and undeformed length (L_o).

2.5.3 Equibiaxial Extension Test

The biaxial extension test simulates a state of strain in which the material maintains an equal level of strain in two orthogonal directions. This requires that a planar specimen be used with all sides extended at an equal rate. This may also be done for a radial specimen in an equivalent equibiaxial test shown in figure 5.

The state of equibiaxial extension is similar to that of pure frictionless compression however the difference being in the converse manner in which the load is applied. In pure compression, load is applied axially and the extension is measured parallel to it while the specimen deforms radially. In equibiaxial extension, load is applied equally in the radial direction and extension is measured parallel to it while the specimen is free to deform axially. The disadvantage of compressive testing relates to the presence of contact friction which artificially stiffens the material behavior because of the restraining of radial deformation. The state of equibiaxial stress is described as follows:

$$\sigma_1 = \sigma_2 = \frac{F}{A_o} = \frac{F}{w \cdot t} \quad \sigma_3 \neq 0 \quad (19)$$

Engineering stress is measured as the sum of the tensile forces in each pulling cable over the sum of the cross-sectional areas for the neck of each radial ‘tab’ of width (w) and thickness (t).

$$\lambda_1 = \lambda_2 = \frac{L}{L_o} \quad \lambda_3 = \lambda_1^{-2} \quad (20)$$

Extension is measured unidirectionally at the center of the planar surface as measured by a non-contacting extensometer. It is assumed that the extension in both co-planar directions is equal as a result of perfectly radial deformation.

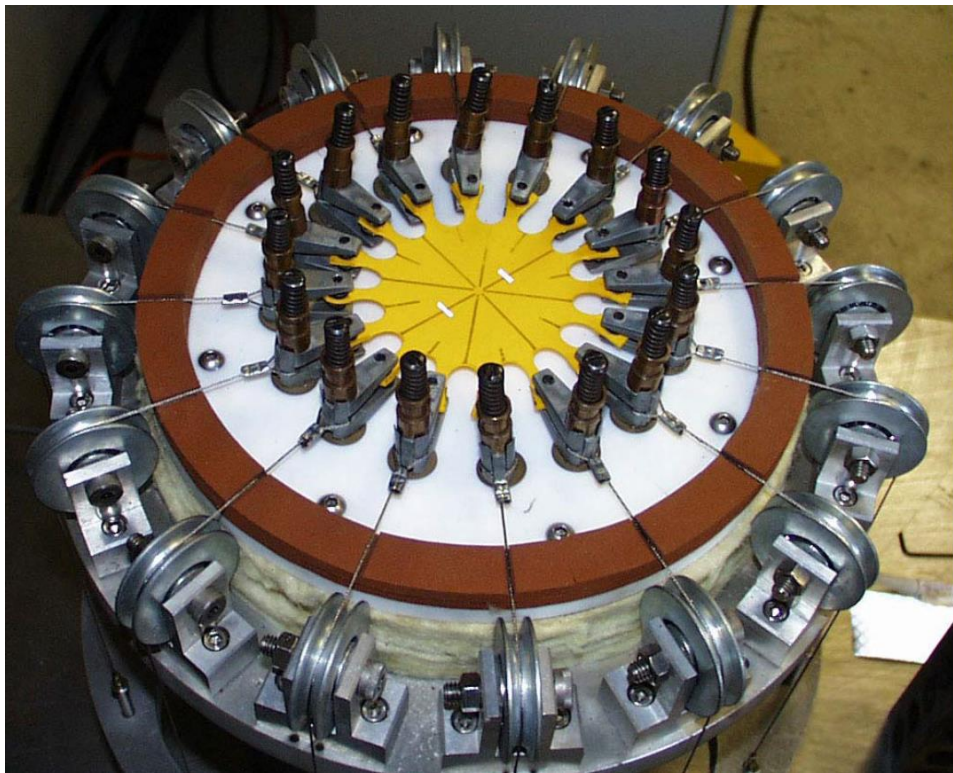


Figure 5: Equibiaxial Extension Test [22] (Used with Permission)

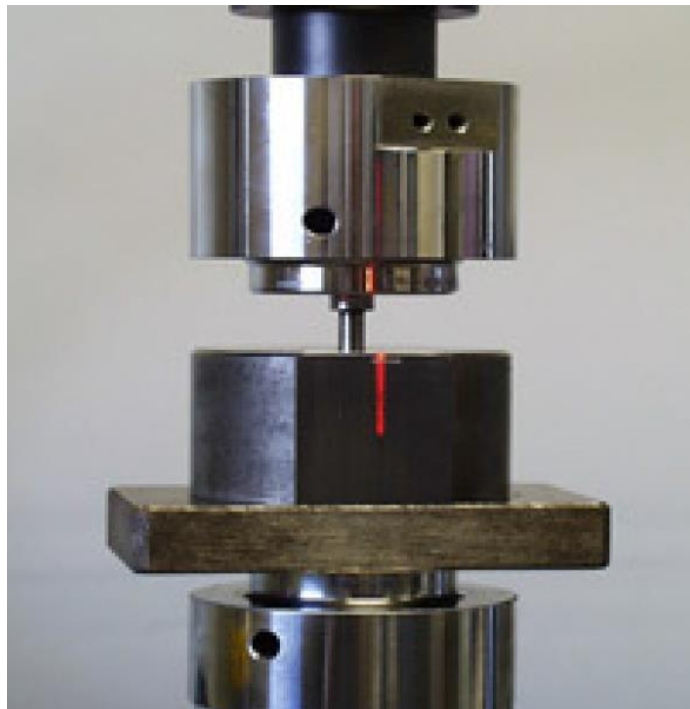


Figure 6: Volumetric Compression Test [24] (Used with Permission)

The equivalency between pure compression and equibiaxial extension can be calculated through the use of the following equations:

$$\sigma_c = \sigma_b (1 + \varepsilon_b)^3 \quad (21)$$

$$\varepsilon_c = \frac{1}{(1 + \varepsilon_b)^2} - 1 \quad (22)$$

where $\sigma_{b,c}$ and $\varepsilon_{b,c}$ are the engineering stresses and strains in biaxial extension and pure compression respectively.

2.5.4 Volumetric Compression Test

In most cases, hyperelastic materials carry the assumption that they are incompressible or that they have a Poisson's ratio of 0.5. However, in cases characterizing the bulk behavior of a polymer, it is important to include the fact that hyperelastic materials are in reality 'nearly' incompressible. Near-incompressibility rises from the fact the bulk modulus can exceed the tensile modulus by several orders of magnitude meaning that the Poisson's ratio is in fact very close but never equal to 0.5. As the Poisson's ratio cannot be directly measured, it is possible to calculate it based on the bulk modulus and the tensile modulus at low strain levels using equation 1 and equation 2.

A volumetric compression test shown in figure 6 is performed by axially compressing a cylindrical specimen or stacked buttons in a fully constrained fixture of stiffness higher than the specimen. In most cases, thick-walled steel fixtures are adequate in restraining elastomer specimens. The engineering stress is measured simply by the force over the area of the plunger while the volumetric compression ratio is calculated as the ratio of the final to initial specimen length.

2.6 Chemical Properties of Elastomers

The following section discusses properties attributed to the chemical behavior of elastomers which correspondingly change the mechanical properties. For this application, viscoelasticity and the effect of aging are discussed for consideration in the corresponding material tests.

2.6.1 Viscoelasticity

Viscoelastic behavior represents the partial combination of elastic and viscous behavior as demonstrated in figure 7. Perfectly elastic behavior closely resembles the behavior of metals under linear elastic loading. If an elastic specimen is instantly loaded with stress σ_0 and unloaded after some time t, the specimen instantly incurs the corresponding level of strain with respect to Hooke's law and fully reverses at time t. On the other hand if a viscous fluid incurs the same loading program, upon the instant application of stress, it continues to accept an increasing strain where upon unloading at time t, it retains its strain permanently. In summary, the following assumptions are made to discern the two materials for a simplified model of viscoelasticity:

- **Elastic Material:**

- Behavior is independent of loading rate
- Linear relationship between stress and strain
- Fully reversible deformation due to internal stiffness

- **Viscous Material:**

- Behavior is linearly dependent on loading rate
- No internal stiffness
- Irreversible deformation

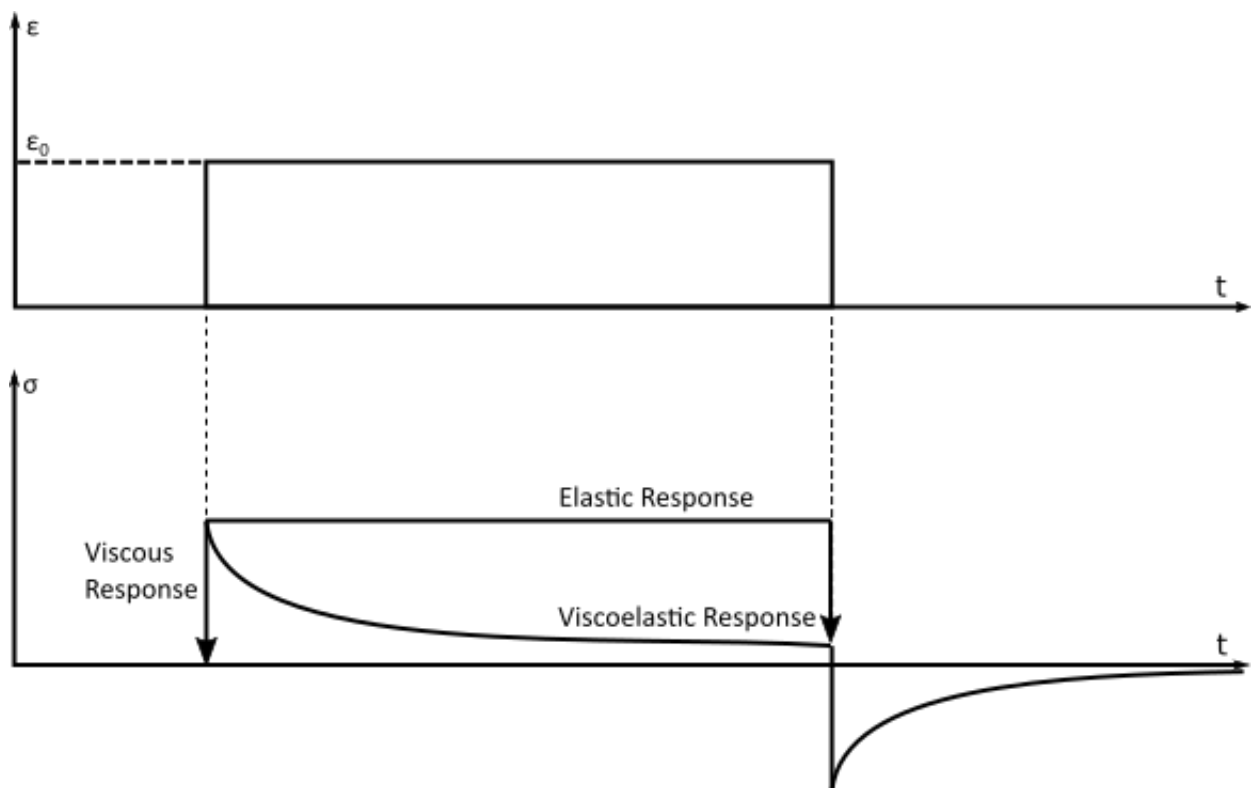


Figure 7: Elastic, Viscous, and Viscoelastic Stress-Strain Behavior

The majority of polymers exhibit phase changes dependent on both temperature and the timeframe of observation. The glass transition temperature T_g is the temperature at which a polymer transitions from being glassy to being rubbery. Below the glass transition temperature, a polymer exhibits glassy behavior while above, it exhibits rubbery behavior. Viscoelasticity is predominant at the glass transition temperature and continues to influence the material behavior within the rubbery region. Under loading, the polymer chains begin to unkink and align themselves towards the load by travelling through the free volume within the bulk of the polymer. Five sequential steps occur:

1. Rotation of side-groups about the chain axis
2. Rotation of main chain bonds
3. Uncoiling & unkinking of the chain
4. Chain sliding
5. Straightening

Each successive step contributes further deformation and takes more time to complete than its predecessor which means that at high loading rates, only a few of the steps occur rather than all of them. Moreover, in correspondence with free volume theory, the free volume is maximized at T_g which results in facilitating the chain motion. As a result, viscoelastic materials are said to be time and temperature dependent.

2.6.2 Linear Viscoelasticity

The linear behavior of an elastic solid and a viscous fluid are governed by Hooke's Law in equation 23 and Newton's Law of Viscosity in equation 24 respectively. By Hooke's Law, shear stress τ is proportional to the shear strain γ while for Newton's Law of Viscosity, shear stress is proportional to the rate of shear strain hence its time dependency. Here, G is given as the modulus of rigidity and η is the dynamic viscosity.

$$\tau = G\gamma \quad (23)$$

$$\tau = \eta \frac{d\gamma}{dt} \quad (24)$$

It is assumed that a linear viscoelastic material will satisfy both laws and thus, through the superposition of shear stresses, equation 25 is formed which serves as the governing differential equation for linear viscoelastic behavior.

$$\tau = G\gamma + \eta \frac{d\gamma}{dt} \quad (25)$$

Following equation 25, the question becomes whether it is applicable to viscoelastic materials. The answer lies in the application of the Boltzmann Superposition Principle which states that the effects of linear viscoelasticity are additive. Unlike classical superposition in linear materials however, Boltzmann Superposition depends at what time each effect occurs. Thus each application of stress causes an independent contribution to strain. However, this assumption is valid only for small deflections whereas large deflections are accounted for in non-linear viscoelastic models.

2.6.3 Creep

Creep is a property where strain, under the application of a constant stress, changes as a function of time. Considering two levels of stress, σ_0 and $2\sigma_0$, the time-dependent strain response $\varepsilon(t)$ shown in figure 8 initiates with an immediate elastic strain (ε_1) followed by a delayed elastic strain response (ε_2) where upon unloading, it is assumed that the loading strain response is applied in reverse. After a given time t , ε_2 converges to zero where the remaining strain is the Newtonian flow (ε_3).

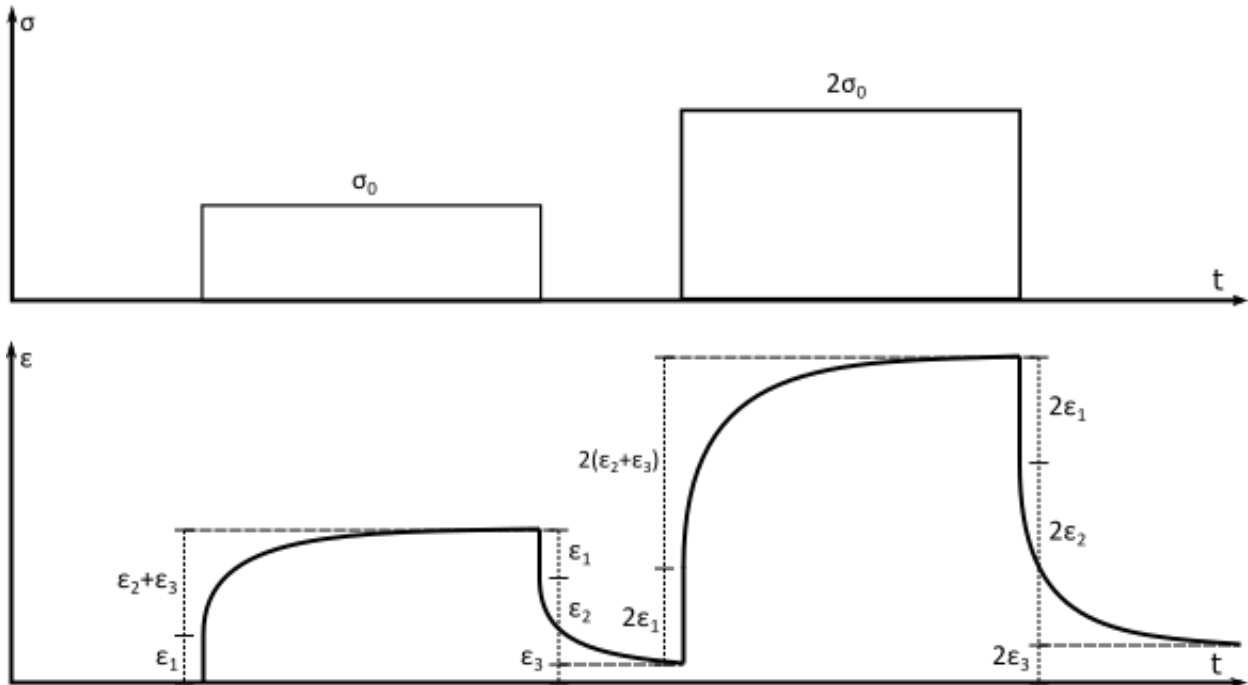


Figure 8: Creep of a Linear Viscoelastic Polymer

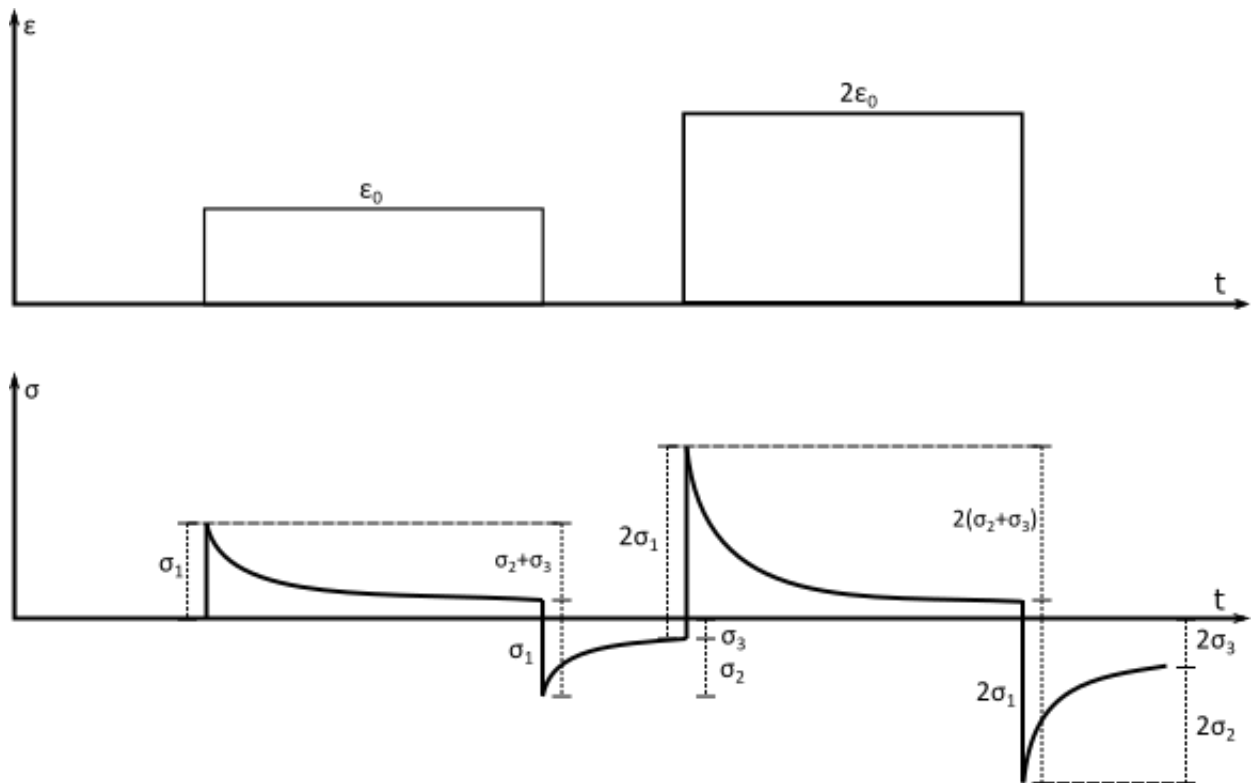


Figure 9: Stress Relaxation of a Linear Viscoelastic Polymer

Assuming a linear behavior and the additive nature of strain components, the creep compliance $J(t)$ is defined in equation 26 as a function of time to describe the strain response at a constant level of stress.

$$\frac{\varepsilon(t)}{\sigma} = J(t) = J_1 + J_2 + J_3 \quad (26)$$

J_1 describes the immediate creep compliance, J_2 is the delayed creep compliance and J_3 is due to Newtonian flow. However, due to the dependency on both the timescale and the temperature at which a loading period occurs, the creep compliance changes as a polymer incurs phase changes.

2.6.4 Stress Relaxation

Stress relaxation is the converse of creep, it is defined where stress, under the constant application of strain, changes as a function of time. Similar to creep compliance, stress relaxation defines the relaxation modulus $G(t)$ which describes the stress response as function of time under constant strain.

$$\frac{\sigma(t)}{\varepsilon} = G(t) \quad (27)$$

The difference between $J(t)$ and $G(t)$ lies in the behavior of the polymer in the same timeframe. Due to the time and temperature dependency when testing a polymer at a fixed temperature below T_g , the polymer will start glassy then become viscoelastic and rubbery and finally flow or disintegrate as a function of time. In the glassy region, the moduli J and G remain approximately constant which do not demonstrate viscoelastic behavior. In the viscoelastic region, J and G are a function of time where $J(t)$ increases with time while $G(t)$ decreases with time as shown in figure 10 and figure 11.

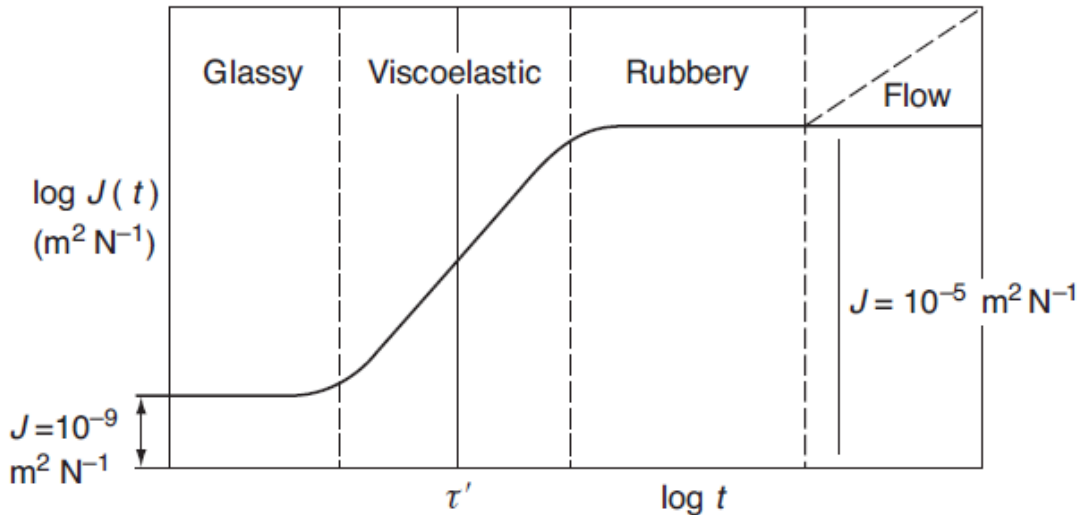


Figure 10: Time-Dependence of Creep Compliance [26] (Used with Permission)

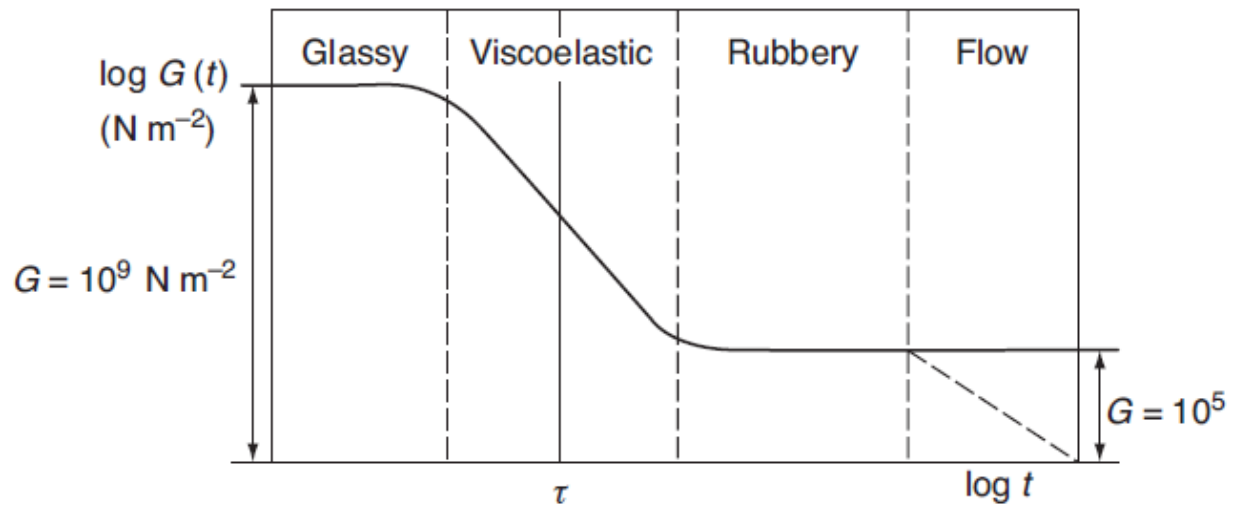


Figure 11: Time-Dependence of Relaxation Modulus [26] (Used with Permission)

The characteristic times τ' and τ are the times at which creep and stress relaxation reach a certain level of progress relating to the material properties. The two terms are called the retardation time and the transition time respectively. Additionally, due to the temperature dependency of a polymer in a constant time frame, the temperature change is said to have a similar effect to changing the time-scale.

2.6.5 Boltzmann Superposition Principle

The previously mentioned Boltzmann Superposition applies to the direct superposition of strain responses. The same applies for creep under the application of a discrete number of constant stress values contributing independent strain values. Given that assumption, it is possible to integrate stress functions as an infinite number of discrete contributions ranging from time $-\infty$ to any time t using the DuHamel integration of equation 26. Equation 28 demonstrates the sum of all stress contributions in integral form where $J(t - \tau)$ applies to a loading response delayed at time τ . The integrand of equation 28 is attributed to the delayed elastic response and the first term applies to the elastic strain response where σ is the total stress and G_u is the relaxed modulus of rigidity.

$$\varepsilon(t) = \frac{\sigma}{G_u} + \int_{-\infty}^t J(t - \tau) \cdot \frac{d\sigma(\tau)}{d\tau} d\tau \quad (28)$$

The superposition principle is visually demonstrated in figure 12 where the addition of strain corresponds to the loading of the specimen. The top image shows stress increments at time interval τ_1 , $\tau_2 \dots \tau_n$ and the corresponding addition of strain responses. The bottom image displays two independent stress-strain responses ABD and A'B'D' which superimpose to form the final response.

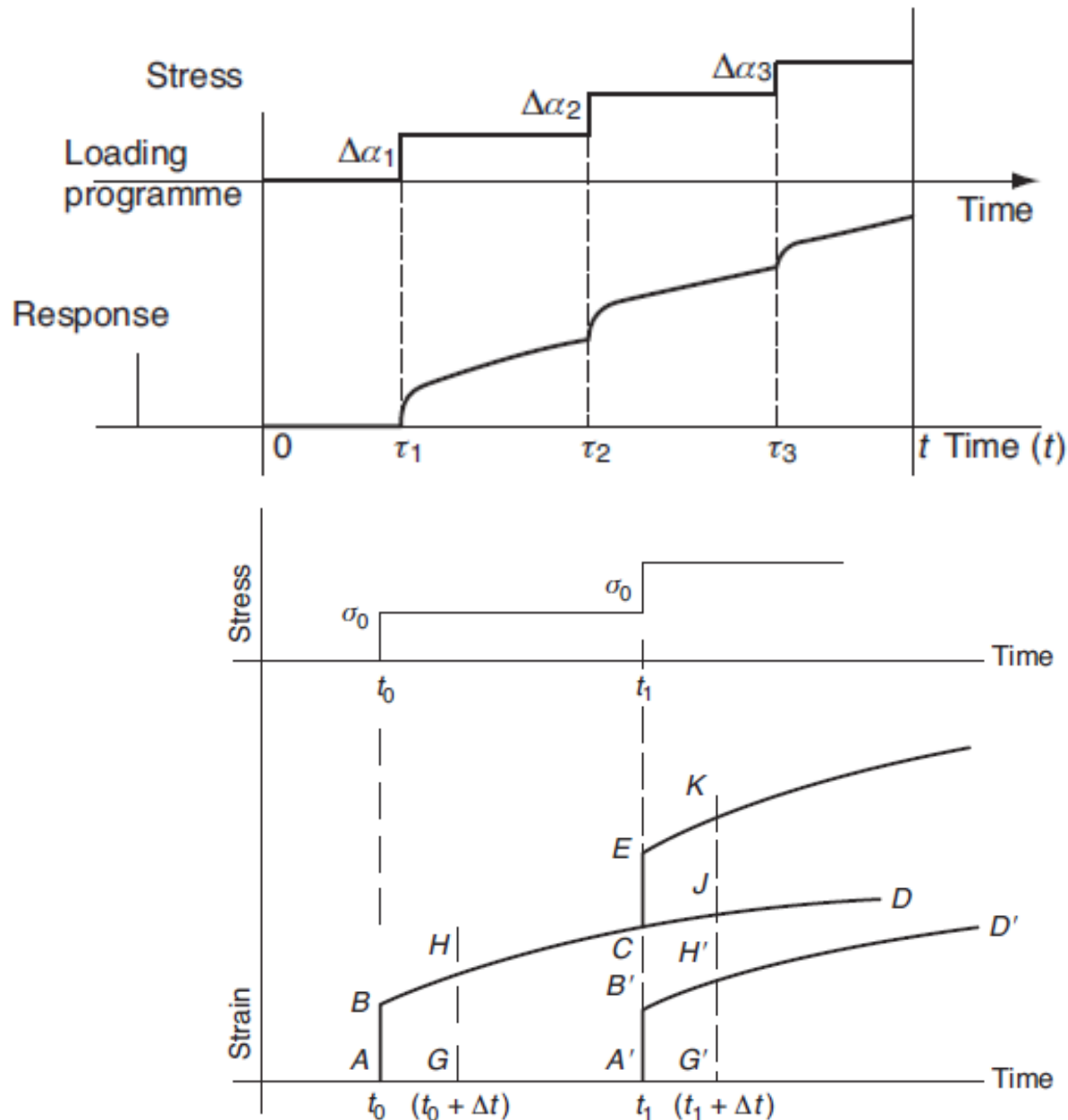


Figure 12: Boltzmann Superposition Principle [26] (Used with Permission)

One limitation to the Boltzmann superposition is attributed to the assumption that every discrete contribution of stress since the manufacture of the polymer ($t = -\infty$) contributes to the overall superposition. As a result it is assumed that one must consider the entire history of the specimen prior to testing. In fact, the deformation eventually reaches a steady-state after a certain period of time which means only recent history is relevant. This behavior is indicative that viscoelastic materials have a 'fading memory'.

2.6.6 Thermo-Rheological Simplicity

A polymer that can apply the Boltzmann Superposition Principle is said to be thermo-rheologically simple wherein load history is irrelevant and all contributing viscoelastic mechanisms have the same time and temperature dependence. Under the assumption of linear viscoelasticity and thermo-rheological simplicity, stress relaxation and creep can be predicted using linear models notably the Maxwell, Kelvin-Voight, and Standard Linear Models.

For the direct and immediate modelling of viscoelastic behavior in FEA, it is easiest to model using linear models fit to material tests in a similar range of operation as the application (i.e., temperature, timeframe, and magnitude of stress or strain). A generalized model valid for several timeframes, temperatures, and magnitudes of stress or strain would require non-linear viscoelastic modelling which is significantly more complex.

2.6.7 Aging

When elastomers are stored and used for periods of time, they are physically and chemically aged which alter the properties of the polymer. Physical aging is the tendency of an amorphous polymer to reach a state of equilibrium when aged below T_g which decreases toughness, viscoelastic response, and permeability.

Chemical aging is attributed to an ongoing change in the molecular structure as a function of time. On-going cross-linking and the rearrangement of bonds along with the oxidation caused by air or ozone on the outer surface of an elastomer cause the mechanical properties of an elastomer to change. Hardness tends to increase with age and oxidation tends to cause localized hardening and cracking on the surface. Aging is important to acknowledge when simulating rubbers because material testing may not be representative of materials with similar composition however with different histories and storage conditions.

2.7 Testing of Elastomers for Viscoelastic Modelling

The testing of elastomers for viscoelastic modelling for quasi-static analyses is accomplished using stress relaxation or creep tests. The tests can take form in several modes of strain such as those described in 2.5 because the difference only lies in the loading of the specimen. For both stress relaxation and creep tests, a fixed stress or strain is provided as a step function in that the specimen is firstly, instantaneously deformed to eliminate any viscoelastic effects during loading and secondly, held at fixed stress or strain for a period of time. The output data produced by the experiment includes time, stress, and strain with which the instantaneous tangential modulus at each measurement interval provides the change in the modulus as a function of time.

Depending on the experiment, the measured modulus can be in terms the elastic, shear, or bulk modulus. This research will make use of the Prony series which requires the relaxation of the shear and bulk moduli as a function of time. For viscoelastic testing, the following considerations must be addressed to produce consistent and accurate data:

- Each viscoelastic test should be performed at constant temperature.

- Loading should be performed as fast as possible without overshoot due to the inertia of the test fixture.
- Fresh specimens should be used for each trial.
- Viscoelastic data should not be extrapolated beyond its range of time; transitions may occur at later points in time.

Creep tests are typically simple to set up for most modes of strain. The most common type of creep test is to suspend calibrated weights on a tensile specimen where the elongation is measured at decades of time (0.1, 1, 10, 100s...). One such standard for testing vulcanized rubbers for creep is ISO 8013 [27]. Stress relaxation tests require a fixed input displacement which is best performed using screw-driven apparatuses where load is measured in decades using a load cell, strain gauge or equivalent. One such standard for testing stress relaxation in compression is ISO 3384 [28].

2.8 Elastomer Friction

By nature, the surface of solids when viewed under a microscope can be commonly described as a rough surface characterized by a random distribution of peaks and valleys. When two surfaces contact, physical contact is initiated at the location of major asperities between the two materials whereas depressions remain separated. The locations at which major asperities contact each-other produce a particular shared contact area A_i at every i^{th} asperity with an ensuing particular contact pressure p_i . When a normal force W is applied between two contacting parallel surfaces, by equilibrium, the normal force is equal to the sum of the force applied at each contacting asperity.

$$W = \sum_{i=1}^{M} p_i A_i \quad (29)$$

As the normal force increases, the individual contact areas can no longer support the entire load thereby reaching plastic flow or the yield pressure p^* . Through the deformation of major asperities, the

minor asperities support the remainder of the load over each area A_j with pressure p_j . As a result, the normal force is the sum of the force applied at the major and minor asperities.

$$W = p^* \sum_{i=1}^{M_1} A_i + \sum_{j=1}^{M_2} p_j A_j \quad (30)$$

However it can be assumed that the majority of the normal load is supported by the major asperities due to plastic deformation such that the contribution from the minor asperities is negligible.

$$W = p^* \sum_{i=1}^{M_1} A_i = p^* A_{act} \quad (31)$$

As a result of plastic deformation, the actual area A_{act} expands proportionally to support any additional increase in normal force. For metals, the plastic flow around the tips of the asperities indicates that the metal surfaces are welded together. For elastomers on rough solid surfaces, the material drapes over the asperities thereby filling the depressions causing an elastic pressure distribution. It was shown by Hertz that if it is assumed the asperities are hemispherical in shape and contact is elastic, the actual area varies with load as follows where K_1 is an elastic constant.

$$A_{act} = K_1 W^{\frac{2}{3}} \quad (32)$$

The frictional force between unlubricated surfaces is said to have two contributions. The first is due to deformation where contacting asperities deform and flow over each other under relative parallel motion. The second is due to adhesion caused by chemical bonding. If the force contributions F are divided by the normal load, the friction coefficients μ_{def} and μ_{adh} for deformation and adhesion are obtained.

$$\frac{F}{W} = \mu_{def} + \mu_{adh} \quad (33)$$

To minimize friction, it is thus required to minimize deformation and adhesion. To minimize deformation, the contacting surfaces must be ground or polished until major asperities are smoothed out; such a surface is called ‘optically-smooth’. To minimize adhesion, lubricating the surfaces helps prevent the chemical bonding of the contacting surfaces and introduces an intermediate surface which can flow or slide easily. Traditionally, friction was described from the early works of da Vinci, Amontons, and Coulomb:

1. Friction force is proportional to normal load.
2. Coefficient of friction is independent of apparent contact area (i.e., perceived area).
3. Static coefficient is greater than the kinetic coefficient.
4. Coefficient of friction is independent of sliding speed.

While these laws hold as an approximation to describe most cases based on observation, they do not fully apply to elastomers. The first law only applies up until the actual area is equal to the apparent area. The second applies only to materials with yield points. The third does not apply to viscoelastic materials. The fourth is not true for any material. As a result, for elastomers, specialized friction models have been produced to characterize specific loading cases which seldom describe any other. However, some fundamental concepts exist to describe elastomeric friction.

It was experimentally demonstrated by Bartenev and Lavrentjev in 1961 [29] that vulcanized rubbers sliding across smooth steel and aluminum surfaces exhibit both a linear and non-linear relationship between the tangential frictional stress and the applied normal pressure. It was classically stipulated by Coulomb’s law that frictional and normal stresses are linearly proportional. Lesser known, it was stipulated by Thirion’s law [2] that rubbers at high pressures on hard non-lubricated surfaces exhibit a non-linear proportionality between tangential and normal stresses. Coulomb’s law and Thirion’s law take the form of equation 34 and equation 35 respectively:

$$F_T = \mu F_N \quad (34)$$

$$\frac{1}{\mu} = a + bF_N \quad (35)$$

where F_T is the tangential force, F_N is the normal force, and a & b are constants. In this form, Thirion's law is used in conjunction with Coulomb's law. Additionally, it was experimentally demonstrated that Thirion's law was able to accurately predict highly elastic material friction on lubricated surfaces [30].

Bartenev and Lavrentjev determined that for vulcanized rubbers sliding on smooth surfaces, Coulomb's law applied for low normal pressures (0.05 to 10 kg/cm²) and Thirion's law applied for high normal pressures (10 to 200 kg/cm²) and proposed a model combining the two laws:

$$\frac{1}{\mu} = \frac{1}{C} \cdot \frac{1 + \alpha\rho}{\frac{S_o}{S_N}\rho} \quad (36)$$

where C and α are constants, ρ is the nominal normal pressure ($P = \rho S_N$), S_N is the nominal contact area, and S_o is the residual contact area at $\rho \rightarrow 0$. Despite describing both Coulomb's Law and Thirion's Law, equation 36 cannot be formulated with simple frictional tests due to its requirement for well-defined apparent contact areas.

2.9 Testing of Elastomers for Frictional Modelling

The experimental frictional characterization of elastomers is difficult for a number of reasons. Similar to hyperelastic testing, the same dependencies exist at a microscopic scale at the interface between two dissimilar materials experiencing contact and relative motion. As the material deforms into and overtop of the asperities of a stiffer material such as steel, there is equally a time and temperature dependence of the elastomer in motion. However, this behavior is very difficult to characterize theoretically. To make effective use of this model, frictional testing must conform to the following criteria to maintain an equivalency to the real-world application:

- Constant temperature and humidity
- Constant material composition and age
- Constant sliding velocity
- Constant normal pressure
- Identical mating surface (materials, surface roughness, lubrication)
- One fresh specimen per trial

In most cases, low normal pressures can be characterized using a sled test shown in figure 13 in which a flat rectangular specimen is placed under a number of weights and paired to a contact surface. The specimen is tethered to an actuator with a load cell and displacement sensor. The test involves pulling the specimen under constant normal force and relative sliding velocity while measuring the ensuing frictional force and displacement parallel to the surface. The experimental output describes the friction coefficient as a function of displacement which is calculated using:

$$\mu(x) = \frac{F_T(x)}{F_N} \quad (37)$$

where μ is the friction coefficient, F_T is the measured tangential force, and F_N is the applied normal force. For high levels of normal pressure where the use of weights is unfeasible, it is possible to apply large normal pressures using hydraulic actuators. One effective experiment for use with higher normal pressures is an axial-torsion friction test shown in figure 14 where a hydraulic actuator capable of rotating at a fixed rotational velocity applies a given normal force on a steel cup with a thin wall thickness pressed directly onto a specimen. The lower side of the specimen is fixed to a platen while the upper side of the specimen is being pressed on by the rotating steel cup. An axial-torsion load cell consequently records the normal force and the torque on the steel cup.

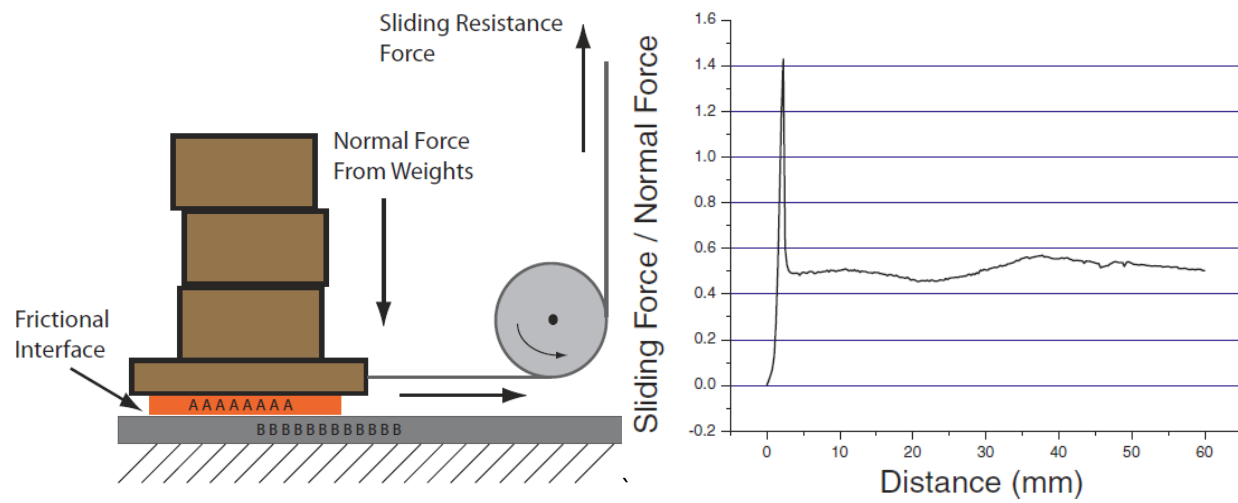


Figure 13: Sled Test for Frictional Testing [31] (Used with Permission)

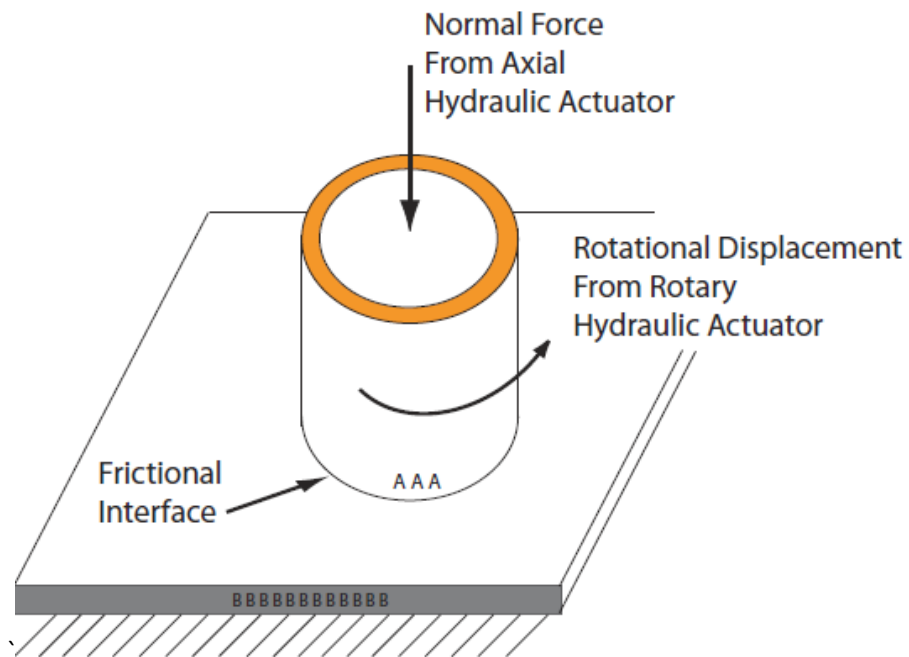


Figure 14: Axial-Torsion Test for Frictional Testing [31] (Used with Permission)

The friction coefficient can be characterized as a function of tangential displacement using the following relation:

$$\mu(x_T) = \frac{2 \cdot T(x_T)}{d_{nom} \cdot F_N} \quad x_T = \frac{\theta \cdot d_{nom}}{2} \quad (38)$$

where $T(x_T)$ is the measured torque, d_{nom} is the nominal cup diameter, and θ is the angular displacement. One axial-torsion test is able to measure the static and kinetic coefficients at a constant normal force and relative sliding velocity. Several tests must be performed to create a dataset of friction coefficients at various normal pressures.

When testing elastomers in friction, it is important to acknowledge certain phenomenon which may affect results. Firstly, as the specimen is pulled across surface, hysteretic losses generate heat build-up which may alter the properties of the elastomer during the test. Secondly, due to the difference in hardness of the two surfaces, the elastomer will experience damage to the contact interface immediately after sliding begins. Thirdly, the contact surfaces may alter and become contaminated following each test especially at high pressures. These sources of inconsistency are simply mitigated by using fresh specimens for each trial, maintaining a low relative sliding velocity, and cleaning and re-abrading contact surfaces after each test.

2.10 Material Models

The following section is a description of the material models selected for use with 2D planar and contact elements in ANSYS.

2.10.1 Hyperelastic Models

Hyperelastic models in FEA are input as strain-energy functions in the form of various models previously discussed in 2.4.1. Their use in ANSYS requires curve-fitting of experimental data to produce the required coefficients to complete a model of a given order.

For a given strain-energy function, the second Piola-Kirchhoff stress tensor S_{ij} can be derived by differentiating the strain-energy function in terms of the LaGrangian strain tensor E_{ij} and the Cauchy-Green deformation tensor C_{ij} .

$$S_{ij} = \frac{\partial W}{\partial E_{ij}} \equiv 2 \frac{\partial W}{\partial C_{ij}} \quad (39)$$

The Cauchy-Green strain tensor is expressed in terms of the components of the deformation gradient F_{ij} .

$$\begin{aligned} F_{ij} &= \frac{d(X_i + u_i)}{dX_j} \\ C_{ij} &= F_{mi} \cdot F_{mj} \end{aligned} \quad (40)$$

where X is the undeformed position and u is the displacement from X to the deformed position ($x = X + u$). The LaGrangian strain may be expressed in terms of the Cauchy-Green deformation tensor and the Kronecker delta.

$$\begin{aligned} E_{ij} &= \frac{1}{2} (C_{ij} - \delta_{ij}) \\ \delta_{ij} &= \begin{cases} 1 & i=j \\ 0 & i \neq j \end{cases} \end{aligned} \quad (41)$$

Through algebraic manipulation of equation 39, the Cauchy (true) stress tensor can be derived in terms of the Cauchy-Green strain tensor and the strain-energy function.

$$\sigma_{ij} = -p\delta_{ij} + 2 \frac{\partial W}{\partial I_1} C_{ij} - 2 \frac{\partial W}{\partial I_2} \frac{1}{C_{ij}} \quad (42)$$

where p is the hydrostatic pressure. In summary, the stresses and strains for a hyperelastic material can be written in matrix-form in any configuration of the principal stretch ratios using a strain-energy function fit to experimental data in pure states of strain.

2.10.2 Frictional Models

The simplest form of frictional modelling in ANSYS is through the use of a simple stick-slip Coulomb's Law in terms of a limiting frictional tangential stress τ_{lim} . Slip occurs when the equivalent friction stress τ exceeds τ_{lim} , and stick when τ_{lim} is not exceeded as summarized in figure 15.

$$\begin{aligned}\tau_{lim} &= \mu P + b \\ \|\tau\| &\leq \tau_{lim}\end{aligned}\tag{43}$$

where μ is the friction coefficient, P is the normal pressure, and b is the contact cohesion which may be adjusted to allow sliding resistance at zero normal pressure. As an extra feature for CONTA174 elements, a maximum allowable shear stress τ_{max} can be defined.

A second model is also provided to model slip-velocity dependent decay between a static and kinetic friction coefficient:

$$\mu = \mu_k \left(1 + \left(\frac{\mu_s}{\mu_k} - 1 \right) e^{-DC \cdot V_{rel}} \right)\tag{44}$$

where the friction coefficient can decay between the static and kinetic friction coefficients μ_s and μ_k at a decay rate determined by the decay coefficient DC as a function of the relative velocity between the 2 surfaces V_{rel} . An example is shown in figure 16 which demonstrates a 99% decay at a velocity of 1 mm/s for static and kinetic friction coefficients of 0.5 and 0.4 respectively.

Unfortunately, to create a custom frictional model, the use of continuous friction functions requires complex user-defined subroutines to dynamically adjust the friction.

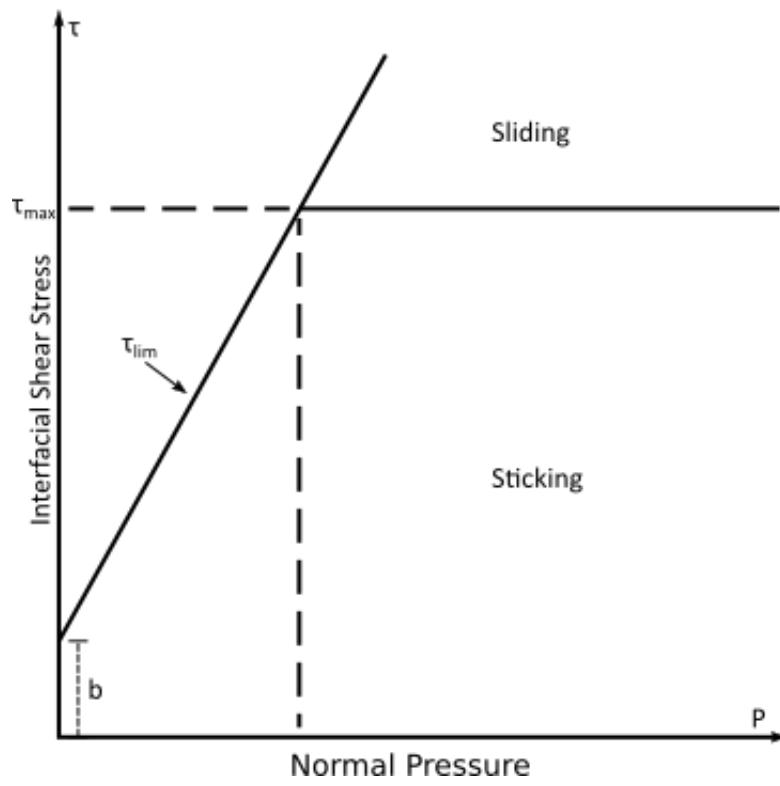


Figure 15: Coulomb's Law in ANSYS

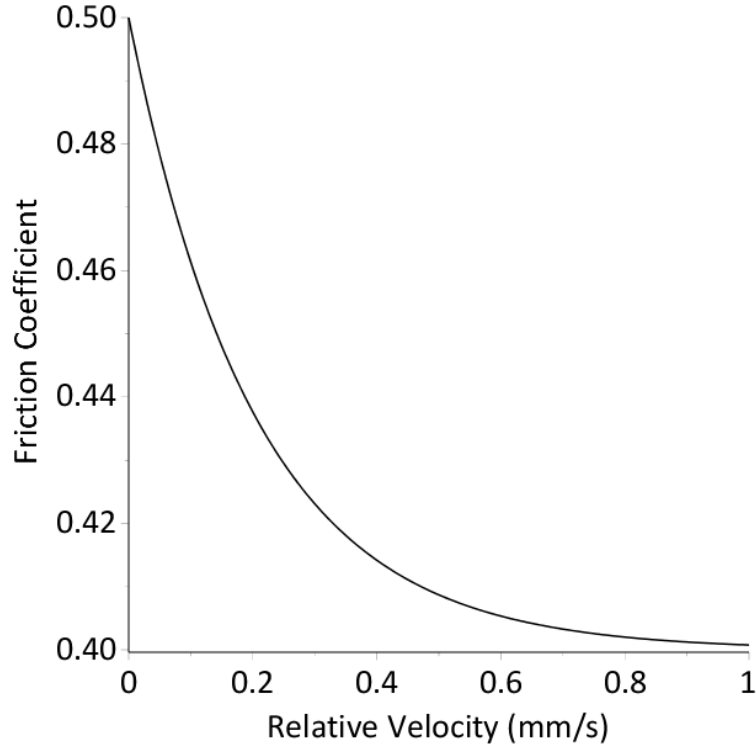


Figure 16: Velocity-Dependent Frictional Decay Model

However, if a continuous function is converted into a discrete piecewise dataset, ANSYS is able to accept tabulated friction coefficients as a function of time, temperature, normal pressure, sliding distance, or relative sliding velocity which are subsequently linearly interpolated between 2 adjacent intervals for intermediate values. Beyond the minimum and maximum endpoints of the tabulated values, the friction coefficient is assumed constant rather than extrapolated.

2.10.3 Viscoelastic Materials

For linear viscoelasticity in quasi-static loading, stress relaxation and creep are simulated by directly modifying the shear and bulk moduli as a function of time. It was previously explained in 2.6.3 and 2.6.4 that the creep compliance and relaxation modulus change as a function of time given a constant stress or strain. A Prony series captures the change in the shear and bulk moduli based on experimental data and normalizes the function in terms of shear and bulk moduli that are generated using a hyperelastic model rather than using fixed shear and bulk moduli. The Prony series can be used under the following assumptions:

- The material is thermo-rheologically simple; its viscoelastic behavior is not dependent on time or temperature.
- The material is linearly viscoelastic.
- The viscoelastic behavior does not change with the magnitude of stress or strain.

The shear $G(t)$ and bulk $K(t)$ moduli represented by the Prony series are shown in equation 45 and equation 46 respectively:

$$G(t) = G_{\infty} + \sum_{i=1}^n G_i \exp\left(-\frac{t}{\tau_i}\right) \quad (45)$$

$$K(t) = K_{\infty} + \sum_{i=1}^{n_K} K_i \exp\left(-\frac{t}{\tau_i^K}\right) \quad (46)$$

where G_{∞} & K_{∞} are the moduli at $t \rightarrow \infty$, G_i & K_i are the moduli at a point in time, and $\tau_i^{G,K}$ is the relaxation time for each term in the series. The shear and bulk Prony series are subsequently curve-fit to experimental data using a non-linear absolute or normalized least-squares curve-fitting algorithm. The result of curve-fitting is normalized in terms of G_o and K_o ; the modulus at $t = 0$ as shown below:

$$\frac{G(t)}{G_o} = \alpha_{\infty}^G + \sum_{i=1}^{n_G} \alpha_i^G \exp\left(-\frac{t}{\tau_i^G}\right) \quad (47)$$

$$\frac{K(t)}{K_o} = \alpha_{\infty}^K + \sum_{i=1}^{n_K} \alpha_i^K \exp\left(-\frac{t}{\tau_i^K}\right) \quad (48)$$

where $\alpha_{\infty}^{G,K}$ is G_{∞}/G_o & K_{∞}/K_o and $\alpha_i^{G,K}$ is G_i/G_o & K_i/K_o . The normalized Prony series can thus draw upon the shear and bulk moduli calculated using the hyperelastic model which represents the change in the moduli at any level of strain rather than using static values for shear and bulk moduli.

If the Prony series is used for stress relaxation, the decay in the modulus at a constant strain will decrease the stress. Conversely, if the Prony series is used at constant stress, the decay in the modulus will increase the strain.

2.11 Curve Fitting

For the implementation of the hyperelastic and viscoelastic models, curve-fitting was required to develop the models based on experimental data. For the hyperelastic and viscoelastic models, 2 types of curve-fits exist: normalized and absolute each relying on linear or non-linear least-squares fit. For simpler hyperelastic models such as Mooney-Rivlin, Yeoh, and Neo-Hookean, ANSYS employs a linear

least-squares fitting procedure with different stress and strain input data depending on different cases.

Three cases exist which requires a different organization of the input experimental data [32]:

- Totally Incompressible
- Nearly Incompressible
- Compressible

The NBR composing the seal is considered to be of type 2 given that the expected state of highly constrained deformation may require simulated compressibility for an accurate representation. The data must be input as shown in table 1 for the experiments shown.

The benefit of using Axel Products' hyperelastic testing package is that the obtained engineering stress and strain data can be directly input into ANSYS for curve fitting. However, the same loading curve from each type of experiment at the desired loading cycle and level of elongation must be isolated. Each curve must then be offset such that the beginning of the loading curve starts at the origin (0,0). Otherwise, a certain amount a permanent or temporary deformation and slack may offset the data away from the origin and impair the curve fitting procedure. With the data, a linear absolute least-squares fit in ANSYS [33] takes the form of the following equation:

$$E = \sum_{i=1}^n \left(\sigma_i^E - \sigma_i(C_j) \right)^2 \quad (49)$$

where E is the least squares error, σ_i^E is the engineering stress of a certain experiment, and $\sigma_i(C_j)$ is the curve-fit stress value based on C_j , one of the fitting coefficients for the hyperelastic model. The normalized least-squares fit is an alternative fitting procedure which takes the form of:

$$E = \sum_{i=1}^n \left(\frac{\sigma_i^E - \sigma_i(C_j)}{\sigma_i^E} \right)^2 \quad (50)$$

Table 1: Case 2 Experimental Input [32]

Experimental Type	Column 1	Column 2	Column 3
Uniaxial Test	Engineering Strain	Engineering Stress	
Biaxial Test	Engineering Strain	Engineering Stress	
Planar/Shear Test	Engineering Strain (in loading direction)	Engineering Stress	
Simple Shear Test	Engineering Shear Strain	Engineering Shear Stress	(Optional) Engineering Normal Stress (normal to the edge of shear stress)
Volumetric Test	Volume Ratio (J)	Hydrostatic Pressure	

which tends to favor the entire range of experimental stress data equally which is generally accepted to produce a better fit.

The least squares error in a linear curve-fit is minimized by setting the variation of the square error δE^2 to zero which yields a series of equations which can be solved for the hyperelastic coefficients (C_i) as shown:

$$\frac{\partial}{\partial C_n} E^2 = 0$$

The fitting process is performed iteratively until a best-compromise fit is achieved across all experimental datasets. A non-linear least-squares fit is used for more complex hyperelastic models such as Ogden, Arruda-Boyce, and Gent which from an operator's standpoint requires nearly the same amount of user input as a linear least-squares fit however one must employ a coefficient feedback process to achieve a best fit. The user performs this by producing an initial curve-fit using experimental data, examining the curve-fit to see whether it is sufficient, and if insufficient, feeding the curve-fit coefficients as 'seeds' into another curve-fit iteration and repeating the process until the curve-fit converges to an unvarying set of coefficients.

The viscoelastic curve-fitting procedure for a Prony series is similar to that for a hyperelastic model. Employing a similar absolute and normalized least-squares curve-fit, one inputs the relaxation modulus as a function of time for shear and bulk stress relaxation, selects whether the fit is absolute or normalized and examines the curve-fit. If the curve-fit is insufficient, the user can opt for more coefficients to the series for a more accurate but computationally expensive fit.

Chapter 3: Methodology

The following chapter discusses and details the methodology developed to examine the axial-compressive behavior of the seal constrained in a pipe. All aspects of developing the FE model are discussed in detail in this chapter.

3.1 Experiment

To explore the compressive behavior of an annular elastomer seal under axial compression and to produce data for the experimental validation of the FE model, Shaha [3] developed an experiment to control the axial compression of a constrained annular seal. The experiment provided visual and numerical data pertinent to characterizing the compressive behavior of the seal. The following is a brief summary describing the experimental methodology and identifying the pertinent elements for its combined use with a FE model.

Two different size seals were provided for testing as shown in figure 17. Each is made of Spareage NT-5A NBR with a SHORE A hardness of approx. 78. The manufacturer's specification is shown in Appendix A. The age and previous history of these seals were unknown however it was known that these seals were previously in service. A single 102.5 mm seal was purchased created from the same material and batch as the hyperelastic material test samples. The dimensions for these seals are listed as follows in terms of the Outer Diameter x Inner Diameter x Thickness.

- Seal A: 96.3 x 47 x 31.5 mm
- Seal B: 102.5 x 47 x 31.5 mm

An experimental jig was designed to control the compression of the seals and to restrain and align them concentrically within a pipe shown in figure 18.

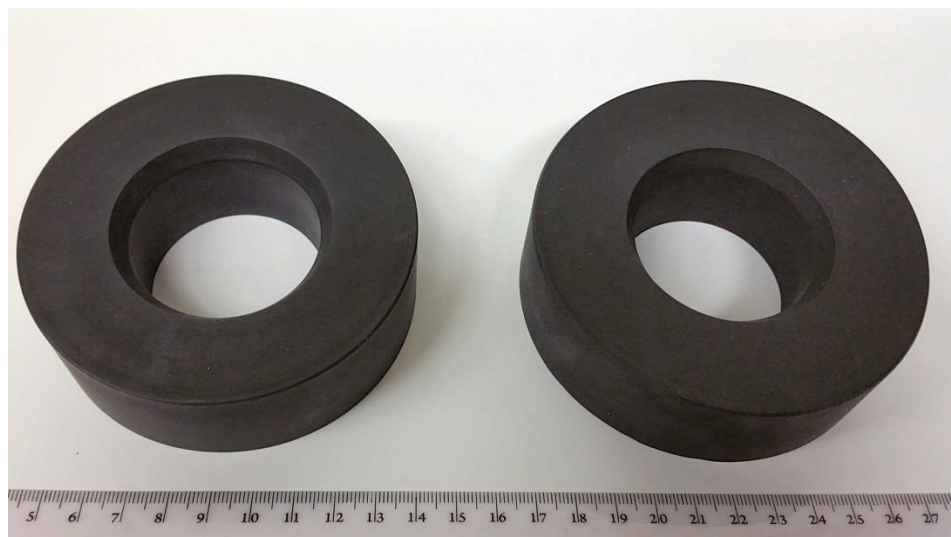


Figure 17: Seals Tested – Left to Right: A, B

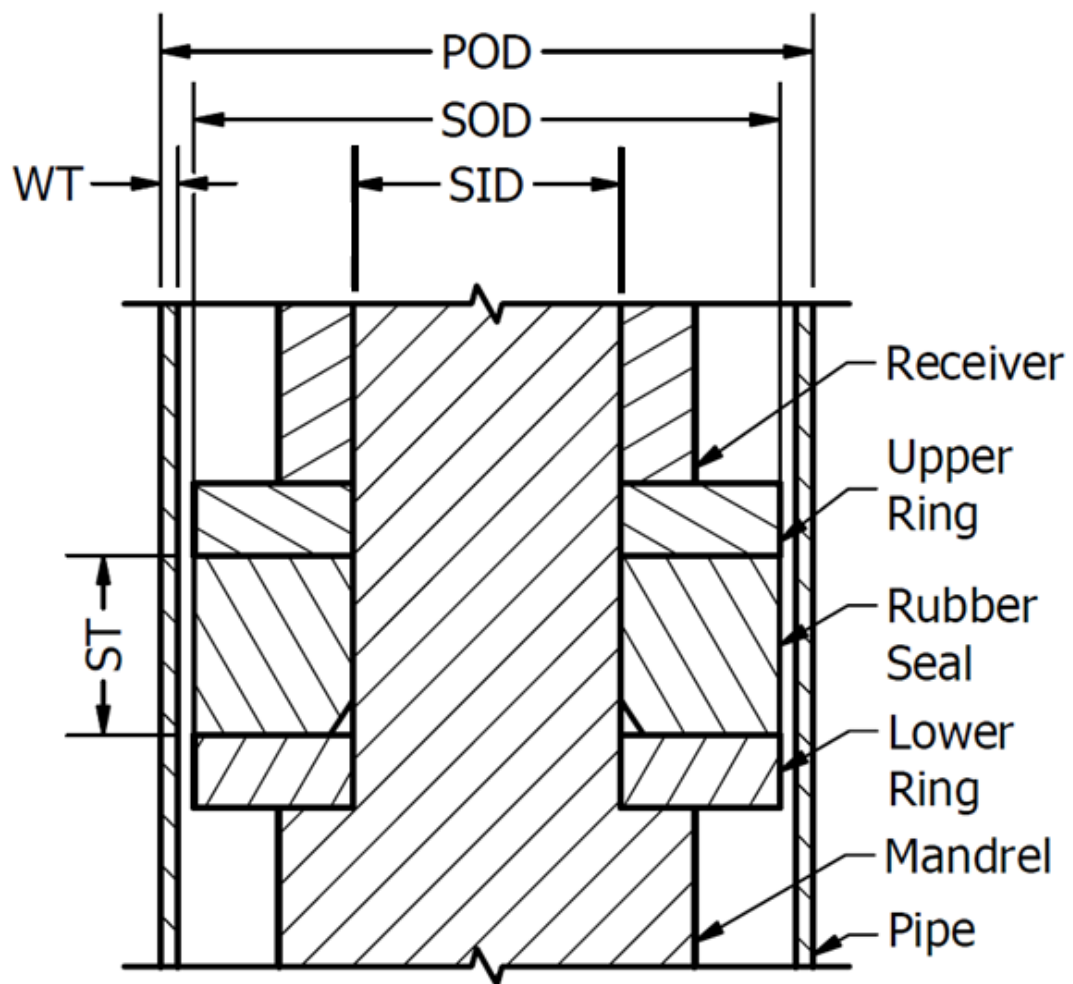


Figure 18: Experimental Jig Cross Section

The NBR seal, sandwiched between two annular steel rings with inner and outer diameters equal to those of the seal, was mounted on a mandrel that held the seal at the center of a 200 mm long segment of steel pipe sized as per ASME B36.10M [34].

The pipe length was selected based on Roark's formulas for stress and strain, table 31.2, case 12 [35] which approximates the strain gradient of a thin-wall pipe caused by a localized uniform internal pressure. Case 12 applies to pipes of 'infinite length' which requires one fixed end and one open end with a uniform localized pressure at a distance away from either end sufficiently far enough to neglect the effects of the strain gradient at the ends of the pipe.

The experiment was designed in a way that could incorporate several seal sizes that correspond to different pipe sizes. Table 2 shows the pipe-to-seal pairings for the experiment. The mandrel passes through the center of the two rings and the seal and slides into a hollow receiver. The mandrel moves up compressing the lower ring and the seal against the upper ring held in place by the stationary hollow receiver.

The entire compression jig assembly was inserted into an Instron electro-hydraulic 250 kN load frame where the mandrel was threaded onto a hydraulic actuator and the receiver was threaded onto a load cell. The load frame allowed for experiments to be performed using load-control, displacement-control, or both each being capable of cyclical loading. The entire assembly is shown in figure 19. In order to control and accurately examine the behavior of the rubber seal, the following experimental parameters were controlled to ensure that consistent datasets could be developed:

- Temperature and humidity
- Strain rate
- Pipe & seal size
- Seal-ring contact interface conditions

Table 2: Pipe-Seal Pairings

Seal (SOD x SID x ST)	Pipe Schedule	Pipe Dimensions (POD x WT x LENGTH)
96.3 x 47 x 31.5	4" NPS Schedule STD	114.3 x 6.02 x 200
102.5 x 47 x 31.5	4" NPS Schedule 10	114.3 x 3.05 x 200

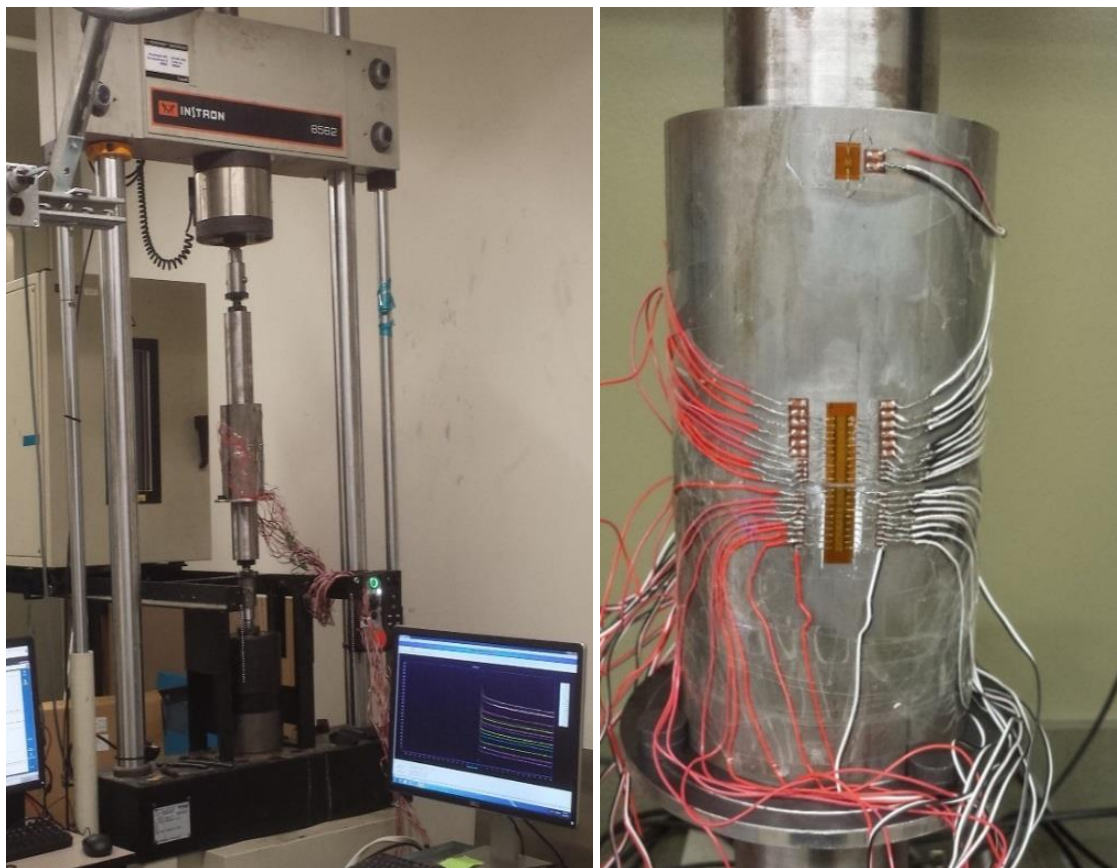


Figure 19: Experimental Setup

Based on the specific input parameters, 3 sets of data were produced for analysis. The first was the load-displacement-time output from the load frame. The second was contact pressure measured at the contact interface between the pipe wall and the seal using FujiFilm Pressure Indicating Film [36] for pressures of 2.5 to 10 MPa. The Fujifilm Prescale is composed of two sheets which are mated facing each-other; one sheet is a micro-encapsulated color-forming layer and the other is a developer. When pressure is applied onto the two sheets, micro-capsules containing a color-forming chemical ruptures relative to the amount of contact-pressure, the chemical deposits onto a developer which displays a color of varying intensity which is read optically relative to a pre-calibrated visual scale. Thus it is possible to obtain a one-time static reading of the maximum pressure applied over a period of time. The advantage to this technique is that the film requires very little thickness and can be cut into any shape which offers great flexibility in the contact pressure measurement. The disadvantages are that the film pairs are of one-time use only, the pressure-sensitive range is limited, and the accuracy of the measurement as read by a scanner and software, is approx. 10% [37].

The third data source is produced via strain gauge chains placed on the membrane of the steel pipes aligned parallel to the direction of hoop strains. The strain gauges shown in figure 19 were used for the analysis of the 4" Sch. 10 pipe as a baseline for the FE model development. 2 strain gauge chains containing 10 gauges each were aligned end-to-end at the mid-length of the pipe. Each chain has a measuring grid length of 1.7 mm and a pitch of 2 mm all with a resistance of 120 ohms providing a near-continuous hoop strain gradient. All strain gauges were operated using a Vishay 7000 series 32 channel data acquisition system using StrainSmart software. The output data included hoop strain readings as a function of time.

3.2 Hyperelastic Testing

In 2.4.1, it was discussed that the NBR composing the seals are best modeled using a hyperelastic model. To develop a hyperelastic model suitable to large deformation, 4 tests have been discussed to isolate pure states of strain such that curve-fitting can provide a best compromise for any mixed state of strain. These tests are the uniaxial tension, planar tension, equibiaxial extension, and volumetric compression tests.

Testing was performed in correspondence with Axel Products using their proprietary test methodologies to create consistent datasets between each test. Several sources of error and inconsistency exist when testing elastomers:

1. Different chemical compositions between each specimen.
2. Different histories for each specimen.
3. Inconsistency between subsequent loading cycles due to Mullins effect.
4. Inconsistencies in set up between individual specimens (e.g., alignment, slack in the system).
5. Difference between true stress/strain and engineering stress/strain due to cross-sectional thinning during testing at large deformation.

The first inconsistency was remedied by ensuring all specimens were created from the same batch of rubber and stored away from UV light at constant temperature and humidity. The second was eliminated by ensuring no specimen was re-used for analysis; all testing was performed on fresh specimens.

The third inconsistency was controlled using Slow Cyclical Loading (SCL) proprietary to Axel Products. Due to Mullins effect, SCL was designed to mitigate all of the listed observations by ensuring each strain level measurement is based on stabilized behavior. For this experiment, the strain levels

were 20, 40, 60, and 100%. The experiment starts by cyclically loading and unloading the specimen 5 times up to 20% strain then moving onto 40% and cycling another 5 times, and so on at a fixed strain rate. Each SCL test was repeated for 3 trials using a fresh specimen for each. SCL was performed for the uniaxial tension, planar tension, and equibiaxial extension tests. Examples of the specimens are shown in figure 20.

Inconsistencies 4 and 5 are normally up to the operator to mitigate however these experiments used a non-contacting laser extensometer which can measure the extension over the gaging area to a high degree of accuracy. Thus, error in the rubber specimen strain measurement was greatly reduced because the measurement was taken directly from the specimen without physical interference.

Volumetric compression tests were much simpler to set up as compared to the hyperelastic tests. Six small fully-constrained elastomer buttons were stacked in a rigid steel cylinder and a plunger compressed them creating a state of uniform hydrostatic pressure within the rubber specimen inside the steel cylinder as shown in figure 21. The plunger was lowered at a constant strain rate and the ensuing stress-strain curve provided the data for volumetric compressibility. 3 trials were performed for consistency.

The hyperelastic and volumetric compression test packages were performed for 2 constant strain rates at room temperature. The first strain rate tested was 0.05 s^{-1} because it was the fastest available test speed for Axel Products. The second strain rate tested was 0.00264 s^{-1} which corresponded to testing a 31.5 mm thick seal at 5 mm/min selected by Shaha [3].

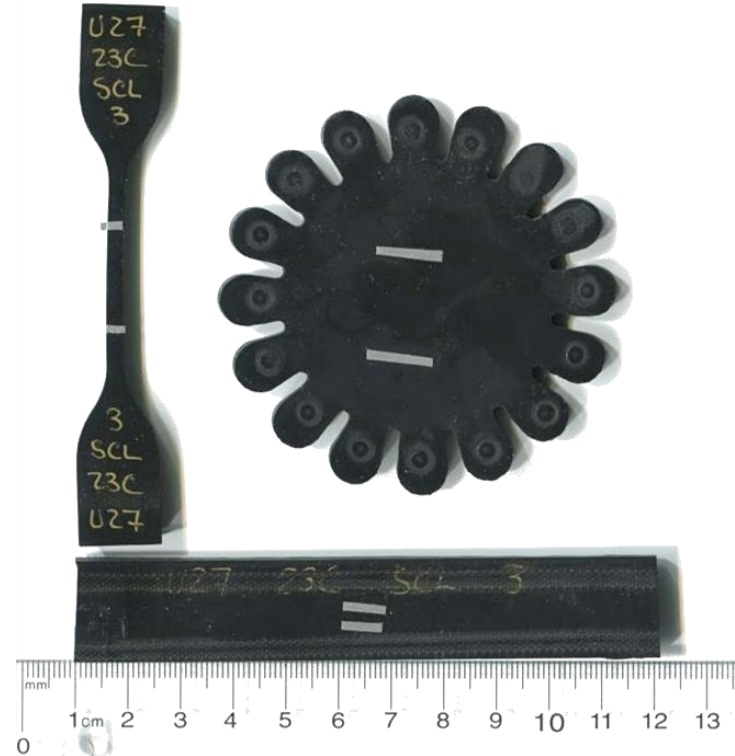


Figure 20: Hyperelastic Test Specimens



Figure 21: Volumetric Compression [22] (Used with Permission)

3.3 Frictional Testing

It was observed by Gent [5] and demonstrated experimentally by Shaha [3] that the apparent compressive modulus of a disk or annulus in axial compression is dependent upon the friction at the contact surfaces between the compressive platens and the rubber. In general, an increase in the apparent compressive modulus occurs with an increase in the friction coefficient. Shaha additionally observed that the contact pressure and pipe strain in a sealing application is dependent on friction by examining 2 cases. In one case, the compressive platens were abraded with 400 grit sandpaper and in the other, the contact surfaces were lubricated with Lubriplate No. 105 petrolatum-based grease. It was important to characterize the frictional behavior in the FE model to the precise experimental conditions used by Shaha [3].

Frictional testing was performed in accordance with Axel Products. Two types of tests were offered: sled test or axial-torsion test. The sled test was however unsuitable because the allowable normal pressures for the test cannot exceed 0.006 MPa while the normal pressures for these applications have been estimated to exceed 1 MPa. The axial-torsion test operates at normal pressures between 0.03 and 30 MPa which was suitable for this application.

For the axial-torsion apparatus at Axel Products, the steel cup has an outer diameter of 25.08 mm and an inner diameter of 19.94 mm meaning its walls are sufficiently thin enough to assume there is negligible difference in tangential velocity across the contacting radius. Figure 22 demonstrates the indentation of the steel cup onto the rubber specimens. Each test yields tangential force as a function of tangential displacement at a controlled normal force where the friction coefficient is simply the ratio of tangential to normal force in the static and dynamic regions.

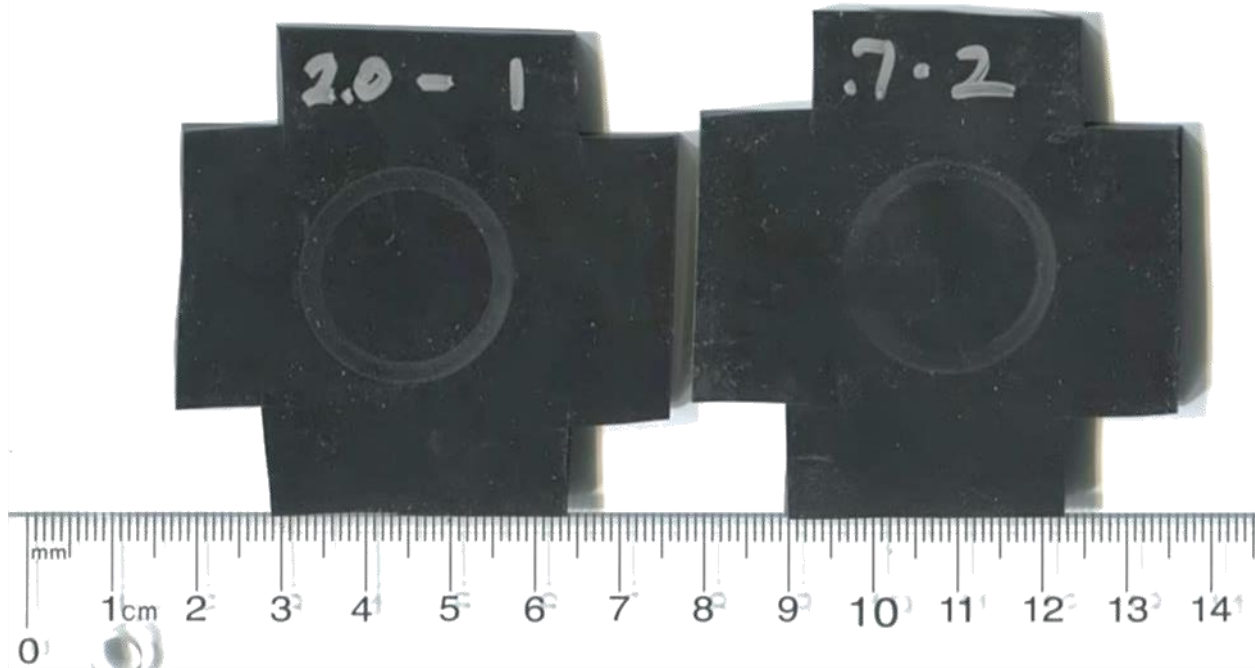


Figure 22: Rubber Friction Specimens

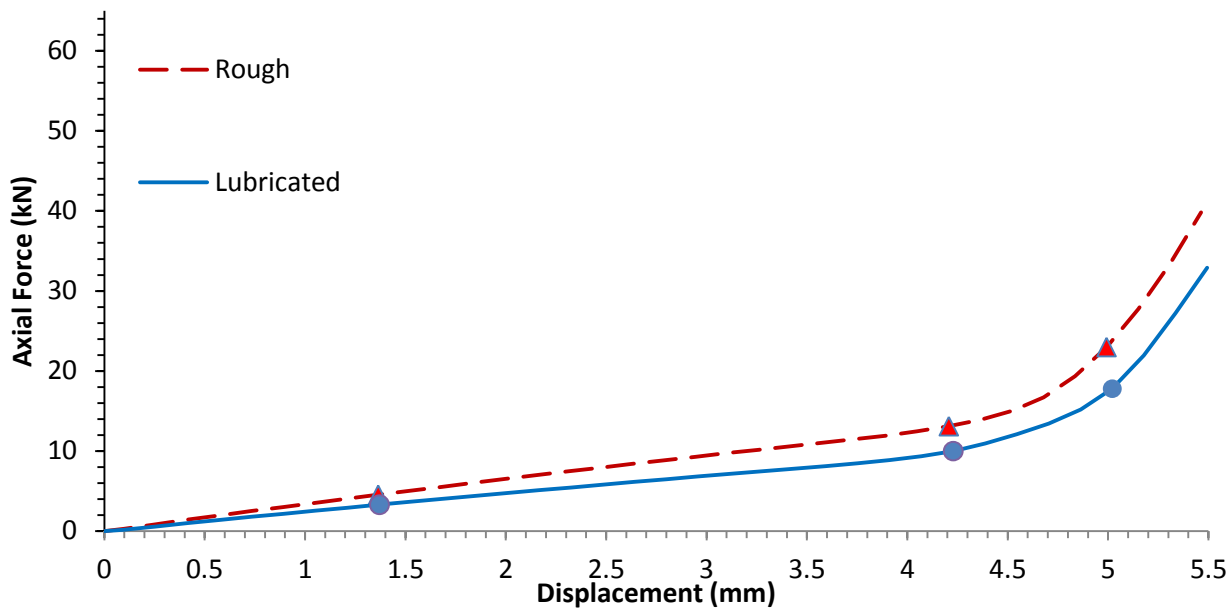


Figure 23: 102.5 mm Rough and Lubricated Data with 4" Sch. 10 Pipe

For rubber, it was discussed in 2.8 that the friction coefficient at normal pressures between 10 and 200 kg/cm² demonstrates an inverse proportionality to normal pressure. The axial compression of the seal at a fixed strain rate demonstrates a ramping of the normal pressure as a function of time. Thus it is necessary to measure friction coefficients in the range of normal pressures present during loading.

To determine the normal pressures at which to test, it was necessary to examine the behavior of the rubber seal constrained in the pipe for both the rough and lubricated contact conditions. Data collected by Shah [3] for a 102.5 mm seal for both rough and lubricated contact conditions shown in figure 23 were examined to determine the range of normal pressures present during the majority of the relative sliding between the seal and the rings. It was assumed that after contact with the pipe wall, the amount of sliding between the rings and the seal is significantly less than it is prior to contact so frictional characterization was required up until slightly after the point of contact between the seal and the pipe wall.

One frictional testing package from Axel Products included 3 trials performed for 3 normal pressures at a given displacement rate and surface condition. Three normal pressure values were selected using data from figure 23 for both rough and lubricated contact conditions at the following events:

1. At the point of inflection (seal-to-pipe contact)
2. 1/3rd of the point of inflection (near the start)
3. At the point where contact is stabilized (constant slope after the seal contacts the pipe)

The normal pressures at the selected points were calculated by the force at that point and the known axial-compressive area of the seal:

$$A = \frac{\pi}{4} (102.5^2 - 47^2) \text{ mm}^2 \quad (51)$$

$$N = \frac{F}{A} \quad (52)$$

where A is the cross-sectional area, N is the normal pressure, and F is the normal force. The corresponding results are shown in table 3.

The rotational velocity required for all tests required estimation. The rotational velocity was estimated using the known strain rate and the assumption that the constant volume of rubber is displaced at a uniform rate. The volume of rubber as a function of time can be written as follows if completely frictionless radial extrusion is assumed:

$$V = \frac{1}{4} \pi (OD(t)^2 - ID^2) L(t) \quad (53)$$

where OD(t) and L(t) are the seal outer diameter and length as a function of time and V and ID are the constant volume and inner diameter. Differentiating both sides with respect to time provided that volume and inner diameter is constant gives:

$$0 = -ID^2 \left(\frac{d}{dt} L(t) \right) + OD(t)^2 \left(\frac{d}{dt} L(t) \right) + 2 OD(t) \left(\frac{d}{dt} OD(t) \right) L(t) \quad (54)$$

Solving for the first derivative of OD(t) with respect to time gives:

$$\frac{d}{dt} OD(t) = \frac{1}{2} \frac{\left(\frac{d}{dt} L(t) \right) (ID^2 - OD(t)^2)}{OD(t) L(t)} \quad (55)$$

It is known that when t=0, OD(t) and ID(t) are equal to the initial geometry prior to deformation. It is also known that the first derivative of L(t) is constant provided by the experiment. Substituting the initial conditions at t=0, one can calculate the required relative sliding velocity (V_{slip}) for frictional testing using:

$$V_{\text{slip}} = \frac{1}{2} \frac{d}{dt} OD(t) \quad (56)$$

For a seal of outer diameter 102.5 mm and a strain rate of -0.05 s^{-1} , the relative sliding velocity is 1.13 mm/min.

Table 3: Friction Testing Values

Type	Test No.	Displacement (mm)	Axial Force (N)	*Normal Pressure (MPa)
Rough	1	1.4	4541	0.7
	2	4.2	13301	2.0
	3	5.0	22990	3.4
Lubricated	1	1.3	3290	0.5
	2	4.2	9991	1.4
	3	5.0	17776	2.5
*Area for 102.5 x 47 x 31.5 mm Seal: 6516.64 mm ²				

Two testing packages were specified each with 3 normal pressures with 3 trials each. The first was to simulate rough conditions in which the steel parts in contact with the rubber specimens were abraded with 400 grit sandpaper in a random orbital motion for each trial. The specified re-abrasion method was also implemented by Shaha [3] to make sure the seal compression experiments constrained in a pipe paralleled the frictional testing. The second test package simulated lubricated conditions where all steel parts were abraded with 400 grit sandpaper at each trial and then flooded with Lubriplate No. 105 also in accordance with experiments by Shaha [3]. Like the hyperelastic tests, the following sources of inconsistency required control to ensure a consistent dataset:

- Difference in chemical composition between specimens
- Difference in surface conditions
- Modification of the steel contact surface during subsequent trials
- Viscoelastic effects

The first inconsistency, like the hyperelastic tests, was remedied by using a fresh specimen for each trial created from the same batch. The second and third sources were controlled by ensuring each trial had a new rubber specimen and the contact surfaces re-abraded and re-flooded with lubricant between each trial. The fourth source required that the normal force be controlled and held constant otherwise stress relaxation would reduce the normal force as the test underwent thus creating error in the measurement of the friction coefficients. All of these inconsistencies were accounted for in the testing schedule provided to Axel Products.

3.4 Viscoelastic Testing

The Prony series was selected to simulate both the creep and stress relaxation behavior of the seal under axial compression in ANSYS. As previously discussed in section 2.10.3, a Prony series operates

using an exponential decay function relating the change in the shear and bulk moduli as a function of time. Therefore an experiment was necessary to provide the relaxation of the shear and bulk moduli for curve fitting.

Since the Prony series assumes that the material in question is linearly viscoelastic and thermo-rheologically simple such that the relaxation functions are independent of the magnitude of stress or strain applied to the material, it is best practice to use magnitudes of stress and strain similar to the application. It was estimated that for this application, it was possible to see magnitudes of shear strain up to 100% and bulk strain up to 1% in the rubber seal when viscoelasticity was implemented in 4.10.

The equipment requirements for such strain magnitudes are specialized as the experiments require that the stress or strain loading be done by impulse rather than ramping such that little or no creep or stress relaxation occurs during the loading phase which would affect the final measurement. This is especially challenging for fixed displacement experiments because the displacement would be required to be applied instantaneously which may introduce overshoot. Therefore, a traditional load frame is unsuitable for stress relaxation testing. Preferably, specialized low-force elastomer load frames should perform viscoelastic experiments.

If the rubber is assumed to be linearly viscoelastic and thermo-rheologically simple, stress relaxation tests can be performed at lower strain levels which would equally be representative of the behavior at high strains. Such testing can be performed using a Dynamic Mechanical Analyzer (DMA) for low forces and displacements.

For shear testing, a DMA performs a 'Shear Sandwich' test in which 2 flat square elastomer specimens with side lengths of approx. 10 mm are clamped between 3 serrated steel plates shown in figure 24.

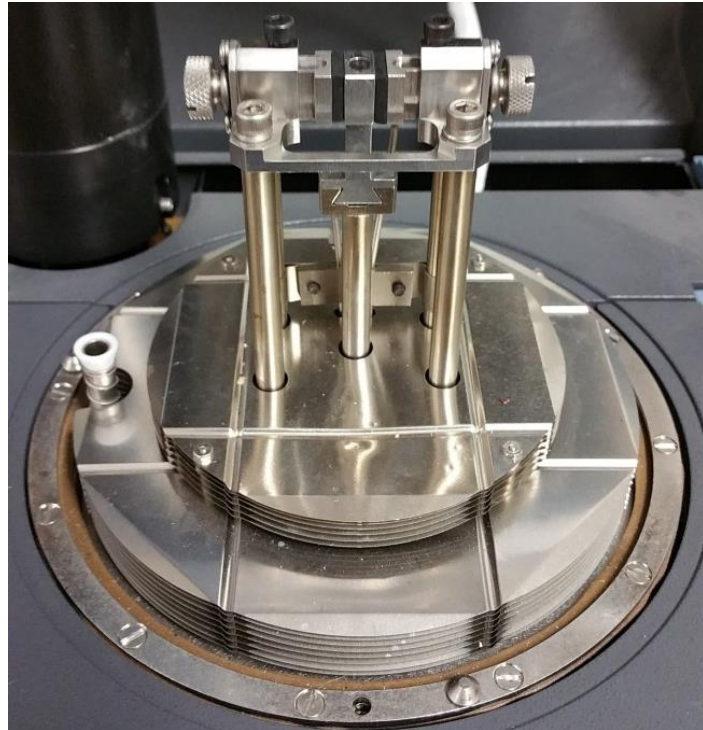


Figure 24: DMA Shear Sandwich



Figure 25: DMA Bulk Compression

The center mandrel then displaces downward at a set strain level and holds the desired strain for a period of time while measuring the decrease in force. The benefit to the use of a DMA includes full temperature control and the ability to perform quasi-instantaneous displacements due to the use of an electromagnetic actuator suspended in an air bearing. The force and displacement resolutions for the TA Instruments Q800 DMA [38] are 10 μ N and 1 nm respectively however it is limited to a maximum force of 18N. Given the size of the specimens, this instrument was suitable for this analysis. All tests were performed in-house.

For all tests, it was desired to run the tests at the highest possible strain level. The shear sandwich was capable of operating at a strain level of 3.5% for a specimen size of 2.31 x 9.38 x 9.38 mm as measured by slide calipers with an accuracy of ± 0.03 mm. 3 trials using fresh specimens were performed for 24 hours.

Similar to the shear sandwich tests, bulk compression was performed in a DMA using a custom-fabricated steel plunger and cylinder shown in figure 25 with an inner diameter of 0.125 inches corresponding to the use of 3 stacked rubber buttons with a thickness of 2.4 mm. The fully constrained rubber in a rigid cylinder experiences a state of hydrostatic compression which is subject to a constant volumetric compression in the DMA. The ensuing change in hydrostatic pressure is recorded by the DMA. The buttons were laser cut and adjusted for an interference fit within the cylinder to eliminate as much slack and empty voids as possible to ensure the rubber experiences a state of volumetric compression. Due to the high bulk modulus of the rubber, it was expected that a maximum deflection of approx. 4 microns could be achieved with the available 18N of force which is within the operating resolution of the device. Like the shear sandwich, 3 stress relaxation trials were performed each over a period of 24 hours.

It was noted that all tests could not be held at a room temperature of 23°C without external liquid nitrogen cooling. The minimum stable temperature was 35°C hence all tests were performed at a higher temperature than room temperature since it was unfeasible to run 24 hour tests on liquid nitrogen cooling.

3.5 Finite-Element Model Setup

The following section discusses the set up for the finite-element model including the details pertaining to the selection of finite-element code, preprocessing setup, and solution settings.

3.5.1 Finite-Element Code Selection

For FE modelling, ANSYS was the only software available for use. Two versions of ANSYS were available for use; APDL and Workbench. Other finite-element codes more suitable for use with non-linear analyses such as MARC and ABAQUS were not available.

ANSYS Workbench is an integrated user-friendly finite-element code which includes several software packages pertaining to different simulations. Available for use with quasi-static analyses in the ANSYS Mechanical package is Design Modeler (a CAD and de-featuring tool), various curve-fitting tools, and a robust meshing, loading, and solving program. The benefit of using Workbench is primarily that it requires much less time to set up a model due to its many automated processes. The automation of several of the modelling processes (e.g., modelling, meshing, and loading) is helpful for most common analyses.

ANSYS Parametric Design Language (APDL) is the embedded code which ANSYS Workbench is based upon. The graphic-user interface (GUI) with which users would classically interact with ANSYS is often called ‘ANSYS Classic’. ANSYS Classic fully integrates all aspects of modelling in a single program unlike

Workbench which separates modelling, material selection, and model set up. It is also possible to write code for each of these aspects to be automated and easily compiled. The benefits of coding ANSYS are in the very high level of control over all aspects of the simulation more so than Workbench. For example, it is possible to directly select the element types in use whereas Workbench would select them contextually. ANSYS Classic is however primitive and time-consuming in its use. For this analysis, APDL was written as code and fed into ANSYS Classic directly for a number of reasons:

- Simple geometry can easily be modified and re-generated.
- A full level of control was required for element selection, contact setup, boundary conditions, and solver settings.
- User-defined results could be generated automatically and exported as text files to be read by Excel, Maple, or Matlab.

3.5.2 Geometry and Mesh

Given that the experimental jig is symmetric about its axis of rotation, it was possible to input the geometry into ANSYS as either a 3D solid model or as a 2D axisymmetric model. If it is assumed that the pipe and seal are perfectly symmetric about their center axes, then the advantage of using a 2D model lies in its simplicity, its computational efficiency, and its high element density. As such, the simulation was performed using a 2D axisymmetric setup.

To accurately simulate the experiment, it was important to input the experimental parameters with a high level of accuracy because nearly-incompressible materials in volumetric compression are very sensitive to the amount of confinement volume. Geometry for the finite-element model was measured directly from the experimental jig with slide calipers with an accuracy of ± 0.03 mm. The model shown in figure 26 is a 2D axisymmetric representation of the experiment in figure 19 revolved about the central Y-Axis. The seal and rings were divided into multiple areas to facilitate mapped meshing.

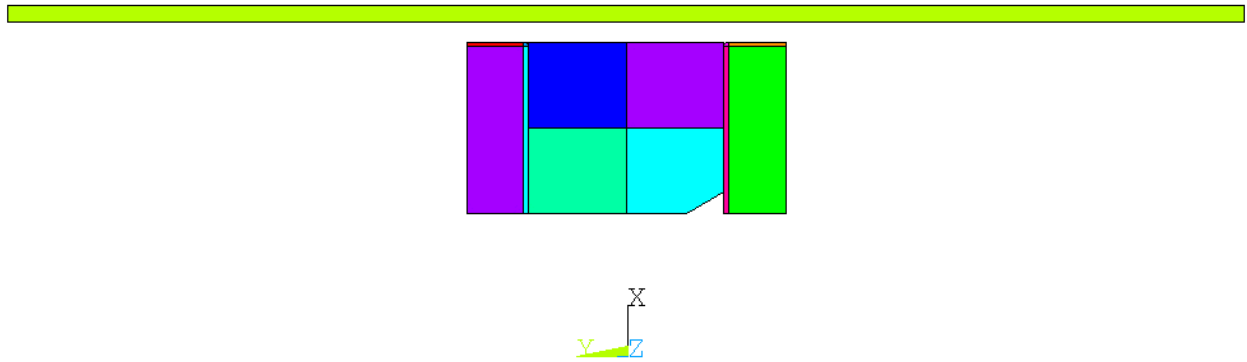


Figure 26: 2D Axisymmetric Finite-Element Geometry

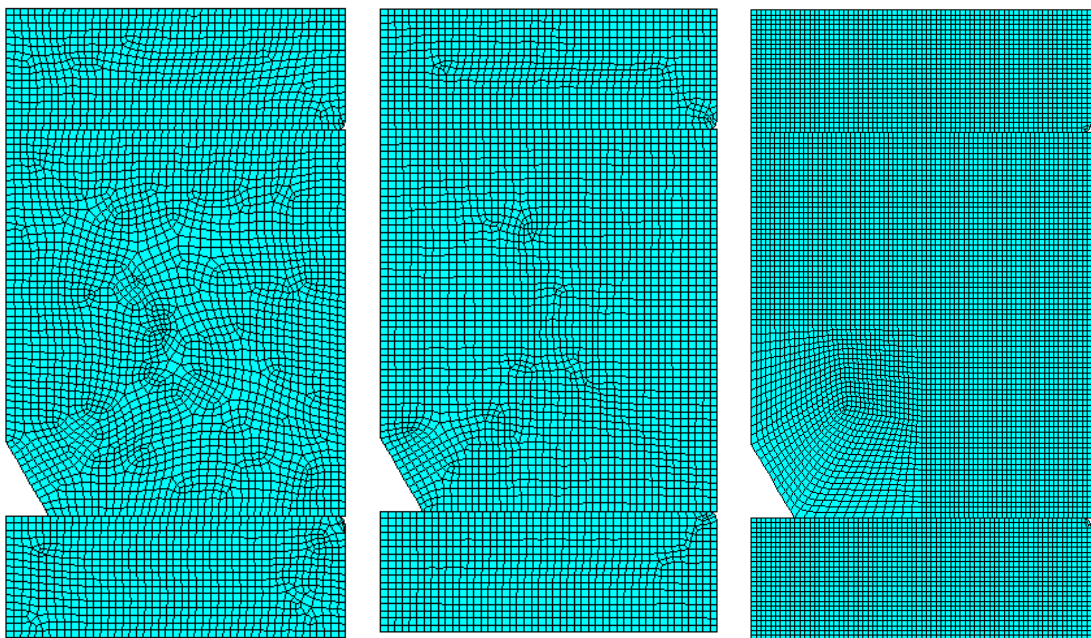


Figure 27: Manual Free Mesh; Smart-Size Free Mesh; Mapped Mesh

ANSYS provides 2 means of meshing areas: free and mapped meshing. Free meshing is performed using automatic sizing calculations depending on the topology of the area to be meshed and also any manually defined line or element sizes or divisions. It requires very little setup for free meshing however free meshing may give rise to triangular elements and misshapen transitional zones which are undesirable in large deformation analyses.

Mapped meshing requires more setup however the advantage to its use provides highly aligned and symmetrical areas which are an ideal starting point for large deformation analysis as the mesh will be significantly deformed during the solution. An additional advantage to mapped meshing is the possibility to skew the mesh opposite to the direction of deformation such that the deformed mesh has an improved alignment following deformation. Figure 27 demonstrates the difference between a manual, smart-size manual, and a mapped mesh. It is clear that the mapped mesh has a very high mesh quality whereas the free meshes have ill-conditioned transitions between different parts of the mesh shown as ‘swirls’.

3.5.3 Elements

For the meshing of 2D areas, two types of ANSYS elements suit the needs of this simulation: PLANE 182 and PLANE 183. Both elements are capable of large deformation analysis with hyperelasticity and viscoelasticity enabled and mixed u-P formulation ideal for use with near-incompressible materials. Moreover, both are capable of axisymmetry. The difference between the two elements is that PLANE 182 is a low-order element with 4 nodes whereas PLANE 183 is an 8-node element including 4 mid-side nodes more suitable to irregular geometry. PLANE 183 is however, not associated for use with axisymmetric incompressible hyperelastic materials. Due to the inclusion of volumetric compressive data into the FE model, this application is considered near-incompressible.

For preliminary purposes, all areas were meshed as follows using the simpler axisymmetric PLANE 182 using the following option keys (KEYOPT):

- Element Type: PLANE 182
- Element Technology: KEYOPT(1) = 0 (Full Integration with B-bar method)
- Element Behavior: KEYOPT(3) = 1 (Axisymmetric)
- Element Formulation: KEYOPT(6) = 1 (Mixed u-P)

The potential for the use of PLANE 183 elements for both the steel and rubber parts were examined once the final model was optimized.

For the creation of contacts between adjacent meshed areas, 2 types of elements are required:

Target and Contact. For this application, surface-to-surface contacts were used rather than node-to-node and node-to-surface contacts as they support mid-side nodes on higher order elements, they provide better contact results, and they have no restrictions on the shape of the contacting surfaces.

2 elements exist for surface-to-surface contact surfaces: 2-node CONTA 171 and 3-node CONTA 172.

Both are very similar in nature however CONTA 172 is suitable for use with higher-order elements because it shares a mid-side node with the underlying element unlike the 2-node CONTA 171 which is meant for use with low-order elements. Therefore, contact surfaces were meshed with CONTA 171 elements when using PLANE 182 elements and CONTA 172 elements when the underlying element was PLANE 183.

For target surfaces in 2D surface-to-surface contact, 1 element exists which is TARGE 169 which is compatible for use with both CONTA 171 and CONTA 172.

In general, when designating which surface is the contact and which surface is the target; one can conform to the following principles [39]:

1. If contacting surfaces are convex, flat, or concave; the flat or concave surface should be the target.
2. If two surfaces have different mesh sizes; the coarser one should be the target.
3. If one surface is stiffer than the other; the stiffer surface should be the target.
4. If one surface has low-order elements and another has high order elements; the low-order surface should be the target.

In summary, the diagram shown in figure 28 displays the contact elements and the surfaces onto which they have been applied. Contact pairs 1, 2, and 3 were established between the rings and seal, pipe and seal, and mandrel and seal respectively. The contact setup details are shown in table 4. For all contact pairs, the Augmented Lagrange algorithm was used for a number of reasons. It iteratively adjusts contact penetration to maintain convergence below the allowable FTOLN value which when compared to pure penalty, decreases the amount of penetration. When compared to all other methods, it allows a set amount of penetration which improves the robustness of the solution and suits large amounts of sliding and complex frictional behavior.

Small amounts of penetration are acceptable for this simulation as the deformation of a highly constrained nearly-incompressible volume is difficult to solve if zero-penetration is enforced. The allowable penetration was set to 0.1 mm which corresponds to the default factor of 0.1 for an element depth of 1 mm. It was determined by trial-and-error that this value suited most solution attempts.

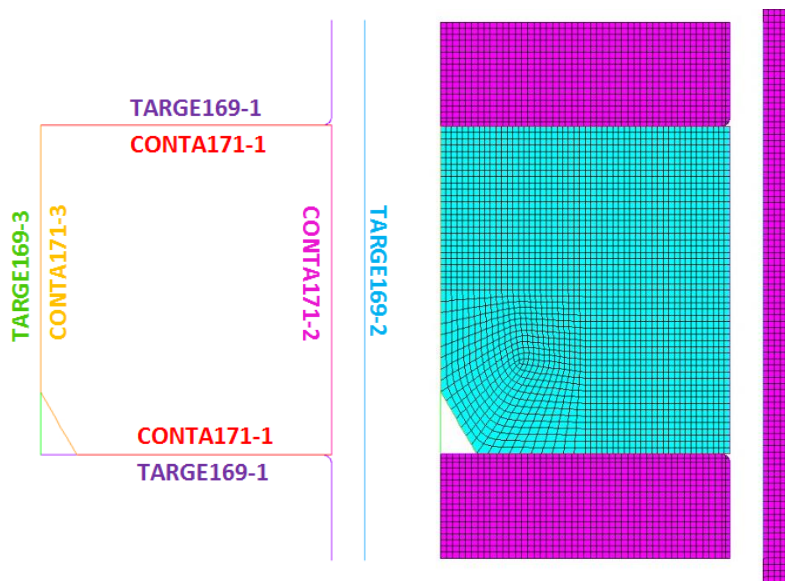


Figure 28: Contact Diagram

Table 4: Contact Element Setup

Element Options	Contact pair 1 - Contact	Contact pair 2 - Contact	Contact pair 3 - Contact
Element Type:	CONTA171	CONTA171	CONTA171
Contact Type:	Flexible-Flexible	Flexible-Flexible	Rigid-Flexible
KEYOPT(0) (Contact Algorithm)	0 (Augmented Lagrange)	0 (Augmented Lagrange)	0 (Augmented Lagrange)
KEYOPT(4) (Contact Detection Point)	0 (On Gauss Point)	0 (On Gauss Point)	0 (On Gauss Point)
KEYOPT(5) (Gap Adjustment)	1 (Close Gap)	0 (Nothing Done)	0 (Nothing Done)
KEYOPT(10) (Contact Stiffness Update)	0 (FKN redefined each loadstep)	0 (FKN redefined each loadstep)	0 (FKN redefined each loadstep)
KEYOPT(12) (Surface Behavior)	0 (Frictional 'Standard')	0 (Frictional 'Standard')	0 (Frictional 'Standard')
Contact Stiffness (FKN)	1.0E11	1.0E11	1.0E11
Allowable Penetration (FTOLN)	0.1 mm	0.1 mm	0.1 mm
Pinball Region	Auto Detect	$\frac{1}{2} (\text{ID-SOD}) \cdot 1.1$	Auto Detect
Element Options	Contact pair 1 – Target	Contact pair 1 – Target	Contact pair 1 – Target
Element Type:	TARGE169	TARGE169	TARGE169

Contact stiffness was set to a constant value of 1E11 which corresponded to the default factor of 1.0 for an underlying element size of 1 mm modelled using a steel material ($E = 210$ GPa). It is recommended to update contact stiffness at each iteration however this introduced a significant amount of mesh distortion error and convergence failure. Hence, it was determined by trial-and-error that the contact stiffness remained constant during each load-step.

For contact gaps, contact pair 1 is known to have an initial state where both surfaces are in contact with a gap size of 0 mm, hence the initial contact gap adjustment was adjusted to touch. For the gap between the seal and the pipe wall, the pinball region which is the sphere of influence where contacts elements detect target elements in ‘near-contact’, was set to the calculated gap size between the seal outer diameter (SOD) and the pipe inner diameter (ID) with an extra allowance of 10%.

3.5.4 Solver Setup

The first step was to establish the type of analysis required. ANSYS provides the possibility to simulate static or transient analyses for small or large deformation. Clearly, the nature of rubber in this application is capable of large deformation however, due to viscoelasticity, there is a time-dependency required for this model. Transient behavior in ANSYS relates to the inertial and damping effects present in the model which in static analyses are neglected. Static analyses are still however, able to simulate time-dependent behavior. The strain rates expected for this model did not exceed 0.05 s^{-1} which was assumed to be quasi-static. Therefore, the static large deformation solver was selected.

The next step was to configure the solver for use with non-linearity and frictional effects. A minimum of 20 sub-steps per load-step was implemented with automatic time-stepping should intermediate sub-steps be needed for convergence. Additionally, for use with friction, the global

stiffness matrices were fully unsymmetrical which is suitable for use with large friction coefficients at the expense of being computationally expensive.

4 load-steps were defined for the simulation each with unique boundary conditions:

- Load-Step 1: 0 to 0.0001 s Ramped Displacement Loading
- Load-Step 2: 0.0001 to 1 s Short-Term Viscoelasticity
- Load-Step 3: 1 to 300 s Medium-Term Viscoelasticity
- Load-Step 4: 300 to ‘t’ s Long-Term Viscoelasticity (until desired time ‘t’ if needed)

For non-linear problems, the Newton-Raphson Convergence Algorithm was used to iteratively solve each sub-step. Convergence is achieved in an iterative solution when the sum of the residuals of a given convergence criterion drops below a threshold for each iteration.

By default, ANSYS automatically applies the appropriate convergence criteria depending on the expected non-linearity of the problem and is able to automatically create intermediate sub-steps and adjust the convergence criteria to aid the solution process. This technique is called Solution Control which is used rather than fixed convergence criteria because of the difficulty in solving models with a high amount of non-linear behavior. For the majority of the model development, solution control was active with the following default convergence criteria:

- Force / Moment:
 - Tolerance: 0.5%
 - Norm: L2
 - Reference: Automatically Calculated
 - Min Ref: 0.01

- Displacement:
 - Tolerance: 5%
 - Norm: LINF
 - Reference: Automatically Calculated
 - Min Ref: 0.01

For the final model optimization however, the convergence criteria were manually modified to ensure convergence was as stringent and consistent as possible for improved accuracy.

3.5.5 Viscoelastic Time Approximation

The hyperelastic testing already incorporates the effect of viscoelasticity inherent to the loading because the loading is not instantaneous. Figure 29 shows the 5th loading cycle for the uniaxial tension (UT), planar tension (PT), and equibiaxial (EQ) tests at the largest available strain level tested at a rate 0.00264 s^{-1} and 0.05 s^{-1} . It can be seen that due to viscoelastic effects, the stress-strain curves for the same material tested at different rates do not superimpose. Higher strain rates display stiffer behavior due to less time allotted to the molecular movement of the rubber.

A hyperelastic curve-fit does not predict the effect of time on the material behavior; it is a snapshot of the material being tested at a single rate. Time in ANSYS is therefore used as a solution tracking metric if it is not used as a part of a time-dependent model. For example, implementing a hyperelastic model for a displacement ramp of 10 mm over 1 s or 1,000,000 s would yield an identical result because ANSYS uses time as a solution tracker but not part of the material behavior.

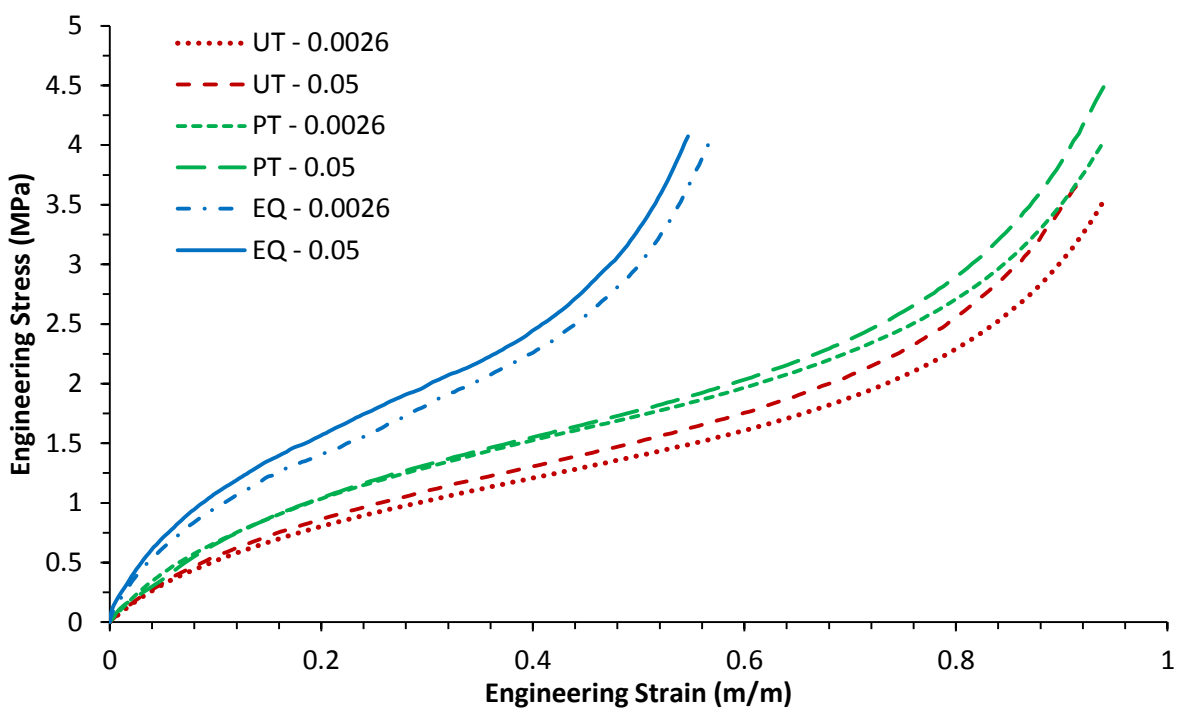


Figure 29: Material Strain Rate Dependency

However, implementing a viscoelastic model introduces a time-dependency which would then use the tracking of time as part of the solution. Therefore, a displacement ramp of 10 mm over 1 s would yield vastly different results than over 1,000,000 s. If a hyperelastic model already incorporates viscoelasticity at a given strain rate, the addition of a viscoelastic model will double the viscoelastic effects. The viscoelastic model thus cannot be allowed to take effect until it is necessary and no known built-in solutions in ANSYS exist for this problem. Several techniques are possible to solve or mitigate this problem:

1. Introduce the viscoelastic model at each load-step where displacement or force is held constant using a multi-frame restart.
2. Create two materials: One with a hyperelastic model, one with a hyperelastic model and viscoelastic model. Then exchange the material model on all rubber elements at each load-step where displacement or force is held constant.
3. A hyperelastic and viscoelastic model is introduced throughout the solution but load-steps attributed to loading are ran over a very short period of time where viscoelastic effects are negligible.

The first technique was able to initiate a solution however ANSYS does not support mid-solution changes to a material model; the solution fails promptly. The second creates an internal error which crashes the program. The third technique was successful however it was important to set the load-step over a low enough time interval to produce negligible viscoelastic effects.

Therefore, the first load-step discussed in 3.5.4 was set in ANSYS as 0 to 0.0001 s however, in reality, the data corresponded to a load-step from 0 to τ which is calculated using the following equation:

$$\tau = \frac{\Delta L}{\varepsilon' \cdot L} \quad (57)$$

where ΔL is the axial displacement, L is the seal thickness, and ϵ' is the strain rate.

3.5.6 Boundary Conditions

Boundary conditions were applied separately for all load steps in conformance with what is shown in figure 30. For the displacement ramp in the first load-step, the following boundary conditions were established:

1. Lower Ring: $UY = \text{Input Displacement}$ $UX = 0$
2. Upper Ring: $UY = 0$ $UX = 0$
3. Mandrel: $UY = 0$ $UX = 0$
4. Pipe End: $UY = \text{Input Displacement}$ $UX = 0$

In reality, the UX displacement on the lower ring and pipe end are not 0 as they sit on frictional surfaces. However, all experimental fixtures were aligned concentrically and, under the assumption that the rubber seal extrudes evenly all the way around, no radial motion of any part should occur. Therefore, it was assumed that the rings and the lower pipe end could be held fixed in the radial direction.

For subsequent stress relaxation and creep load-steps, boundary conditions 2 to 4 were held identical to the first load-step. For stress relaxation, the input displacement was held constant for boundary condition 1.

For creep, it was necessary to perform a multi-frame restart and extract the reaction forces from all nodes on boundary condition 1 and re-apply them as a distributed load on all of the nodes along the surface. The input displacement was deleted and substituted for the nodal loads.

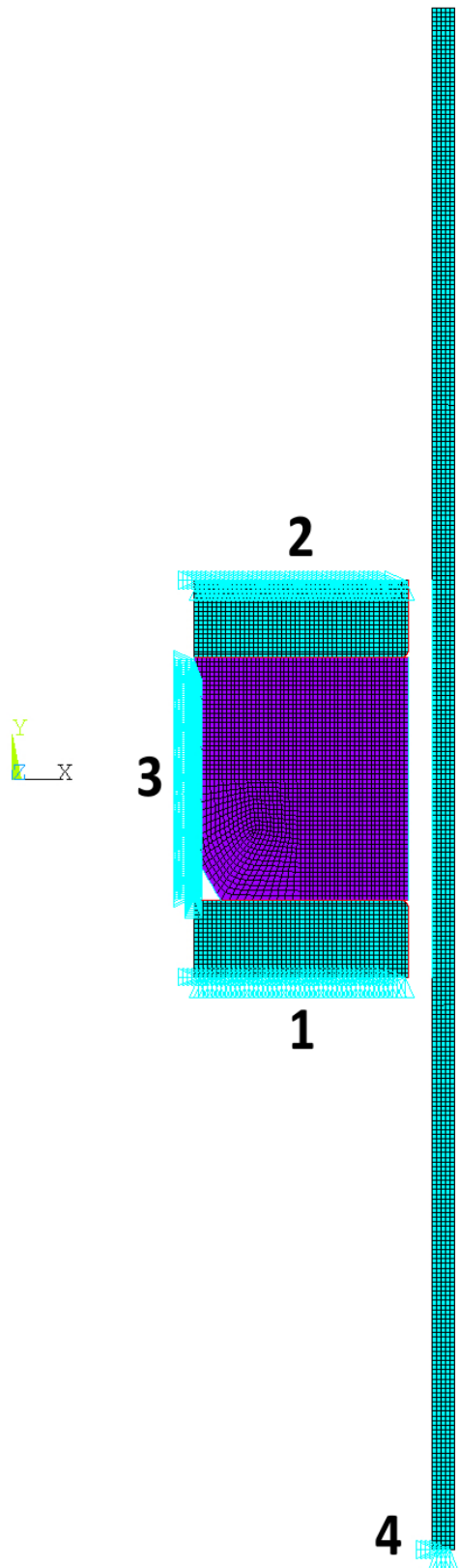


Figure 30: Boundary Conditions

3.6 Methods of Experimental Comparison

To ensure results were compared in an accurate manner, it was important to compare FEA results directly to experimental values. Three sources of validation data were supplied for each experiment performed by Shaha [3]:

- Load Frame Data:
 - Displacement reading on the lower ring from the mandrel connected to the actuator
 - Force reading on the upper ring from the receiver connected to the load cell
 - Time reading from the internal clock
- FujiFilm Prescale Data:
 - One-time-use maximum pressure gradient between the pipe inner wall and the seal
- Strain Gauge Chain Data:
 - 20 hoop strain readings centered at the pipe mid-length at a pitch of 2 mm
 - Time reading from the internal clock (unsynchronized with load frame)

Using APDL, it was possible to write a script which could extract nodal and element results from the database in ANSYS for each of the sub-steps and load-steps. The following results were taken from the model in accordance with figure 31:

1. Displacement taken from 1 node (All nodes along line 1 carry the same displacement).
2. Load taken as the sum of reactions forces in the Y direction along line 2.
3. Contact pressure vs. global Y location of contact elements along line 3.
4. Hoop strains (z-direction) vs. global Y location of nodes along line 4.

After a complete solution, a results script was executed in ANSYS to collect the necessary data and store them as text files which could be read by a variety of programs.

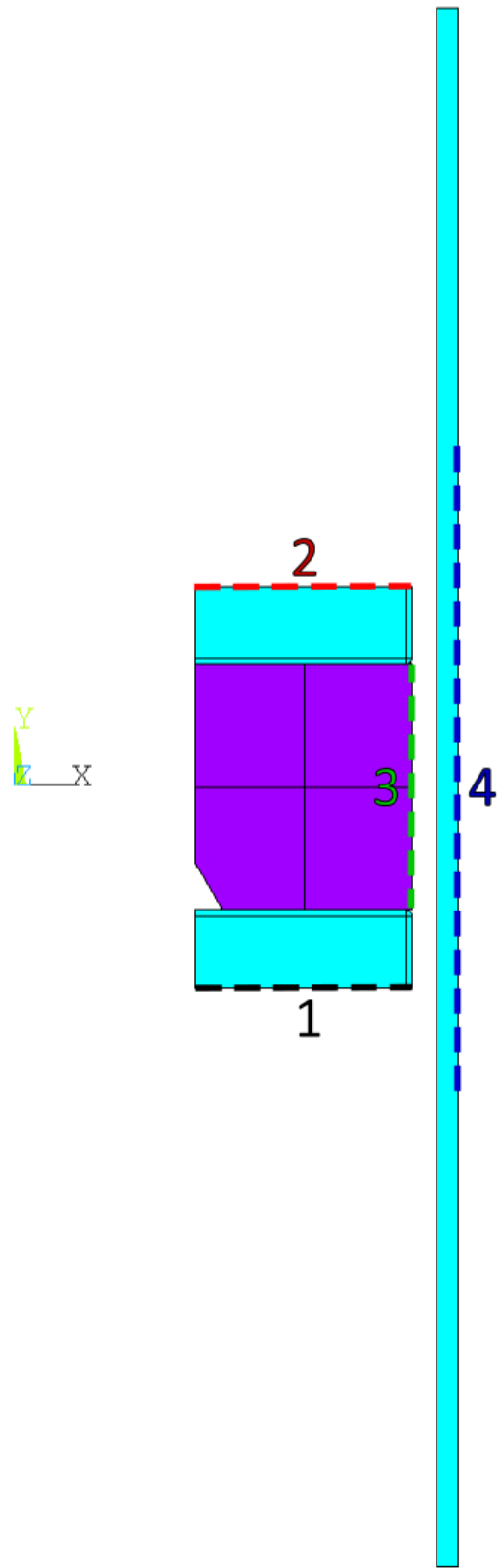


Figure 31: Results Collection Diagram

Those in use for this analysis were Maple 17 and Microsoft Excel. Maple 17 was selected for its automation in comparing the experimental and simulation data for quickly comparing results while Excel was used for compiling results.

For the numerical comparison of the experimental and FE results, traditional methods such as the least-squares absolute or normalized errors could not be used because they require 2 datasets with data points synchronized in terms of a common parameter which is most commonly time. The experimental datasets were recorded at 10 or 100 Hz whereas FEA datasets for this analysis do not follow time in a periodic fashion. Rather, the FEA results follow the time at which sub-step results are recorded which may vary due to the solution control automatically controlling the sub-step intervals depending on the difficulty of convergence. It is possible to synchronize the two datasets by limiting ANSYS to perform sub-steps at fixed time intervals however this increases convergence difficulty.

Another option was to fit the two datasets to high-order polynomial equations and perform mathematical comparisons based on the continuous functions or on artificial discrete synchronized datasets. However, polynomial curve-fitting was abandoned because it introduced error into the comparison since the regressions were inaccurately fitting the original datasets.

In the end, 3 methods were used to compare the unsynchronized experimental and FE results. The first method was visual inspection and comparison of experimental and theoretical data. Notable behaviors are irregularities, spikes, inflections, or difference in slopes. The second was a maximum axial force deviation calculated by equation 58.

$$\text{Maximum Deviation} = \left| \max(F^{fea}_n - F^{\exp}_m) \right| \quad (58)$$

where F^{fea}_n is the axial reaction force (Result 1) for the n^{th} sub-step and F^{exp}_m is the experimental axial reaction force for the m^{th} time. The datasets did not need to be synchronized because they are performed over the same period of time and they have equal axial displacement endpoints.

The third method was a numerical integration deviation which subtracts the areas beneath the experimental and FEA result curves. This method was only applied to the force-displacement data to get a general idea of the conformance between the FE and experimental loading periods. Integral deviation was calculated using equation 59.

$$\text{Integral Deviation} = \left| \sum_{i=2}^n F_i^{fea} \cdot (d_i^{fea} - d_{i-1}^{fea}) - \sum_{j=2}^m F_j^{exp} \cdot (d_j^{exp} - d_{j-1}^{exp}) \right| \quad (59)$$

where n and m are the lengths of the FE and experimental datasets respectively and F^{fea} , F^{exp} , d^{fea} , d^{exp} are the FE and experimental axial force and displacement values at a given sub-step or time interval.

3.7 Model Development Procedure

The following section describes the procedure created to develop the finite-element model in steps to achieve the final optimized model capable of simulating various pipe and seal sizes.

3.7.1 Linear Isotropic Model For Estimation

The first step in the analysis was to create a simple model with only the rubber seal to estimate the magnitude of strain present in the rubber seal. Since the hyperelastic testing packages were performed at 20, 40, 60, and 100%, it was necessary to select material test datasets for curve-fitting and modelling which were representative of the magnitude of strain in the seal.

The linear model was set up with the geometry shown in 3.5.2 however the pipe, rings, and mandrel were not meshed thus it was simply the compression of the rubber seal. A linear isotropic model was

formulated using the bulk modulus and the Young's modulus from the median volumetric compression curve and the 20% uniaxial tensile data at a strain of 5% respectively for a strain rate of 0.05 s^{-1} . The geometry was meshed with an initial mesh size of 1 mm and an input axial displacement of 5 mm was applied on the bottom nodes of the seal; the top nodes were held fixed. From the solution, the 3 principal strains and the Von-Mises strain were examined to determine the appropriate level of strain for hyperelastic modelling.

3.7.2 Hyperelastic Model Selection

The second step was to select the most suitable hyperelastic model for the level of strain determined previously in 3.7.1 and compare each to experimental force-displacement measurements for both rough and lubricated contact conditions. However, the contact conditions required a different frictional model for both surface conditions. From the frictional test data, the average friction coefficient across all trials and normal pressures was taken separately for both rough and lubricated cases and input as a single friction coefficient into ANSYS. The same geometry, mesh, and loading were taken from the linear isotropic model however a hyperelastic material model was implemented instead of a linear isotropic material model.

The following potential hyperelastic models were examined:

- Neo-Hookean
- Mooney-Rivlin
- Yeoh
- Ogden
- Arruda-Boyce
- Gent

Each model was subject to both absolute and normalized least-squares curve-fitting algorithms for either the 1st or 5th loading cycle; 4 possibilities for each model in total. It was important to examine the 1st and 5th cycles because while the 5th material testing cycle is stabilized, the seals are compressed using only a single loading cycle. Hence, there was the possibility that material test data on the 1st loading cycle was a better representation of the seal being loaded on a single cycle.

Each hyperelastic model was compared to the rough contact experimental data in terms of maximum and integral deviation. The top 4 models were then compared to lubricated contact experimental data. The model was then systematically selected based on the best-fit to experimental seal compression data.

3.7.3 Mesh Convergence Analysis

Following the selection of a hyperelastic model, a mesh convergence analysis was performed to determine the ideal mesh size before proceeding to the addition of a pipe and mandrel in the model. Using a starting value of 1 mm, different mesh sizes were compared in terms of the following criteria:

- Element count
- Maximum Von-Mises strain
- Maximum Von-Mises stress
- Axial reaction force
- Maximum contact penetration
- Solution time & iterations
- Deformed mesh warning elements

Mesh sizes were determined on an iterative basis as to avoid performing several unnecessary analyses which would ultimately not be selected. The optimal mesh size required to be consistent

(approx. 1% deviation) with the finest mesh and also display an acceptable solution time and number of iterations.

To confirm that the shape of the mesh was acceptable, it was necessary to reduce the amount of warning elements as much as possible. Warning elements are highly deformed elements defined by shape-limiting criteria defined by ANSYS in terms of the aspect ratio, angle deviation, parallel deviation, maximum corner angle, and jacobian ratio. An element exceeding the limiting criteria causes error in the solution which must always be investigated to determine whether its effect is significant.

3.7.4 Implement Pipe and Mandrel

Using the selected hyperelastic model and the mesh size from the previous analyses, the pipe and the mandrel were implemented and meshed using a linear isotropic steel material model ($E = 210 \text{ GPa}$, $\nu = 0.3$). The axial displacement was increased to 6 mm to match all of the provided experimental data. This preliminary analysis served to check whether convergence was achieved with a more constrained model and to determine the magnitude of strain present in the seal once more.

Upon convergence, the principal strains were examined to determine the appropriate magnitude of strain for the hyperelastic model. If it was higher than the previous strain magnitude determined in 3.7.1, hyperelastic datasets at a higher strain magnitude were selected for subsequent material modelling.

3.7.5 Mesh Convergence Analysis with Pipe

Similar to the first mesh convergence analysis, another analysis was required to verify whether the current mesh was sufficient for subsequent analyses at higher magnitudes of strain. The second analysis was equally set up to the first however maximum pipe strain was added as a criterion.

3.7.6 Parametric Study

Following the selection of an appropriate mesh size, a parametric study was required to determine the level of control required over certain model parameters. Two notable parameters were expected to create considerable differences:

- Friction
- Pipe size (i.e., the level of precision required in controlling the geometry)

For the effect of friction, the friction coefficient was increased from 0.1 to 0.7 by increments of 0.2 and the following force-displacement curves and the maximum pipe strain were compared to establish the sensitivity of frictional characterization.

For the effect of pipe sizes, 4 cases were examined each in accordance with ASME B36.10M [34] and API 5L [40] to determine the possible range of sizes within acceptable tolerance for a single listed pipe schedule in this case being 4" Sch. 10. The minimum and maximum extrusion gap (i.e., the distance between the undeformed seal and pipe wall) was analyzed because of its influence on axial force at fixed axial displacement. The cases are listed as follows denoted by outer diameter by wall thickness:

- Pipe segment used for experiment as measured by slide calipers:
 - 114.3 x 2.75 mm
- 4" Sch. 10 Nominal Pipe Size
 - 114.3 x 3.05 mm
- 4" Sch. 10 with maximum upper size tolerance (i.e., largest extrusion gap)
 - 115.4 x 2.65 mm
- 4" Sch. 10 with minimum lower size tolerance (i.e., smallest extrusion gap)
 - 113.2 x 3.55 mm

The goal of characterizing the effect of pipe geometry emphasized whether or not precise geometric measurements were required for subsequent simulations.

3.7.7 Implementation of Final Friction and Hyperelastic Models

Provided the results of analyses in 3.7.4 and 3.7.6 required more detailed friction and hyperelastic models, the following two alternatives could have been implemented as needed:

For added frictional control, a frictional model fit using Thirion's law could have been implemented as a discrete dataset of friction coefficients in ANSYS as a function of normal pressure given that the friction coefficient varies as a function of normal pressure.

For conformance to higher magnitudes of strain, curve-fitting to higher magnitudes of strain and higher order models was possible to eliminate extrapolation of the hyperelastic model outside the range of material test data.

3.7.8 Viscoelastic Model Implementation

With all optimal material models implemented, it was possible to implement the Prony series in a series of load-steps operating over a maximum period of 24 hours as permitted by the experimental data. Comparison was be performed in terms of the axial force, axial displacement, and pipe strain as a function of time for the rough and lubricated data for both stress relaxation and creep.

3.7.9 Final Model Optimization

Once all optimal components to the FE model were implemented, optimization was performed by tweaking the following controls in ANSYS:

- Element Types

- Mesh Shape
- Contact Stiffness & Penetration Tolerance
- Convergence Criteria
- Frictional Model (as permitted by the deviation in the frictional data)

Once the model conformed as accurately as possible to the rough and lubricated experimental data, it was possible to use the model for results analysis and additionally, extend the model for use with different seal and pipe sizes.

3.7.10 FE Model Analysis

Using the optimized and validated FE model for a 102.5 mm seal, it was possible to use the results from the solution to examine the behavior the seal and the pipe. For the pipe strain gradient, it was possible to measure the contact pressure and the pipe strain at any location as a function of time. This is especially important for thick-wall pipes as the pipe strain on the outer membrane can be significantly different than strain on the inside membrane.

With the optimal model in place, the FE model could then be compared to a 96.3 mm seal tested in a 4" Sch. STD pipe tested by Shaha [3]. The FE model was compared to experimental data in an identical fashion however with fewer strain gauges for comparison. Upon the comparison with the additional seal and pipe combination, conclusions could be drawn with respect to the scalability and extended use of the FE model developed from this research project.

Chapter 4: Results

The following chapter presents the results of the finite-element model development and analysis arranged systematically in the order which was followed through in the development process.

4.1 Hyperelastic Results

The hyperelastic material testing results were received from Axel Products as continuous datasets provided for each hyperelastic test. 2 strain rates, 4 experiments, and 3 trials make for 24 unique datasets which were treated specifically for their use with a hyperelastic model.

Each dataset included time, engineering stress, and engineering strain collected at a rate of 20 Hz. Figure 32 displays one dataset for uniaxial tension (UT), planar tension (PT), equibiaxial (EQ) extension, and volumetric compression (VC) tests performed at a strain rate of 0.05 s^{-1} .

Comparing each of the 3 tests hyperelastic tests: uniaxial tension, planar tension, and equibiaxial extension; all tests show similar behavior in their cyclical loading. Each test demonstrates a typical elastomer response characterized by a linear elastic region at low strain followed by softening at medium strain and finally strain hardening and/or rupture at high strain near 100%. To a lesser interest, each loading and unloading cycle demonstrates notable levels of hysteresis typical of rubbers. Volumetric compression however behaves significantly different than all of the hyperelastic tests. In comparison to the 3 hyperelastic tests, volumetric compression demonstrates a very high level of stress given the low level of strain with a near-linear behavior and mild hysteresis. 2 cycles are shown which, upon loading, overlap each-other indicating the absence of Mullins effect.

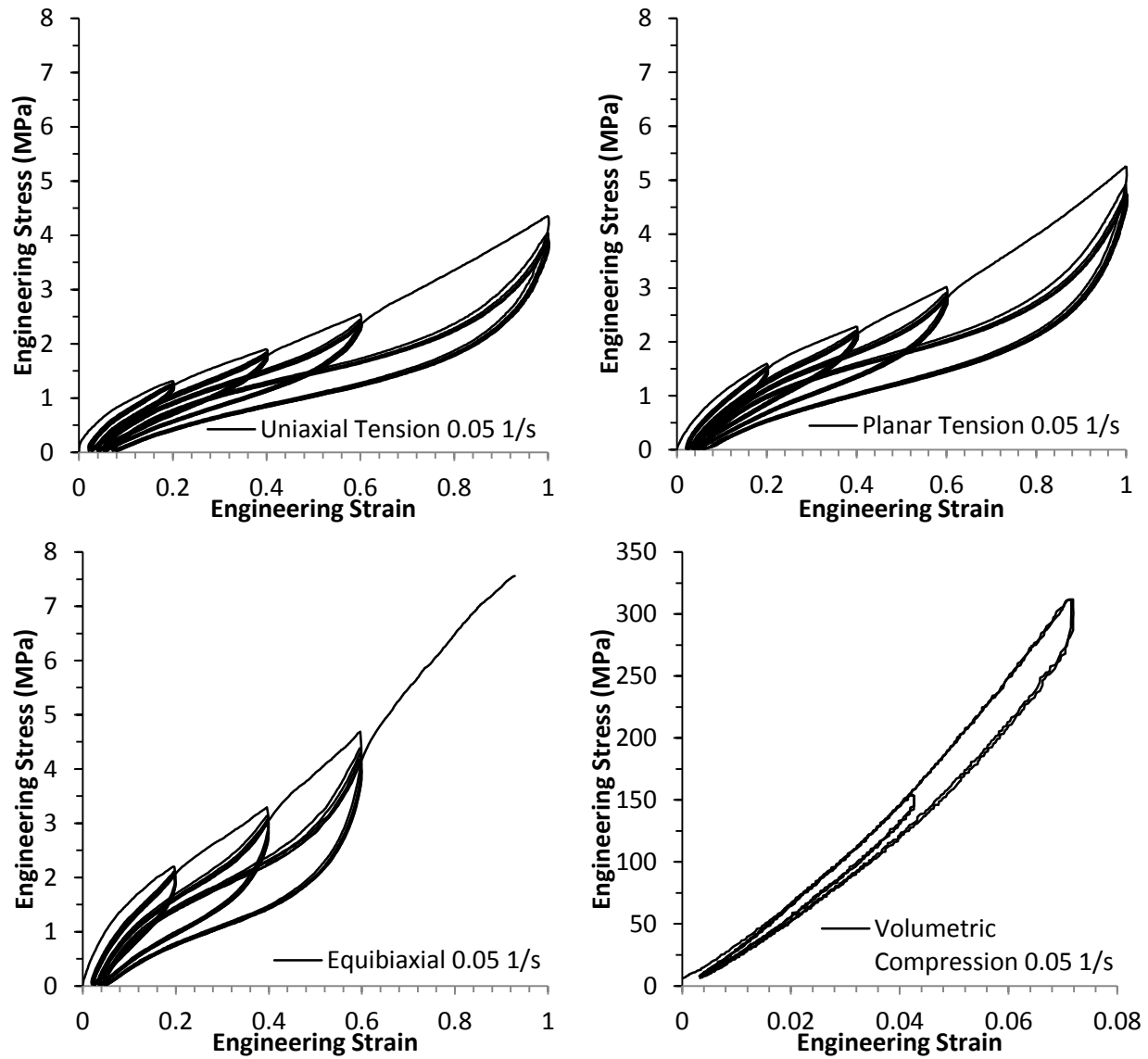


Figure 32: One Complete Trial for Each Hyperelastic Test Performed at a Strain Rate of 0.05 s^{-1} .

Under the assumption that the bulk compressive behavior behaves linearly, the bulk modulus (K) was taken as the slope of the volumetric compression stress-strain curve. For the comparison of the 4 tests, the conditioned 60% and 6.6% stress-strains curves for the hyperelastic and volumetric compression tests respectively are shown in figure 33.

For each of the hyperelastic tests in figure 32, 4 distinct ‘peaks’ are shown at strain levels of 20, 40, 60, and 100%. It was previously hypothesized that at each strain magnitude, cyclical loading would stabilize the stress-strain curve to a near-constant level. 5 cycles were chosen as a recommended means of stress-strain stabilization based on previous experience from Axel Products. At each strain magnitude for each hyperelastic test, the cyclical loading is shown to stabilize sufficiently after 5 cycles however it was also noted that each subsequent cycle produced a mild offset in strain in its un-stressed state as the curves do not return to the origin. This may be permanent deformation or viscoelastic effects preventing the material from instantaneously returning to its original shape. In either case, for this purpose, each selected curve was offset back to the origin for curve-fitting. The 1st and 5th cycles for each of the hyperelastic tests are compared in figure 34.

When transitioning from one strain magnitude to another it was also hypothesized that any previous pre-cycling would no longer apply as the curve would revert back to its original course on the first cycle. It is shown that in each case, after the 5th cycle, the curve converges back to its original path after exiting the previous pre-conditioned strain magnitude. Each of the 1st cycles for each strain magnitude are demonstrated to form a near-continuous stress-strain curve isolated from the rest of the cycles as demonstrated in figure 35.

When comparing the 5th cycles to each other at different strain levels shown in figure 36, unlike the 1st cycles, the loading paths do not converge onto a single path.

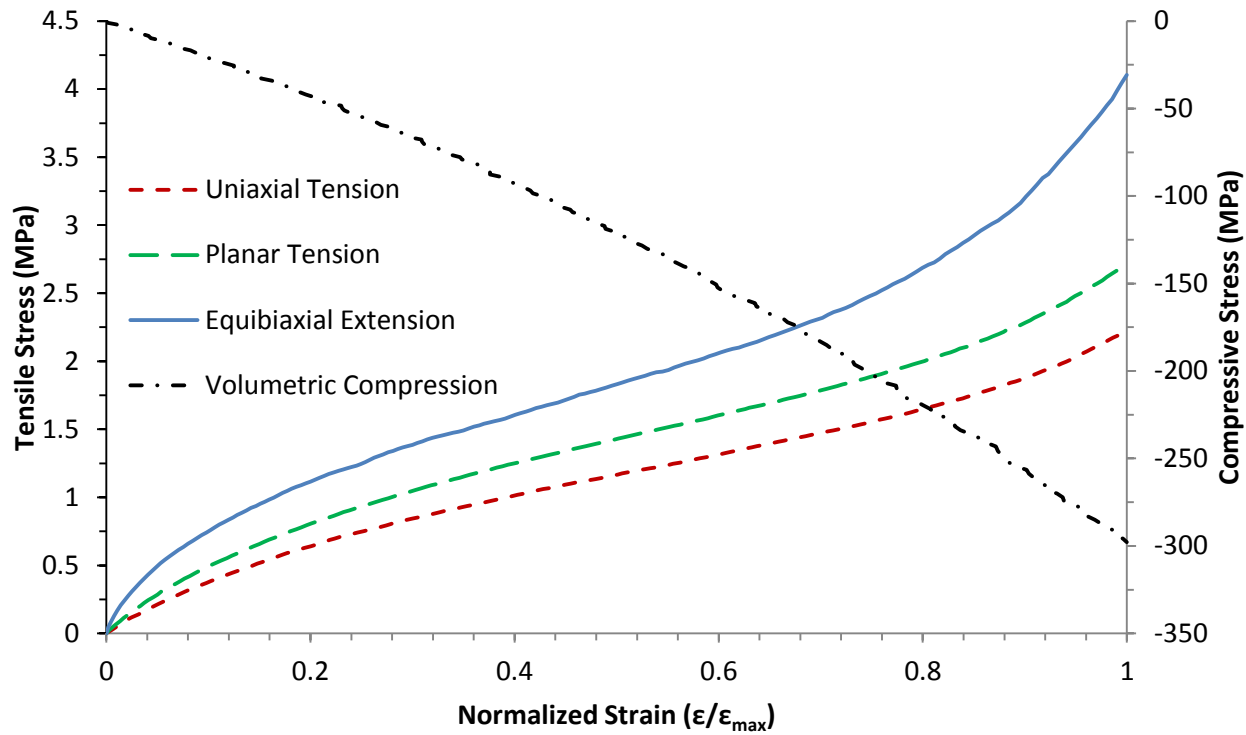


Figure 33: Conditioned Stress-Strain Curves at 60% Hyperelastic and 6.6% Volumetric Strain

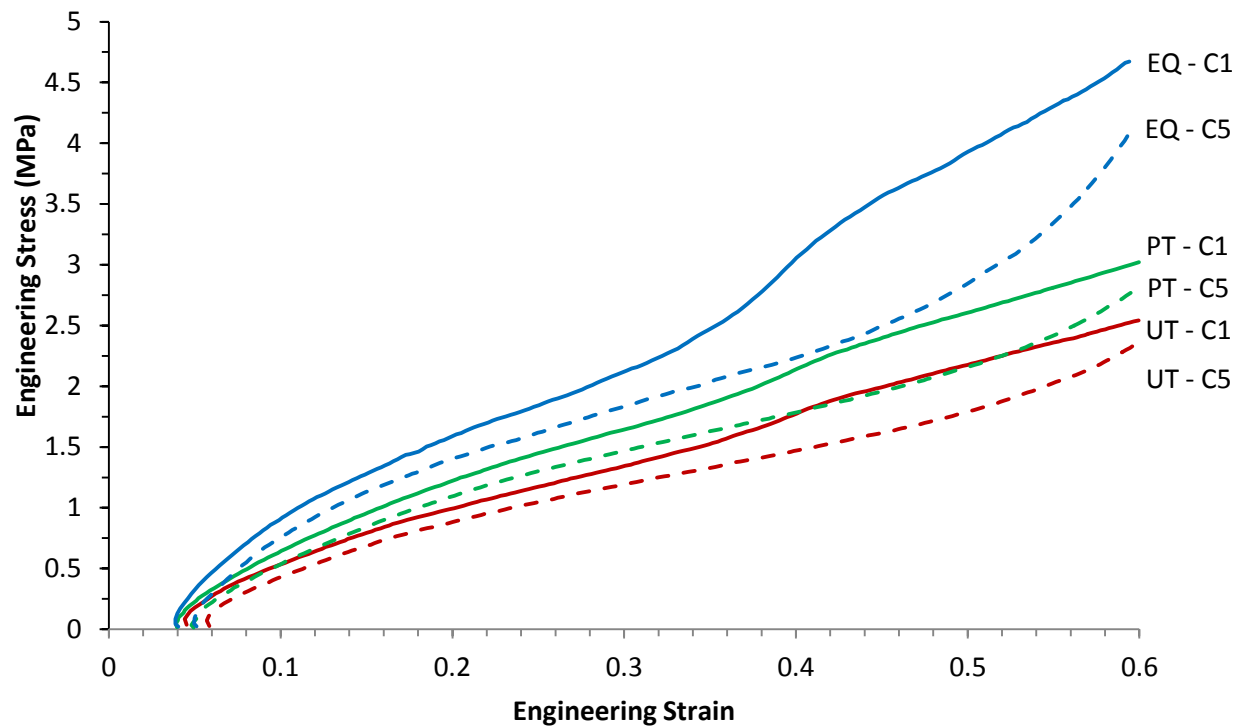


Figure 34: Comparison of 1st and 5th Cycles for each Hyperelastic Test at 60% Strain

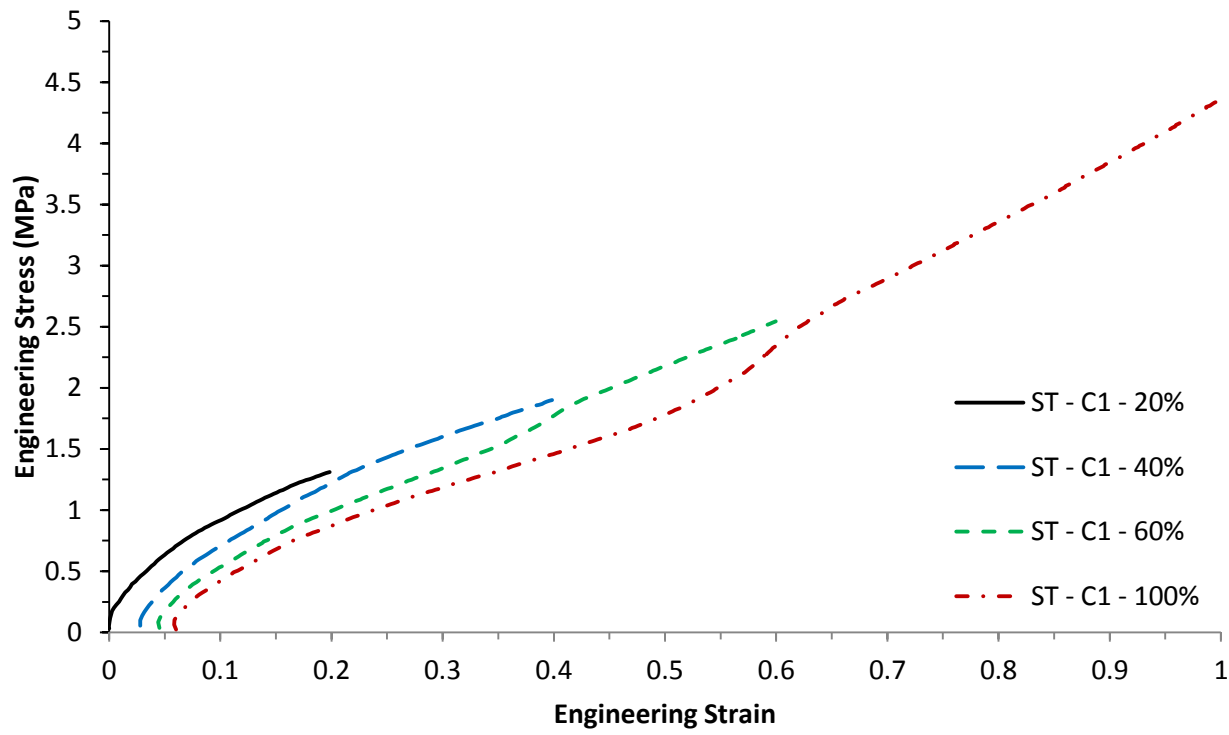


Figure 35: 1st Cycle Overlap for Uniaxial Tension

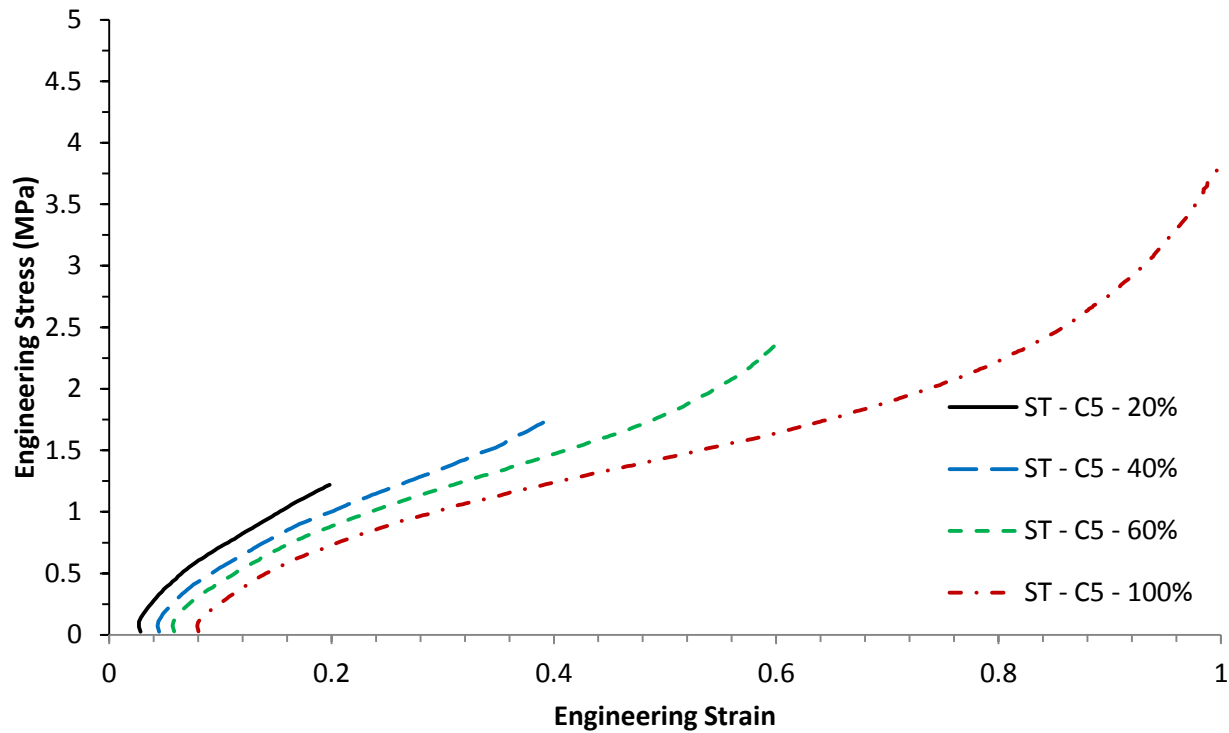


Figure 36: 5th Cycle Comparison for Uniaxial Tension

Rather, the end of each 5th cycle for the different levels of strain demonstrates an inflection indicating that strain-hardening does not occur at the same strain for each curve. From the perspective of application, the divergent behavior indicates that for instance, a model selected for 100% strain will perform differently than a model selected for 20% strain as the extrapolation of a low-strain hyperelastic model beyond its curve-fit range will falsely represent higher strain behavior.

The final notable material testing behavior is the effect of time on the behavior of rubber which is demonstrated in figure 37 by the difference in the stress-strain curves as a function of strain rate. All of the tests performed at 0.05 s⁻¹ were also performed at 0.00264 s⁻¹ as a means of testing 2 extremes for which the stress-strain behavior was expected to be different. It was hypothesized that the decrease in strain rate would reduce the stiffness of the rubber by some amount. There is a decrease in stiffness when comparing loading at 0.05 s⁻¹ to loading at 0.00264 s⁻¹ however it was observed that reducing the rate by a factor of 19 produces little difference. The small amount of behavioral difference between significant changes in loading rate opens up the possibility for interpolation of the experimental data at any rate between the 2 extremes. For example, if the desired strain rate is 0.01 s⁻¹, it is possible to create an artificial dataset through the linear interpolation of the experimental data points for 0.05 s⁻¹ and 0.00264 s⁻¹.

From the material test data, it was possible to generate suitable hyperelastic models based on permutations of the following categories for each of the tests depending on the required behavior:

- Strain magnitude: 20, 40, 60, 100%
- Loading cycle: 1st or 5th
- Strain rate: 0.05 or 0.00264 s⁻¹

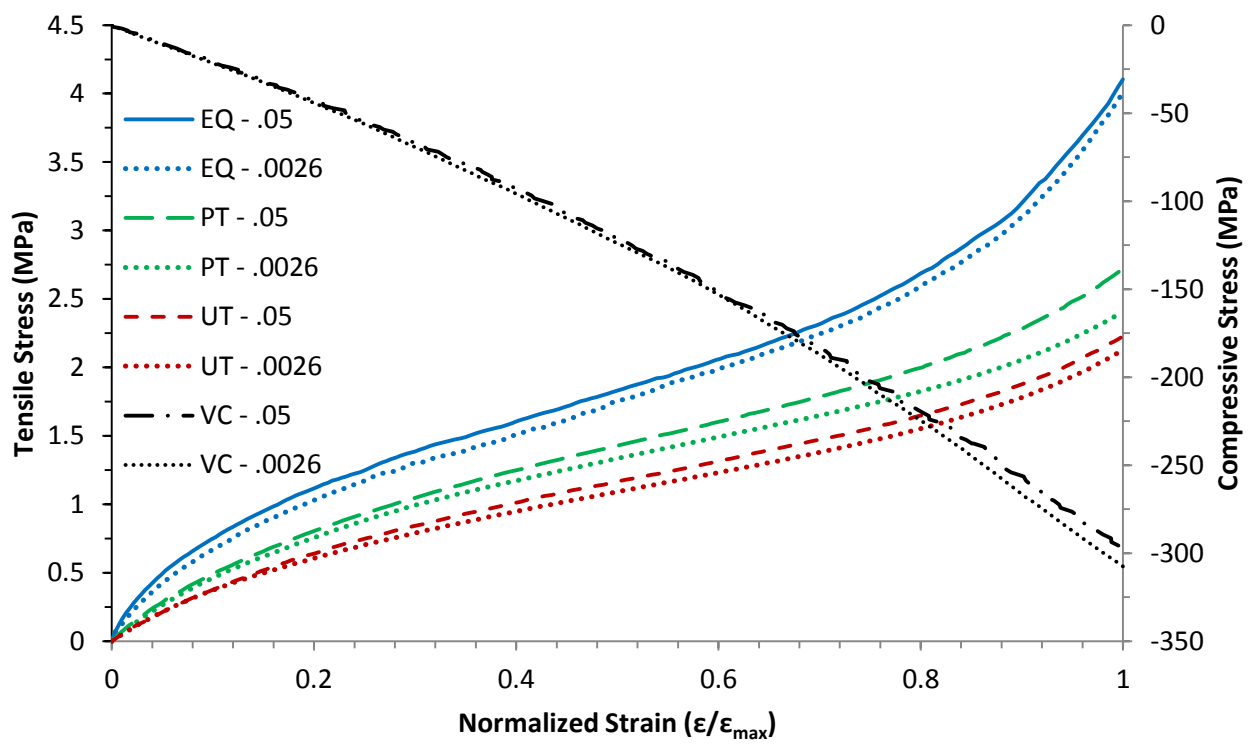


Figure 37: Comparison of Strain Rates 0.05 s^{-1} and 0.00264 s^{-1}

4.2 Frictional Testing Results

Frictional testing was conducted using an axial-torsion experiment which was conducted in 2 testing packages: rough surfaces abraded with 400-grit sandpaper and lubricated surfaces flooded with Lubriplate No. 105 as shown in figure 38. Each testing package offered by Axel Products included 3 tests at different normal pressures with 3 trials each for a total of 9 tests per package.

The provided experimental data included time, displacement, normal force, tangential force, and the friction coefficient collected at a rate of 2500 Hz. Figure 39 displays one trial performed for rough surfaces conditions with a normal pressure held constant at 3.4 MPa. The test initiates by setting the rotational cross-head to hold the selected normal pressure; it then rotates at a fixed rotational velocity. As the cross-head rotates and the specimen is held fixed, there is a build-up in tangential force until sliding is gradually permitted across the interface between the steel cup and the rubber specimen. Over the transition between sticking and sliding, the tangential force reaches a peak value which is taken as the static friction coefficient (μ_s) indicating the point at which sliding takes over sticking. Following the transition, the tangential force decays to a steady value as interfacial sliding is predominant. The point at which tangential force becomes steady is taken as the kinetic friction coefficient (μ_k). In the period after sliding is achieved, a build-up in heat and the modification of interfacial surfaces occurs which may present itself as a rise or a decay in tangential force.

The aforementioned procedure to collect the static and kinetic friction coefficients was implemented for all frictional tests and plotted in figure 40. Here, the friction coefficient appears to decrease as a function of normal pressure which is prevalent for rough contact conditions.

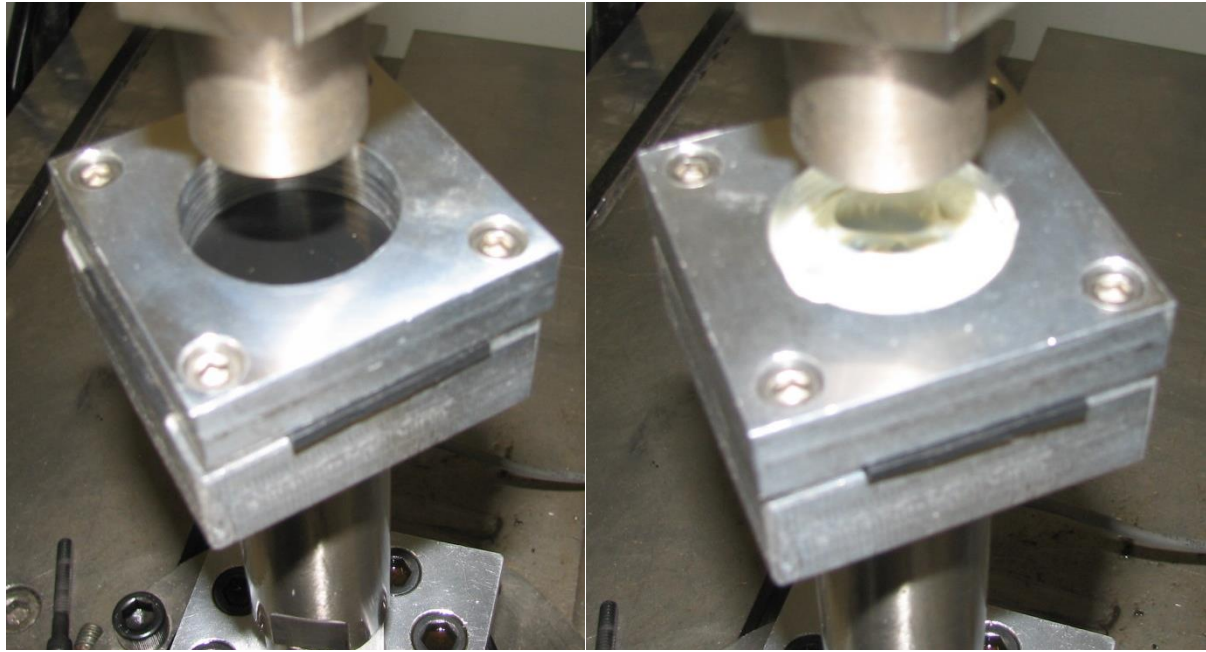


Figure 38: Axial-Torsion Friction Testing: Rough (Left) and Lubricated (Right)

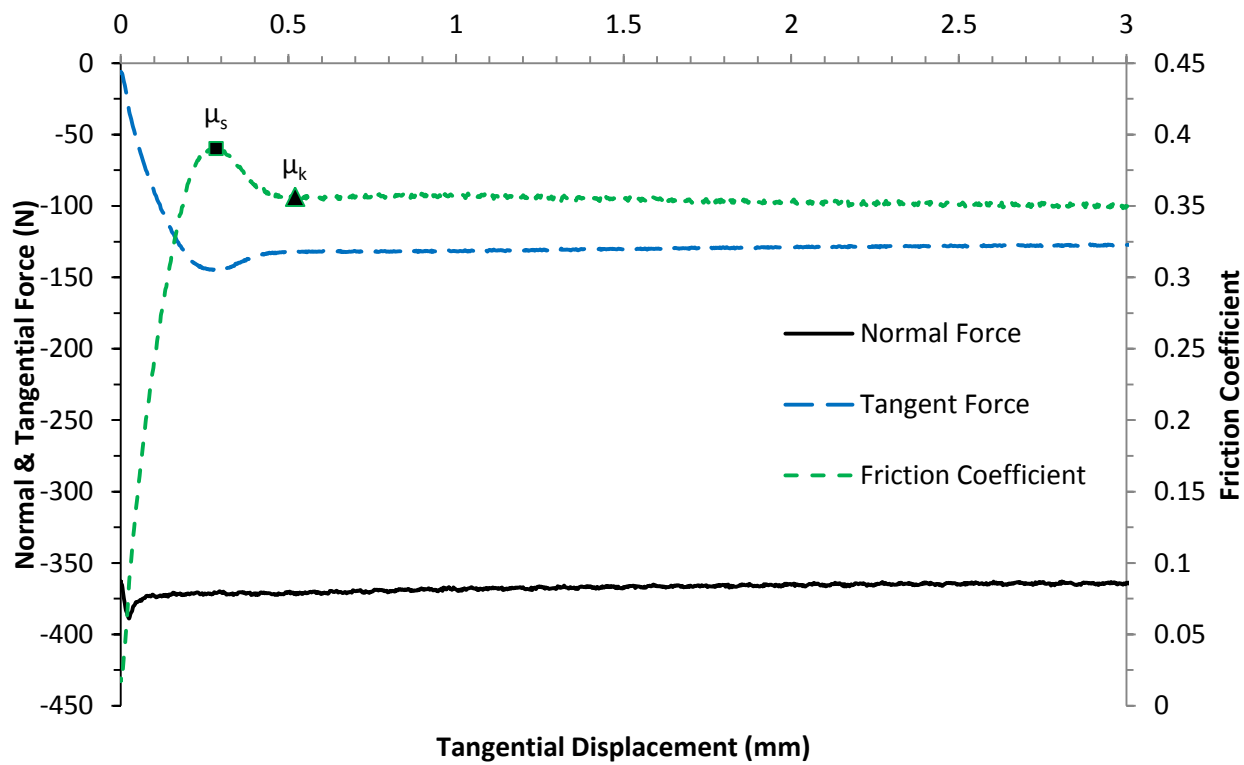


Figure 39: Single Axial-Torsion Test Tested at 3.4 MPa with Rough Surface

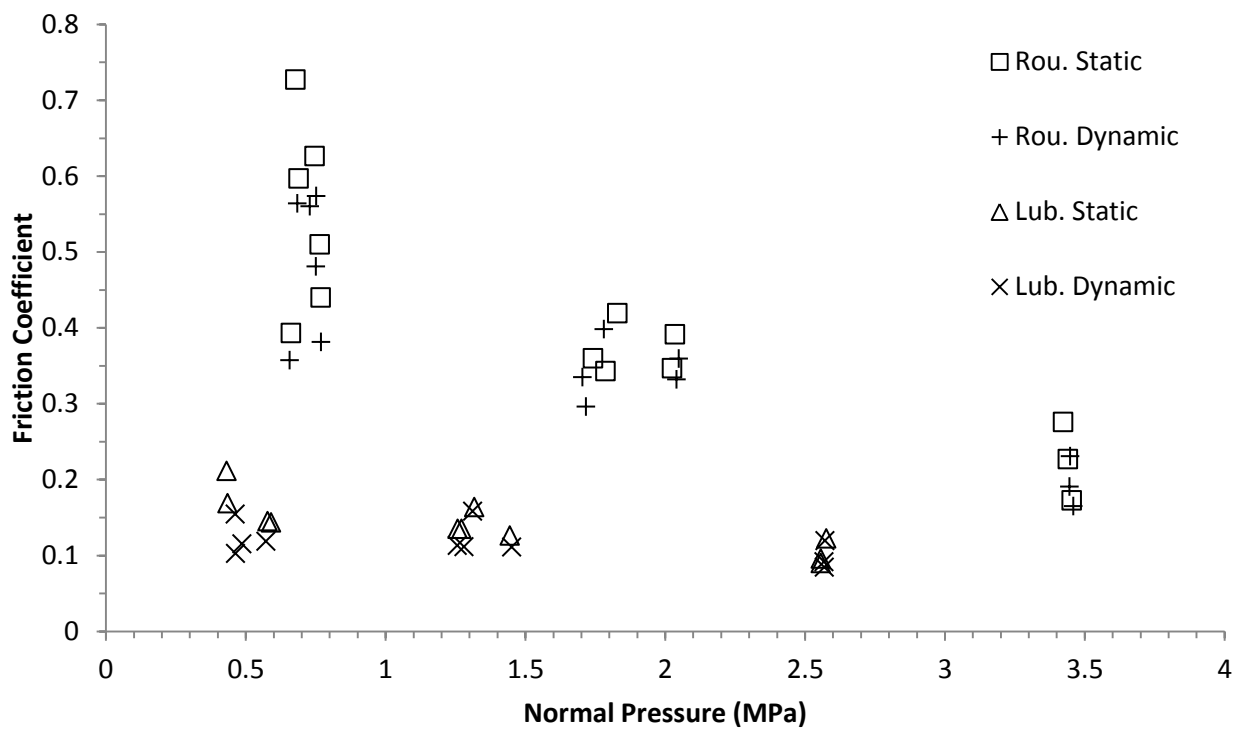


Figure 40: Static and Kinetic Friction Coefficient Results

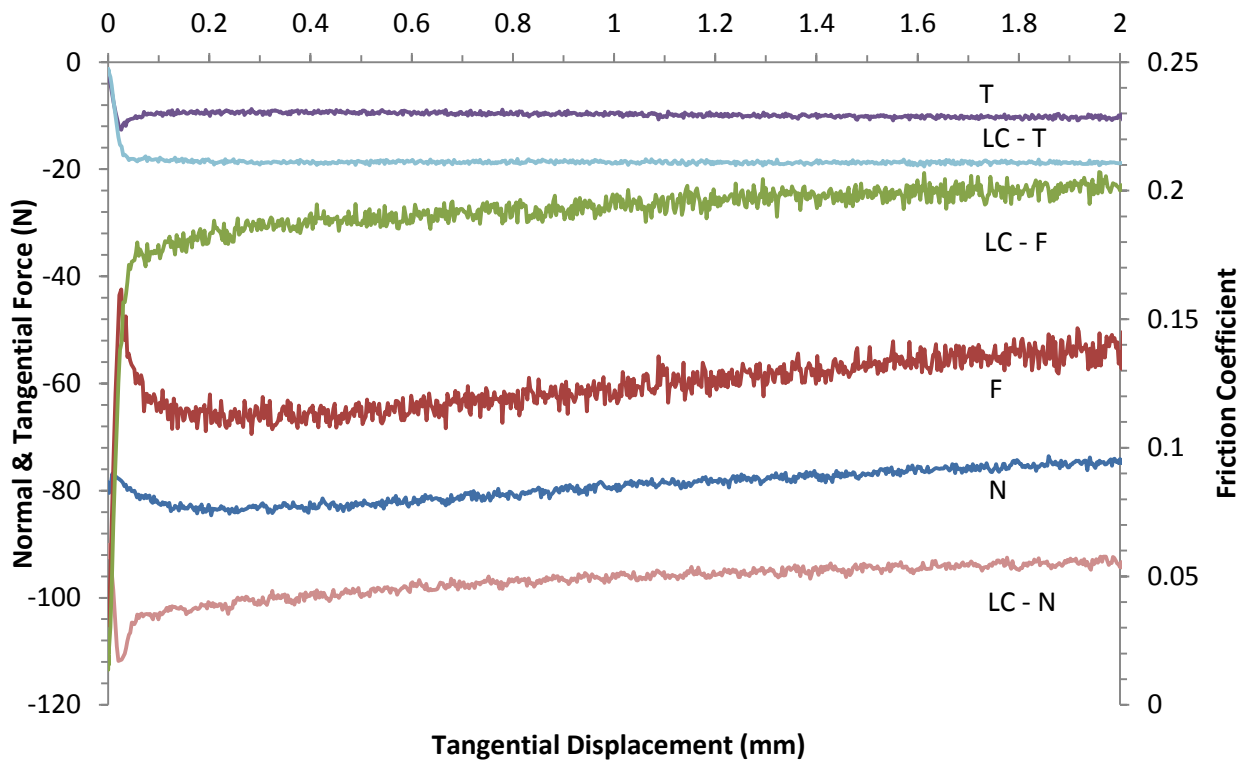


Figure 41: Testing Difficulties for a Lubricated Surface at 0.5 MPa Normal Pressure

Certain difficulties were encountered during the collection process causing the notable deviation between subsequent trials especially at lower normal pressures. Two of such examples are shown in figure 41 for a normal pressure of 0.5 MPa for lubricated contact where three sources of inconsistency are demonstrated. The first is signal noise for low pressures and non-repeatability between trials which may indicate equipment insensitivity at low pressures and a higher sensitivity of the rubber to the surface if the rubber asperities have not fully depressed into the steel surface. The second source is the lack of load control for certain trials which demonstrated stress relaxation in the application of normal pressure. Relaxation is prevalent in the 'N' curve where the normal pressure reduces as a function of time while the tangential force 'T' curve displays normal behavior which subsequently caused the friction coefficient 'F' curve to rise. The third source was the absence of a peak in the friction coefficient curve even under load-control in the load-controlled 'LC' curves. The cause of this error may be due to initial preliminary sliding offering an extended transition to full sliding which may be caused from an improperly conditioned interface.

For trials exhibiting stress relaxation, the static and kinetic friction coefficients were gathered from the peak and minimum values following the peak respectively. All trials exhibiting no peak were discarded. It must be emphasized that frictional testing should always be performed at constant normal pressure with fresh contact surfaces on both steel and rubber specimens with instrumentation operating at an appropriate level of sensitivity to achieve consistent results.

Two possibilities were presented to create a friction model in ANSYS. The simplest method was to take a single average friction coefficient for use in the default Coulomb model. This simple model was created using the average kinetic friction coefficient for both rough and lubricated contacts:

- Rough: $\mu_k = 0.3732$
- Lubricated: $\mu_k = 0.1163$

For more accurate frictional behavior, the Coulomb model was used in conjunction with Thirion's law. In accordance with Thirion's law, a linear regression was performed through the experimental datasets for both rough and lubricated interfaces in the form of $1/\mu_d$ as a function of normal pressure N as shown in figure 42. If the slope of the regression is denoted as 'm' and the intercept as 'b', then the friction coefficient function takes the form of equation 60 which is then plugged into Coulomb's law.

$$\mu(N) = \frac{1}{m \cdot N + b} \quad (60)$$

For use in ANSYS however, the friction coefficient function had to be tabulated as a function of normal pressure in a discrete dataset as it does not by default support continuous friction coefficient functions. Friction coefficients were collected over a range of 0 to 10 MPa at intervals of 1 MPa. Figure 43 displays the tabulated friction coefficients as a function of normal pressure for both rough and lubricated contact conditions. The black symbols indicate the calculated friction coefficients at the normal pressures used in the experiments. The black symbols are compared alongside the experimentally measured friction coefficients with their respective range of experimental deviation. Overall, Thirion's law provides a sufficient level of agreement with experimental values.

In ANSYS, the tabulated friction coefficients are input as a table with which intermediate values between subsequent intervals are linearly interpolated over the lines shown in figure 43. At the extremities of the table, friction coefficients larger than the largest tabulated value or lower than the lowest are held constant as no interpolation can be performed.

For this application, the friction coefficients were established in an expected normal pressure range of 0 to 10 MPa to provide data over the entire range of seal compression. Should the normal pressure exceed 10 MPa, the friction coefficient varies negligibly with normal pressure.

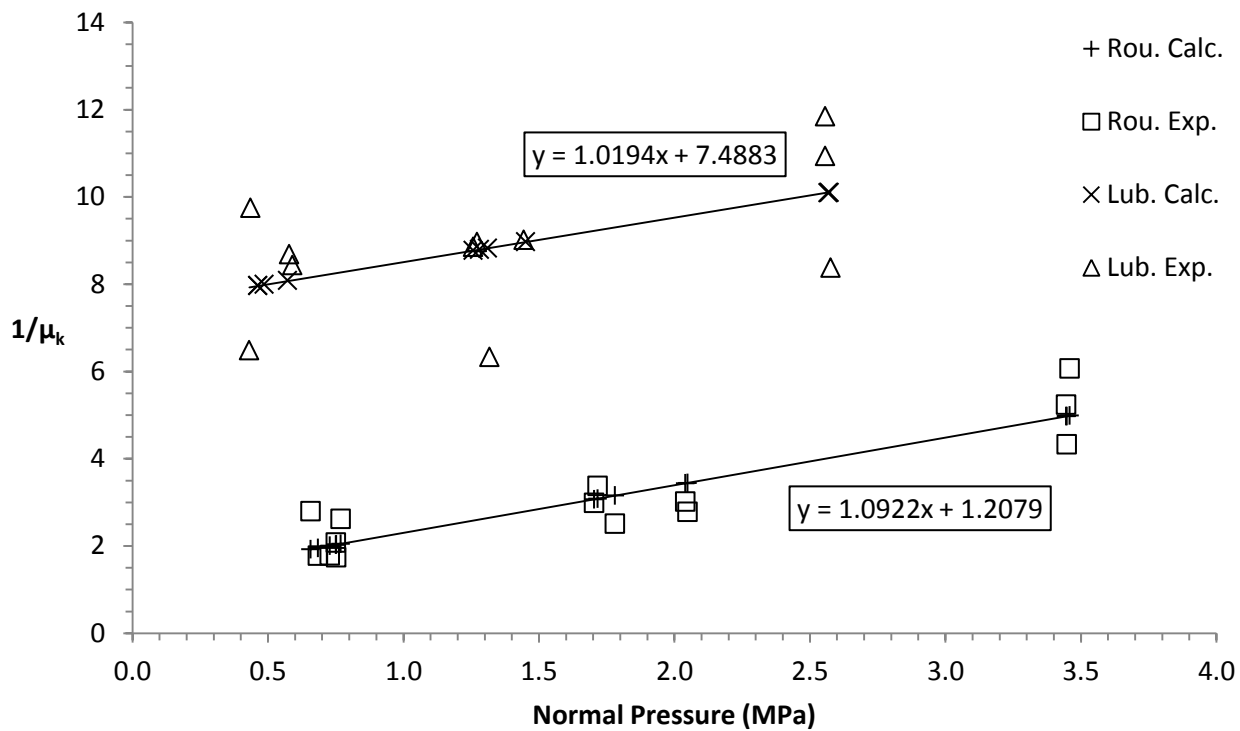


Figure 42: Thirion's Law Linear Regression

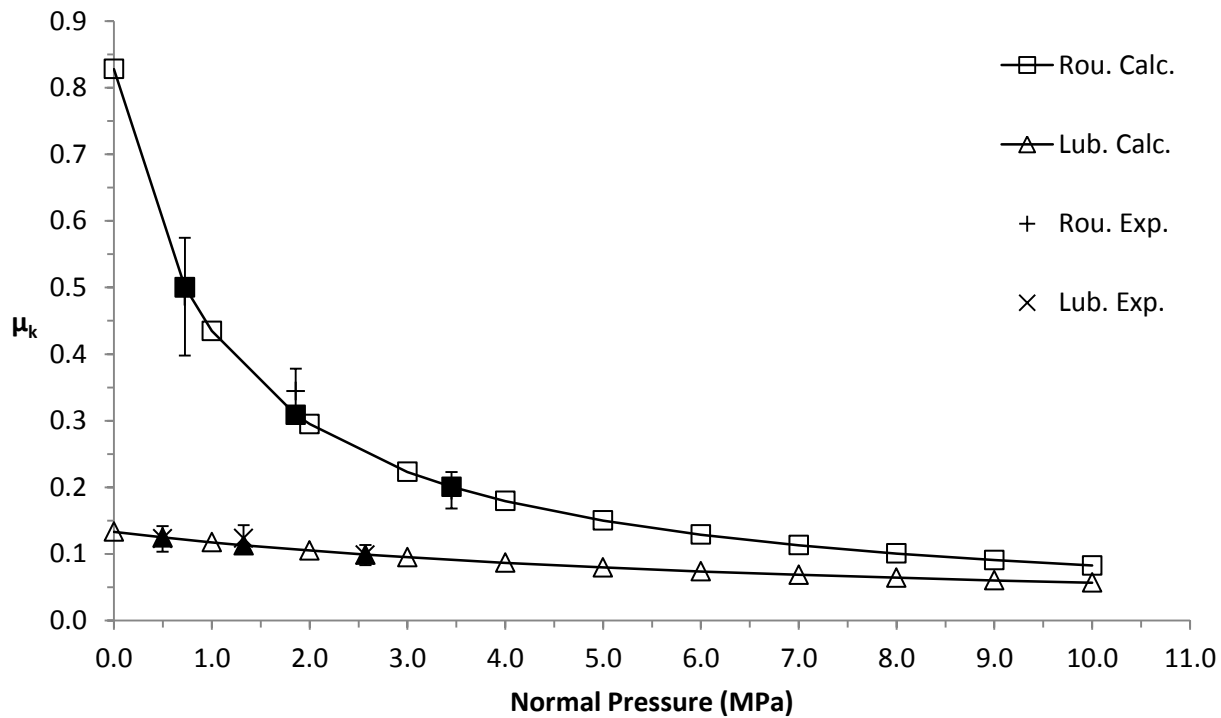


Figure 43: Thirion's Law Model (Black Points Indicate Experimental Values)

4.3 Linear Isotropic Approximation

As a first attempt, it was necessary to provide an approximation to the shape of the deformation and the expected magnitude of strain present in the rubber to select the appropriate hyperelastic material testing datasets for the creation of a preliminary hyperelastic model.

An axisymmetric linear isotropic model was constructed using a Young's modulus gathered from the 0 to 5% strain region for the uniaxial tensile test performed at 0.05 s^{-1} for 20% strain on the 5th loading cycle. The Poisson's ratio (ν) was gathered using the Young's modulus (E) and the bulk modulus (K) taken from a volumetric compression test performed at 0.05 s^{-1} on the final loading curve.

- $E = 8.61\text{ MPa}$
- $K = 3.38\text{ GPa}$
- $\nu = 0.4996$

A mesh size of 1 mm was implemented for a $102.5 \times 47 \times 31.5$ mm seal (see section 3.1) and a 5 mm axial displacement was applied on the bottom of the seal while the top was held fixed similar to figure 30. Both the top and bottom surfaces were held fixed in the radial direction representing a 'fully-bonded' constraint.

Figure 44 displays the results of the linear isotropic approximation showing the three principal element strains in addition to the Von-Mises strain. As this is a coarse mesh, strain concentrations are shown near the constrained nodes on the upper and lower corners. Strains of higher magnitude are shown in the 1st and 3rd principal strains where the majority of elements exceed 20% strain but aside from concentrations, most elements do not exceed 40% strain.

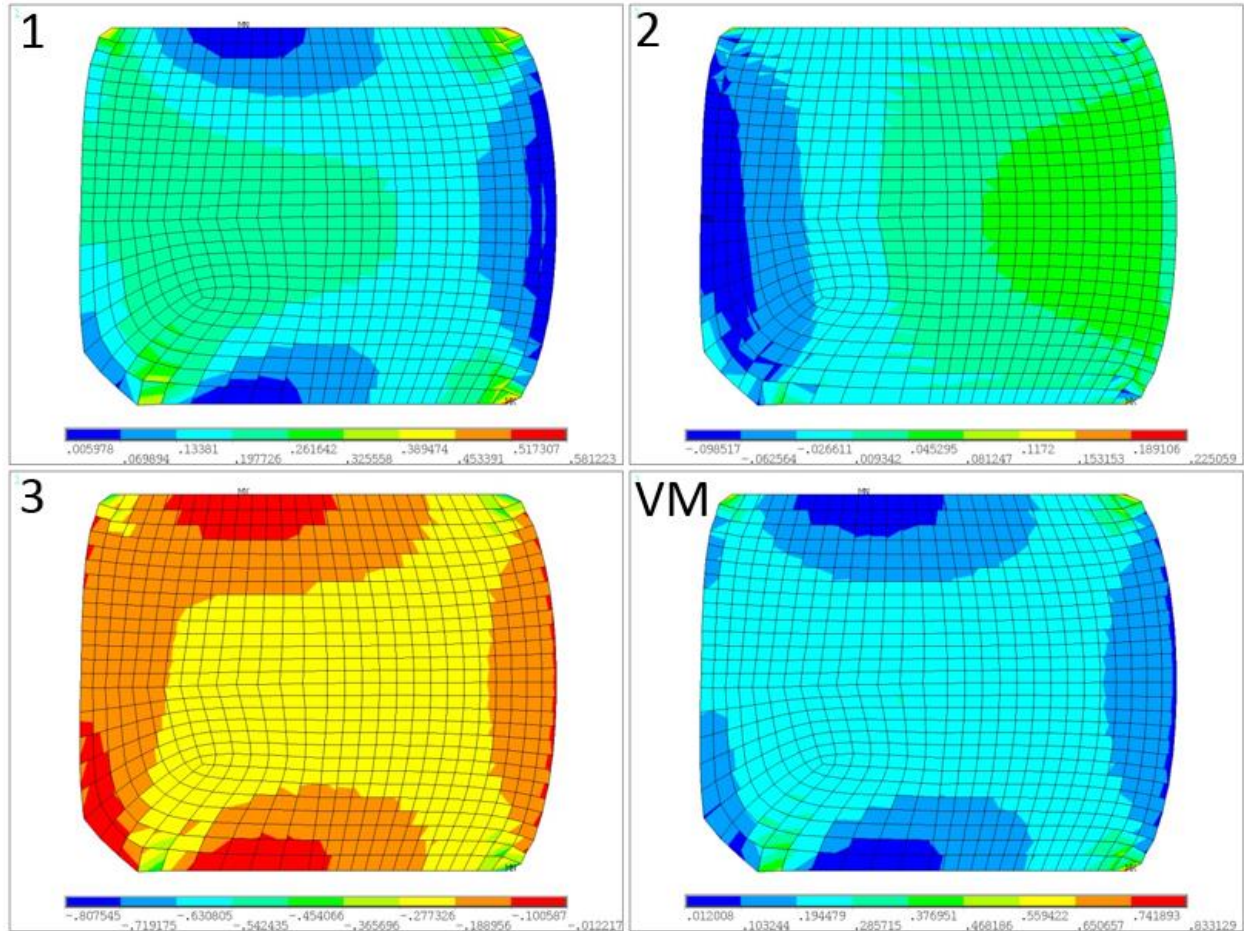


Figure 44: 1st, 2nd, 3rd Principal Strains; Von-Mises Strain

Because a hyperelastic model operates upon the use of principal extension ratios, it is important that the curve-fitting data encompasses the majority of the strain present in the volume of the rubber seal to avoid the extrapolation of the material model beyond its range of curve-fitting. In conclusion, the preliminary hyperelastic model required a fit to a minimum of 20% strain.

4.4 Preliminary Hyperelastic Model Selection

To initiate the implementation of a hyperelastic model, it was necessary to provide a simplified setup which would facilitate convergence in order to compare a variety of hyperelastic models curve-fit to several experimental datasets. The following hyperelastic models were considered: Neo-Hookean, Mooney-Rivlin, Yeoh, Ogden, Arruda-Boyce, and Gent. By default, each model was fit to material test data performed at 0.05 s^{-1} for 40% strain on the 5th cycle. Because of the many possibilities for curve-fitting, most attempts were performed using trial-and-error with selection performed based on ease-of-convergence and overall accuracy. Only the most suitable models were selected for a quantified comparison.

The FE model was prepared again with a 1 mm mesh size with a 102.5 x 47 x 31.5 mm seal however geometry for the rings were included and frictional contacts were established between the seal and the rings using a single average friction coefficient of 0.3732 for rough contact and 0.1163 for lubricated contact. Rough contact was employed for primary comparison and lubricated for secondary because rough contact had a higher difficulty in convergence. In other words, a model which converges for rough contact will usually converge for lubricated contact. A vertical displacement of 5 mm was applied to the bottom ring and the upper ring was held fixed. Both rings were held fixed in the radial direction.

The models were compared in terms of reaction force as a function of axial displacement compared to experimental data supplied by Shah [3] where the criteria was to minimize the maximum force

deviation and integral deviation. The models were assigned a rank in terms of both criterions and summed up to a total. The top 4 highest ranking models were then compared to data for a lubricated interface after which one was selected for future use. The force-displacement curves are shown in figure 45 and the ranks are tabulated in table 5.

From the presented comparison data, the 3rd order Yeoh model was the most successful hyperelastic model which offered both adequate accuracy and the highest rate of successful convergence with the lowest number of required iterations. The next most successful model was Neo-Hookean however it does not offer sufficient accuracy as it is recommended for use in low-strain models.

Mooney-Rivlin was hypothesized to be the most successful model as it is one of the most commonly used models in practice. However in all cases and orders (1, 3, 5, and 9th order), the solution failed because ANSYS reaches material instability over certain ranges of strain for uniaxial tensile, planar tension, and equibiaxial extension. The magnitude of the ranges differ for different orders of Mooney-Rivlin models however all were unsuitable to the required level of strain for this application. In addition, Ogden, Arruda-Boyce, and Gent are all models developed for higher levels of non-linear strain however upon trying them all, each displayed difficulty in convergence or failure.

The top 4 ranking models for the rough contact comparison were also compared to lubricated contact conditions with results shown in figure 46 and tabulated in table 6 with an equal comparison performed as for rough contact.

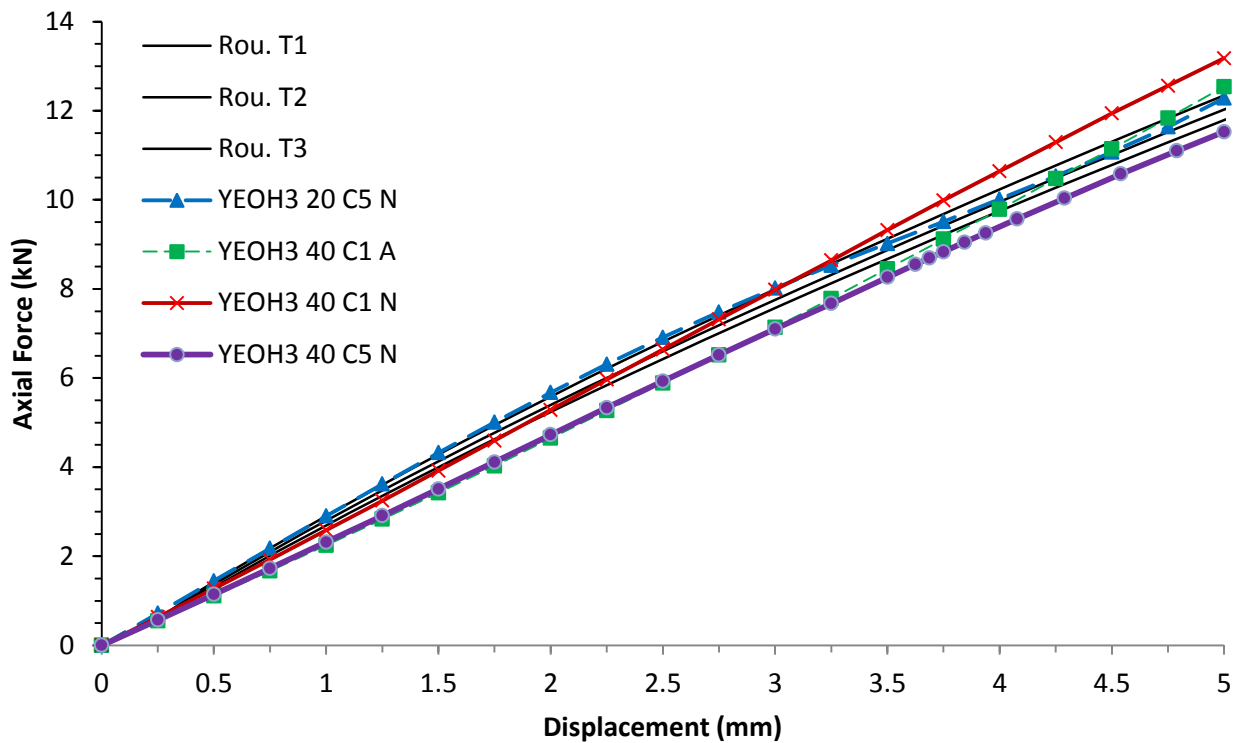


Figure 45: Rough Contact Comparison: Top 4

Table 5: Rough Comparison Results

Model				Maximum Deviation (%)		Integral Deviation (%)		Total Rank
Type	Fit	Cycle	%					
Neo-Hookean	NORM	5	40	5.4	4	14.6	3	7
YEOH-3	NORM	1	20	11.3	2	21.6	1	3
YEOH-3	NORM	1	40	8.7	3	3.9	6	9
YEOH-3	NORM	5	20	1.3	7	2.6	7	14
YEOH-3	NORM	5	40	4.9	5	8.3	4	9
YEOH-3	NORM	5	60	13.8	1	19.9	2	3
YEOH-3	ABS	1	40	3.5	6	5.4	5	11

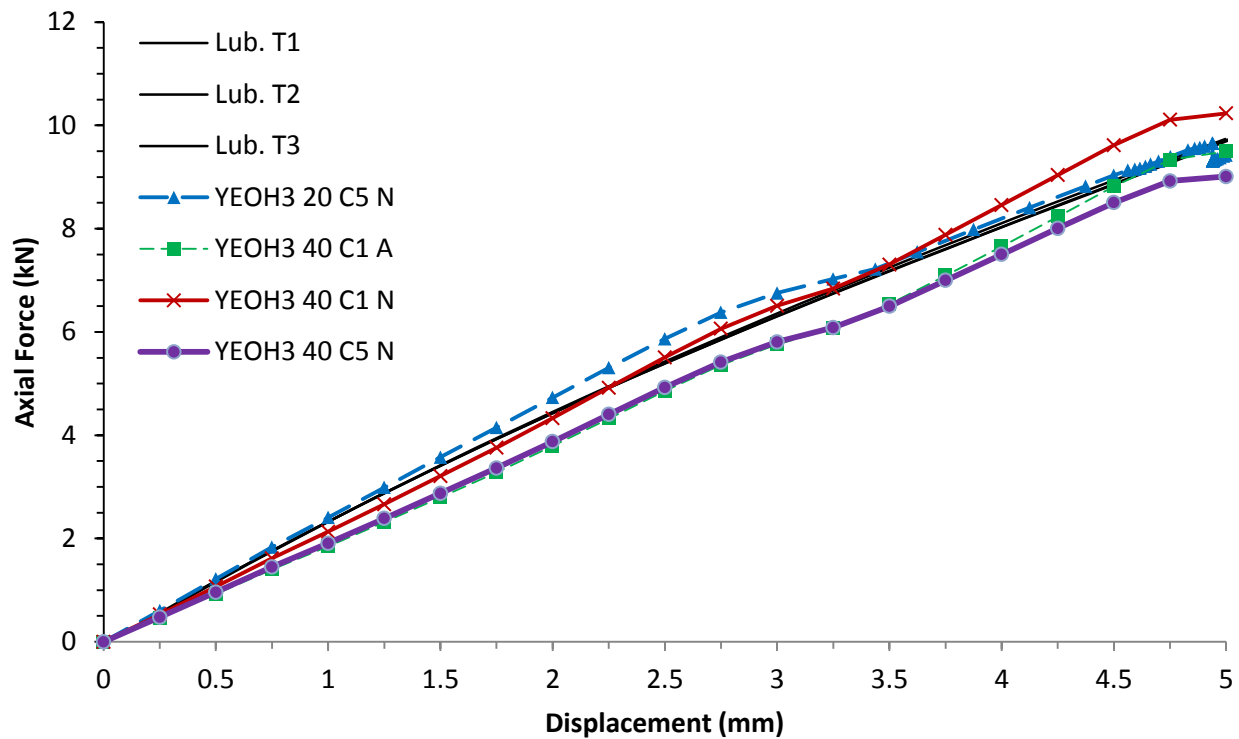


Figure 46: Wet Comparison Top 4

Table 6: Lubricated Contact Comparison Results

Model				Maximum Deviation (%)		Integral Deviation (%)		Total Rank
Type	Fit	Cycle	%					
YEOH-3	NORM	1	40	4.7	2	3.4	4	6
YEOH-3	NORM	5	20	1.3	4	4.0	3	7
YEOH-3	NORM	5	40	7.9	1	8.1	1	2
YEOH-3	ABS	1	40	2.9	3	7.1	2	5

Comparing the results for both rough and lubricated contact conditions, both showed that a 3rd order Yeoh model fit to 20% strain on the 5th cycle with normalized fitting displayed the highest rank overall. However, for the lubricated contact comparison, convergence became difficult at higher displacement as shown by the increase in automated sub-steps likely caused by premature strain-hardening in an incorrect extrapolation of the hyperelastic model beyond 20% strain. Thus, the 20% model was not selected.

The second best model was tied between the 3rd order Yeoh models fit to 40% strain on the 1st cycle using an absolute curve-fit versus a normalized curve-fit. The former was more suitable to the rough contact and the latter for the lubricated contact. Both models however do not follow the trend in the experimental data as their slopes tend to rise above the experimental data. Equally for the third best model, the 3rd order Yeoh model fit to 40% on the 1st cycle using a normalized fit, the slope towards the end caused the FE curve to rise above the experimental curve.

The next model was the 3rd order Yeoh model fit to 40% strain on the 5th cycle using a normalized fit. Despite displaying a maximum force deviation and integral deviation lower than the previously compared models, the trend followed the experimental data more accurately than other models. Additionally, the model was fit to a conditioned hyperelastic curve for the correct amount of strain using the recommended normalized fitting approach. Since the subsequent analysis was a mesh convergence analysis, the axial force was expected to rise for higher mesh densities therefore logically, the 3rd order Yeoh fit to the 5th cycle of 40% strain using normalized fitting was suitable and selected for future analyses.

4.5 Preliminary Mesh Sensitivity Analysis

Following the selection of a hyperelastic model, it was necessary to perform a mesh sensitivity analysis to determine the appropriate element size to produce consistent results in an acceptable amount of solution time. A traditional mesh sensitivity analysis was set up in that a progressive series of mesh refinements was performed and compared to criteria expected to converge to a relatively constant value at a given mesh size.

The FE model used for the hyperelastic model selection in 4.4 was employed for rough contact conditions given its higher level of mesh distortion with a baseline mesh-size of 1 mm. It was important to select the case of highest mesh distortion to ensure stress and strain concentrations as well as distorted elements were mitigated in the selection of a mesh.

Using 1 mm as a baseline mesh size, refinements were made both increasing and decreasing mesh size; the highest being 2 mm and the lowest being 0.25 mm as shown in figure 47. Several criteria were employed to compare the different element sizes:

- Maximum Von-Mises stress
- Maximum Von-Mises strain
- Reaction force
- Maximum contact penetration
- Solution time
- Iterations
- Warning element count

All of the results for all criteria used in the mesh sensitivity analysis are listed in table 7 as a function of element size and count.

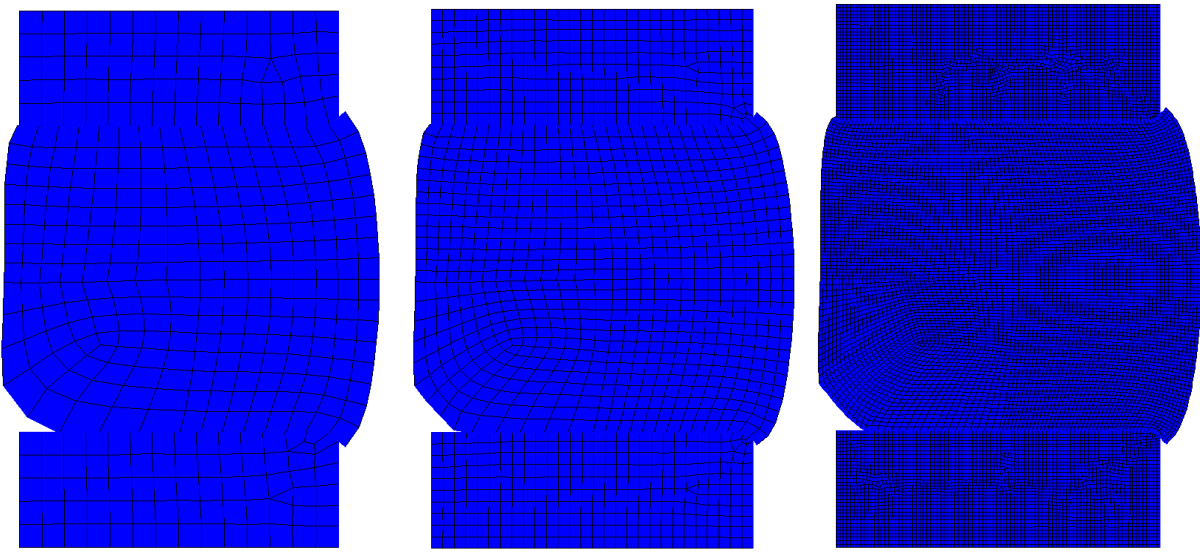


Figure 47: Maximum (2 mm), Baseline (1 mm), Minimum (0.25 mm) Mesh Sizes

Table 7: Preliminary Mesh Sensitivity Summary

Element Size (mm)	Element Count	Max Von-Mises Element Strain (%)	Max Von-Mises Element Stress (MPa)	Max Axial Force (N)	Max Penetration (mm)	Solution Time (mins)	Iterations	Deviation From Finest Mesh (%)
1	1442	40	8.9	11019	0.07	1.2	115	6.0
2	457	39	6.1	10106	0.05	0.6	141	13.8
0.5	4670	48	13.7	11455	0.07	2.1	97	2.3
0.25	18039	54	8.0	11720	0.09	19.1	185	0.0
0.4	8692	52	7.0	11523	0.08	6.7	170	1.7
0.3	14681	55	7.6	11661	0.08	10.1	152	0.5
0.5 (refined)	9043	55	14.1	11782	0.08	4.0	95	0.5

For the purposes of this model, the two most important criteria were the maximum Von-Mises strain and the axial reaction force as they directly dictate both the required strain magnitude for the hyperelastic model and the accuracy of the primary experimental result. Figure 48 displays the mesh sensitivity results in terms of axial reaction force and maximum Von-Mises strain.

However some notable behavior occurs in the other criteria. The maximum Von-Mises stress does not converge and increases with element count. The location of this maximum occurs at a 90-degree corner on the bottom rings where nodes are held fixed. As the behavior of the rings was assumed to be rigid and therefore unimportant to the behavior of the seal given their very low stress, this result was neglected. Maximum penetration was consistent as the enforced maximum was 0.1 mm; no contact element exceeded allowable penetration which indicated successful contact formulation. Finally, the number of iterations is shown to increase with element count which is counter-intuitive to most FE analyses. In most cases, mesh refinement improves the rate of success of convergence however in the case of highly non-linear materials and contact problems; a greater number of elements offer a greater number of highly deformed elements which may require additional iterations to solve.

Examining figure 48, convergence is initiated for both axial force and maximum Von-Mises strain at 4670 elements (0.5 mm mesh size) displaying an acceptably uniform behavior in comparison to the results at the maximum count of 18039 elements (0.25 mm). A mesh size of 0.4 mm however offers a relatively fast solution time of 6.7 minutes with an axial force and maximum strain deviation of 1.7 and 2.7% respectively. Therefore, a mesh size of 0.4 mm was selected for future analyses.

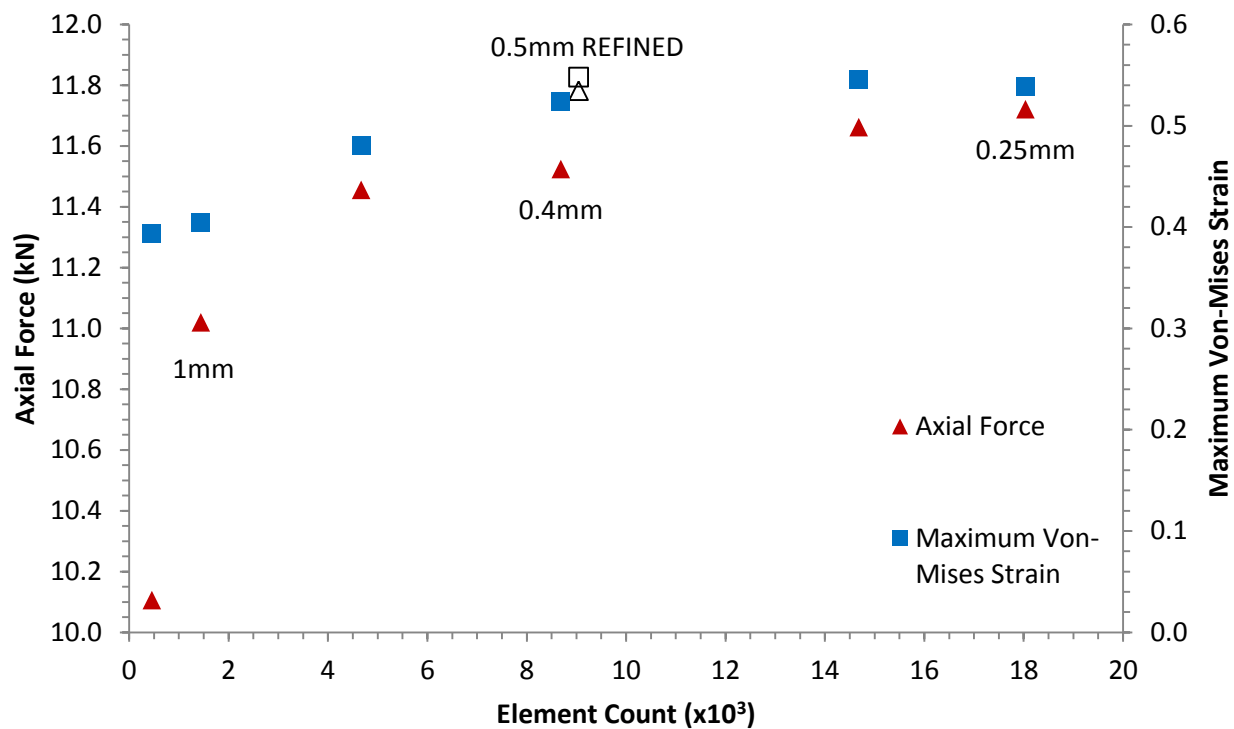


Figure 48: Mesh Sensitivity Analysis – Key Results

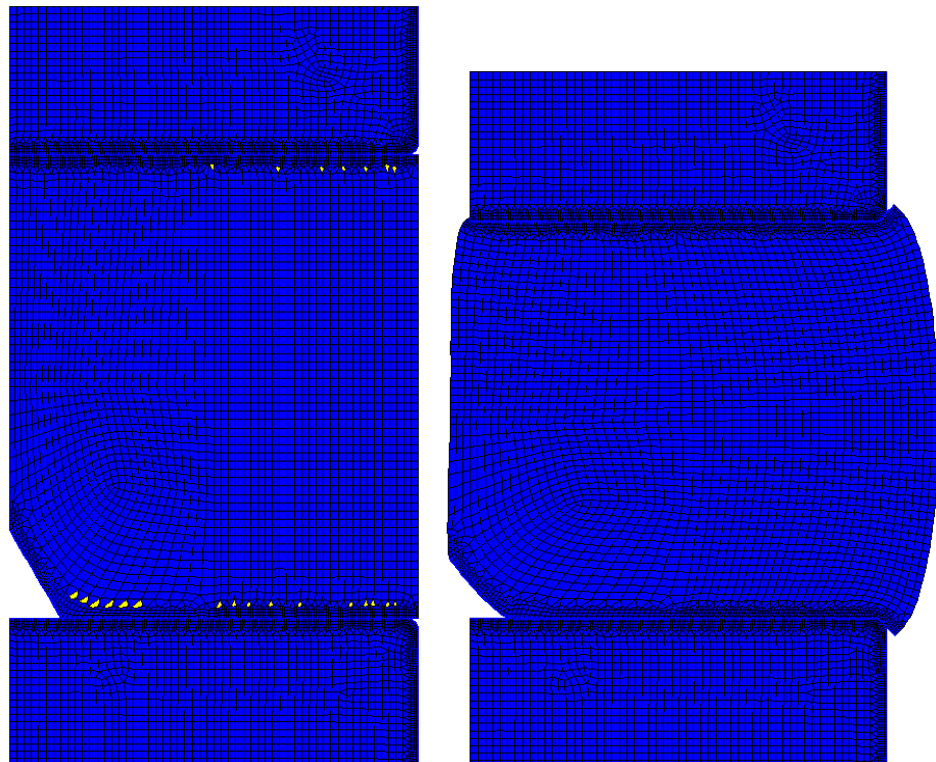


Figure 49: Localized Mesh Refinement Analysis (Yellow Indicates Warning Element)

One more possibility was examined for optimizing the mesh which was to locally refine contact areas as shown in figure 49. In theory, localized refinement would provide a higher mesh density in areas of contact and high strain. However, without the use of triangular plane elements which are normally too stiff for use in hyperelastic materials, quadrilateral element transitions from 2 mesh sizes degrade the mesh quality prior to analysis and produces poor transition zones with initially highly distorted elements. Upon running the analysis, although the number of iterations was lower, the axial force and maximum Von-Mises strain were significantly increased showing a discontinuity in the mesh sensitivity curves. Additionally, 23 elements highlighted in yellow were shown to distort severely in important areas which contributed to error in the solution. Thus, localized refinements were not employed for any subsequent analyses.

4.6 Preliminary Attempt with Pipe

Following the selection of preliminary hyperelastic and frictional models using an optimized mesh size, the pipe and mandrel were included into the FE model. In accordance with a methodology developed by Shaha [3], the axial displacement was increased to 6 mm and loaded at a rate of 0.05 s^{-1} .

In a similar approach to the linear isotropic model, the 3 principal strains were examined to determine whether the range of strain within the majority of the elements was within the range of the hyperelastic model curve-fit. Both the rough and lubricated contact conditions were examined with friction coefficients of 0.3732 and 0.1163 respectively.

For both rough and lubricated contact conditions, their time-lapse deformations are plotted in figure 50 and figure 51 respectively. Examining the deformation for rough contact, due to higher friction along the ring-seal interface, the rubber extrudes radially with a convex parabolic shape which later, reaches the pipe wall and concentrates the strain gradient with a parabolic pressure gradient.

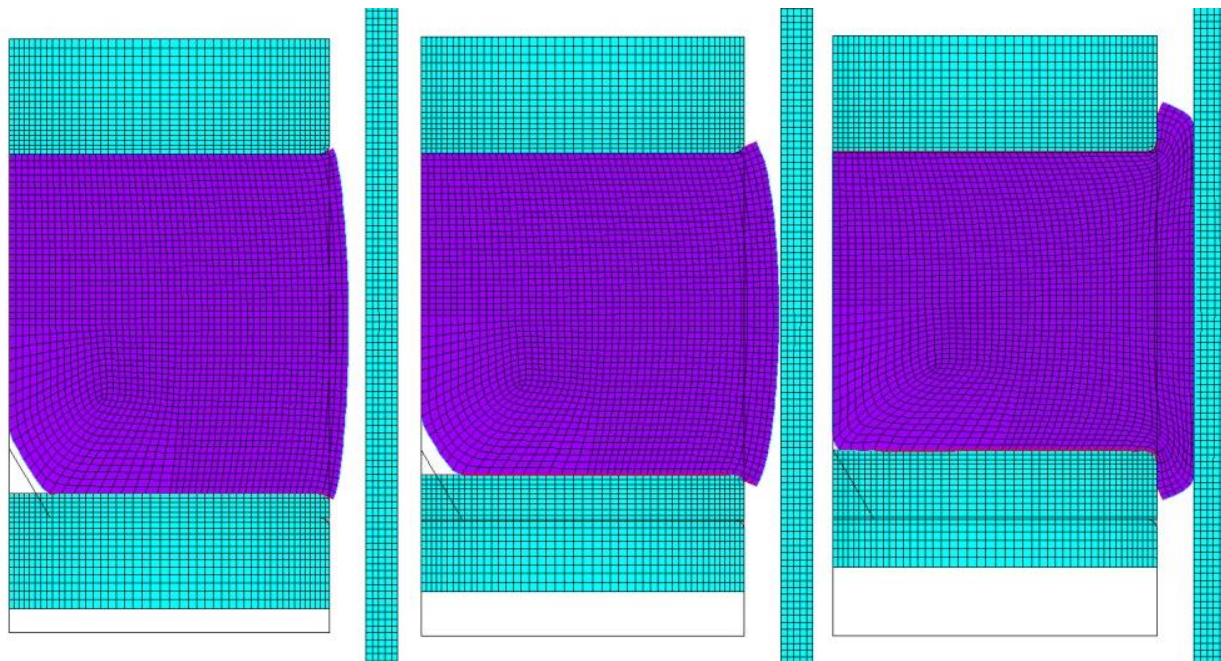


Figure 50: Rough Contact Radial Deformation Time-lapse

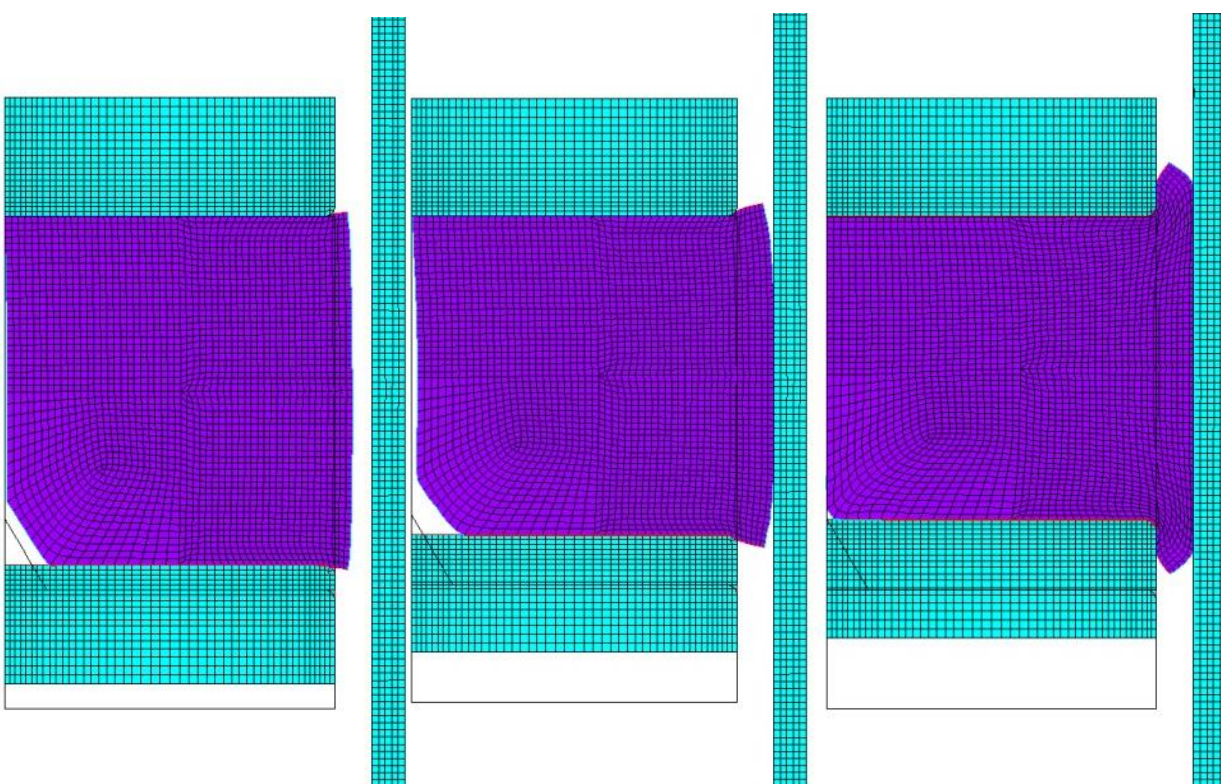


Figure 51: Lubricated Contact Radial Deformation Time-lapse

For lubricated conditions, the rubber extrudes radially with a very mild parabolic shape indicating more slip occurs at the seal-ring interface. The seal then reaches the pipe wall with a more uniform contact area which produces a more uniform pressure and strain gradient. Both of these deformation results agree with qualitative experimental predictions.

Upon viewing the element results, the first and third principal element strains displayed the highest magnitude for both contact interfaces. Figure 52 and figure 53 shows a comparison of the first principal strain result for both rough and lubricated contact where the majority of the rubber elements remains within 40% strain with select regions reaching up to 85% strain. The third principal strain result shown in figure 54 and figure 55 however displays a higher magnitude of strain with select regions reaching up to 103% compressive strain.

It was determined from this analysis that curve-fitting at 40% strain was insufficient to accurately characterize the strain in the majority of the rubber elements. 60% would be sufficient for most of the elements however 100% was selected because it offers a full characterization of the rubber material in the seal with room for higher strain if need-be.

When comparing the results of the preliminary attempt with pipe contact to experimental results shown in figure 56 and Figure 57, two linear trends are observed. As the seal is being compressed at a uniform rate, the axial reaction force increases linearly with axial displacement up until an inflection is caused by the contact between the seal and the pipe wall. As the seal gains more contact with the pipe wall, it becomes more constrained which as result, shifts the rubber into a state of volumetric compression which requires significantly more force to compress. Following the inflection, contact is fully established and axial force increases linearly at a rapid rate.

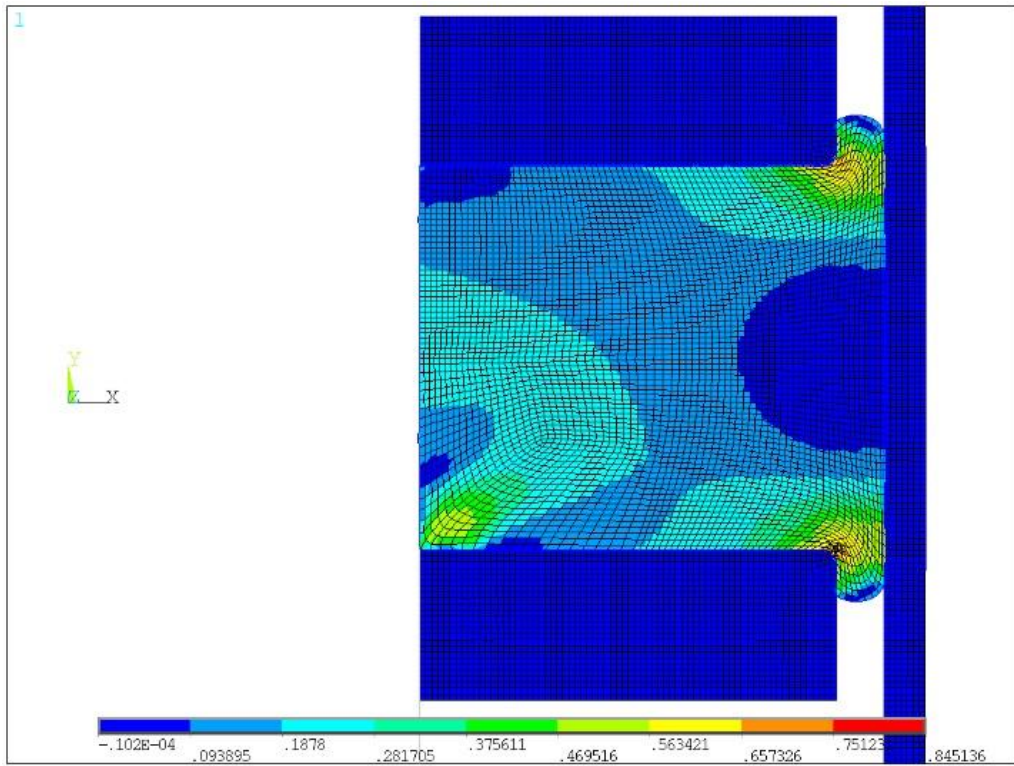


Figure 52: First Principal Element Strain for Rough Interface

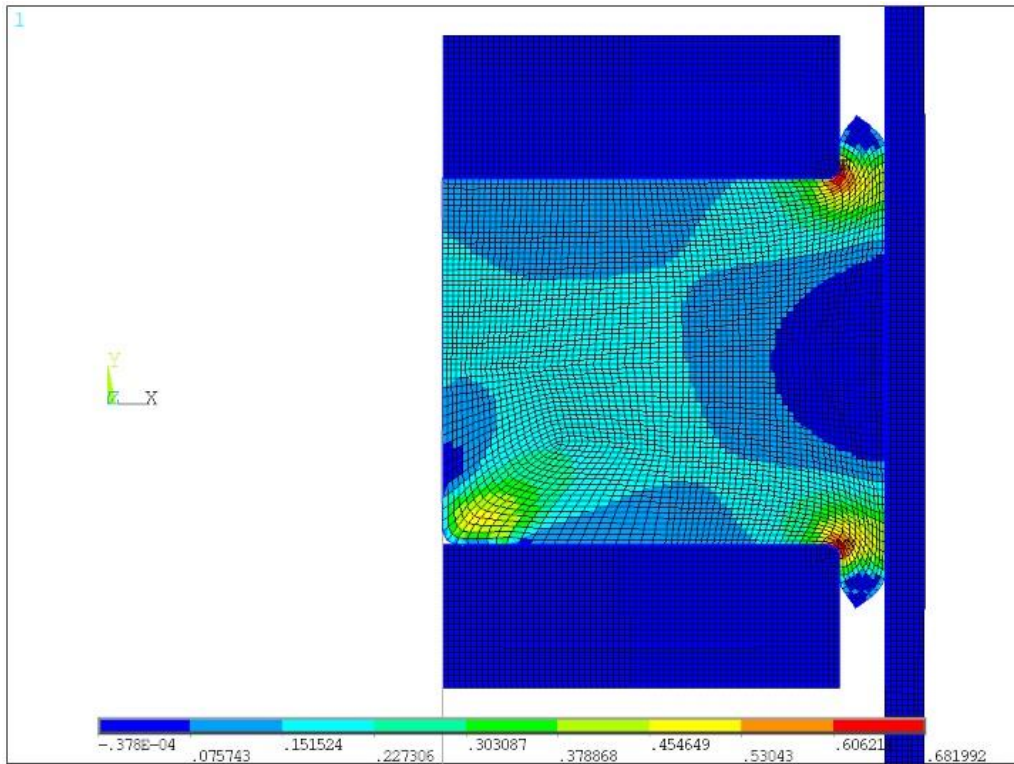


Figure 53: First Principal Element Strain for Lubricated Interface

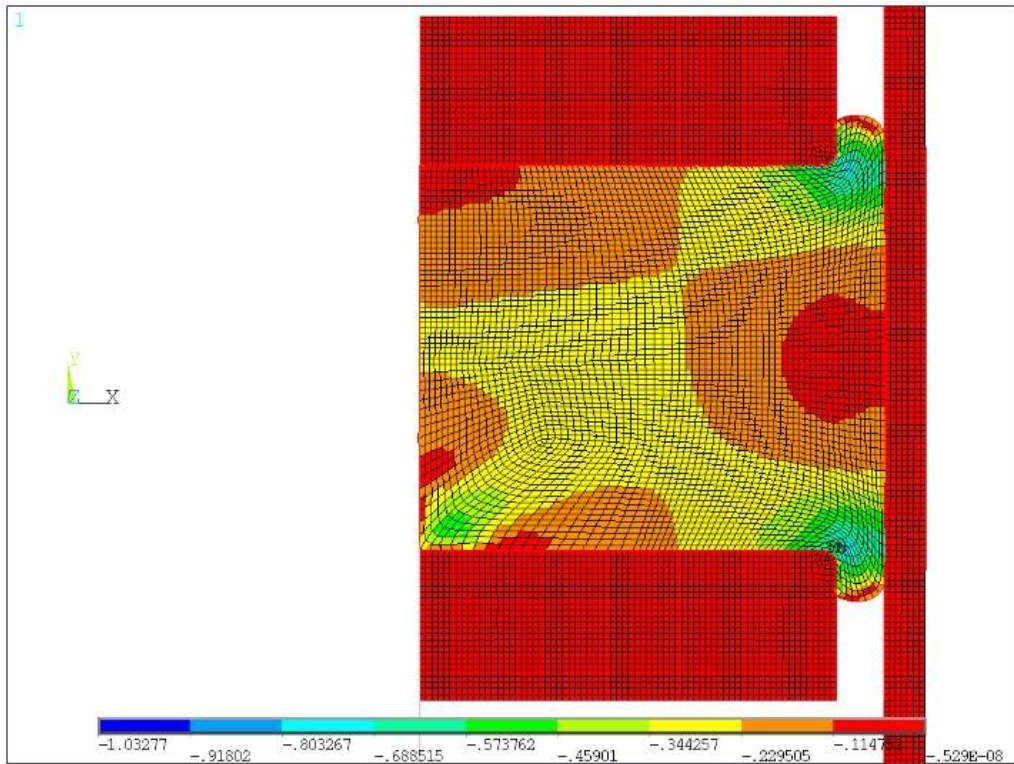


Figure 54: Third Principal Element Strain for Rough Interface

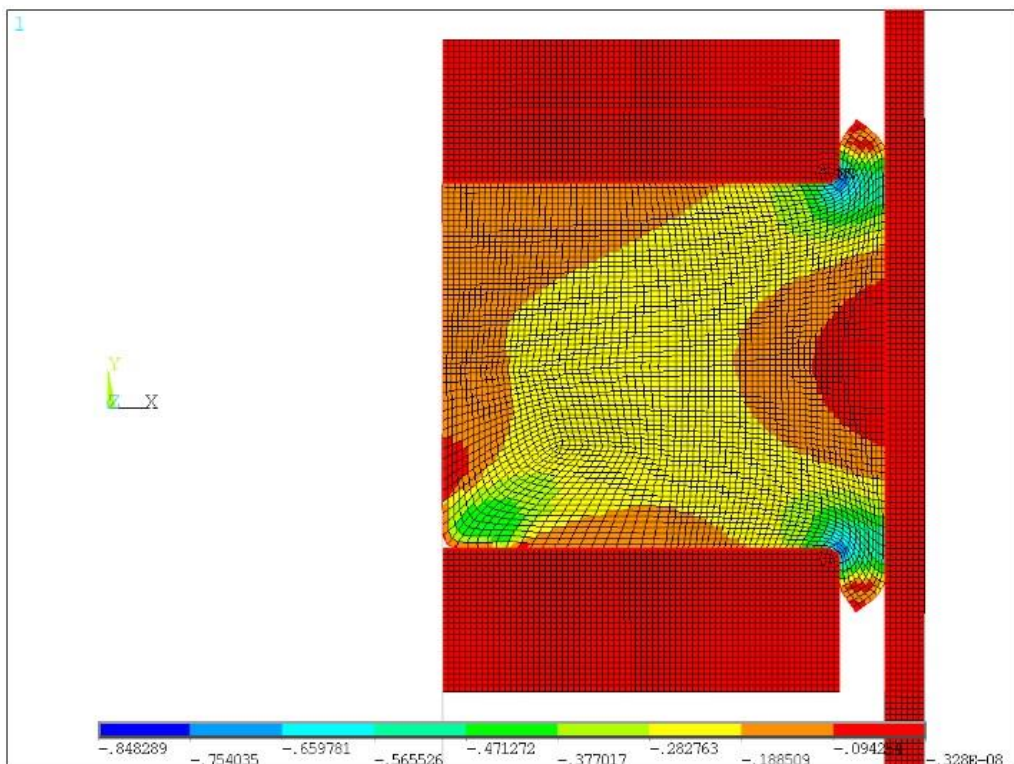


Figure 55: Third Principal Element Strain for Lubricated Interface

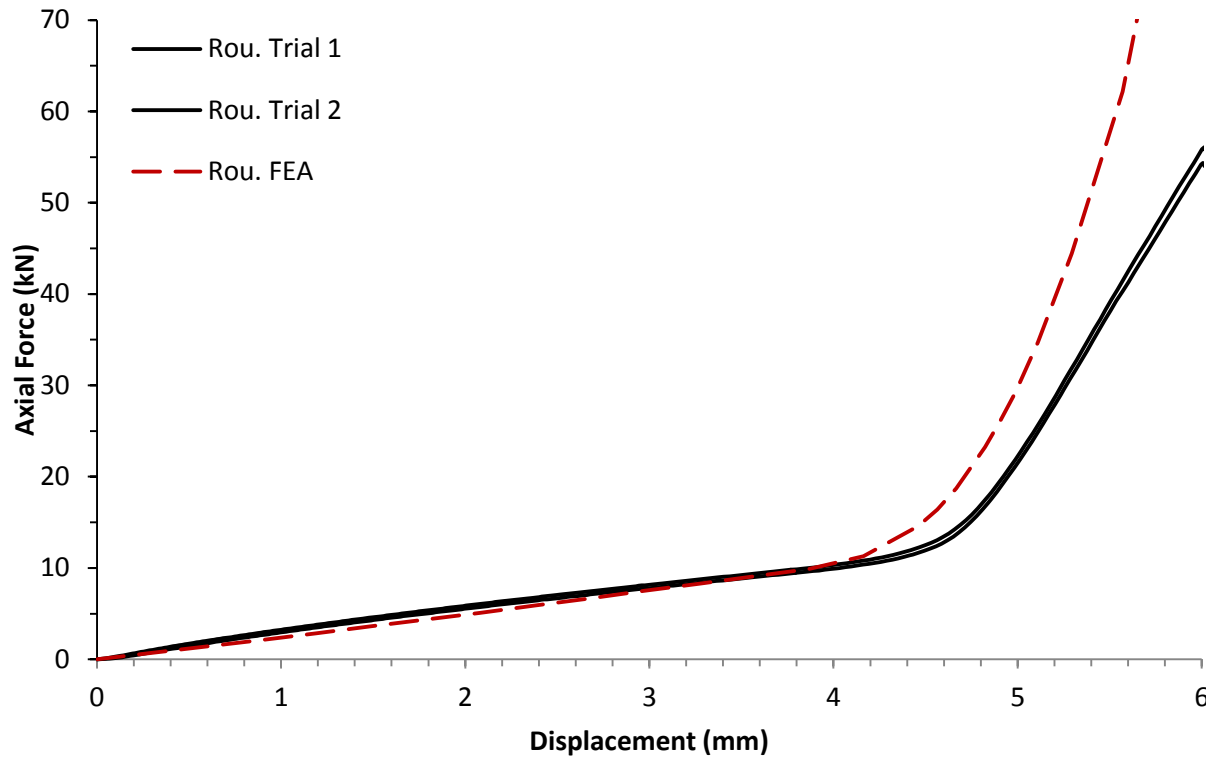


Figure 56: Preliminary Force-Displacement Results for Rough Interface

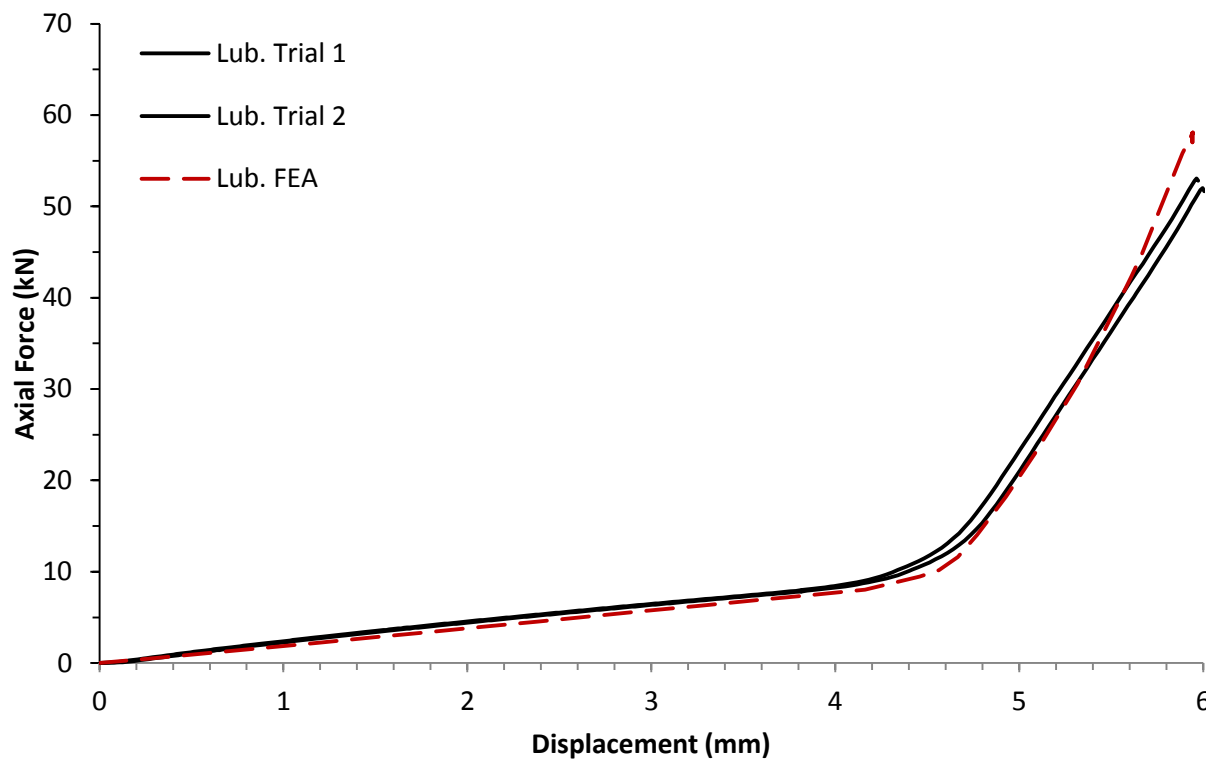


Figure 57: Preliminary Force-Displacement Results for Lubricated Interface

Examining both FE results for rough and lubricated contact, both curves accurately replicate experimental results up until the point of contact. For the rough case, contact was established too early and the force rises at a faster rate. For the lubricated case, the trend remains consistent until 5.5 mm where an inflection is seen causing divergence.

4.7 Final Mesh Sensitivity Analysis

Upon reviewing the applicability of the preliminary 3rd order Yeoh model fit to the 5th cycle for 40% strain, it was necessary to verify the mesh size to see whether it was sufficient as a final mesh size. The FE model from 4.6 was re-used and operated in a similar way as the preliminary mesh sensitivity analysis using rough contact conditions. Progressive uniform mesh refinements were made this time using a mesh size 0.4 mm as a baseline. A mesh size of 0.25 mm was re-used as the finest mesh for comparison of results.

In addition to all of the criteria previously used in the preliminary mesh sensitivity analysis, the maximum pipe strain was added as the primary criterion, second being axial force. Both criteria were directly related to experimental data and must have been shown to converge to a uniform trend. The final results are displayed in figure 58 show the two primary criteria as a function of increasing element count. Examining the results, most results show uniform behavior indicating 0.4 mm was a sufficient mesh size for the FE model including the pipe. A mesh size of 0.6 mm was also shown to produce nearly identical results to 0.4 mm however solution time decreased from 13 mins to 6 mins with a minor change in the number of iterations required. As a result, a mesh size of 0.6 mm was used for the development of all subsequent analyses.

In addition to the final mesh size selection, mesh distortion was increased during the final mesh sensitivity analysis due to the larger deformation present with the inclusion of the pipe.

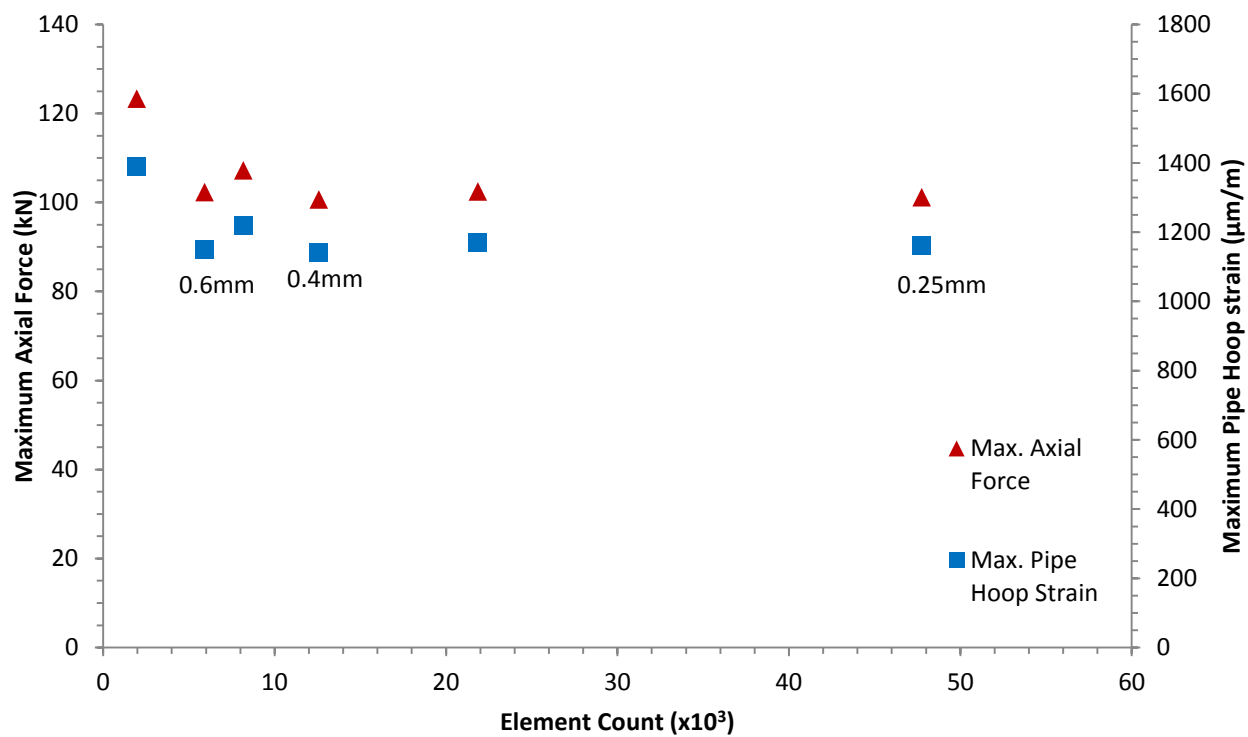


Figure 58: Final Mesh Sensitivity Analysis

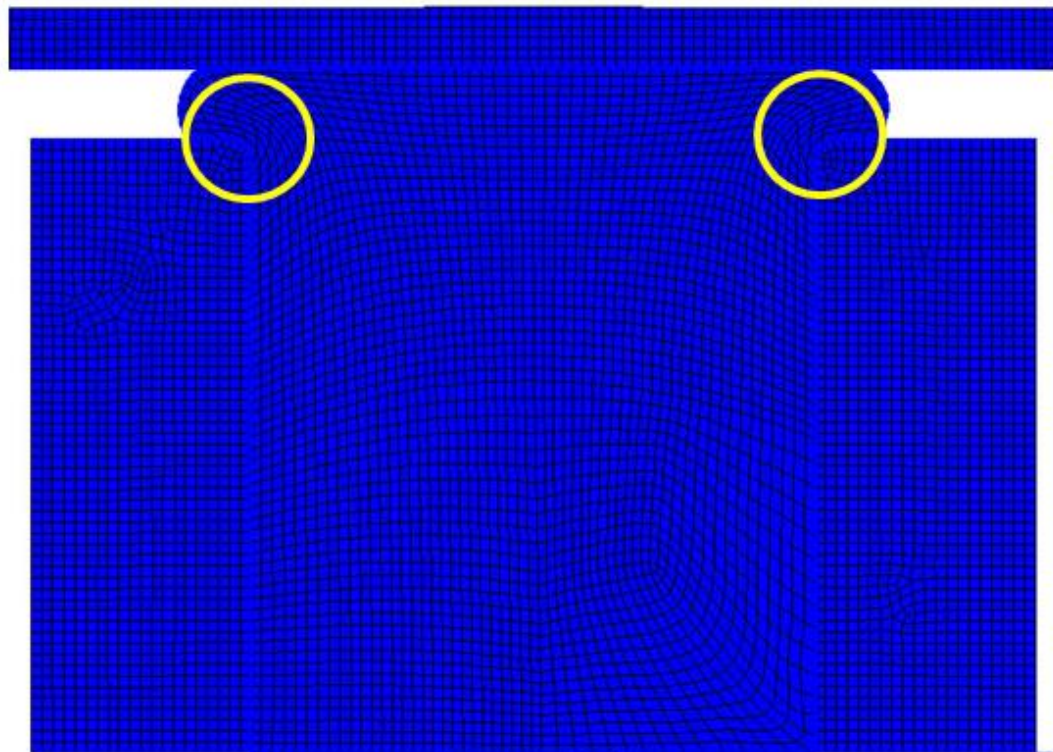


Figure 59: Mesh Distortion Errors

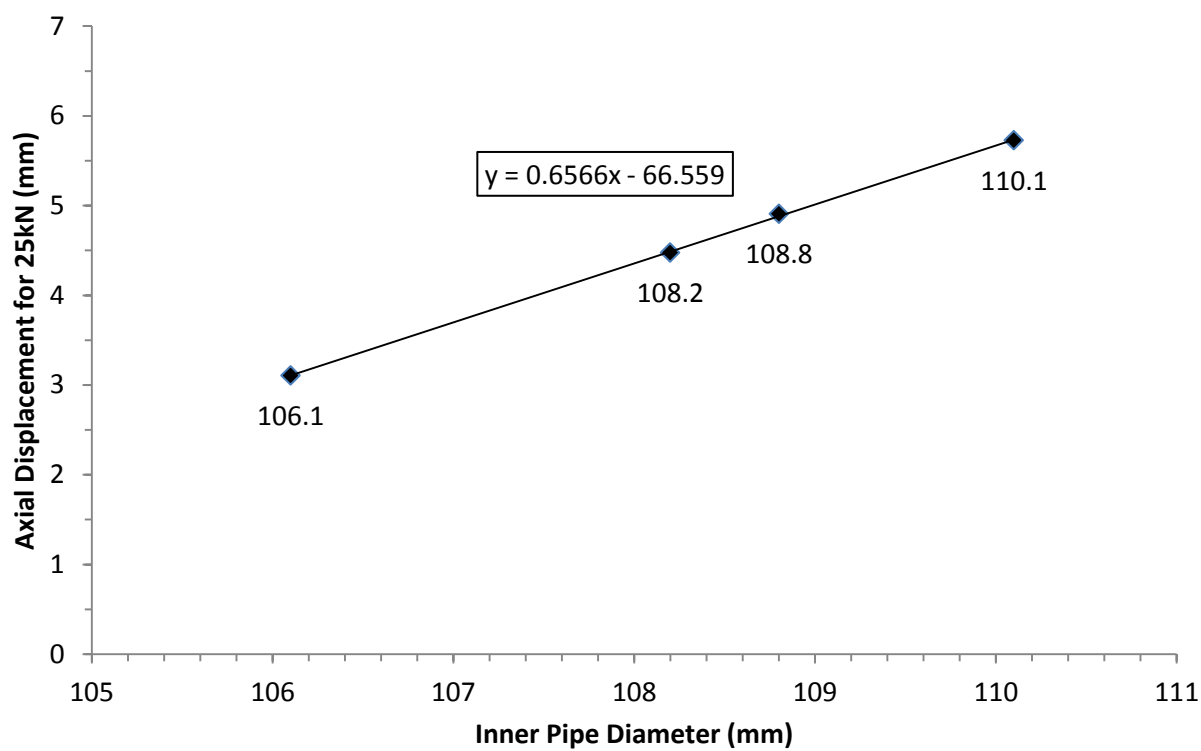
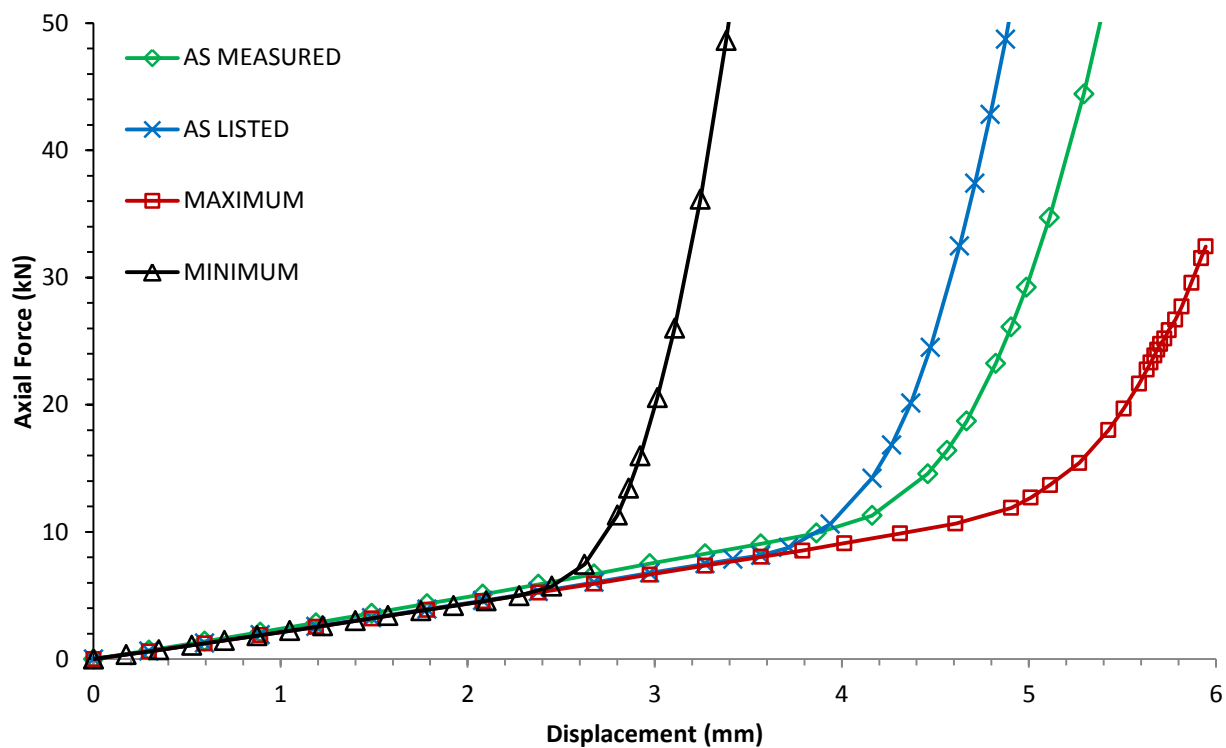
It was noticed that at the interface between the rings' outer corners and the rubber seal under large deformation shown in figure 59, the mesh distorted significantly which produced warning elements.

While it was important to reduce the amount of mesh distortion as much as possible, at this point it was uncertain whether the inclusion of Thirion's law as a friction model would remedy the issues or whether the shape of the mesh required modification. Attempts were made to skew the mesh against the direction of rubber deformation to aid in post-deformation mesh alignment however most attempts caused significant convergence issues. The mesh distortion problem at this point was left until the development of the final FE model.

4.8 Parametric Study

For a better understanding of the effect of certain parameters and to help identify points requiring more control, a parametric study was performed in terms of geometry and friction. A geometric study took into account the dimensions of the pipe and the degree of sensitivity the seal has with respect to changes in pipe geometry. A frictional study took into account the sensitivity of the force-displacement behavior with respect to changes in friction between the seal and rings.

In accordance with the listed pipe sizes in 3.7.6, each was input into ANSYS using the setup used previously in 4.7. The results in figure 60 display the difference in the force-displacement curve and the point-of-contact as the pipe geometry was changed. Examining the change in force-displacement curves, there is a clear dependence between the displacement required for contact and the inner pipe diameter. For the case of a controlled axial displacement input, geometric accuracy is important as the pipe geometry must be accurately measured in order to establish the appropriate point of contact otherwise the force produced at a given input axial displacement may be too high or too low.



For example, if the listed inner diameters for a 4" Sch. 10 pipe and the as-measured pipe that was used for experimentation are 108.2 and 108.8 mm respectively, a 6 mm axial displacement will require an axial force of 199 and 100 kN respectively.

Due to the high sensitivity with respect to pipe geometry, it was critical to measure the specific pipe geometry used for examination when operating under displacement-control. This is also particularly prevalent in the presence of pipe ovality where the maximum and minimum inner diameters can exist on the same oval pipe which may cause considerable pipe stress concentrations.

To get an approximation of the error caused by the use of slide calipers for geometric measurement, the axial displacement required to produce a force of 25 kN was plotted against inner pipe diameter for each of the 4 geometric cases shown in figure 61. A linear regression showed that a change of 1 mm to the pipe's inner diameter causes a change of 0.66 mm to the axial displacement required to produce 25 kN. If the slide calipers are rated to an accuracy of ± 0.03 mm, the ensuing axial displacement can vary between ± 0.02 mm. If one assumes all force-displacement curves run parallel to each-other after contact is established, the tangential slope after contact is approx. 101546 N/mm meaning an error in axial displacement of 0.02 mm can cause an error in axial force of 2031 N. Given the magnitude of axial force required for a 6 mm displacement is estimated to be approx. 50 to 55 kN, the error caused by using slide calipers to measure pipe geometry may offer error up to 5% in the replication of axial force required for an axial displacement of 6 mm.

For the case of the as-measured pipe, the effect of friction was examined by examining the force-displacement curve and the pipe hoop strain gradient with friction coefficient values of 0.1, 0.3, 0.5, and 0.7 applied to contact pair 1 at the ring-seal interface. For this FE model, the input displacement was 5 mm because 6 mm caused convergence issues for the lower friction coefficients.

The force-displacement results are plotted in figure 62 and the respective pipe hoop strain gradients are plotted in figure 63. It was discovered that increasing the friction coefficient increases the tangential slope of the force-displacement curve at all points resulting in a higher axial force. The maximum variation between the maximum axial forces occurs for friction coefficients of 0.3 and 0.5 causing a rise of 47% in axial force. Thus there is considerable need for accurately describing the frictional behavior of the rubber material. Similarly for the pipe hoop strain gradient, the maximum deviation occurs between friction coefficients of 0.5 and 0.7 which cause an increase of 83% in maximum pipe hoop strain.

In section 4.2, it was demonstrated that for rough and lubricated contact, the friction coefficient decreases as a function of increasing normal pressure. For the rough frictional testing, there was an appreciable drop in the friction coefficient from approx. 0.5 to 0.2. It was also discussed that two approaches were possible for modelling the frictional behavior. The first attempt so far was to calculate an average friction coefficient for all normal pressures for both the rough and lubricated case. However, the results from the preliminary attempt at modelling pipe contact shown in figure 56 showed that the tangential modulus for the force-displacement curve rises at higher axial displacement and normal pressure. The second approach was to input the friction coefficient as a function of normal pressure in accordance with Thirion's law as tabulated data into ANSYS.

Therefore, due to the requirement for accurately characterized frictional behavior, it was necessary to accommodate the fact that the friction coefficient reduces as a function of increasing normal pressure in accordance with Thirion's law.

As an addition to the parametric study performed after the completion of this thesis, the effect of strain rate on the results of the FEA was examined when implemented as a hyperelastic model. The results of this analysis are detailed in Appendix B.

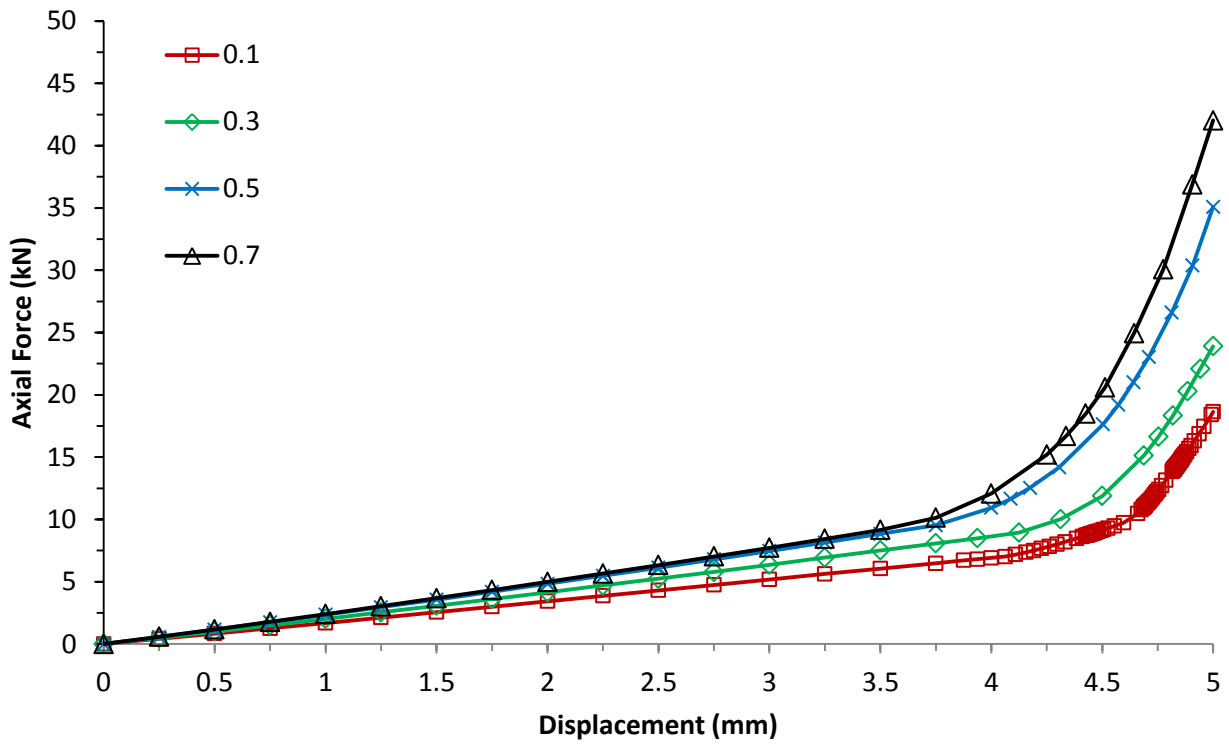


Figure 62: Axial Force vs. Displacement as a Function of Friction Coefficient

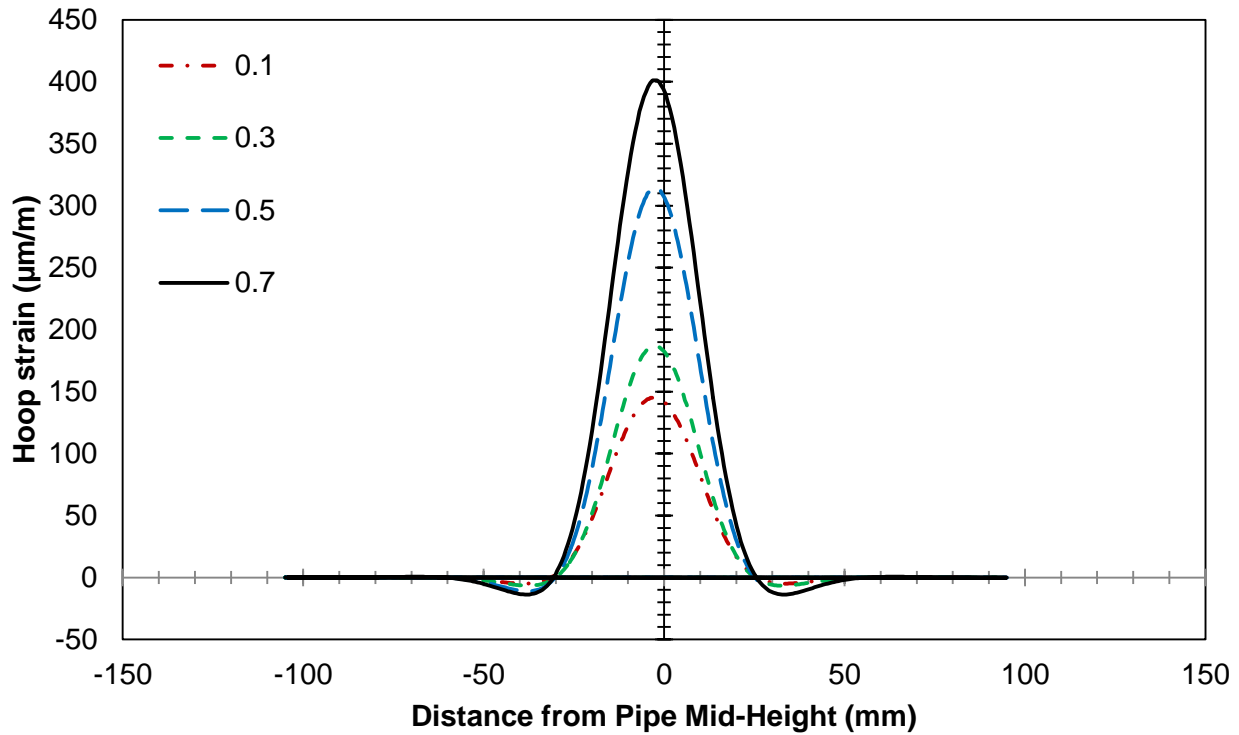


Figure 63: Pipe Hoop strain as a Function of Friction Coefficient

4.9 Final Hyperelastic Model

From 4.6, it was concluded that a hyperelastic model characterizing a range of strain up to 100% was required to accurately describe the entire range of strain within the seal. In a similar approach to the previous hyperelastic model in 4.4, several attempts were performed to curve-fit experimental data for a strain level of 100%.

Due to specimen failure during the first cycle of the equibiaxial test shown in figure 32, the first possibility for curve-fitting was to use data for the 1st cycle performed at 100% strain where equibiaxial data was taken up to failure (at approx. 85%). For improved curve-fitting accuracy, the order for the Yeoh model was taken up to the 5th order and subsequently compared to a curve-fit using the original 3rd order Yeoh model.

Using ANSYS APDL as the curve-fitting program, curve-fits were performed for 1st cycle data at 100% strain for both a 3rd and 5th order Yeoh model as shown in figure 64 and figure 65. There was a noticeable increase in conformance in the 5th order Yeoh model however divergent behavior was noted for the equibiaxial fit at a strain over 85%.

As a second attempt, following the observation that data using the 1st cycle at 100% strain was softened due to the pre-cycling of the specimen up to 60% as shown in figure 35, it was hypothesized that a dataset could be created by taking the 1st cycle for all strain levels and superimposing them. At the time of material testing, literature suggested that the 5th cycle is ideally used for hyperelastic modelling therefore no consideration was given for testing the 0 to 100% strain curve over a single cycle. This superposition method was the most feasible solution.

The trend in figure 35 clearly shows that a curve could be drawn across the tops of the co-linear regions of the 1st cycles at subsequent levels of strain.

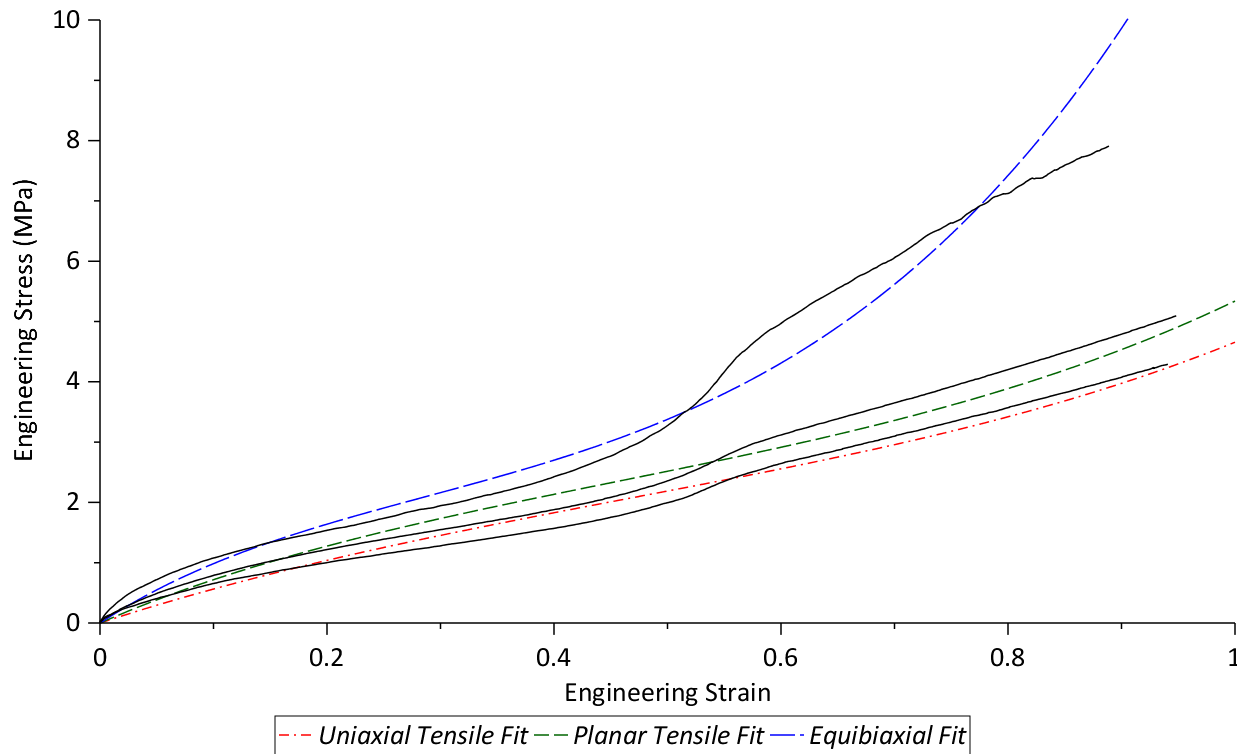


Figure 64: 3rd Order Yeoh Fit to the First Cycle of 100% Strain

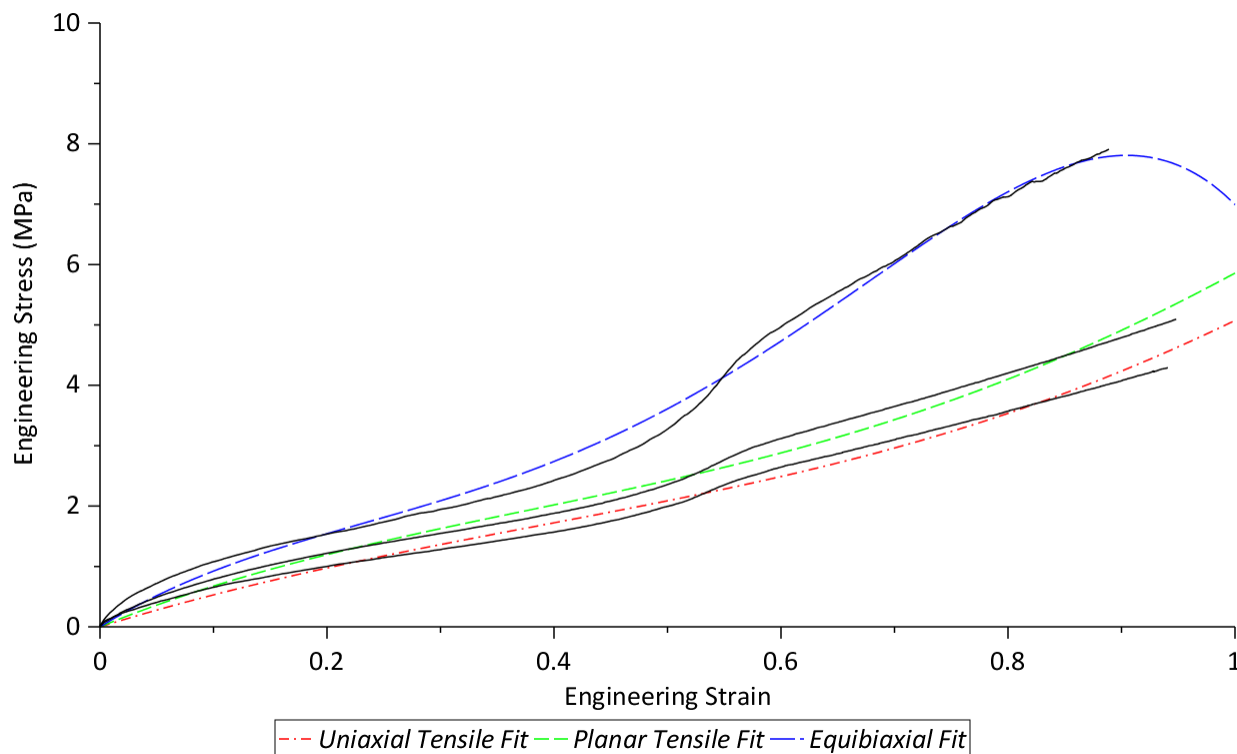


Figure 65: 5th Order Yeoh Fit to the First Cycle of 100% Strain

This method would then approximate the creation of a dataset from 0 to 100% strain without any pre-cycling which was not created using the SCL testing method. The advantage to using this method was to replicate the low-strain behavior at the appropriate non-pre-cycled stiffness shown in tests at 20% and 40% strain while maintaining the high-strain behavior of 60% and 100% strain. If the co-linear regions at subsequent levels of strain were extracted and superimposed onto one plot, an artificial dataset could be created and curve-fit using high-order polynomials as shown in figure 66. Using the polynomial function, discrete datasets for each of the hyperelastic tests were input into ANSYS for curve-fitting to a 3rd and 5th order Yeoh model. Figure 67 and figure 68 display both 3rd and 5th order Yeoh curve-fits for the superimposed experimental dataset.

Once more, the 5th order Yeoh model improves upon the conformance of the previous 3rd order Yeoh model however this time without divergence after 85% strain which is further suitable to the needs of this model. It should also be noted that a 4th and 6th order Yeoh model was examined however the 5th order Yeoh was better suited in terms of accuracy and simplicity. In a similar manner as performed in 4.4, a comparison was conducted between the different 100% hyperelastic models in terms of the force-displacement curves for rough and lubricated contact conditions. The comparison in this case however was performed visually as the performance of each model is clearly differentiable.

Figure 69 displays the comparison for rough conditions. Comparing the models for the superimposed and 1st cycle 100% strain datasets, the 1st cycle 100% strain model results fall significantly below experimental data indicating that the behavior is too ‘soft’. The superimposed dataset which was hypothesized to improve low-strain stiffness proved successful as the force-displacement curve displays high accuracy when the 3rd and 5th order Yeoh models are fit to the superimposed dataset simulating a virgin stretch from 0 to 100% strain without pre-cycling.

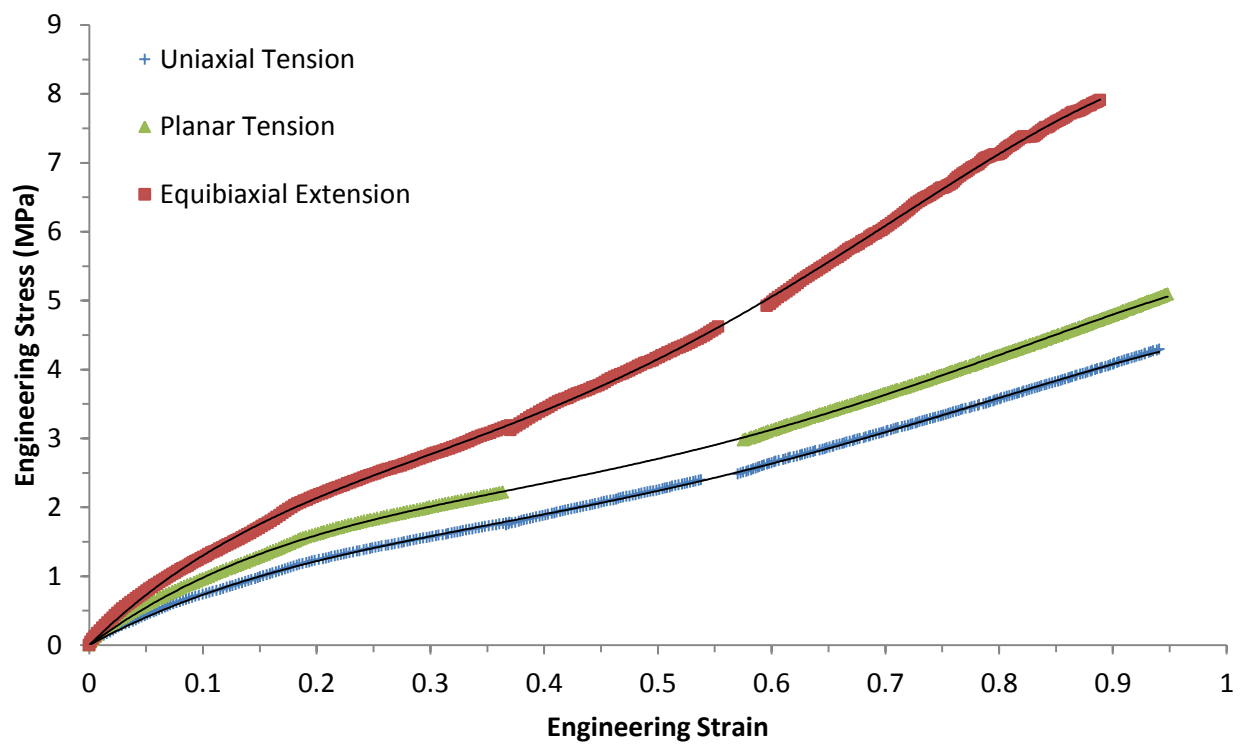


Figure 66: Superimposed 1st Cycle Curve Generation

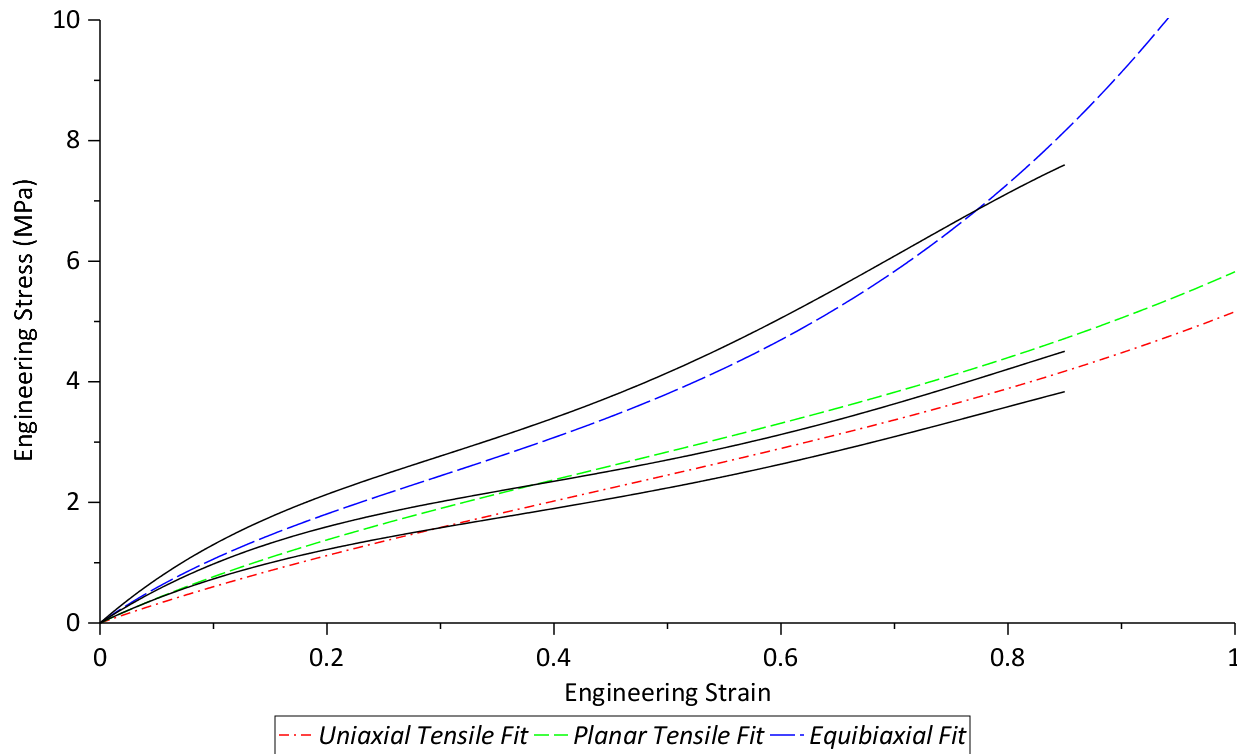


Figure 67: 3rd Order Yeoh Fit to Superimposed 1st Cycle Dataset

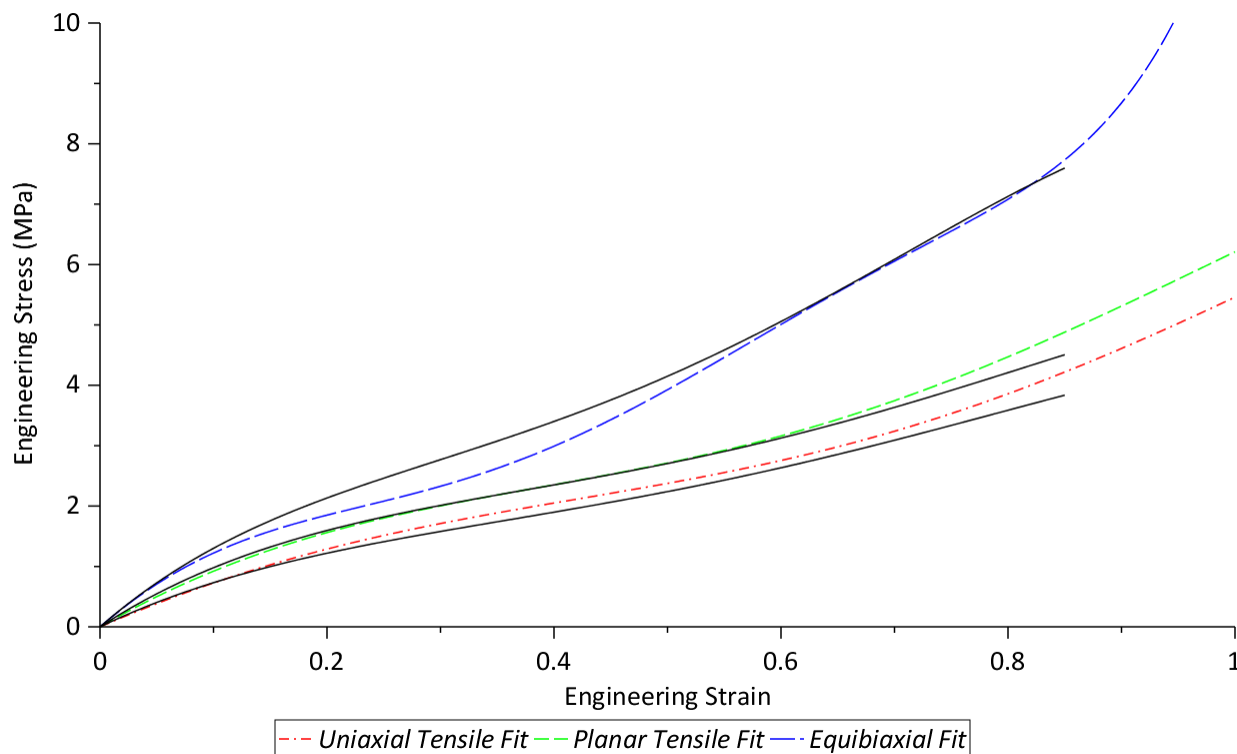


Figure 68: 5th Order Yeoh Fit to Superimposed 1st Cycle Dataset

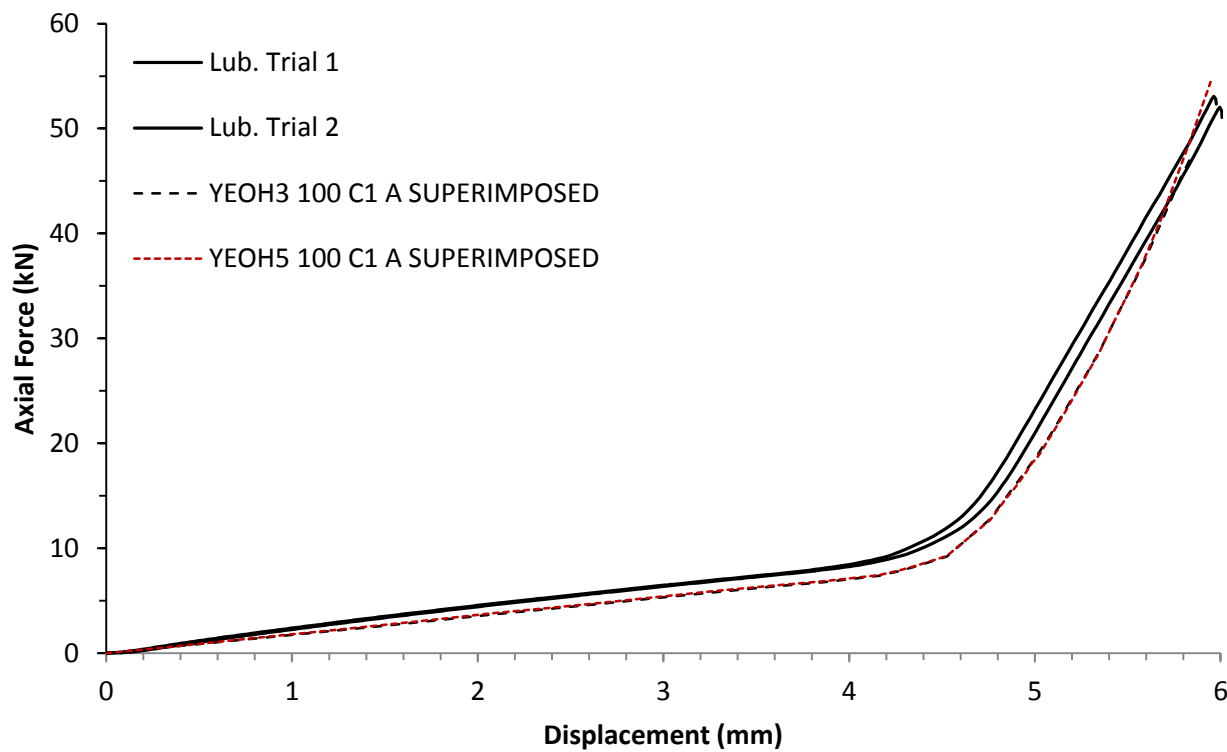
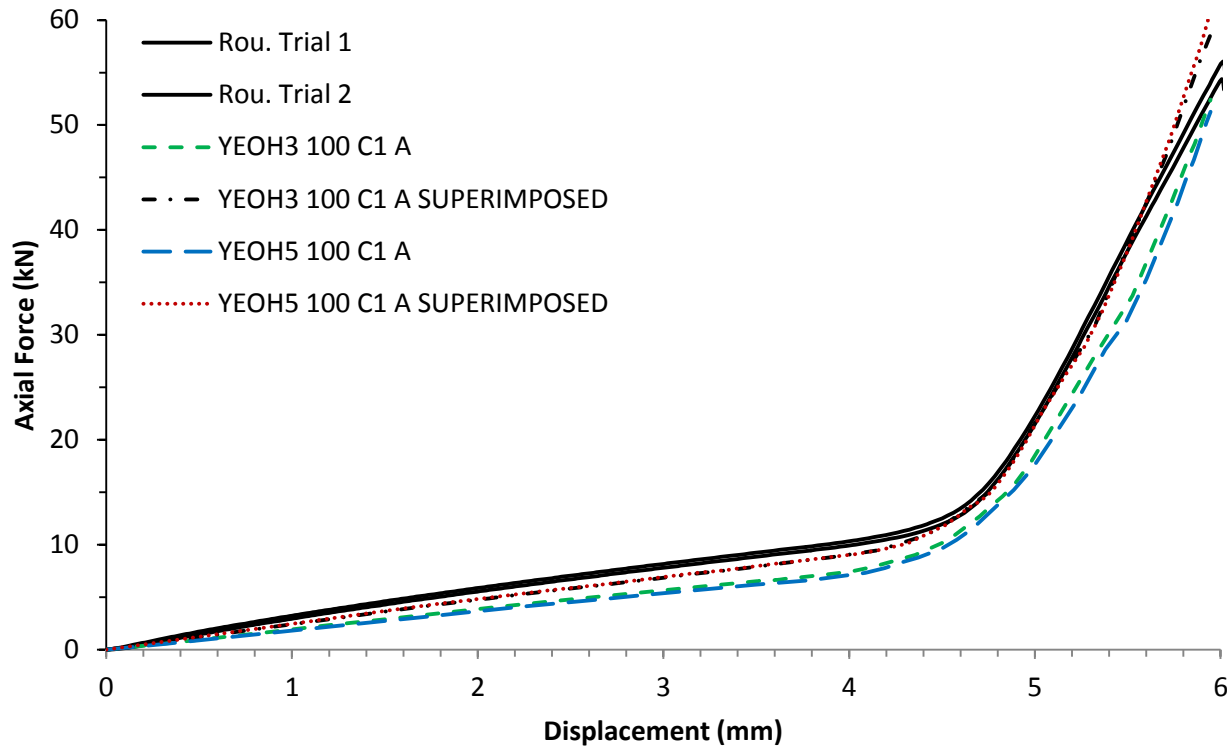


Figure 70 displays the comparison for lubricated contact conditions for the 2 best models: 3rd and 5th order Yeoh fit to the superimposed curve. Both models behave near identically with both showing acceptable accuracy. The 5th order Yeoh model was selected as the final hyperelastic model for this analysis for its more accurate conformance to the material data and for its high accuracy in simulating the seal.

4.10 Viscoelastic Model

The final step required to complete the full simulation of the seal was to implement a viscoelastic model to simulate stress relaxation and creep. Testing began with testing rubber specimens in a shear sandwich test at a maximum strain of 3.5% limited by a maximum force of 18N available in the DMA over a period of 24 hours for 3 trials. The 3 trials shown in figure 71 display sufficient repeatability where trial 2 was selected for curve-fitting because it displayed a higher relaxation rate and the smoothest curve.

Testing then proceeded to the use of the bulk compression jig to measure the relaxation in the bulk modulus as a function of time. The bulk compression methodology was similar to the shear sandwich however the level of strain was inconsistent between datasets. The 3 trials shown in figure 72 do not remain consistent with each other even at varying levels of strain. Due to the DMA's limited amount of force and the comparatively high bulk modulus of the rubber, it was likely that a state of bulk compression was not achieved because the resulting modulus was far below the expected bulk modulus of 3.38 GPa. The state of stress was likely simple compression marred by slack in the device and the compression of air in the bulk compression jig. However, it was noted that all trials display a consistent trend in relaxation after 1 minute.

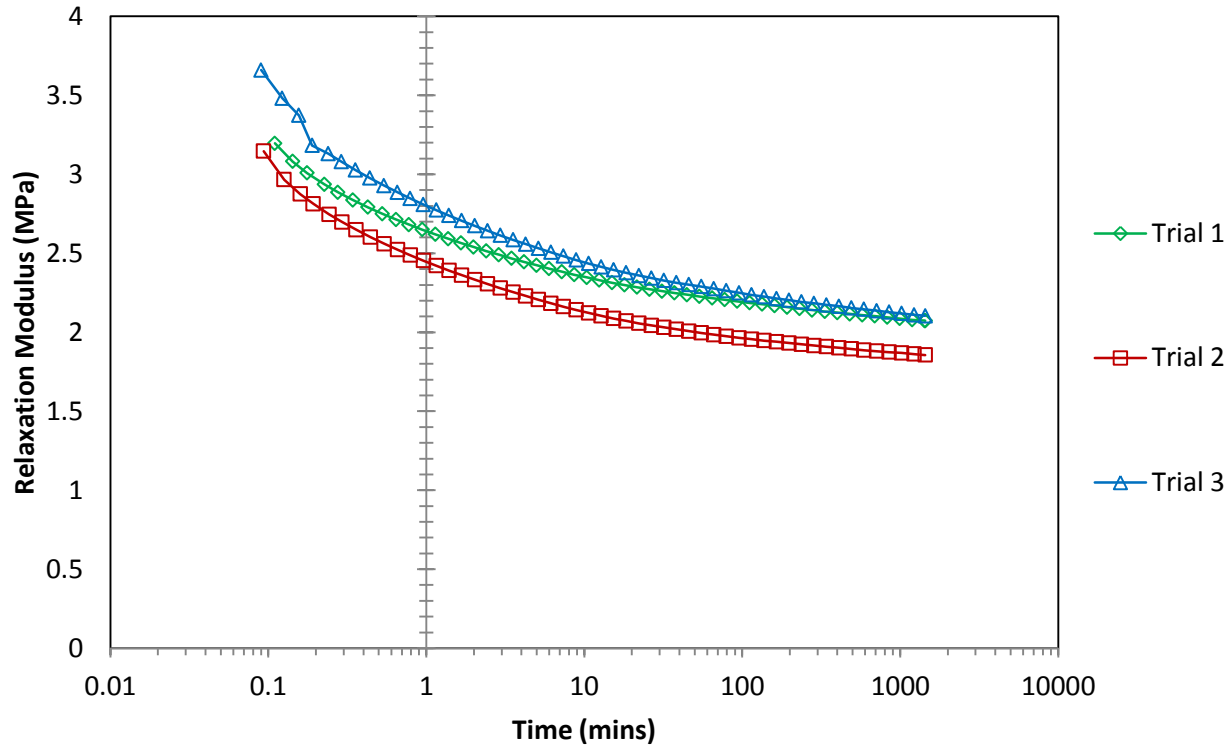


Figure 71: DMA Shear Relaxation: 24 hours at 3.5% strain

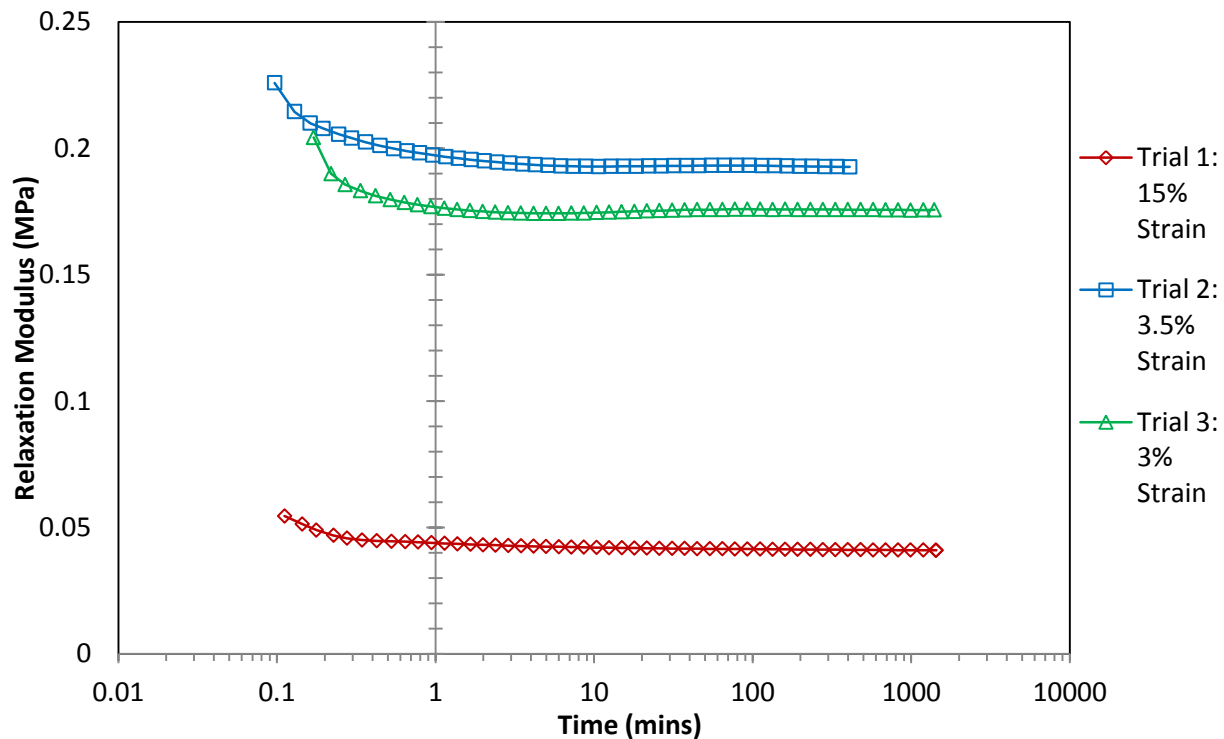


Figure 72: DMA Bulk Relaxation: 24 hours at Various Strain Levels

Due to the difficulties using the DMA for bulk compression tests, it was necessary to use the 250 kN Instron with the bulk compression jig with 10% strain held over a period of 15 mins. Pre-cycling was included this time to help eliminate air and empty voids within the cylinder while maintaining a pre-load to maintain the rubber's conformance to the cylinder volume. A 24 hour test was however not performed due to the prohibition of the unmonitored operation of the device at high forces. The 3 trials are shown in figure 73 displaying sufficient repeatability as in the shear sandwich test. The median trial was selected for curve fitting.

The datasets for both shear and bulk relaxation moduli were input into ANSYS for curve-fitting to a 3-term Prony series. The approach was similar to hyperelastic curve-fitting however a normalized fit was employed for a more uniform fit at all times. Figure 74 displays the datasets and the curve-fitted Prony series. 3 terms was found to be sufficient as higher orders were examined and not beneficial to the overall accuracy of the function.

Certain assumptions were maintained in the use of the Prony series. The first assumed that the extrapolation of the bulk Prony series was valid up to 24 hours despite having been fit to a dataset for 15 minutes of stress relaxation. It was shown in figure 72 that no significant change in the relaxation trend was observed at times over 1 minute. It was also determined in simulation that the bulk relaxation produced significantly less effect on the FE result than the shear relaxation. Therefore, it was assumed that the extrapolation of the bulk Prony series up to 24 hours would not have significant effect.

Second, it was assumed that the use of this Prony series was not valid beyond 24 hours due to the fact that there is no data supporting the absence of material transitions or any change in the observed trend at later times.

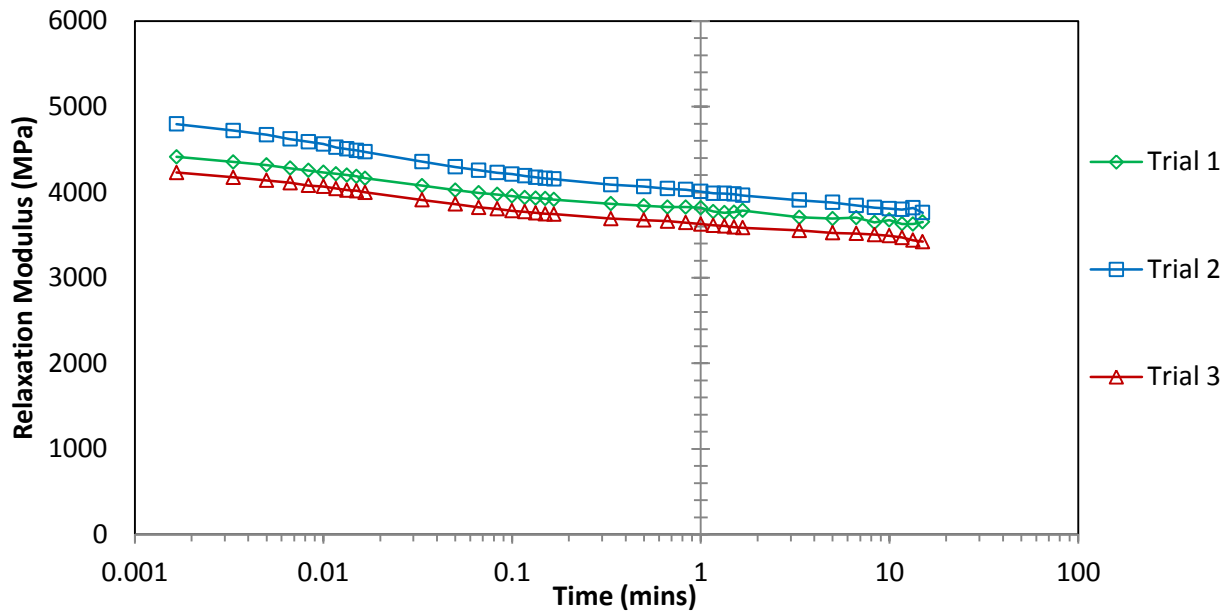


Figure 73: Bulk Compression Re-Test using 250 kN Instron

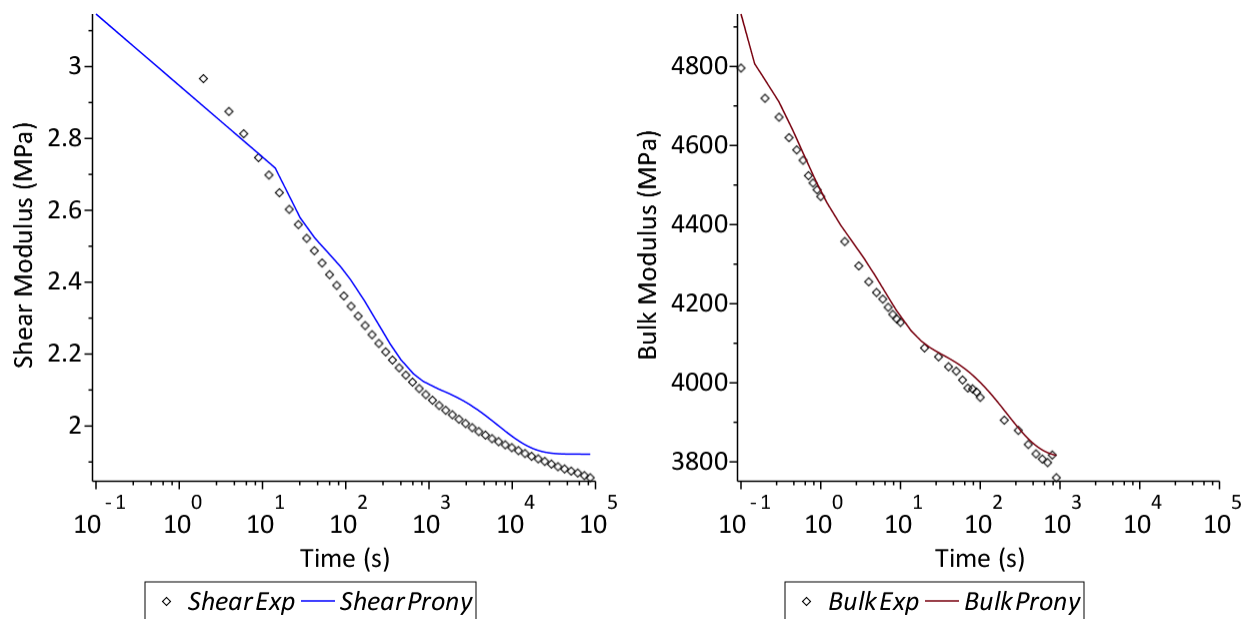


Figure 74: Shear and Bulk Moduli Relaxation Fit to a 3-Term Prony Series

Third, it was assumed that the use of this Prony series was valid for use with creep through conversion of the stress relaxation data rather than explicitly testing for creep and producing a second model. The stress relaxation experiments directly measure the change in modulus as a function of time. For use with creep, the same modulus relaxation function is employed however with stress being controlled and strain acting as a function of the constant stress and the decaying modulus. The validity of this assumption was examined later when compared to creep tests performed by Shaha [3].

4.11 Final Simulation

Following sections 4.7 through 4.10, it was possible to create the final FE model for use with all pipe and seal sizes modeled with 2D axisymmetry. As a benchmark, both the rough and lubricated contact interfaces for a pipe size of 4" Sch. 10 and a seal size of 102.5 mm OD were examined which, if successful, would proceed to a final optimization of the model.

The rough and lubricated models had a 6 mm axial displacement applied at a rate of 0.05 s^{-1} which was subsequently held constant for 300 seconds. The solution times for both cases were 16 and 21 mins while the number of iterations was 506 and 659 respectively. No warning elements were produced in either case indicating the mesh quality was sufficient. The first and primary result examined was the force-displacement data which was compared to two identically set up experimental trials shown in figure 75 and figure 76. Both FE results showed excellent conformance to the experimental data with integral deviations of 2.3% and -9.9% respectively for rough and lubricated cases. The maximum deviation was however high in the case of the rough results due to a sudden inflection at approx. 5.75 mm which equally occurred for the lubricated case. The maximum deviations for both cases were 11.6% and -0.7% respectively.

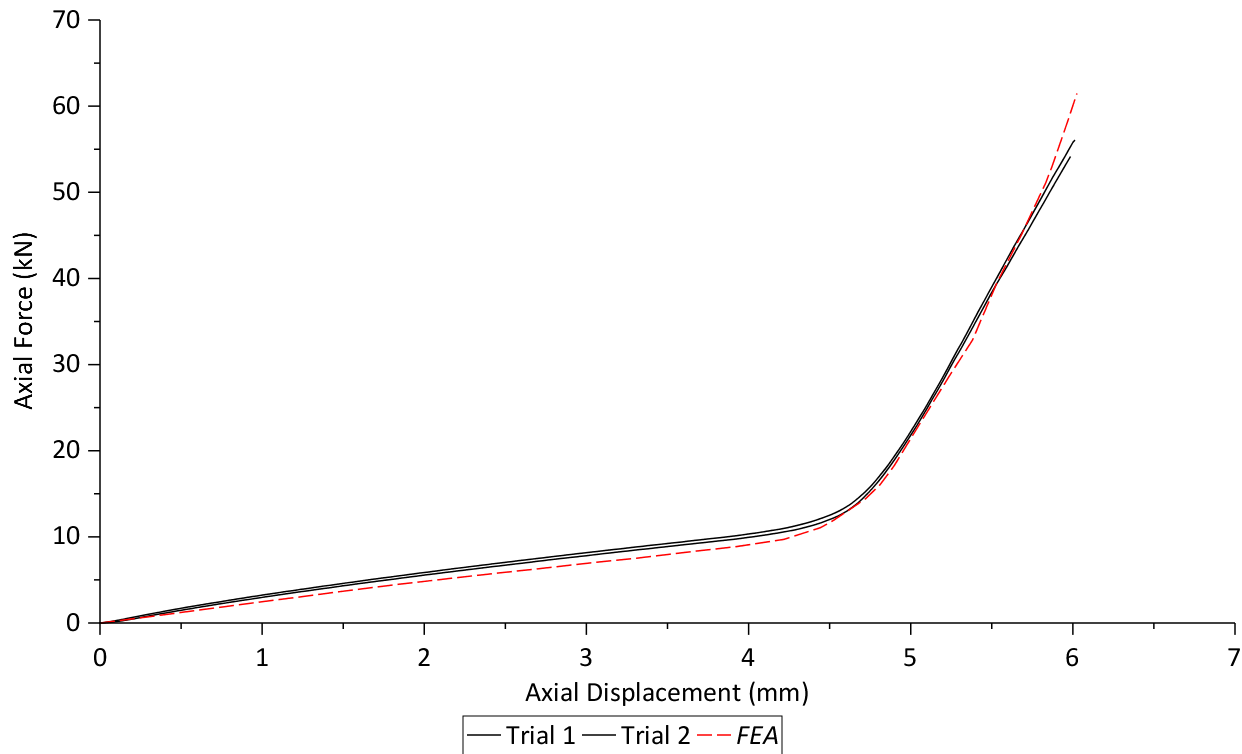


Figure 75: Rough Force-Displacement Curve

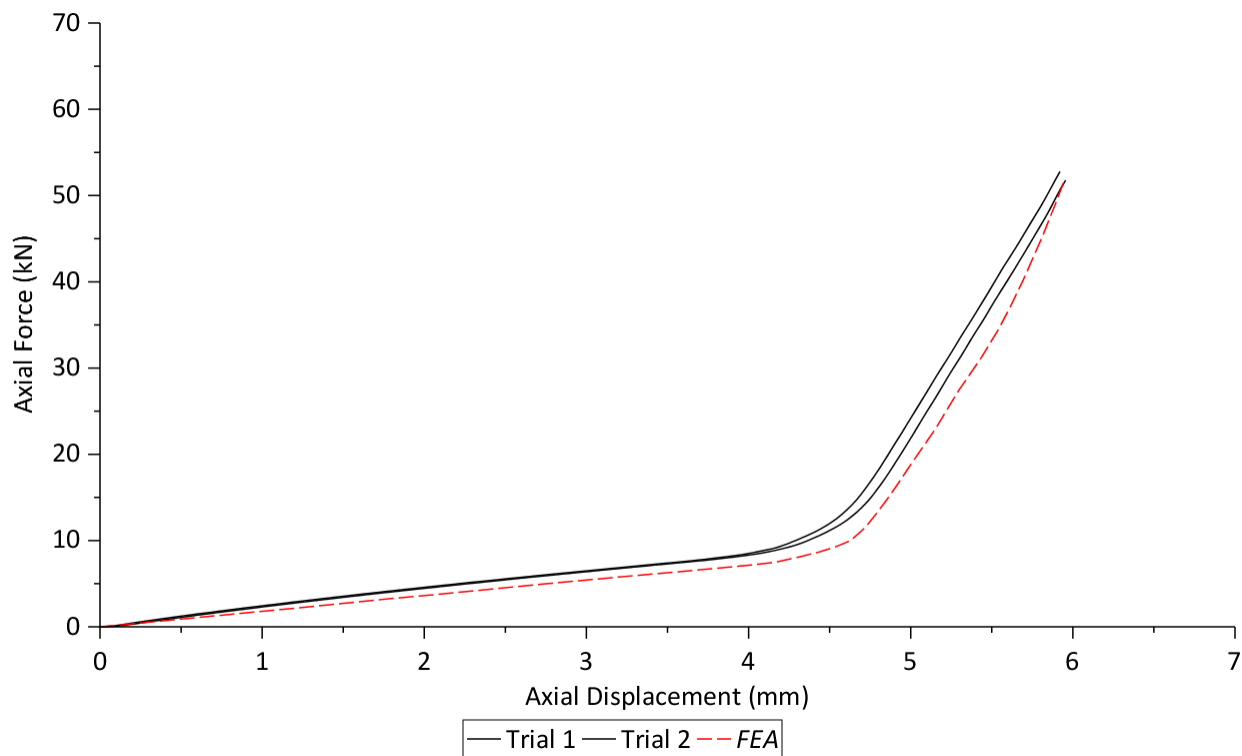


Figure 76: Lubricated Force-Displacement Curve

The second result used for the comparison was the contact pressure between the radially expanded seal and the inside of the pipe as measured experimentally by FujiFilm Prescale sheets. Examining the FE and experimental results in figure 77 and figure 78, the experimental results are noisy due to the fact that the pressure measurement was optically scanned with a listed accuracy of $\pm 10\%$ and a rather coarse resolution. The results were subsequently compared using the average contact pressure across the perceived contact area which produced a deviation of -2.6% and 16.8% respectively for both cases. In the rough case however, there is a small contact pressure distortion on the bottom of the seal which may indicate localized element distortion.

The third examined result was the pipe membrane hoop strain¹ gradient shown in figure 79 and figure 80 as measured by a 20-count strain gauge chain. Both cases showed a similar shape in the distribution however due to the dependency upon axial force, the rough case showed a 20.3% deviation from experimental values due to an 11.6% higher maximum axial force. The lubricated case however only showed a deviation of 3.4% given the axial force maintained a better agreement.

In correspondence with the newly implemented viscoelastic model, 2 results were examined. The first was the relaxation of the maximum axial force at a fixed displacement of 6 mm shown in figure 81 and figure 82. Due to the initial difference in the maximum axial force between FEA and experimental results, the axial force relaxation for both cases was normalized in terms of their respective maximum axial force to show an evenly weighted decrease in force. The second result was the relaxation of the maximum pipe membrane hoop strain shown in figure 83 and figure 84.

¹ One strain measurement trial was performed for lubricated conditions in stress relaxation mode due to experimental difficulties.

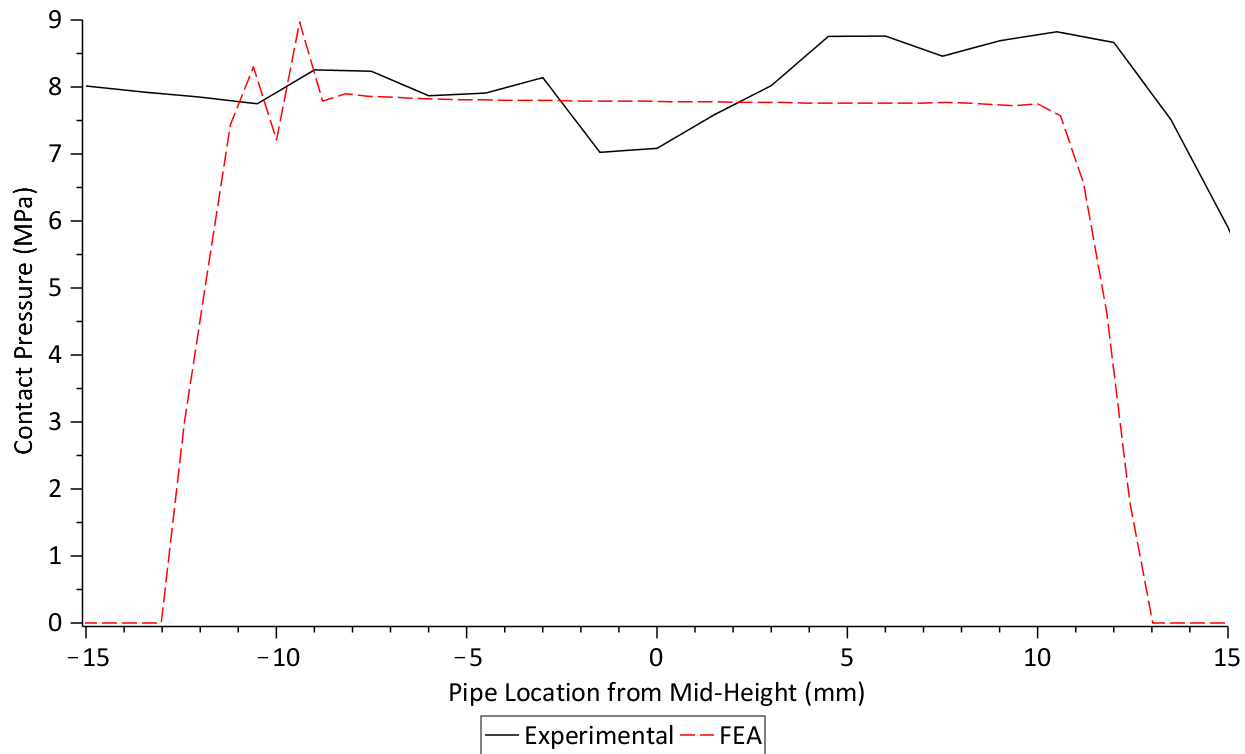


Figure 77: Rough Contact Pressure Gradient

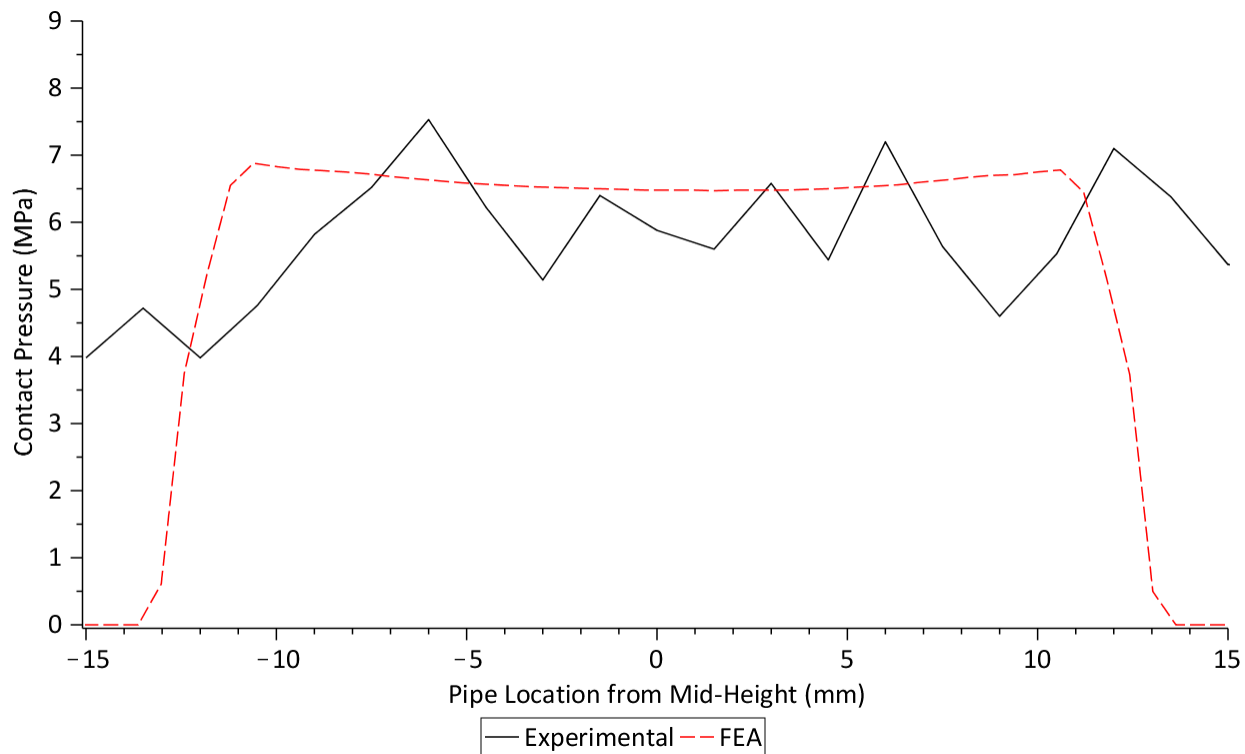


Figure 78: Lubricated Contact Pressure Gradient

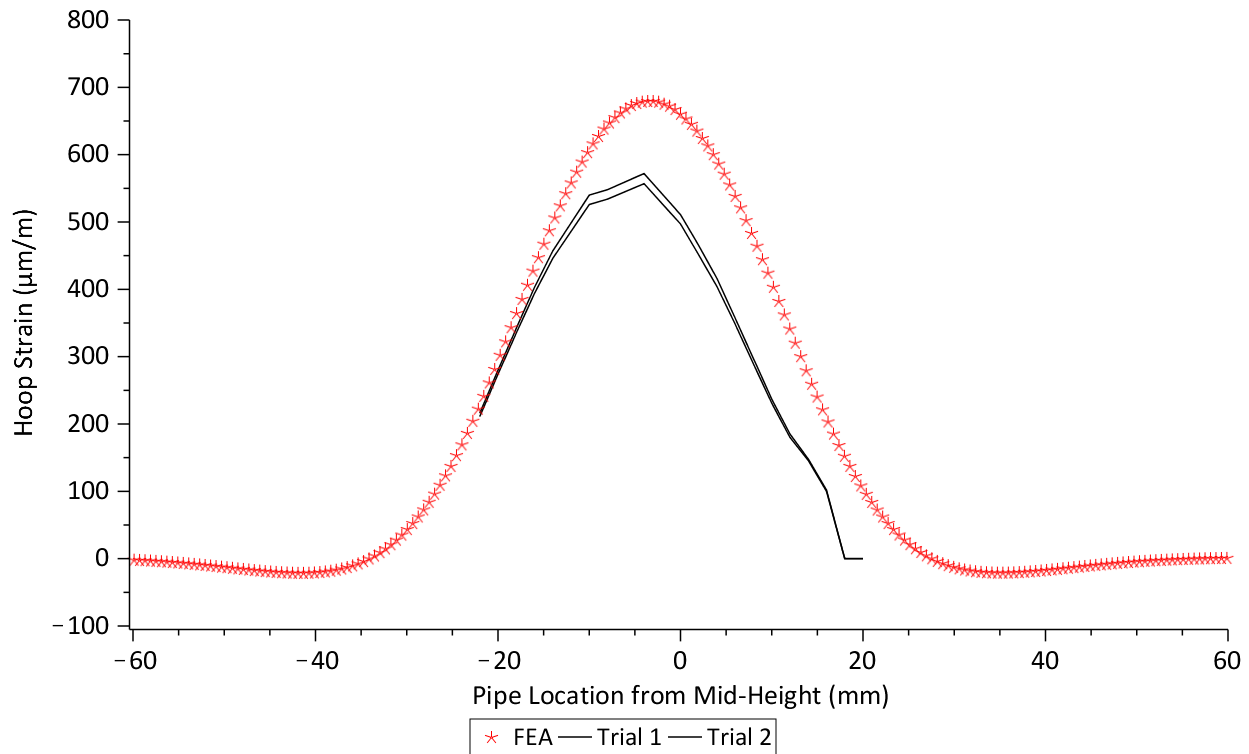


Figure 79: Rough Pipe Membrane Hoop Strain Gradient

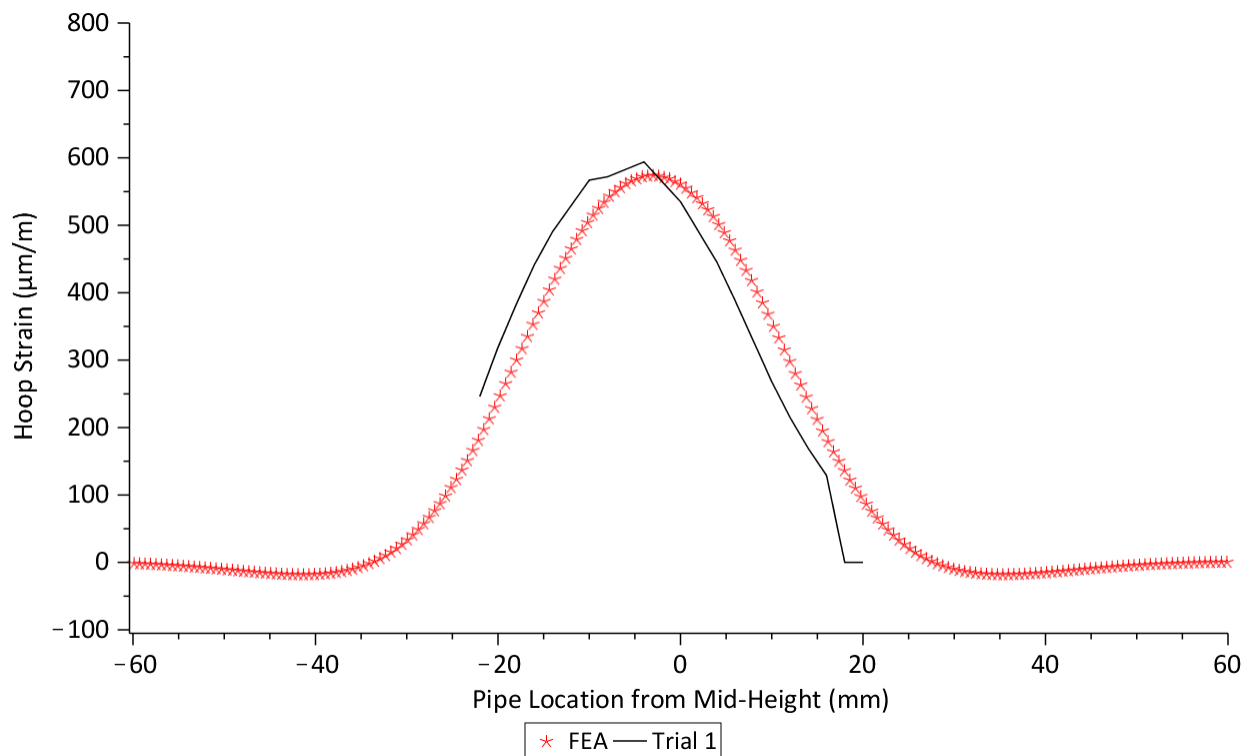


Figure 80: Lubricated Pipe Membrane Hoop Strain Gradient

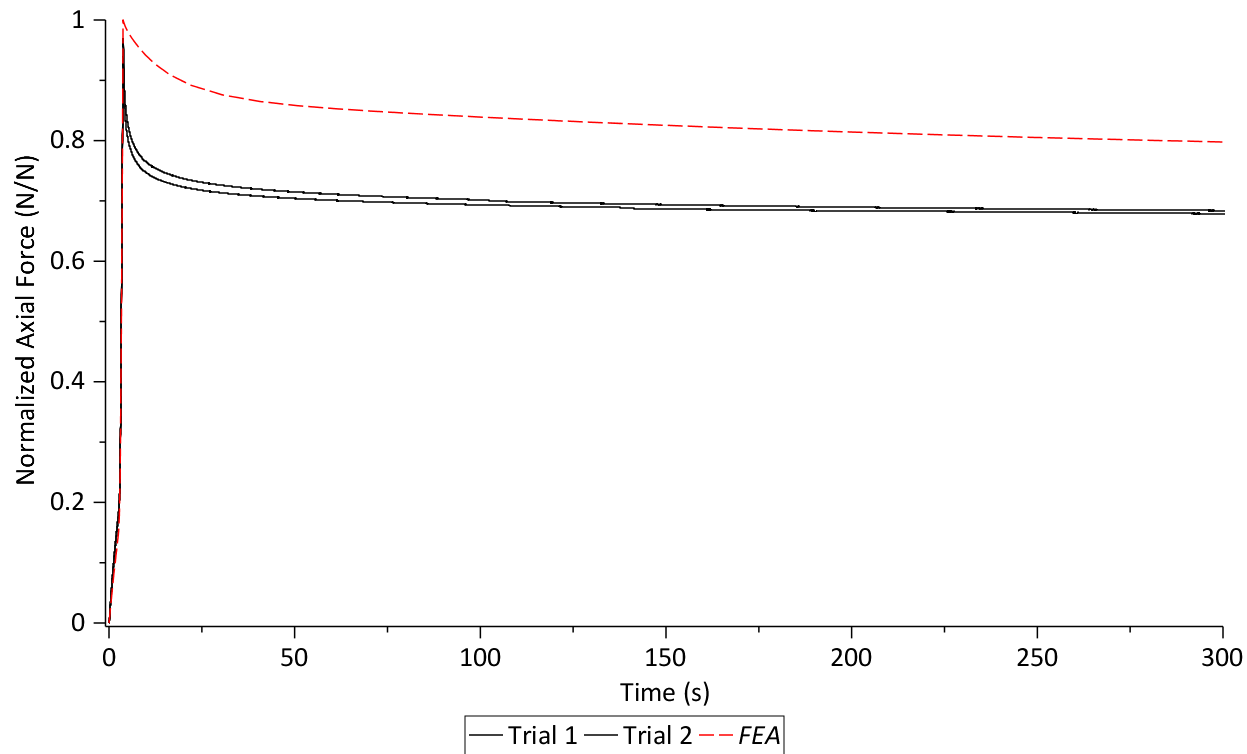


Figure 81: Rough Normalized Axial Force Relaxation

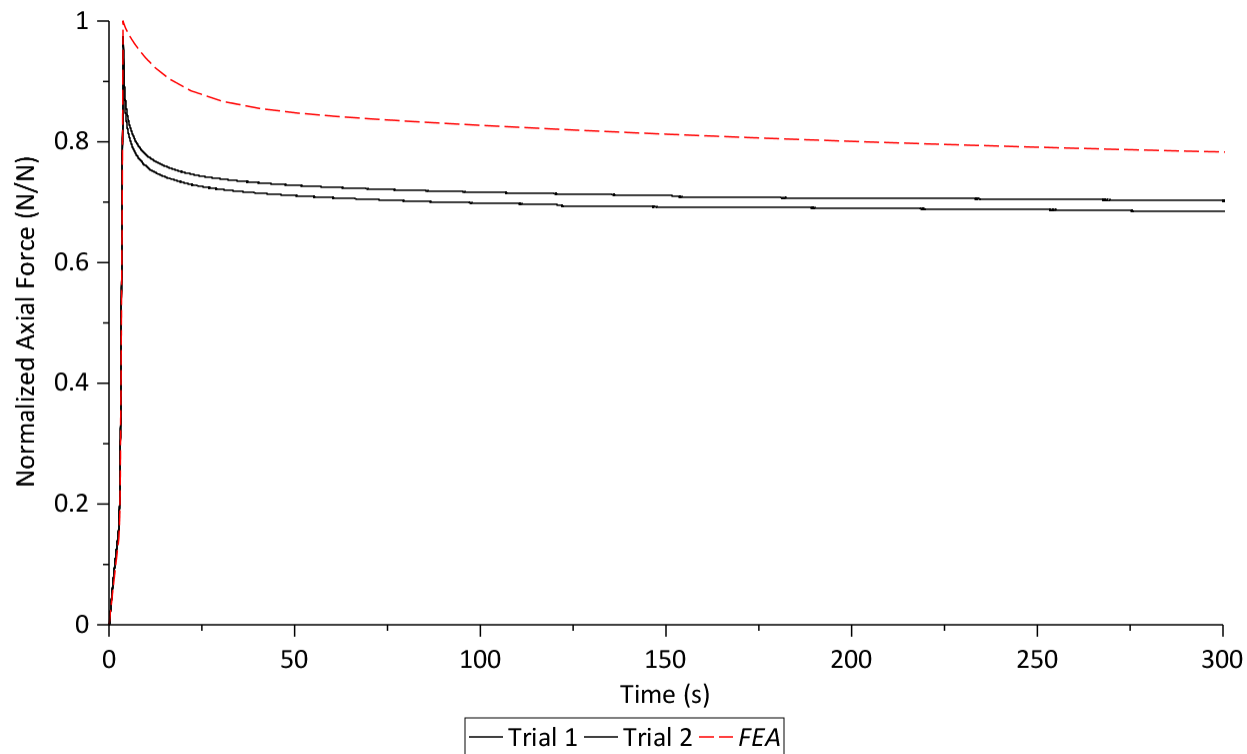


Figure 82: Lubricated Normalized Axial Force Relaxation

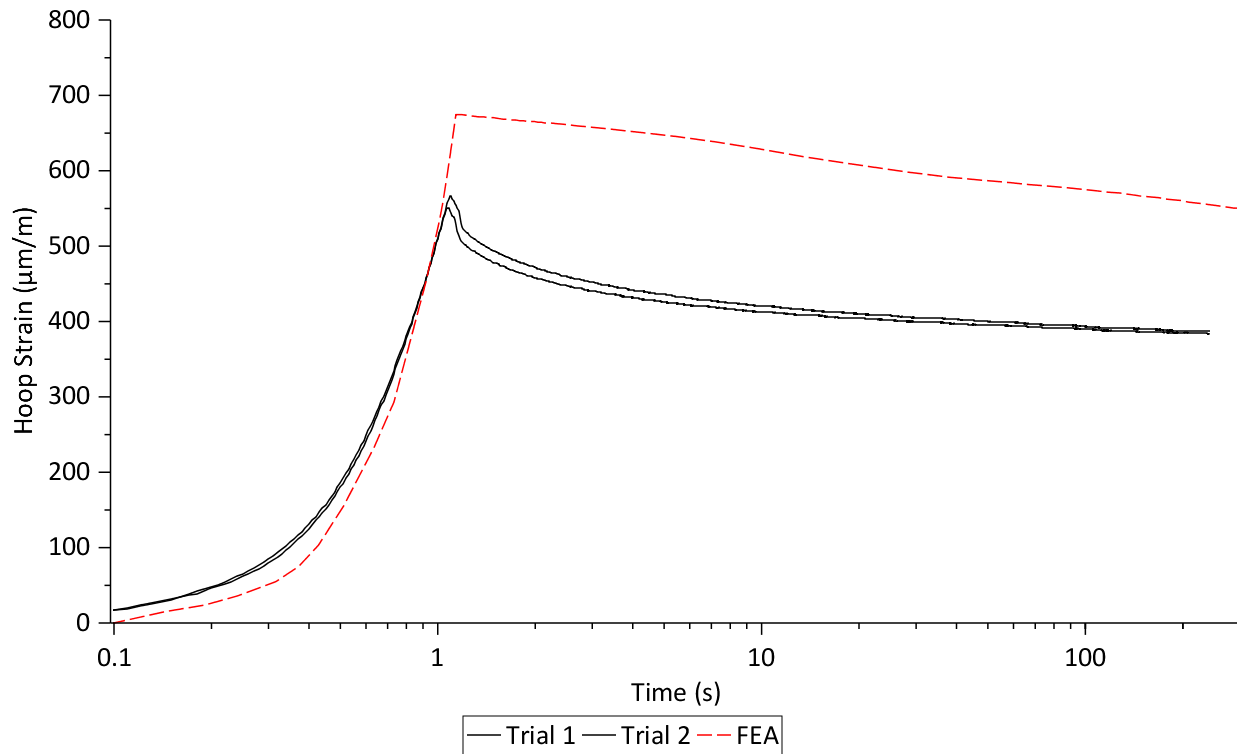


Figure 83: Rough Maximum Pipe Membrane Hoop Strain Relaxation

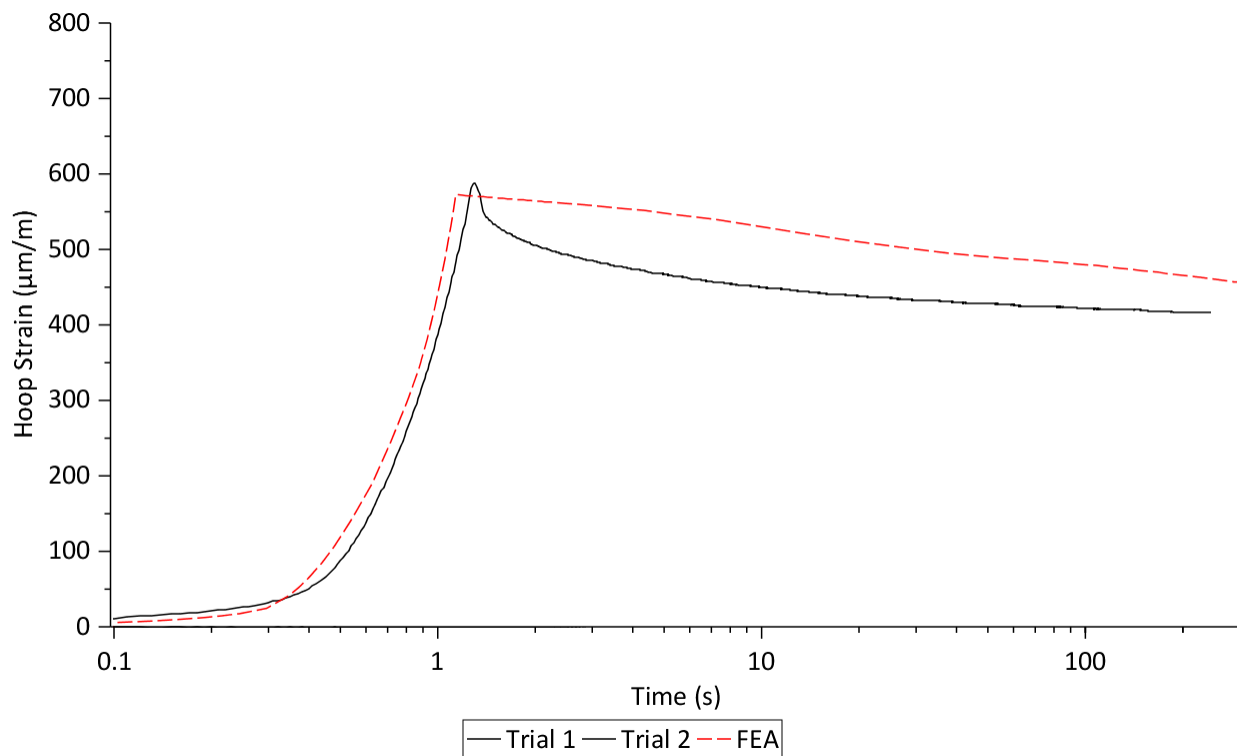


Figure 84: Lubricated Maximum Pipe Membrane Hoop Strain Relaxation

For stress relaxation, the axial force predicted by FEA decayed 11.6-18.5% less than experimental results for rough and lubricated conditions respectively (i.e., by 300 s, the axial force for the FE prediction decreases by 20.3% and for experimental, 31.9%). Similarly, the maximum pipe hoop strain predicted by FEA decayed 13.4-19.0% less than experimental results for rough and lubricated conditions respectively. One possible explanation for the deviation is the fact that the rubber material was assumed to be linearly viscoelastic and thermo-rheologically simple. The relaxation test data conducted at a strain of 3.5% for shear was assumed to be representative of the relaxation behavior at shear strains over 60% present in the rubber seal. It is logical that the axial force would decay more rapidly when the rubber seal is deformed instantaneously to a higher level of strain due to considerably more large-scale molecular displacement than at lower strain. Unfortunately, facilities were unavailable for relaxation testing at an appropriately high level of strain. Improvements were subsequently recommended for future work on this topic.

Creep was also examined in terms of the change in the axial displacement and the pipe hoop strain as a function of time at a held axial force once the loading in load-step 1 was complete. For this, the seal was loaded up to an axial displacement of 6 mm at a strain rate of 0.05 s^{-1} and subsequently held at constant axial force for 300 s. Figure 85 and figure 86 show the change in axial displacement as a function of time where FEA predicted a rise in axial displacement 2.83-3.17% less than experiment for the rough case and 1.92-2.92% less than experiment for the lubricated case.

In the case of maximum pipe strain, it was observed that at a constant force, the increase in axial displacement produced an increase in maximum pipe membrane hoop strain as a function of time. Examining figure 87 and figure 88, the maximum pipe strain was plotted logarithmically versus time to show a small experimental overshoot in the experimental strain curve due to relaxation while the load frame transitioned from displacement-control to load-control.

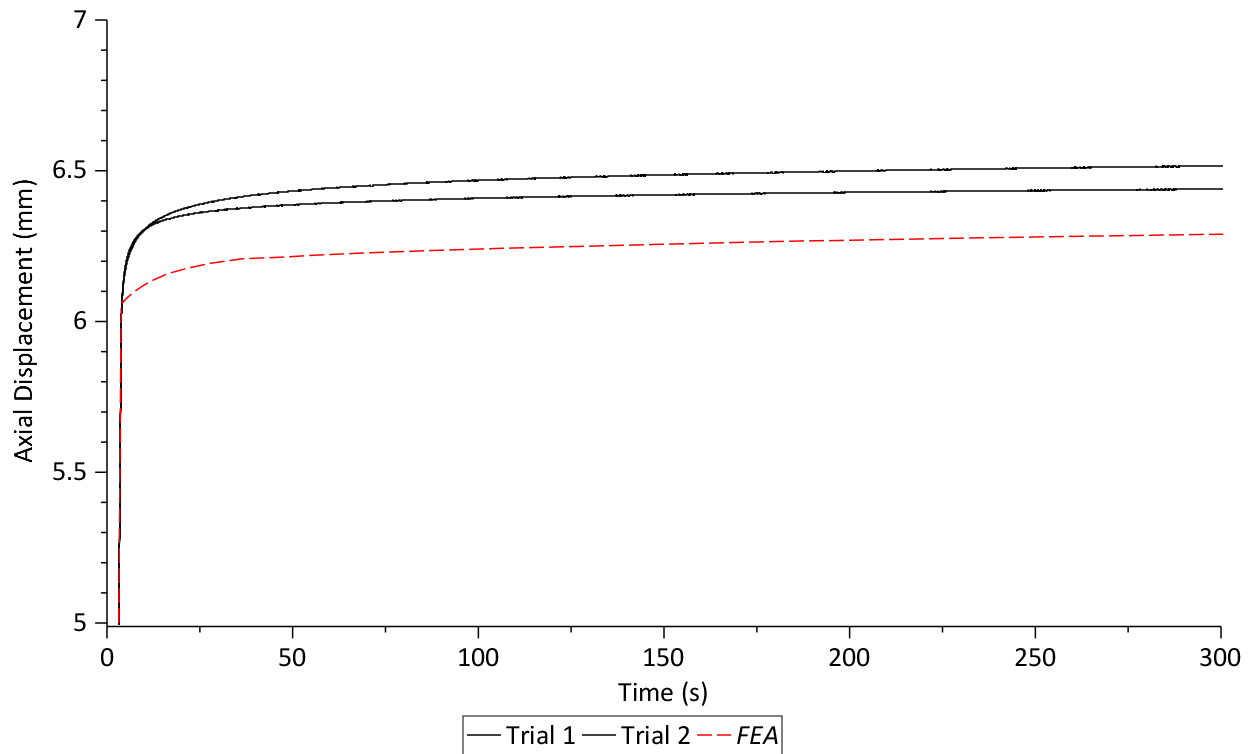


Figure 85: Rough Axial Displacement Creep

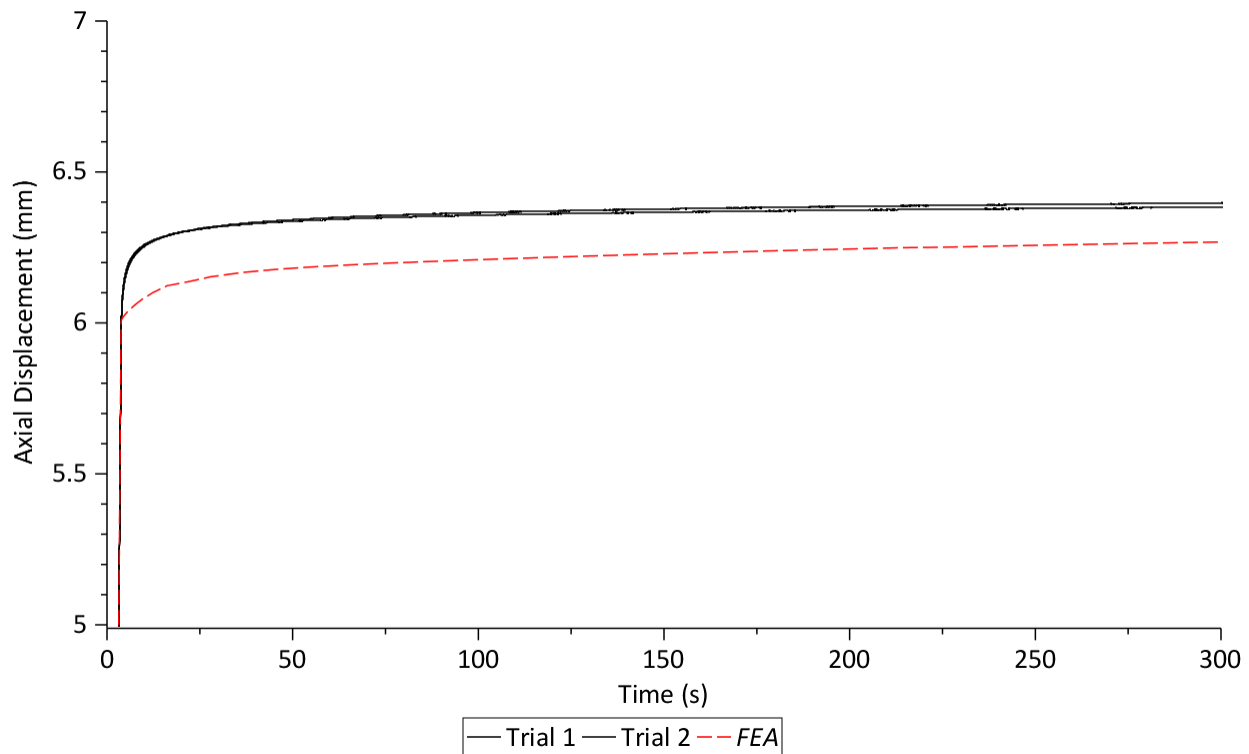


Figure 86: Lubricated Axial Displacement Creep

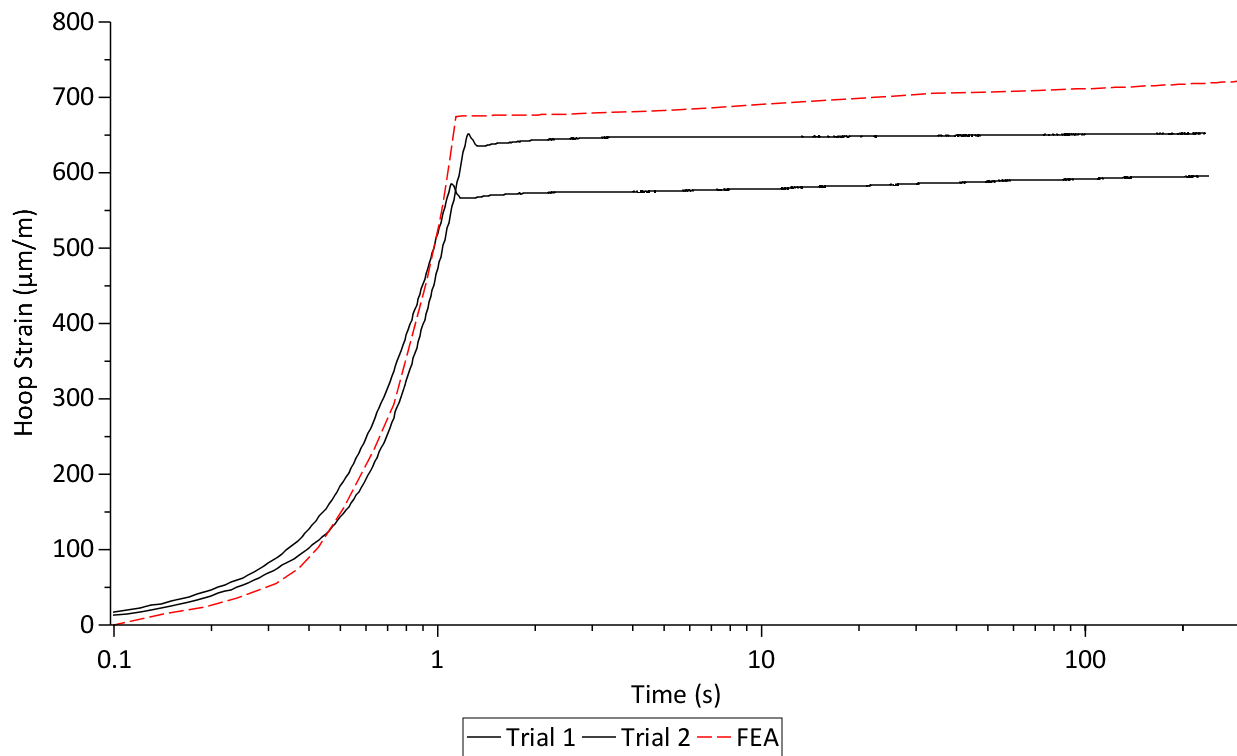


Figure 87: Rough Maximum Pipe Hoop Strain Creep

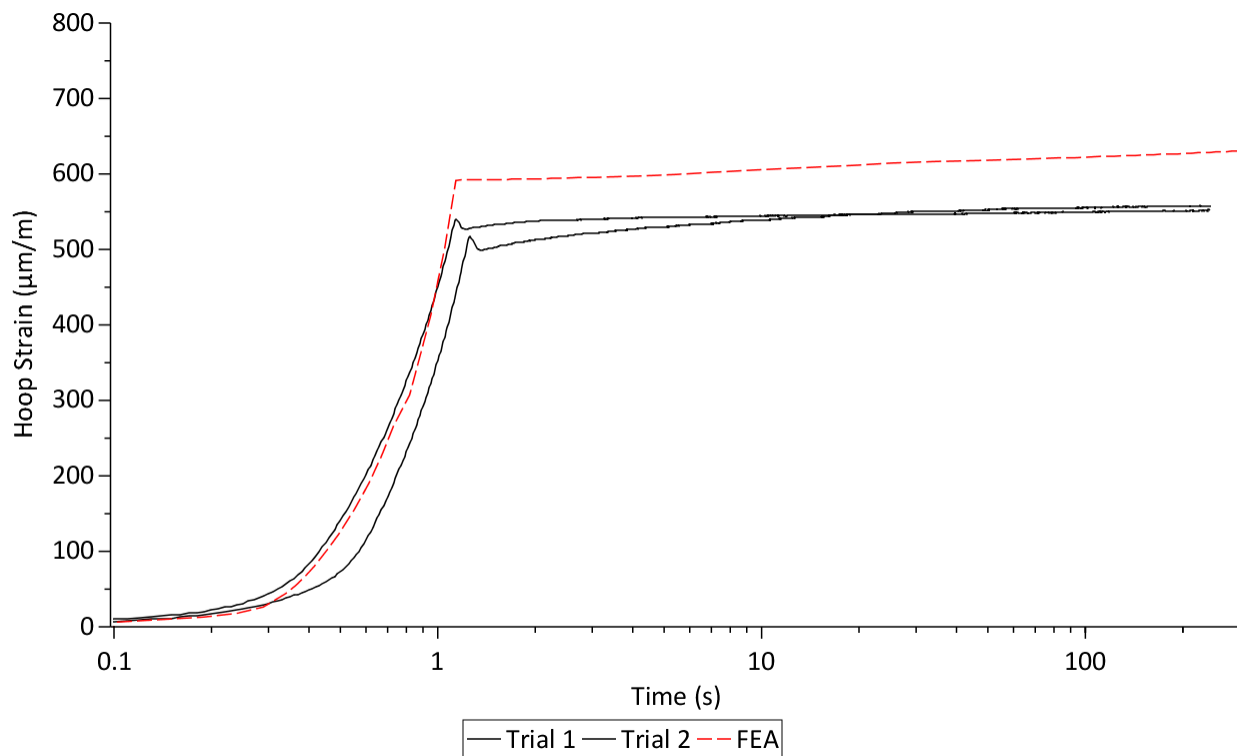


Figure 88: Lubricated Maximum Pipe Hoop Strain Creep

FEA predicted a rise in maximum pipe hoop strain up to 2.6% more than experiment for rough contact and up to 2.5% less than experiment for lubricated contact. It is known that creep is more difficult to characterize because the geometry is changing as a function of time rather than the internal stresses, therefore a larger degree of error occurs here for the FE model. Fortunately, the maximum pipe membrane hoop strain does not change with the same magnitude as it does in the case of stress relaxation. It was observed that under constant axial force, the pipe membrane hoop strain increases as a function of time at a very slow rate.

For the same reasons as for stress relaxation, due to unsuitable experimental testing, the decay in the moduli described by the Prony series may not decay fast enough to firstly, decrease the stress at constant strain and secondly, increase strain at constant stress. Therefore, the poor correlation between the FEA and experimental results in stress relaxation and creep is likely due to unsuitable shear relaxation testing which does not show a fast enough decay in the shear modulus.

4.12 Simulation Optimization

As a final attempt to improve convergence and accuracy as much as possible, the current model was optimized to help mitigate the issues in 4.11. These issues include:

- Change in convergence criteria as controlled by solution controls in ANSYS.
- High number of iterations and a sensitive convergence pattern.
- Inflection created late in the force-displacement curve shown in figure 75 and figure 76.
- Contact pressure distortion shown in figure 77.

As a first attempt, solution controls remained active however the convergence criteria were set to the constant default values in ANSYS as follows rather than having ANSYS dynamically modify them to ensure the solution converges at the expense of overall accuracy:

- Force / Moment – 0.1% residual deviation on the L2 norm
- Displacement – 1% residual deviation on the INF norm

Earlier in 3.5.3, it was discussed that high-order 8-node PLANE 183 elements could be used however they are not compatible with incompressible hyperelastic axisymmetric materials. Due to the inclusion of volumetric compressive data into the hyperelastic model, the model was considered near-incompressible which may be valid for use with high-order elements. Therefore, all plane elements were changed to PLANE 183 which offered improved uniformity of the element behavior and improved conformance of the mesh to the geometry after significant deformation.

Running the optimized solution saw an increase in solution time due to the increase in the number of nodes however there was a decrease in the number of iterations and noticeably smoother convergence behavior with fewer bisection points and sub-step additions. Previous solutions completed within 16 to 20 mins with an iteration count upwards of 500. The optimized model completed its solution within 20 to 25 mins with an iteration count below 500 even with more stringent convergence criteria.

Examining the results, the FEA force-displacement curves shown in figure 89 and figure 90 display exceptional conformance to the experimental data. The inflection shown prior to optimization has been mitigated through the use of higher-order elements which resulted in a maximum deviation and integral deviation below 7%. Similarly for contact pressure shown in figure 91 and figure 92, the use of higher order elements eliminated the discontinuity attributed to contact error previously present when low-order elements were used. The rough case however displayed a lower contact pressure than experimental. For the strain distribution in figure 93 and figure 94, accuracy was improved and the predicted pipe membrane hoop strain gradient was within 7% of the average experimental value similar to the force-displacement curve since force input is proportional to pipe strain.

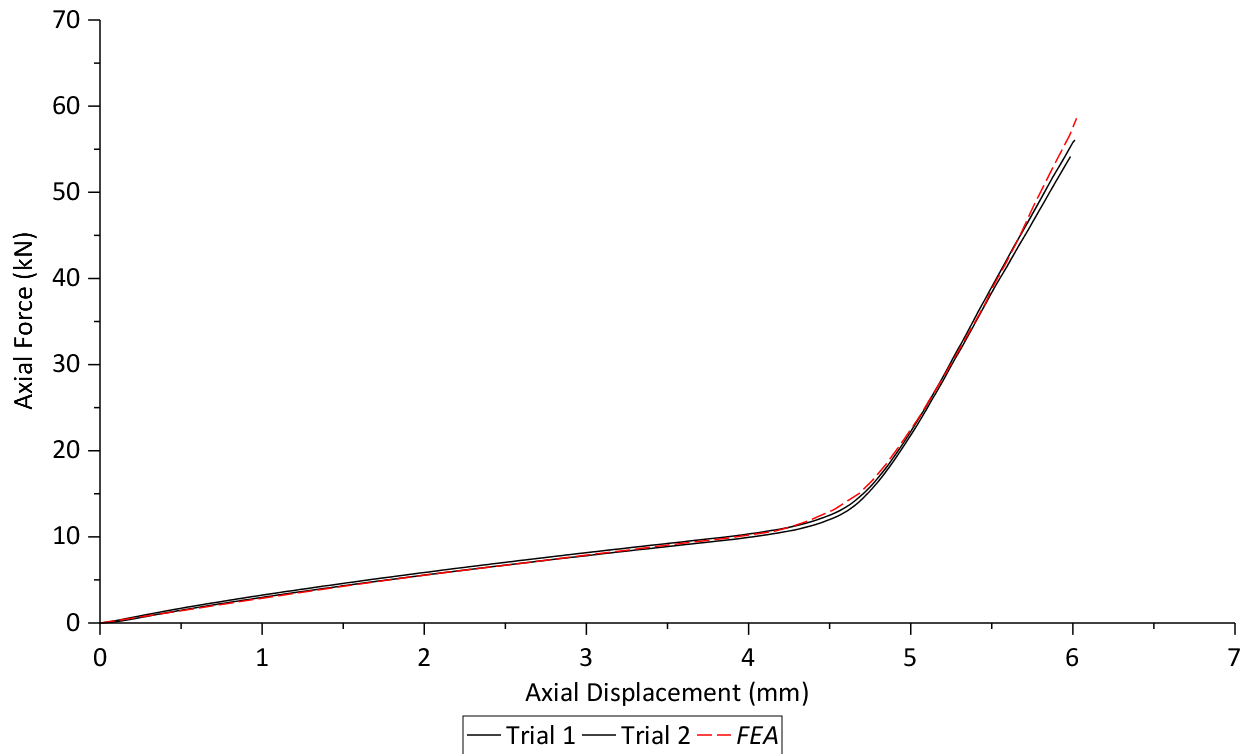


Figure 89: Final Rough Force-Displacement Curve

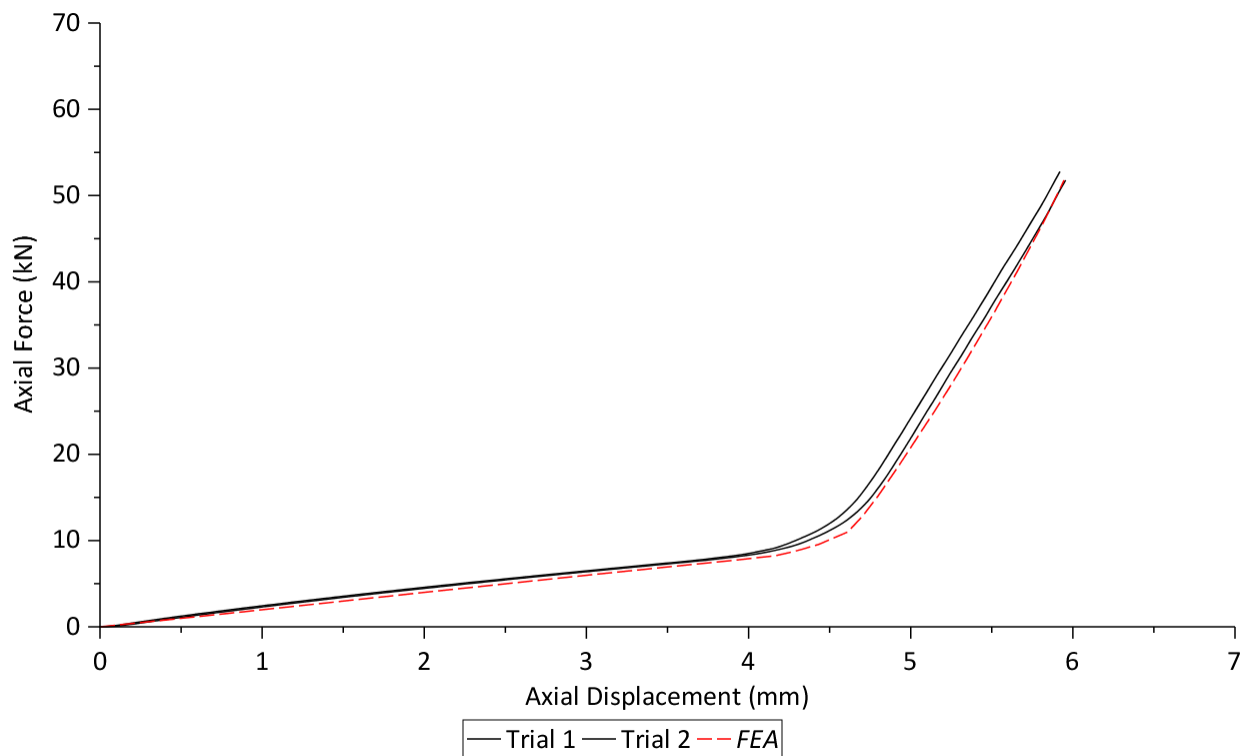


Figure 90: Final Lubricated Force-Displacement Curve

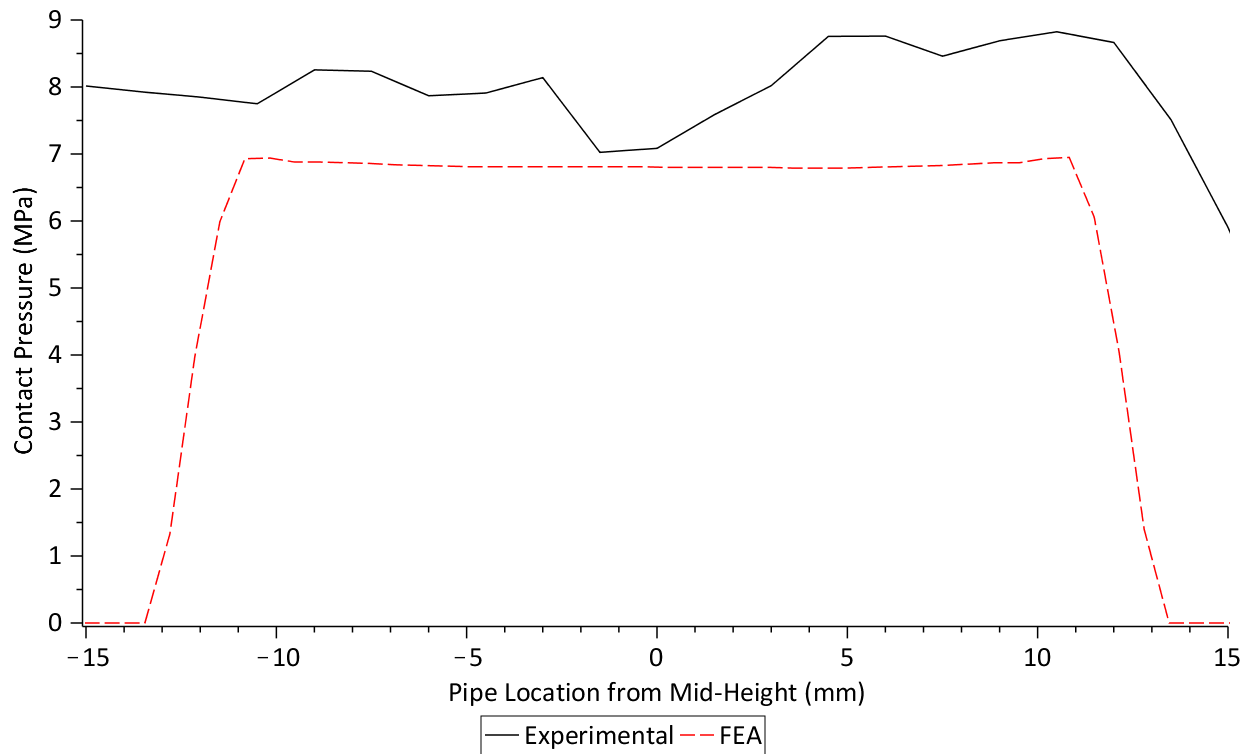


Figure 91: Final Rough Pressure Gradient

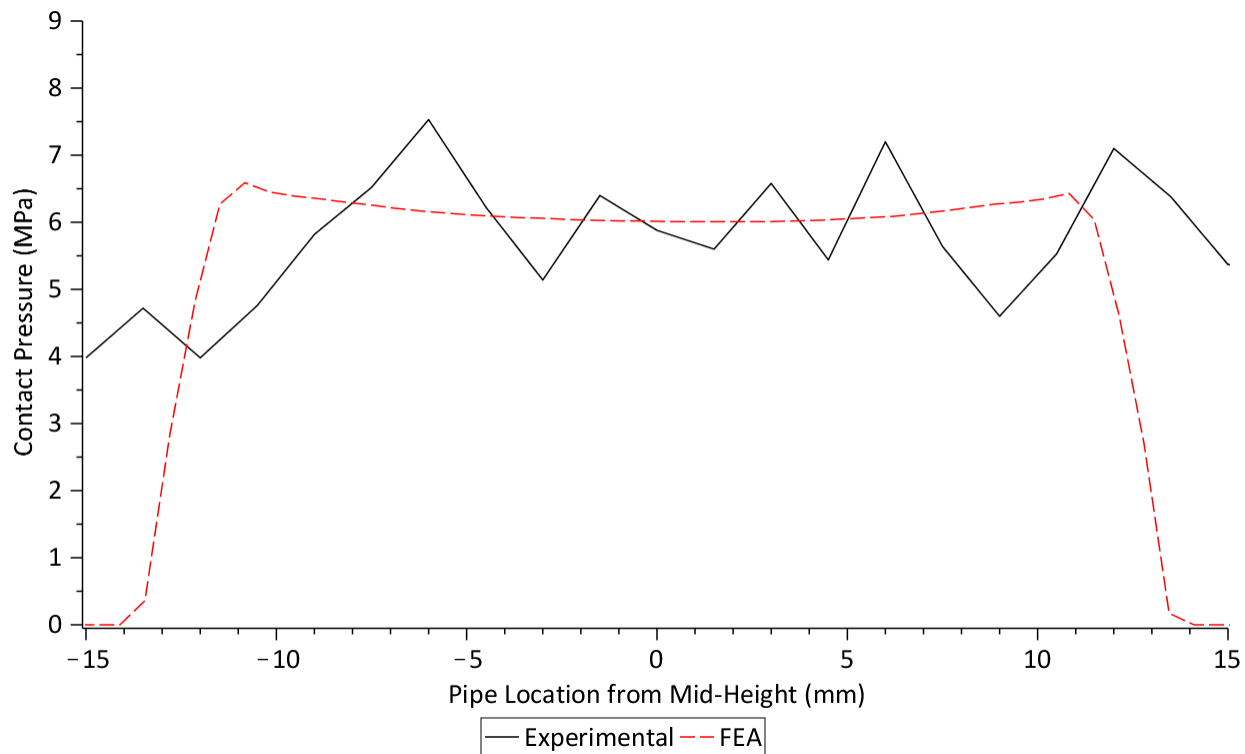


Figure 92: Final Lubricated Pressure Gradient

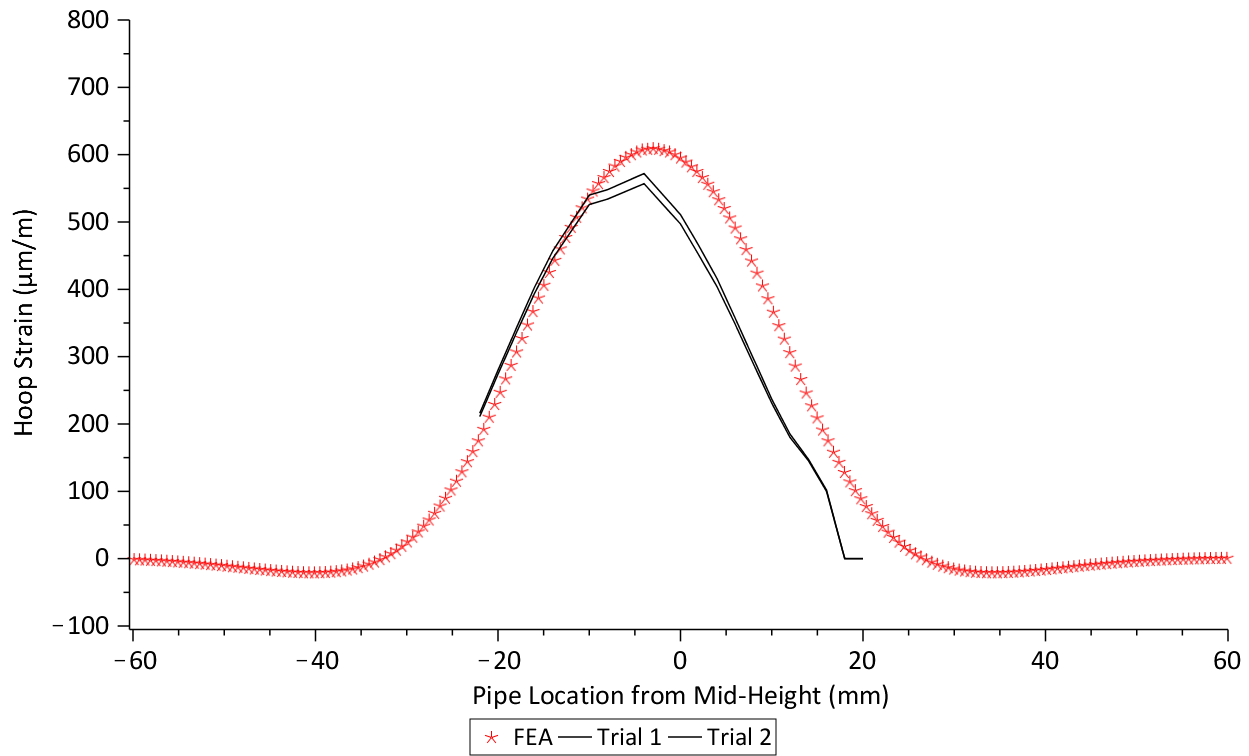


Figure 93: Final Rough Pipe Hoop Strain Gradient

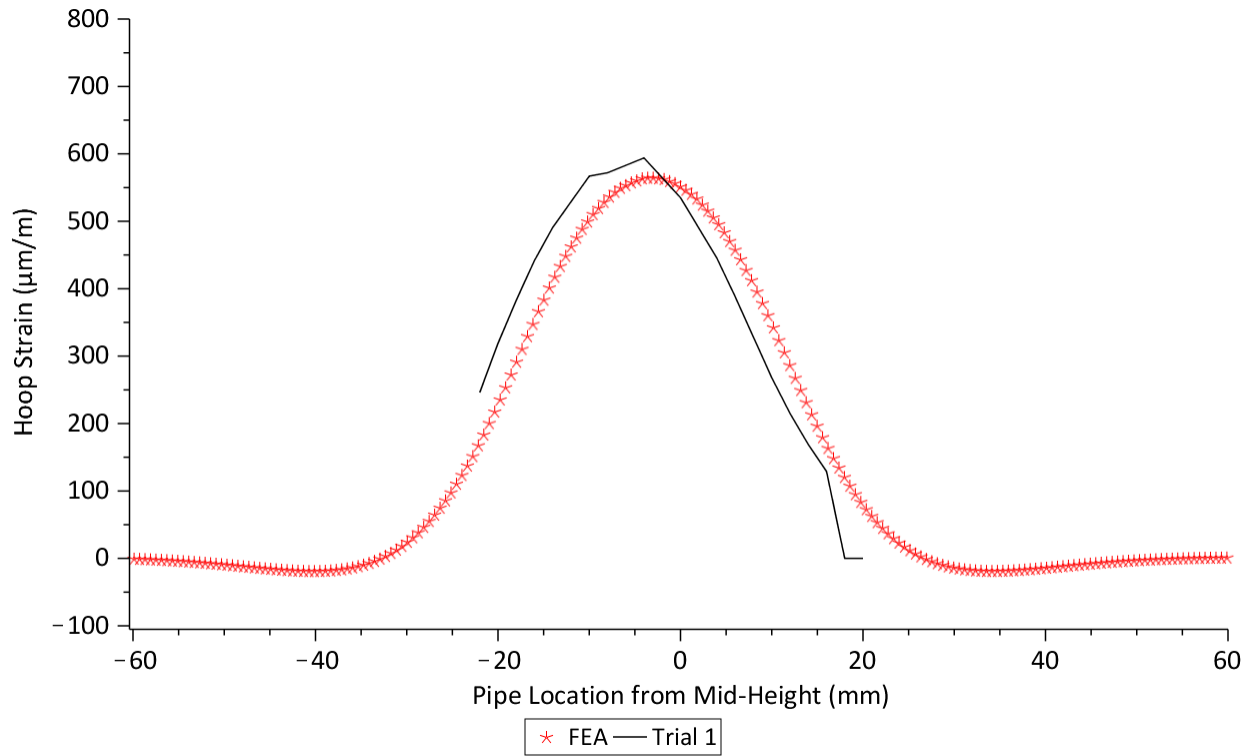


Figure 94: Final Lubricated Pipe Hoop Strain Gradient

Despite the optimization, the viscoelastic effects were still not replicated accurately. Figure 95 and figure 96 displays the normalized axial force relaxation profiles attributed to stress relaxation. For the rough and lubricated cases, the axial force predicted by FEA decays up to 18.2% less than experimental results. Equally for the maximum pipe hoop strain in figure 97 and figure 98, the FEA results predicted a decay in strain up to 18.5% less than experimental results. By visual examination of the axial force and pipe strain relaxation plots, the FEA predicts the relaxation behavior at a slower rate than what is experimentally observed.

For the creep tests, the FE model was equally unable to sufficiently predict the creep behavior of the seal again due to error in characterizing short-term viscoelastic effects. For the creep of axial displacement shown in figure 99 and figure 100, the FEA predicted an increase in axial displacement up to 3.3% less than experimental. Similarly for the creep of maximum pipe membrane hoop strain shown in figure 101 and figure 102, the FEA predicted an increase in strain between 2.4% less and 3.8% more than experimental results.

All of the results for the optimization and the quasi-static results are summarized in table 8. Table 9 summarizes the results for the viscoelastic effects in terms of the percent increase or decrease in axial force or pipe strain with respect to its original value immediately after loading. The viscoelastic result comparisons were taken at the minimum and maximum points of agreement. Following optimization, it was possible to examine the results of the FE model and formulate models for different size seals and pipes.

Table 8: Final Results Summary for Quasi-Static Loading

	Element Size (mm)	Iterations	Time (mins)	Warning Elements	F-D Max Deviation	F-D Integral Deviation	Pressure Deviation	Max Strain Deviation
Rough Relaxation	.06	417	21.30	2	6.33%	6.23%	-20.38%	6.46%
Lubricated Relaxation	.06	364	18.20	0	-0.93%	-1.83%	3.76%	5.05%
Rough Creep	.06	461	24.03	5	0.48%	-0.19%	-20.38%	4.38%
Lubricated Creep	.06	410	21.05	0	-1.44%	-3.69%	3.76%	0.89%

Table 9: Final Results Summary for Viscoelastic Effects

	MIN OR MAX DIFFERENCE	Axial Force Relaxation			Pipe Strain Relaxation		
		FEA (%)	EXP (%)	Difference (%)	FEA (%)	EXP (%)	Difference (%)
Rough Relaxation	MIN	21.5	31.9	10.4	18.7	30.9	12.2
	MAX	6.2	24.4	18.2	4.9	23.4	18.5
Lubricated Relaxation	MIN	22.3	30.8	8.5	19.7	29.3	9.6
	MAX	8.8	24.7	15.9	6.3	22.8	16.5

	MIN OR MAX DIFFERENCE	Axial Force Creep			Pipe Strain Creep		
		FEA (%)	EXP (%)	Difference (%)	FEA (%)	EXP (%)	Difference (%)
Rough Creep	MIN	5.8	8	2.2	0.7	1.6	0.9
	MAX	2.0	4.8	2.8	8.0	4.2	3.8
Lubricated Creep	MIN	5.3	6.4	1.1	8.0	8.4	0.4
	MAX	0.3	3.6	3.3	0.7	3.1	2.4

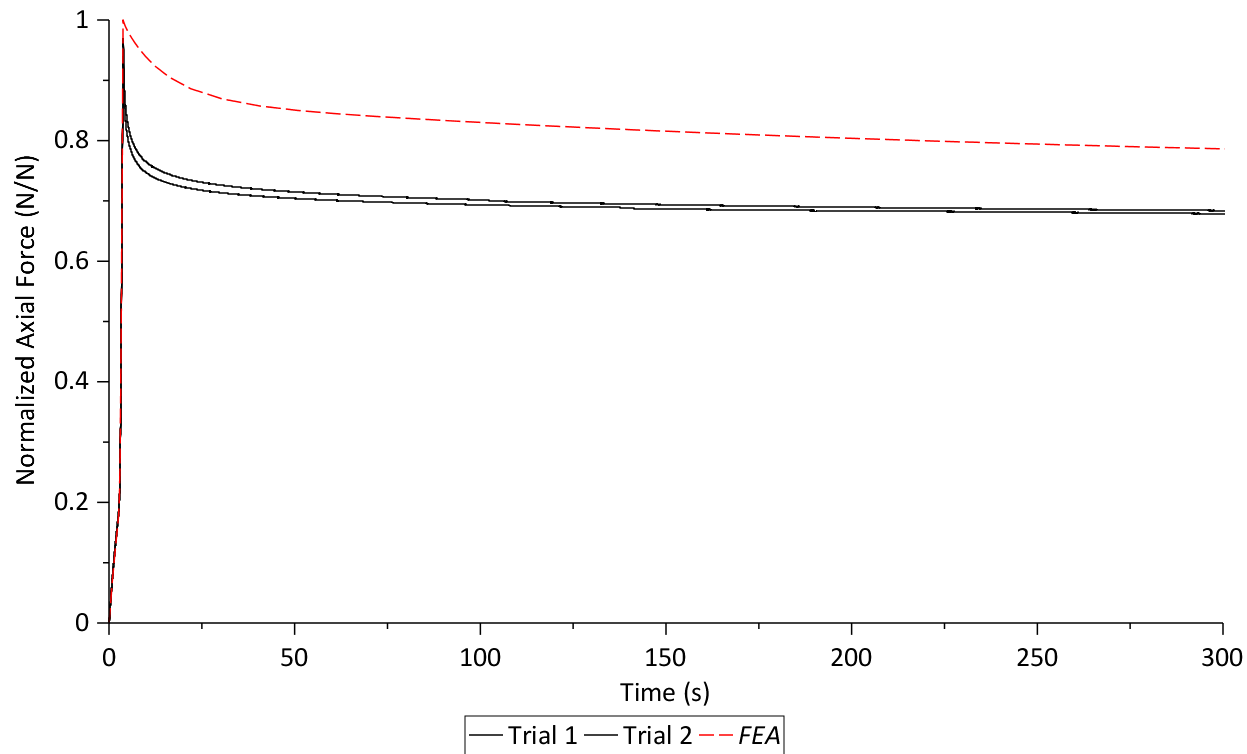


Figure 95: Final Rough Normalized Axial Force Relaxation

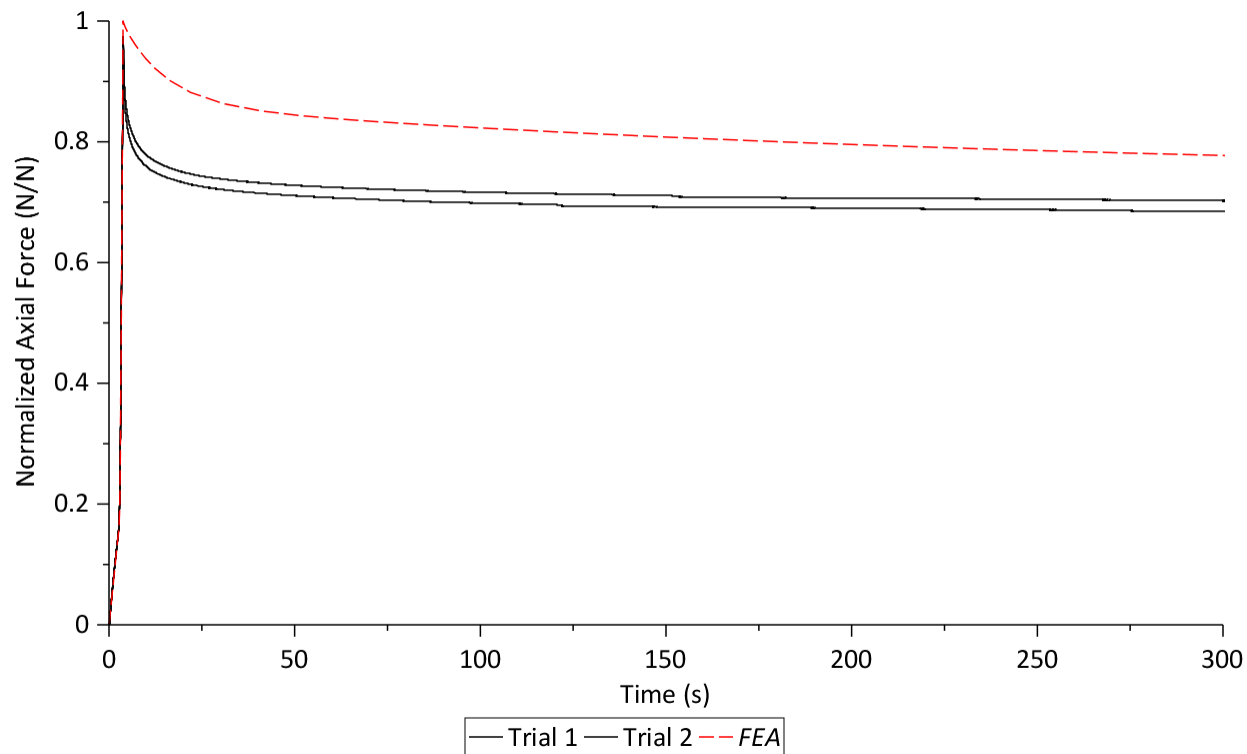


Figure 96: Final Lubricated Normalized Axial Force Relaxation

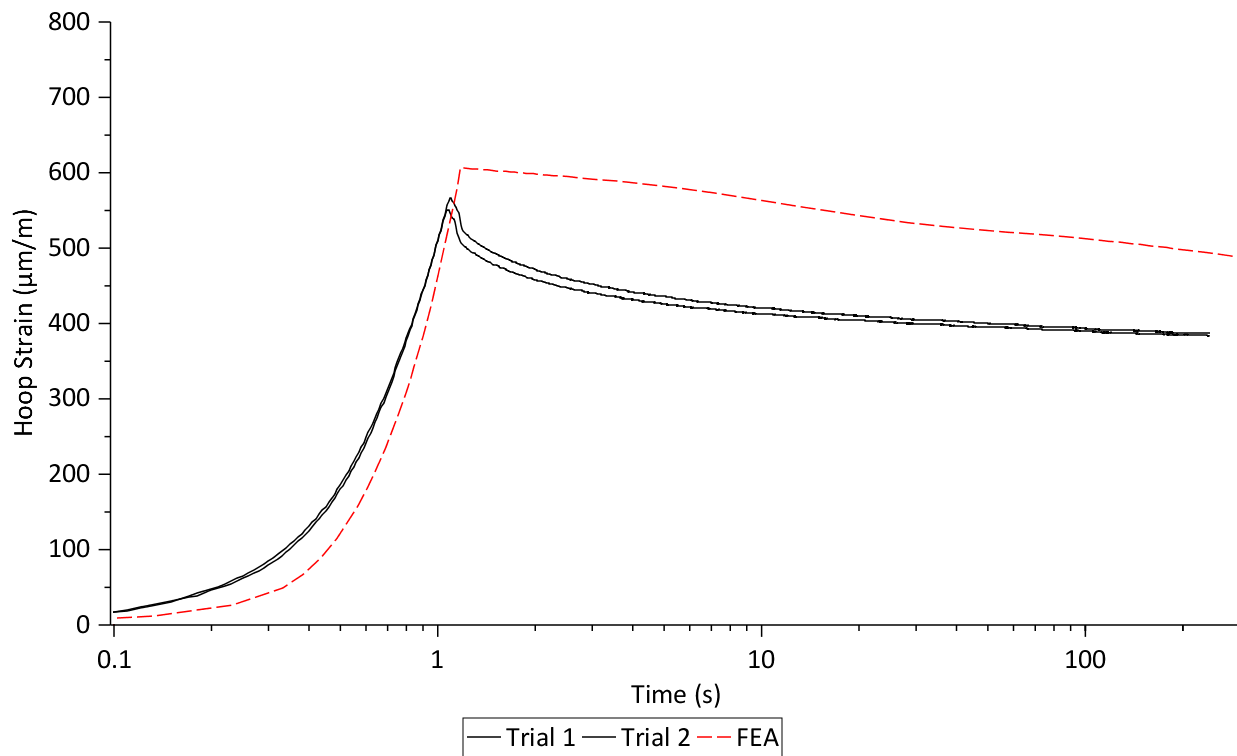


Figure 97: Final Rough Hoop Strain Relaxation

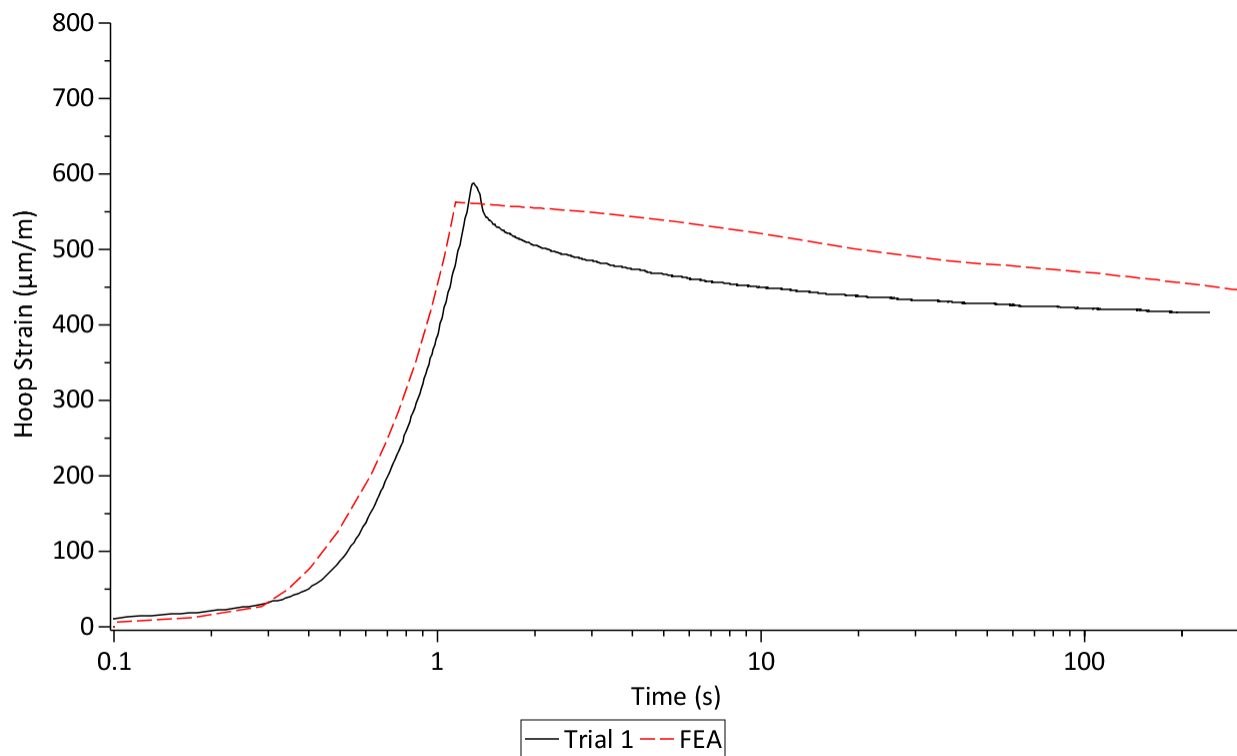


Figure 98: Final Lubricated Hoop Strain Relaxation

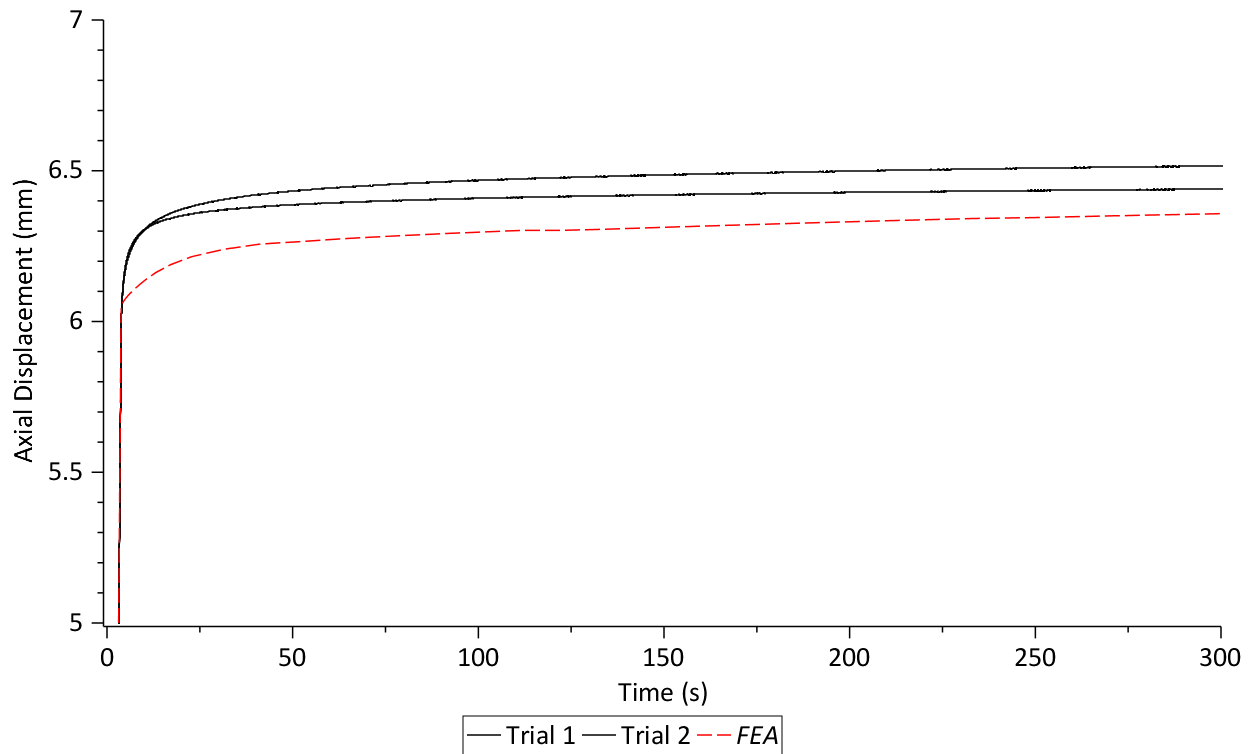


Figure 99: Final Rough Axial-Displacement Creep

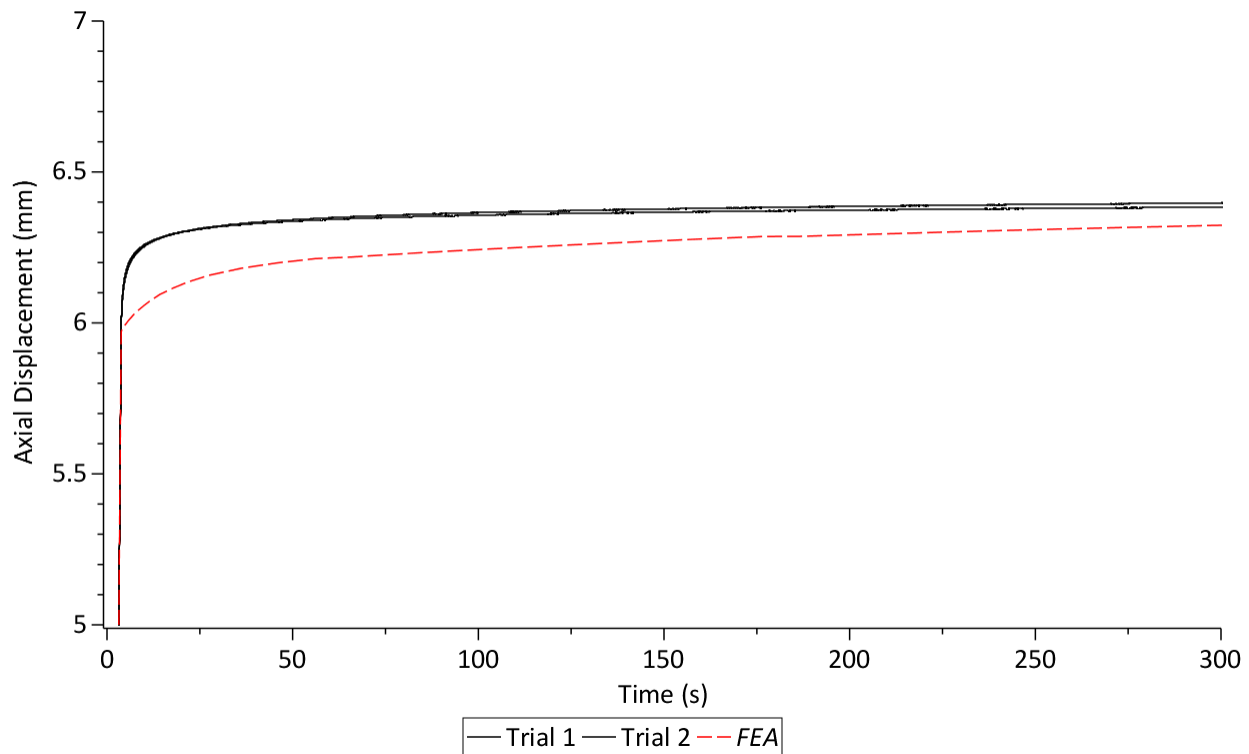


Figure 100: Final Lubricated Axial-Displacement Creep

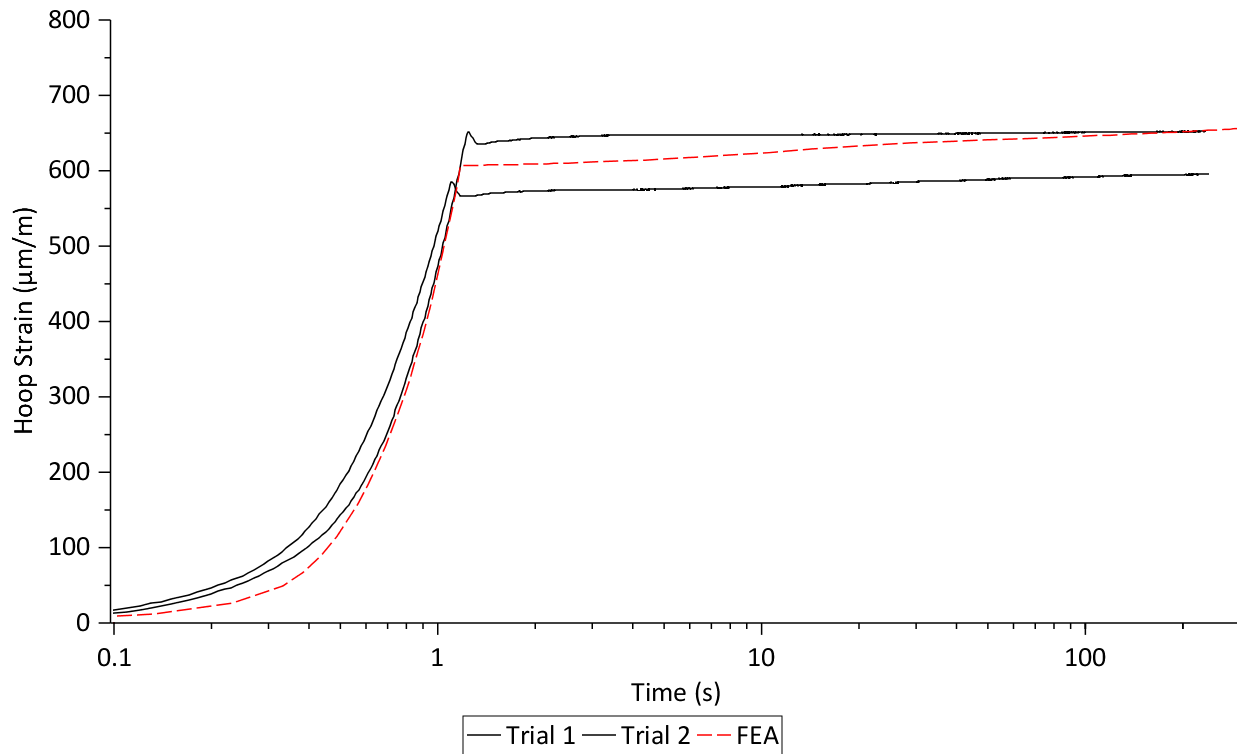


Figure 101: Final Rough Pipe Hoop Strain Creep

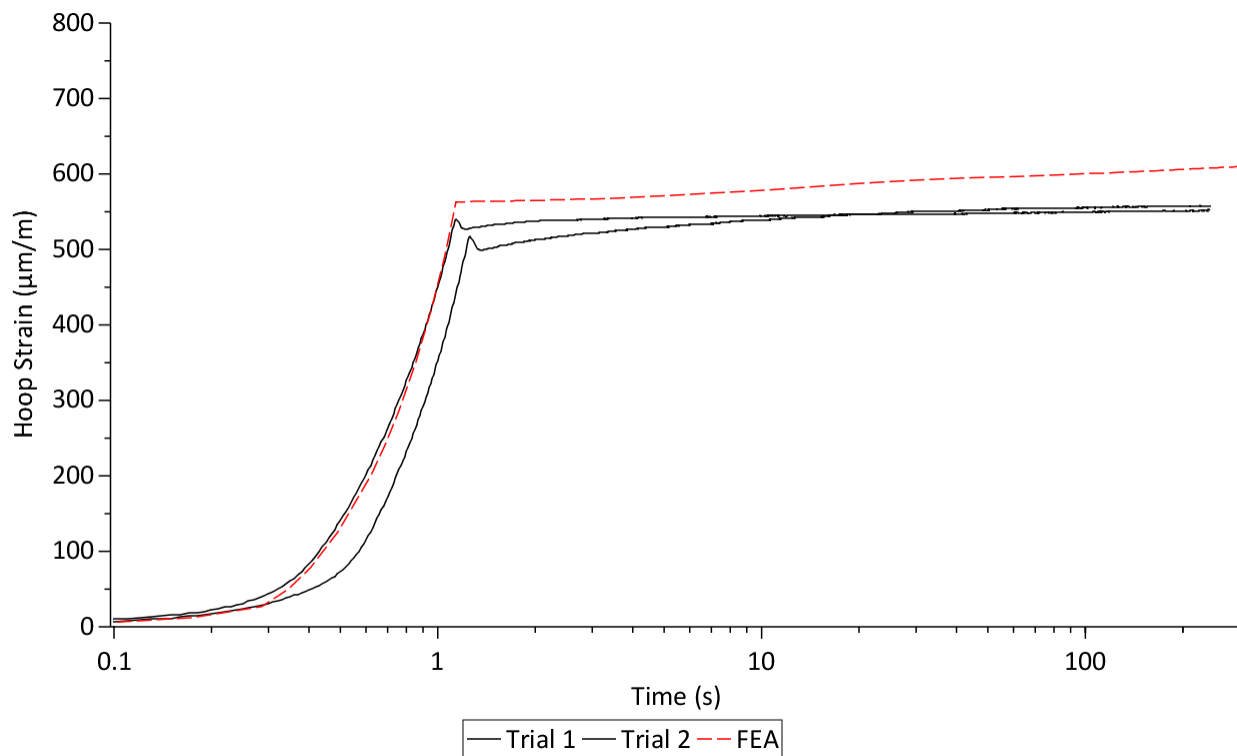


Figure 102: Final Lubricated Pipe Hoop Strain Creep

4.13 Final Results Analysis

Following the optimization and validation of the final FE model for a seal size of 102.5 mm OD, the results from the FE model were analyzed. One of the prevalent topics of high pressure sealing design is the behavior of the pipe sealed by an axially compressed seal. Traditional means of measuring this behavior would be to apply strain gauges in the hoop and longitudinal directions on the membrane of the pipe; the stress and strain on the inner walls of the pipe would remain unknown.

Considering the simulation of a thin-wall Sch. 10 pipe used with a 102.5 mm seal in a creep scenario where the seal is held at a constant axial force, the immediately measureable result was the hoop strain gradient on the outer membrane of the pipe shown in figure 103. Using the FE model, it was possible to examine the strain gradient at the inner surface of the pipe.

If pipe strain is considered with respect to a baseline outer-wall maximum hoop strain of $610 \mu\epsilon$, the inner-wall maximum hoop strain is $650 \mu\epsilon$ which is 6.6% higher. Looking at the through-thickness gradient in figure 104 there is a linear decay in hoop strain from the inner to the outer pipe wall. Thin-wall pipe stress analyses often consider the difference between inner-wall and outer-wall pipe hoop strain to be negligible. However if all of the principal strains including the hoop, longitudinal, and cross-thickness strains at the inner pipe wall are considered using Von Mises's criteria, a significant increase of 20.6% is observed over the baseline value. Furthermore, if 300 seconds of creep at constant pressure is considered, an increase of 28.6% is observed over the baseline value.

Therefore, by using the FE model even for the thin-wall case, there is a significant increase in pipe stress and strain by examining locations inaccessible through conventional means of strain prediction evident in the case including the effects of creep in the rubber material.

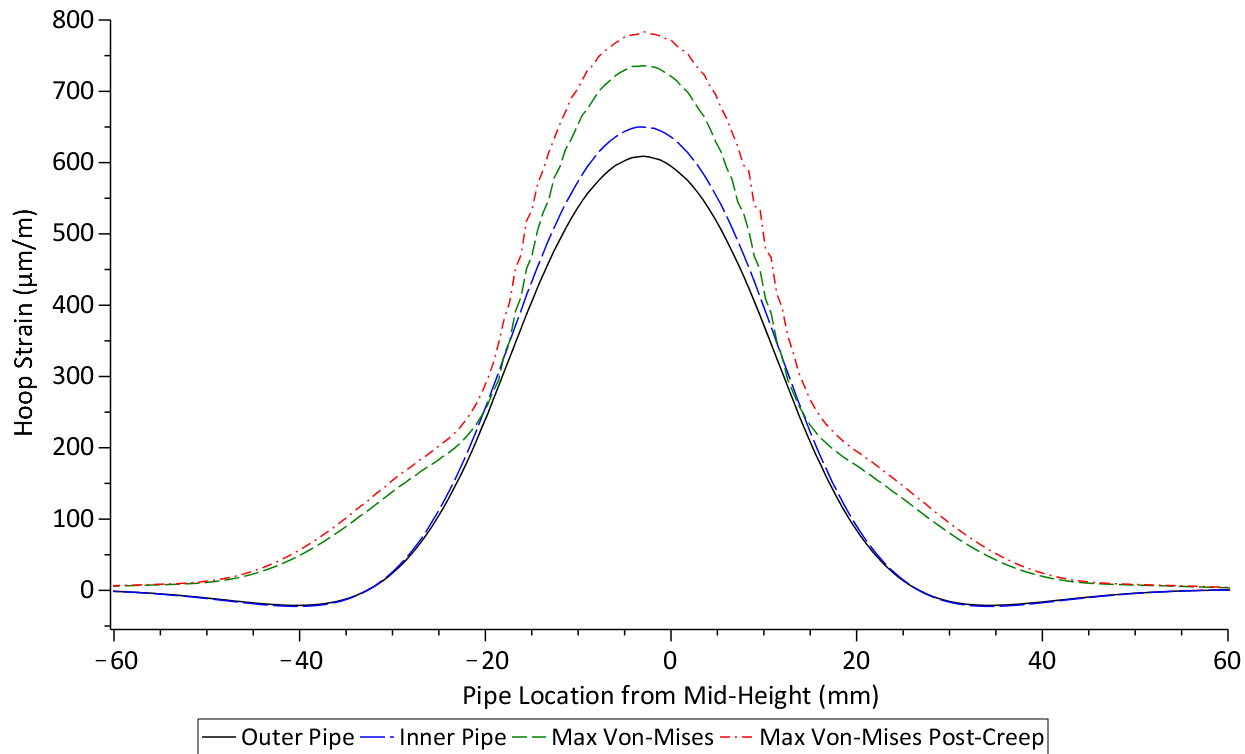


Figure 103: Thin-Wall Pipe Strain Gradient Location Comparison

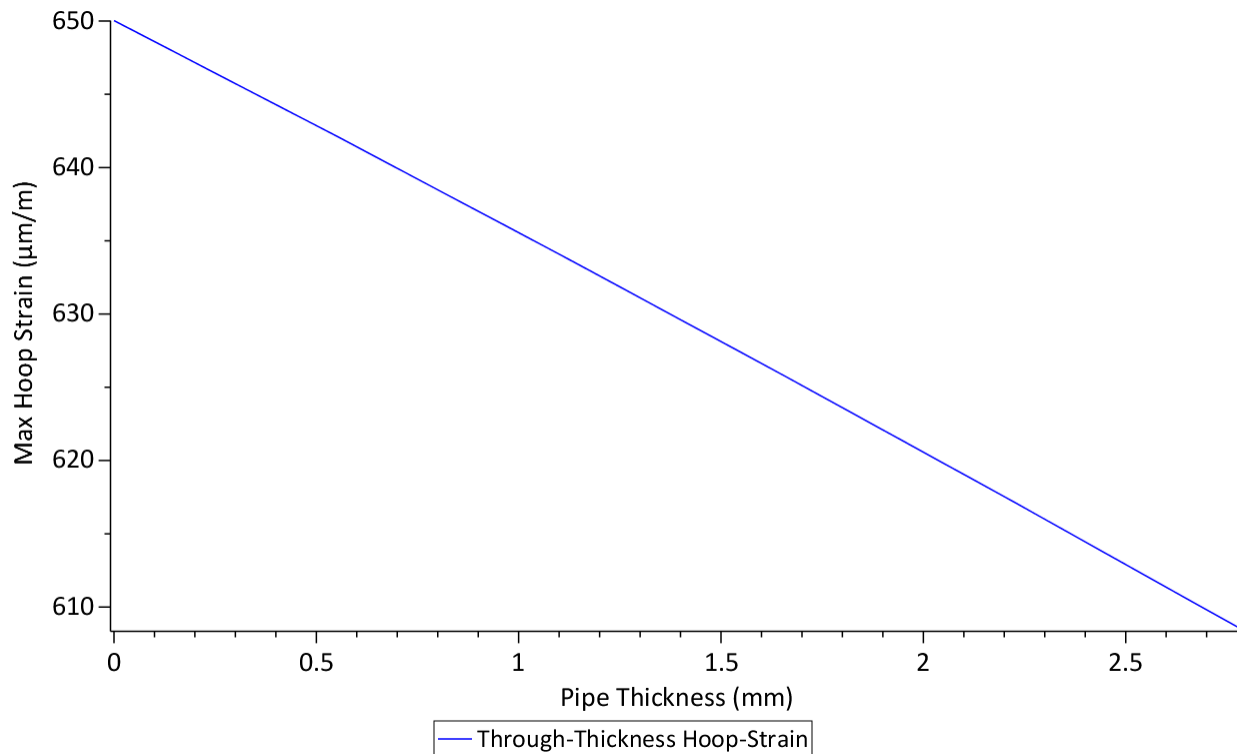


Figure 104: Thin-Wall Through-Thickness Pipe Hoop Strain at Location of Max. Strain

Similarly, if a thick-wall 5" Sch. 160 pipe is considered in use with the 102.5 mm OD seal, conventional measurement techniques do not accurately measure the inner-wall stresses and strains of the pipe due to a significant decay in strain across a large pipe wall thickness. In the case of a 15.88 mm wall thickness and an input axial compressive load of 60 kN on the seal, the maximum hoop strain on the inner and outer walls of the pipe after loading shown in figure 105 and figure 106 are 81 and 55 $\mu\epsilon$ respectively representing an increase in strain of 47% across the pipe thickness. Similar for Von-Mises strain following 300 seconds of creep, the maximum strain is 114 $\mu\epsilon$ representing an increase of 107% over the maximum outer wall hoop strain prior to creep.

The significance of this analysis pertains to the design and use of rubber seals when encountering specific standards and safety factors. If a seal is used for the purpose of flow isolation at constant pressure, the majority of the requirements do not specify details related to localized stress distributions caused by the creep behavior of a seal loaded at constant axial force. Rather, they specify either empirical or simplified analyses pertaining to the stress at the outer surface of the pipe or as 'do-not-exceed' limits. If one was to design a seal for isolation purposes without acknowledging the inner pipe stress distribution and the presence of viscoelastic effects, the stress on the pipe may exceed a given allowable limit.

4.14 Other Cases and Considerations

So far, a single seal size was examined, optimized, and experimentally validated. For other seal sizes and pipe geometry, other considerations exist which must be discussed prior to extending the current FE model.

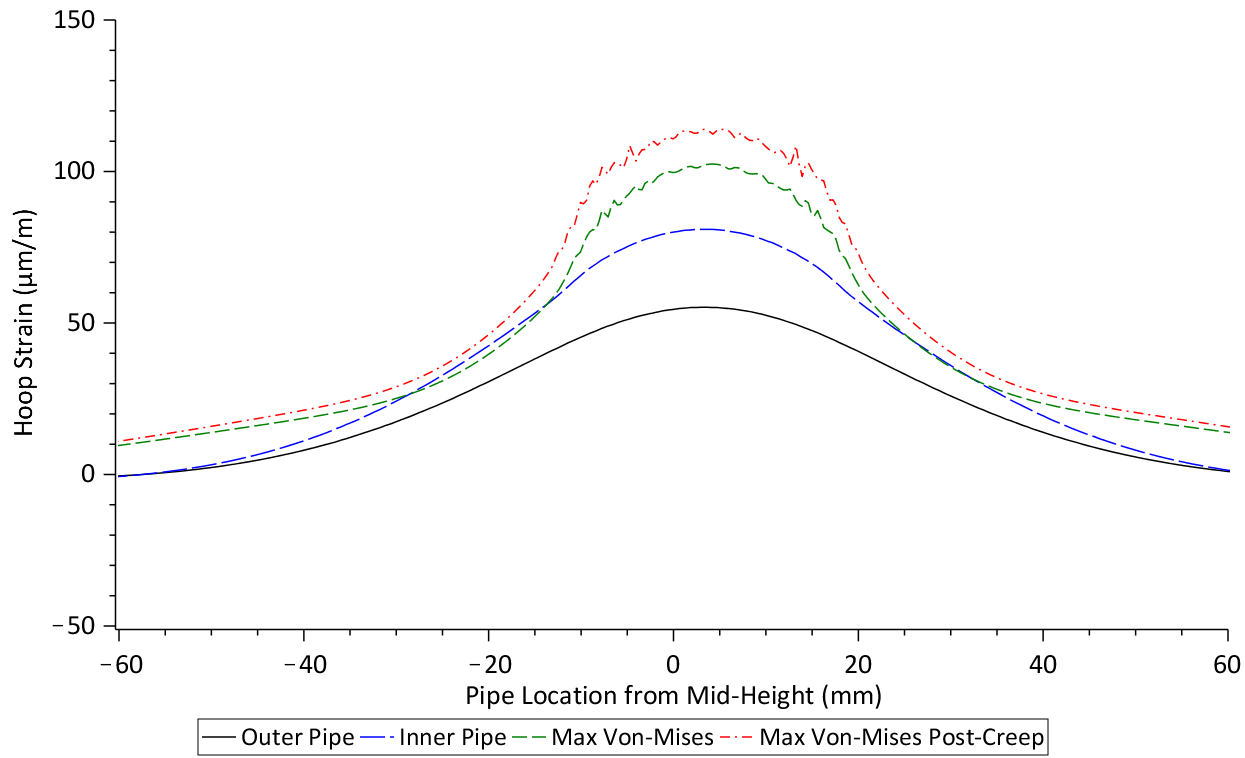


Figure 105: Thick-Wall Pipe Strain Gradient Location Comparison

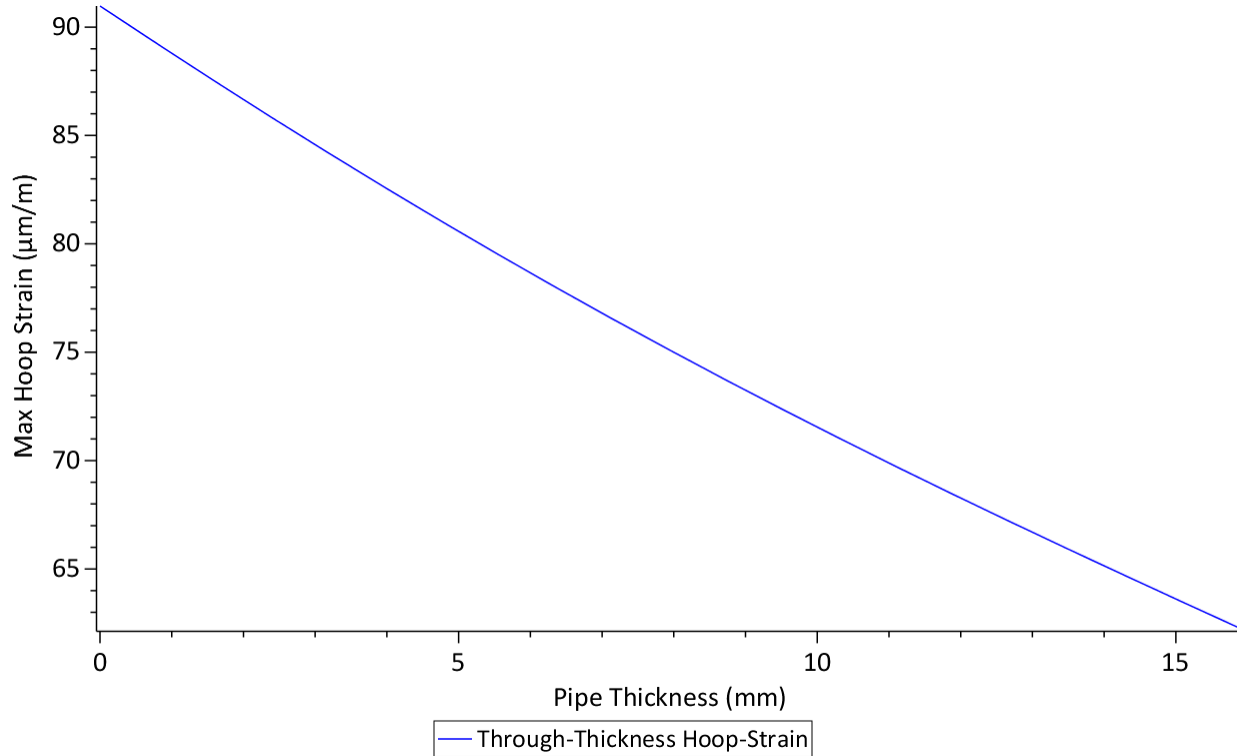


Figure 106: Thick-Wall Through-Thickness Pipe Hoop strain Gradient at Location of Max. Strain

4.14.1 Chemistry Differences

While the optimized FE model was shown to successfully predict the quasi-static compressive behavior a newly manufactured 102.5 mm OD seal manufactured from Spareage NT-5A NBR, there may be differences when simulating similar seals that were manufactured with a different chemical composition and age. For example, stress-strain tests for each of the experimentally tested seals were performed and are shown in figure 107 simply to see the effect that seal size, chemical composition, and age had on the stress-strain behavior of a seal in compression.

While all of the seals should have similar stress-strain curves, it was hypothesized in correspondence with Gent [5] that seals with a ‘narrower’ aspect ratio (i.e., lower shape factor) would each display a lower apparent compressive modulus. The 96.3 mm seal however showed a significantly higher modulus than the largest seal: 102.5 mm. The seals provided for experimental testing were of unknown age and history however they were manufactured in different batches using Spareage NT-5A NBR with the exception of a single 102.5 mm seal which was purchased and produced in the same batch as all rubber material test specimens and subsequently used for experimentation by Shah [3]. The SHORE A hardness for the new rubber seal and specimen batch was 78. Appendix A lists the hardness of the material between 76 and 80 SHORE A. The addition of artificial air aging at 100°C over 70hrs also produces an increase of 3 SHORE A hardness.

Using equation 61 developed by Gent [41], the correlation between SHORE A hardness and the elastic modulus of rubber, the predicted elastic modulus for the new seal is 8.31 MPa which is in fair agreement with the as-tested uniaxial tensile modulus value of 8.61 MPa.

$$E = \frac{0.0981 \cdot (56 + 7.62336 \cdot S)}{0.137505 \cdot (254 - 2.54 \cdot S)} \quad (61)$$

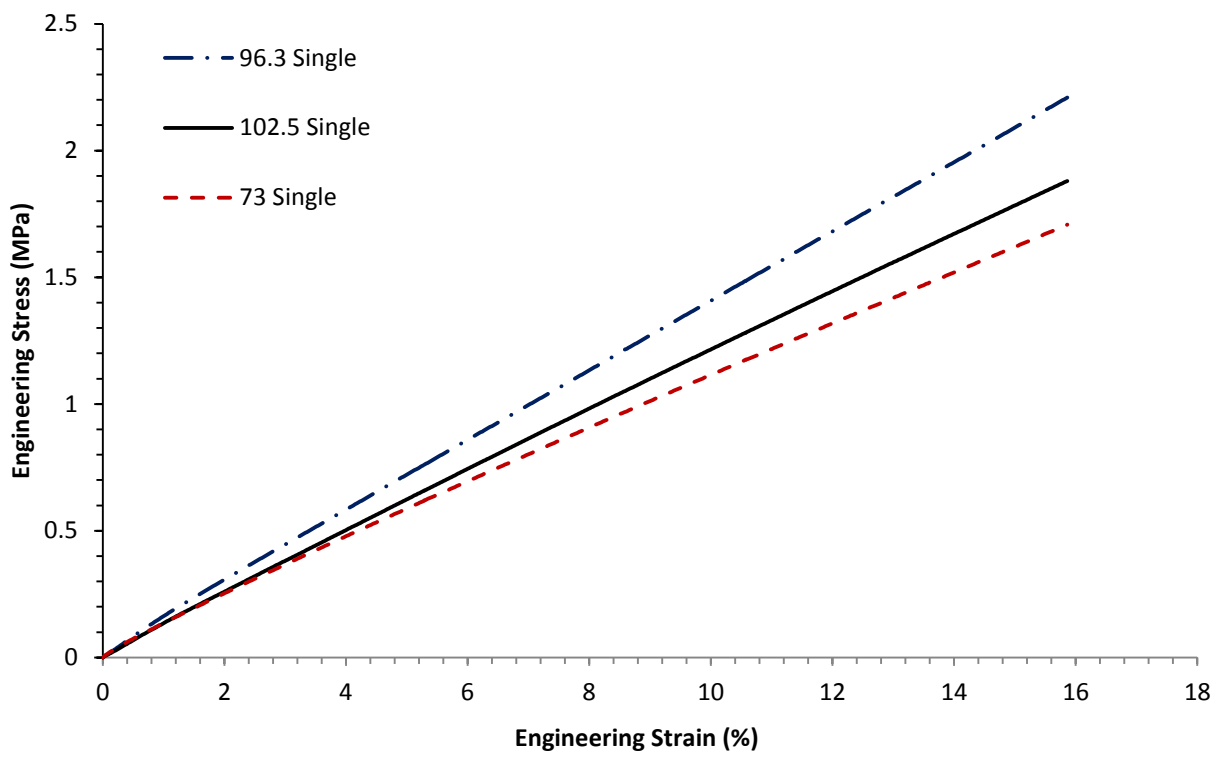


Figure 107: Seal Stress-Strain Compression Tests

where S is the SHORE A hardness and E is the elastic modulus. For the maximum allowable hardness value including the contribution of the aforementioned air aging, a hardness of 83 SHORE A translates to an elastic modulus of 11.38 MPa which is a 32% increase over the hyperelastic model presented in this analysis. It is therefore possible that seals of similar composition can have significantly different mechanical properties if they were manufactured from rubber in different batches and subject to chemical aging.

With the provided 96.3 mm OD seal and 4" Sch. STD pipe, similar experiments were performed as done with the 102.5 mm OD seal however with a less sophisticated setup employing 4 uniaxial strain gauges on the outer pipe membrane. The force-displacement curve and pipe membrane hoop strain gradient were compared equally as in previous analyses in 4.12 and demonstrated in figure 108 and figure 109. In both cases, the FE model does not accurately portray this case. It is clear that there is a large inaccuracy in the material properties because the slope of the force-displacement curve during the loading phase does not conform to experimental results. However, during the constrained phase after the inflection, the slopes of the FE and experimental curves are near-parallel.

However, given the fact that pipe strain is largely proportional to axial force, rather than comparing results at fixed displacement, it is more useful to compare the data at the same axial force as is most commonly done with the hydraulic compression of seals in practice using a fixed hydraulic pressure. Figure 110 and figure 111 displays the force-displacement curve and strain gradient results when an input axial force of 62.9 kN is taken from the experimental curves and fed back into the input loading of an FE model.

The resulting maximum pipe hoop strain is far more accurate with a deviation of 15% from the average experimental maximum hoop strain however it is offset further down the length of the pipe due to a larger axial displacement required to produce the 62.9 kN force.

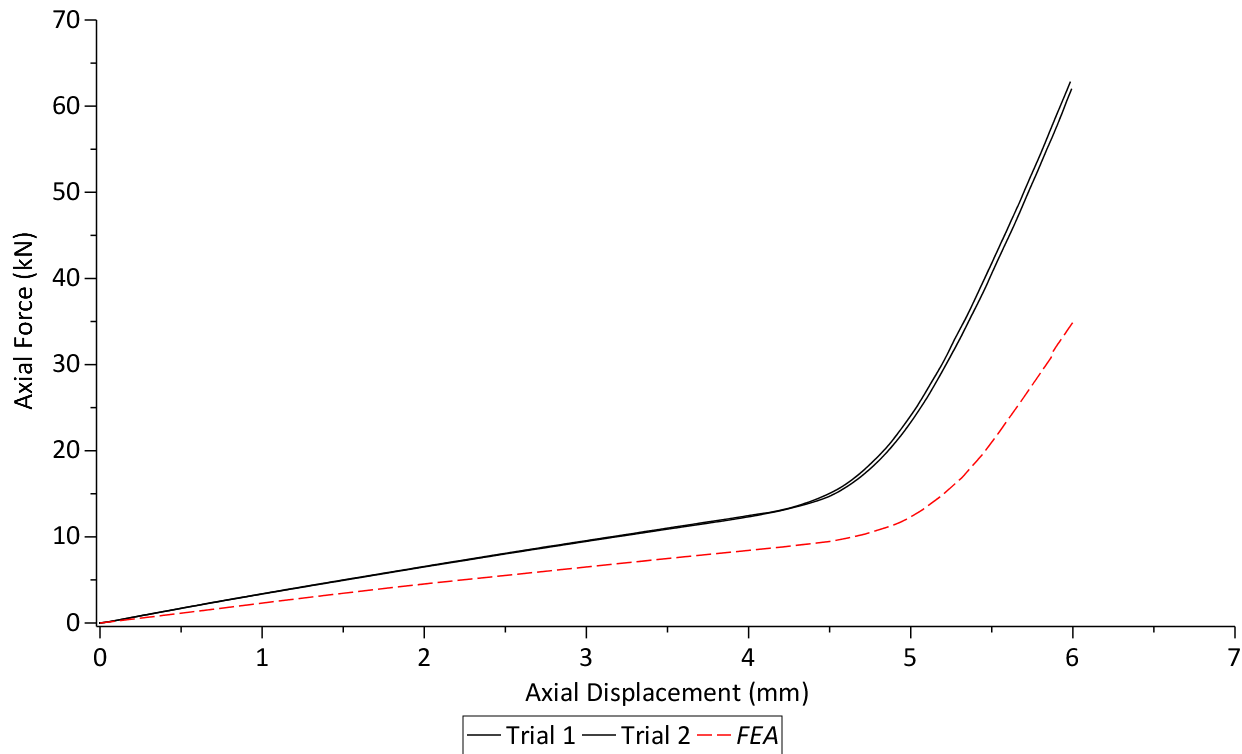


Figure 108: 96.3 mm Force-Displacement Curve

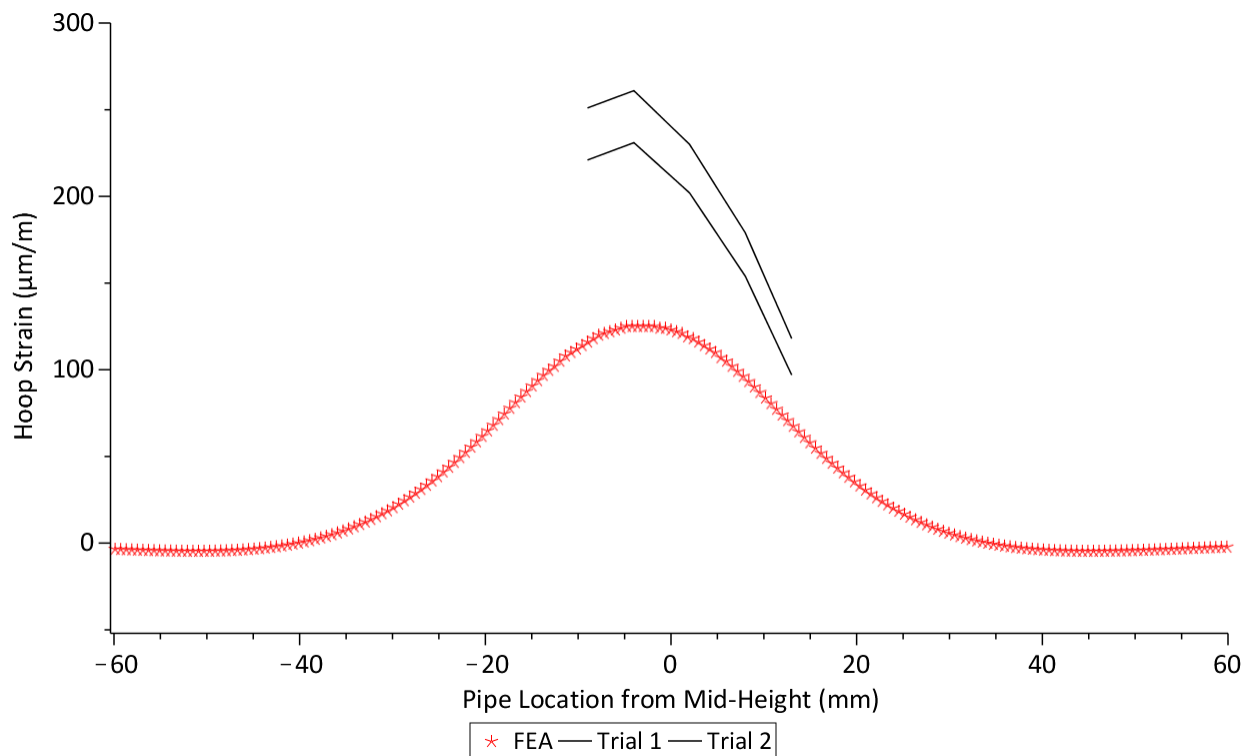


Figure 109: 96.3 mm Pipe Membrane Hoop Strain Gradient

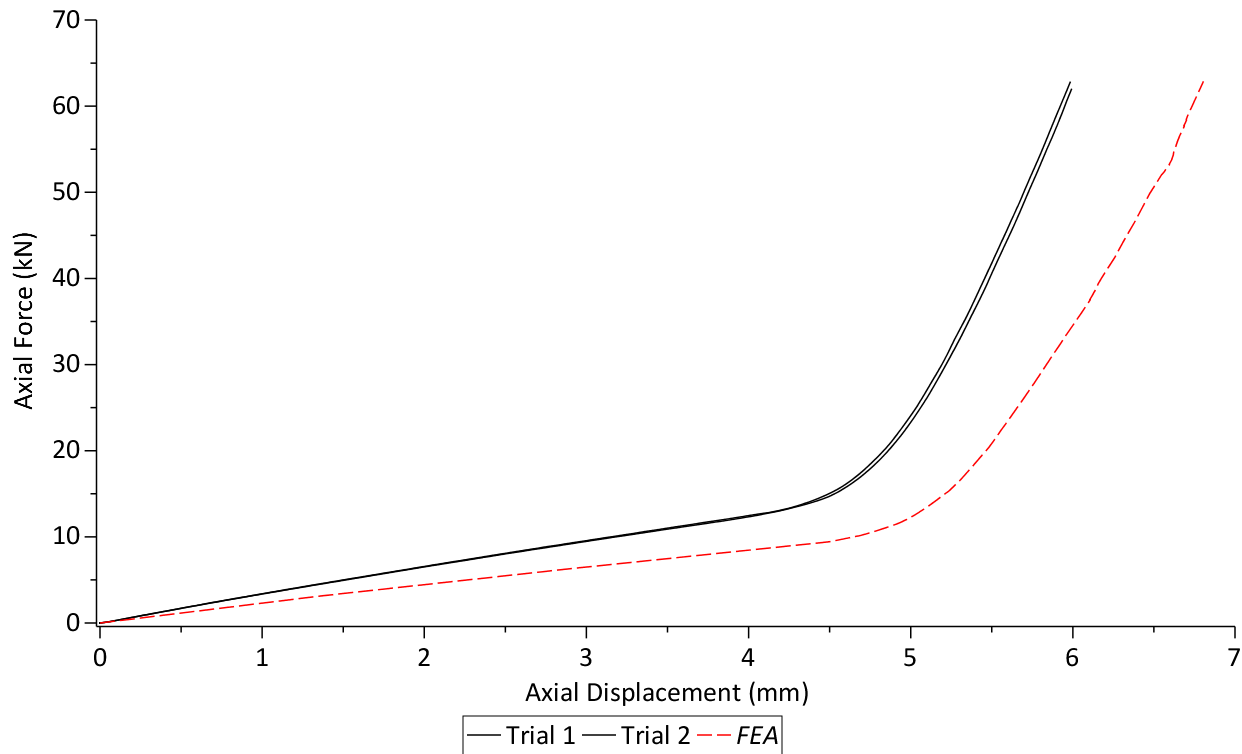


Figure 110: Force-Input for 96.3 mm Force-Displacement Curve

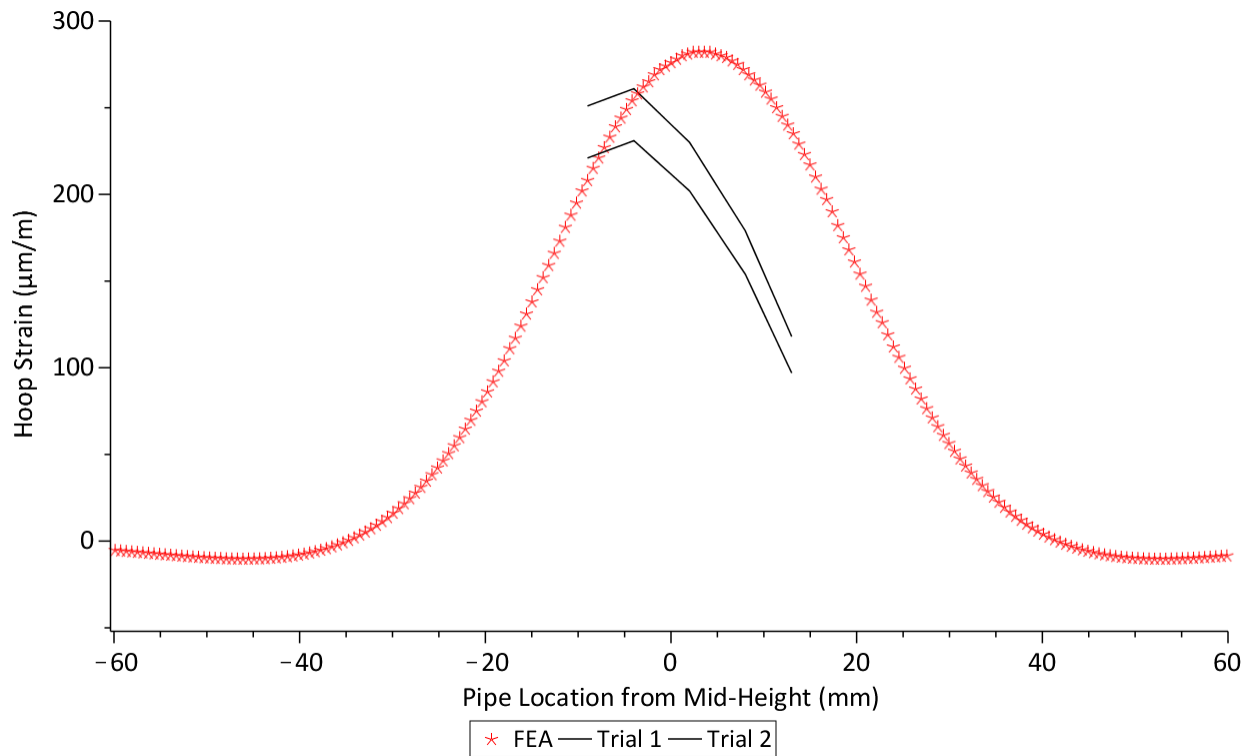


Figure 111: Force-Input for 96.3 mm Pipe Membrane Hoop Strain Gradient

Under fixed input axial displacement, the higher initial stiffness of the seal absorbs more input axial force which thereby distributes less pressure onto the pipe wall. However, at fixed input axial force, a material that is less stiff will allocate more of the axial force into contact pressure on the pipe wall thereby producing a slightly higher strain in the pipe.

The benefit of this behavior is that a given hyperelastic model can simulate similar materials under fixed input axial force conditions provided that the material's mechanical properties are similar to those of the hyperelastic model.

4.14.2 Geometric Irregularities

In most cases, pipes undergoing sealing are not perfectly circular; a certain tolerance is accepted for both wall thickness and pipe ovality. The sensitivity to geometry was explored briefly in 4.8 demonstrating a very high geometric sensitivity under fixed displacement input. Under fixed input force or pressure, it is expected that such sensitivity would be significantly reduced albeit with differences in seal deformation.

However, if the rubber seal is designed for use in pipes with irregular geometry, the FE model could be extended to a quarter-symmetry 3D model shown in figure 112 and figure 113 where both extremities of the oval pipe represents worst cases in pipe thickness and pipe ovality tolerances.

Unfortunately, due to time constraints, this model was not examined in detail however its development was very similar to the 2D model presented in this paper created through the use of low-order solid elements and planar contact elements in addition to 2 planes of symmetry. With a 3D model, the potential exists for future development of a sealing model.

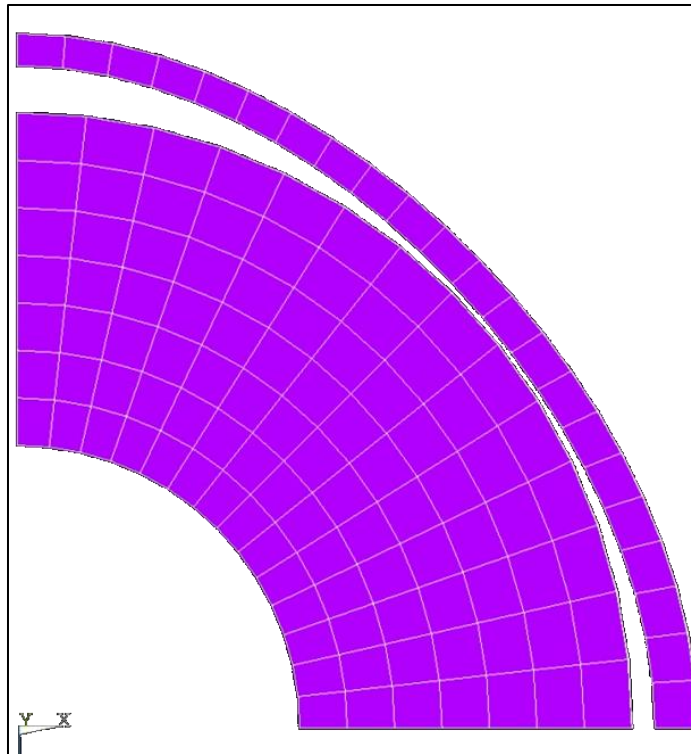


Figure 112: 3D FE Model for Use with Irregular Geometry: View A

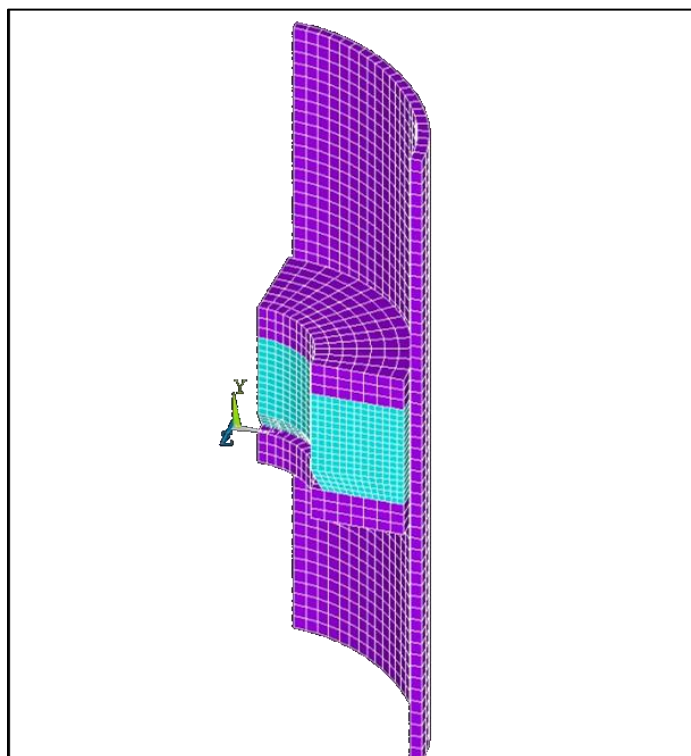


Figure 113: 3D FE Model for Use with Irregular Geometry: View B

4.14.3 Extrapolated Use of this Model

Due experimental constraints, it was not possible to test large seals due to the large force required to compress larger seals. However, as this FE model was validated only for a seal size of 102.5 mm OD for use with 4 or 5 inch pipe, the question remains whether it is possible to set up this FE model for use with larger seals. Without experimental validation it is difficult to determine whether an FE model is accurate however most material models input into the FE model are not dependent on geometry and therefore scalable to any geometry. These inputs include the hyperelastic, frictional, and viscoelastic models which are independent of large-scale geometry; the frictional model does depend on surface roughness which may be of relevance in certain situations. Therefore, as long as the geometry and loads are closely defined to the actual application, the extrapolated use of this model may be used with caution as long as the following measures are accounted for:

- The maximum rubber element strain and maximum normal contact pressure should not exceed 85% and 10 MPa respectively.
- The strain rate and temperature must be similar to those in this FE model. The material behavior with respect to strain rate was fairly insensitive however effects due to temperature are unknown.
- The surface roughness and lubricant must be similar to those examined in this model.
- The relative sliding velocity of frictional surfaces must be similar for use with this model.
- Viscoelastic effects should not be simulated beyond a time of 24 hours.

Chapter 5: Conclusion

The primary objective of this research project was to explore the axial-compressive behavior of an annular rubber seal and to develop a methodology to simulate the axial-compressive behavior of an annular rubber seal constrained in a pipe subject to large deformation and viscoelastic effects. In addition to the development of an FE model, the following phenomena and points-of-interest were also explored:

- Effect of pipe geometry and geometric irregularities
- Performance of various hyperelastic material models and the considerations in selecting the appropriate material tests and test data for accurate case-specific material characterization
- Development of a frictional testing and modelling methodology for use with elastomers in FE simulation subject to large compressive loads
- Development of a viscoelastic model for the simulation of short-term stress-relaxation and creep
- Experimental validation techniques for use in conjunction with experiments in correspondence with Shaha [3]

For this research, the scope was limited to performing all tests at constant room temperature, using simplified geometry, using small seals up to 102.5 mm in diameter, utilizing only one NB rubber compound, and only considering short-term viscoelastic effects.

A 2D axisymmetric FE model was developed in ANSYS 16 based on experimental geometry of a single seal mounted concentrically in a pipe sandwiched between two steel compressive rings. The pipe and compressive fixtures were characterized using a linear isotropic material model for common steel. The rubber seal's mechanical properties were characterized using a 5th order Yeoh hyperelastic model fit

to material test data from uniaxial tension, planar tension, equibiaxial extension, and volumetric compression tests. The viscoelastic effects for the rubber seal were characterized using a 3-term Prony series fit to material test data from shear sandwich and bulk compression stress relaxation tests over a period of 24 hours. The interfacial contact friction between the compressive rings and the seal were characterized using Thirion's law and Coulomb's law for both rough surfaces and surfaces lubricated with petrolatum-based grease. Axial-torsion friction tests were employed for both frictional contact conditions to provide the static and kinetic friction coefficients at different normal pressures which were then fit to a frictional decay model in accordance with Thirion's law. Loading was input on the lower compressive fixture based on an input axial displacement or axial force. In each case, the rate-of-loading was held constant respective to the strain rate at which experimental testing was performed.

Using the developed FE model in comparison to experimental data, the following was concluded:

- The axial force resulting from fixed-displacement loading agreed with experimental results within 6.4%.
- The maximum pipe hoop strain agreed with experimental results within 6.5%.
- Stress relaxation effects were under-predicted by up to 18.2% and 18.5% for axial force and pipe strain relaxation respectively.
- Creep effects were under-predicted by up to 3.3% for axial force creep and over-predicted by up to 3.8% for pipe strain creep.
- Sealing behavior is very sensitive to pipe geometry under fixed input displacement.
- Reducing contact friction between the seal and compressive rings decreases the apparent compressive modulus and pipe strain while improving sealing surface uniformity.
- Differences in chemistry and age for different batches of rubber can significantly change the mechanical properties of the seal which causes error in fixed-displacement loading.

- The maximum pipe strain at the inner and outer pipe walls can deviate significantly from each-other depending on the thickness of the pipe wall.
- The contact pressure and maximum pipe strain changes proportionally to the axial force and displacement of the seal.
- Stress relaxation displays a reduction in pipe strain as a function of time; conversely creep displays an increase in pipe strain however much less prevalent in magnitude as compared to stress relaxation.

Due to experimental constraints and time, and as a recommendation for future work, the following points could be examined in any possible continuation of this research:

- Examine and predict the effects of temperature, age, and susceptibility to the working environment (e.g., chemical degradation and fluid penetration)
- Improve upon the viscoelastic prediction by performing tests at the appropriate levels of stress and strain or by developing a non-linear viscoelastic model.
- Improve upon the viscoelastic timeframe prediction by performing time-temperature superposition (TTS) analyses for long-term viscoelastic predictions.
- Expand the 2D model for use with walls containing pitting or leaks.
- Develop a 3D model for use with irregular or misshapen pipe geometry.

References

- [1] O. H. Yeoh, "Some Forms of the Strain Energy Function for Rubber," *Rubber Chemistry and Technology*, vol. 66, no. 5, pp. 754-771, 1993.
- [2] P. Thirion, "The Coefficients of Adhesion of Rubber," *Rubber Chemistry and Technology*, vol. 21, no. 2, pp. 505-515, 1948.
- [3] R. Shaha, C. Wu and R. Jayaraman, "*Experimental Study of the Axial-Compressive Behavior of an Annular Hyperelastic Seal Constrained in a Pipe*", M.Sc. Thesis, Dept. Mech. Eng, U. of Manitoba, Winnipeg, Manitoba, 2016.
- [4] A. N. Gent, "Compression of Rubber Blocks," *Rubber Chemistry and Technology*, vol. 67, pp. 549-558, 1993.
- [5] A. N. Gent, F. M. Discenzo and J. B. Suh, "Compression of Rubber Disks between Frictional Surfaces," *Rubber Chemistry and Technology*, vol. 82, pp. 1-17, 2008.
- [6] K. Alzebdeh, T. Pervez and S. Qamar, "Finite Element Simulation of Compression of Elastomer Seals in Open Hole Liners," *Journal of Energy Resources Technology*, vol. 132, pp. 0310021-0310028, 2010.
- [7] Parker Hannifin Corp, "Packer Elements for Oil and Gas," 11 2014. [Online]. Available: http://www.parker.com/literature/TechSeal%20Division/Literature%20PDF%20Files/Parker_Tech_Seal_Radial%20Seal%20Design%20Guide_TSD%205440.pdf. [Accessed 1 2016].
- [8] D. Feng, Y. Yuan, B. Tan, C. Yang, G. Xu and P. Wang, "Finite Element Analysis of the Packer Rubbers of Sealing Process," in *International Conference on Mechanic Automation and Control Engineering*, 2010.
- [9] Z. Guo, Y. Wang, Q. Li, G. Li, W. Guo, Y. Lu and H. Hao, "The FEA Contact Analysis of High Pressure Packers," in *Advances in Mechanical and Electronic Engineering*, Berlin, Springer Berlin Heidelberg, 2012, pp. 119-124.
- [10] D. Zhao, C. Wu and D. Krokosz, "Analysis of Contact Stresses and Strains For Pipe with a Rubber Seal," in *Proceedings of The Canadian Society for Mechanical Engineering International Congress 2014*, Toronto, Ontario, Canada, 2014.
- [11] W. L. Semon, "Nitrile Rubber, Synthetic Rubber," Division of Chemistry, American Chemical Society, 1954.
- [12] A. N. Gent, "Chapter 3: Elasticity," in *Engineering with Rubber: How to Design Rubber Components*, Munich, Carl Hanser Verlag, 2001, p. 38.
- [13] M. Mooney, "A Theory of Large Elastic Deformation," *Journal of Applied Physics*, vol. 11, no. 9, pp. 582-592, 1940.
- [14] R. S. Rivlin, "Large Elastic Deformations of Isotropic Materials. IV. Further Developments of Isotropic Materials," *Philosophical Transactions of the Royal Society of London Series A*, vol. 241,

no. 835, pp. 379-397, 1948.

- [15] G. Marckmann and E. Verron, "Comparison of Hyperelastic Models for Rubber-Like Materials," *Rubber Chemistry and Technology*, vol. 79, no. 5, pp. 835-858, 2006.
- [16] R. W. Ogden, "Large Deformation Isotropic Elasticity – On the Correlation of Theory and Experiment for Incompressible Rubberlike Solids," *Proceedings of the Royal Society of London Series A*, vol. 326, no. 1567, pp. 565-584, 1972.
- [17] R. M. J. Garcia, S. O. E. Ruiz and C. Lopez, "Hyperelastic Material Modeling," Laboratorio CAD/CAM/CAE, Departamento de Ingenieria Mecanica, Universidad EAFIT, Medellin, 2005.
- [18] A. N. Gent, "A New Constitutive Relation for Rubber," *Rubber Chemistry Technology*, vol. 69, pp. 59-61, 1996.
- [19] L. R. G. Treloar, "The Elasticity of a Network of Long-Chain Molecules-II," *Transactions of the Faraday Society*, vol. 39, no. 36, pp. 247-253, 1943.
- [20] E. Arruda and M. C. Boyce, "A Three-Dimensional Model for the Large Stretch Behavior of Rubber Elastic Materials," *Journal of the Mechanics and Physics of Solids*, vol. 4, no. 12, pp. 389-412, 1993.
- [21] L. Mullins, "Softening of Rubber by Deformation," *Rubber Chemistry and Technology*, vol. 42, pp. 339-362, 1969.
- [22] K. Miller, "Testing of Elastomers for Finite-Element Analysis," 2002. [Online]. Available: <http://easc.ansys.com/staticassets/ANSYS/staticassets/resourcelibrary/confpaper/2002-Int-ANSYS-Conf-147.PDF>. [Accessed 2016].
- [23] Axel Products Inc., "What Material Tests are Typically Performed to Calibrate a Hyperelastic Material Model?," [Online]. Available: http://www.axelproducts.com/downloads/Tests_Hyperelastic_QA.pdf. [Accessed 2016].
- [24] Axel Products Inc., "Test Description for Basic Hyperelastic Properties Experiments," Axel Products Inc., Ann Arbor, MI, USA.
- [25] D. L. Crocker, A. Maxwell and R. Hunt, "Verification of Hyperelastic Test Methods," NPL Report CMMT(A)226, 1999.
- [26] I. M. Ward and J. Sweeney, Mechanical Properties of Polymers, 3rd edition, Chichester: John Wiley & Sons, Ltd., pp. 91, 92, 93, 95 2013.
- [27] *Rubber, Vulcanized - Determination of Creep in Compression or Shear*, ISO 8013, 2012
- [28] *Rubber, Vulcanized or Thermoplastic - Determination of Stress Relaxation in Compression - Part 1: Testing at Constant Temperature*, ISO 3384-1, 2011.
- [29] G. M. Bartenev and V. V. Lavrentjev, "The Law of Vulcanized Rubber Friction," *Rubber Chemistry and Technology*, vol. 34, no. 4, pp. 1162-1168, 1961.
- [30] D. Denny, "The Influence of Load and Surface Roughness on the Friction of Rubber-like Materials," *Proceedings of the Physical Society of London Section B*, vol. 66, pp. 721-727, 1953.

- [31] Axel Products Inc., "Measuring Rubber and Plastic Friction for Analysis," [Online]. Available: <http://www.axelproducts.com/downloads/Friction.pdf>. [Accessed 2016].
- [32] ANSYS Inc., *ANSYS Mechanical APDL Material Reference*, Canonsburg, PA, USA: ANSYS, Inc, 2013.
- [33] ANSYS Inc., *Theory Reference for the Mechanical APDL and Mechanical Application*, Canonsburg, PA, USA: ANSYS, Inc, 2009.
- [34] *Welded and Seamless Wrought Steel Pipe*, ASME B36.10M, 2004
- [35] W. C. Young, R. G. Budynas and A. M. Sadegh, *Roark's Formulas for Stress and Strain*, New York: McGraw-Hill Education, 2011.
- [36] FujiFilm Corp., "Overview," FujiFilm Corp., [Online]. Available: <http://www.fujifilm.com/products/prescale/prescalefilm/>. [Accessed 2016].
- [37] FujiFilm Corp., "Specifications and Operational Environment," FujiFilm Corp., [Online]. Available: <http://www.fujifilm.com/products/prescale/prescalefilm/#specifications>. [Accessed 2016].
- [38] T. Instruments, "TA Instruments Dynamic Mechanical Analyzer," [Online]. Available: <http://www.tainstruments.com/pdf/literature/TA284.pdf>. [Accessed 2016].
- [39] ANSYS Inc., *Contact Technology Guide*, Canonsburg, PA, USA: ANSYS Inc., 2009.
- [40] *Specification for Line Pipe*, API Specification 5L, 2004.
- [41] A. N. Gent, "On the Relation between Indentation Hardness and Young's Modulus," *Rubber Chemistry and Technology*, vol. 34, no. 4, pp. 896-906, 1958.

Appendix A

SPAREAGE NT-5A Material Specification

Material : Nitrile Butadiene Rubber

Spareage Code : NT 5A

Revision date : 01/03/2009

Physical properties	nominal	actual	units
Hardness BS 903 A 26, 23 °C	76-80	78	Shore A
Tensile strength BS 903 A 2, 23 °C	> 102	158	Kg/Cm ²
Elongation at break BS 903 A 2, 23 °C	> 125	270	%
Compression set BS 903 A 6, 100 °C, 22 h, 25 %	< 25	20.5	%
Air Ageing BS 903 A 19, 100 °C, 70 h			
Hardness Change	<(+15)	+3	Points
Tensile Change	<(-20)	-10	%
Elongation Change	<(-40)	-22	%
Fluid Resistance, ASTM Oil-1 BS 903 A 16, 100 °C, 70 h			
Hardness Change	-5 to +15	+2	Points
Tensile Change	<(-25)	-11.3	%
Elongation Change	<(-45)	-25.9	%
Volume Change	-10 to +5	-4.95	%
Fluid Resistance, ASTM Oil-3 BS 903 A 16, 100 °C, 70 h			
Hardness Change	<(-15)	-3	Points
Tensile Change	<(-45)	-14.5	%
Elongation Change	<(-45)	-25.9	%
Volume Change	-0 to +35	+16.5	%
Specific Gravity BS 903 A 1, 23 °C	—	1.27	Gm/cc
Ash Content 800°C, 2 Hrs	—	7.50	%

Spareage Seals Ltd.

Oil Seal House, Road No. 28, Wagle Estate, Thane, Bombay - 400604.
Tel.: +91-22-2580 0972 (10 lines) | Fax: +91-22-2582 3991, 2582 7480.
E-mail: sales@spareage.com | Website: www.spareage.com



IN TECHNICAL COLLABORATION WITH
UKSEALS & POLYMERS LTD. (ENGLAND)

Appendix B

Effect of Strain Rate on the Sealing Behavior of the Seal

As an addition to this thesis, the effect of strain rate was examined as an extension to the parametric study in section 3.7.6 at a later time. The strain rate had previously been shown in figure 37 to display a weak effect on the hyperelastic material testing curves. It was important to verify whether the strain rate had a similar effect on the sealing behavior of the seal.

With a similar technique detailed in section 4.9, the 1st cycles for the material testing dataset performed at a strain rate of 0.00264 s^{-1} were superimposed for each of the levels of extension used in testing (20, 40, 60, and 100%) shown in figure B1. The dataset formed from the superposition of 1st cycle data was curve-fit using a 5th order Yeoh model shown in figure B2. Using the FE model developed previously in section 4.12, the results from the FE model using the material model for 0.05 s^{-1} were compared to the results from the FE model using the material model for 0.00264 s^{-1} . The results used for comparison were the force-displacement curves and the pipe hoop strain gradient.

In both cases, figure B3 and figure B4 displays a marginal increase in force and pipe strain as a function of increasing strain rate with only a 7.1% and 9.1% difference respectively. These results agree with the sensitivity observed during material testing. In conclusion, the change in sealing behavior of the rubber seal when loaded at strain rates of 0.05 versus 0.00264 s^{-1} is negligible in terms the contribution to changes in axial force and pipe strain.

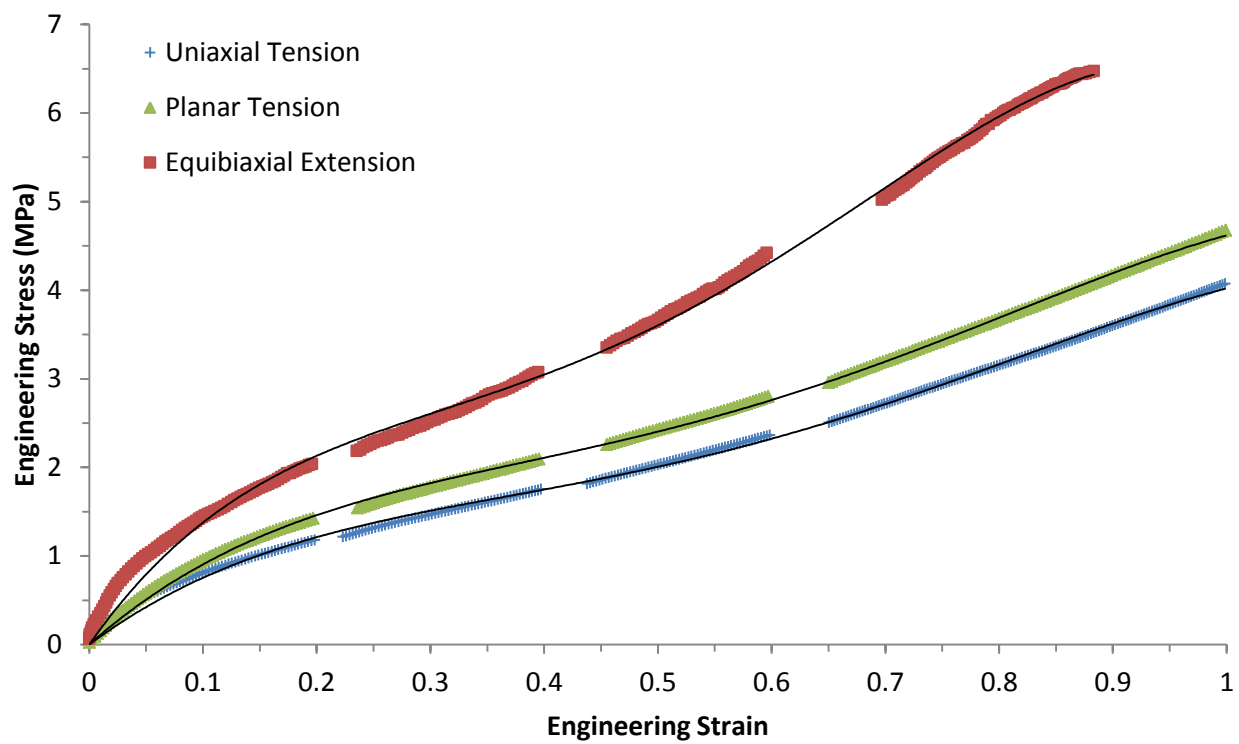


Figure B1: Superposition of 1st Cycle Data for 0.00264 s^{-1}

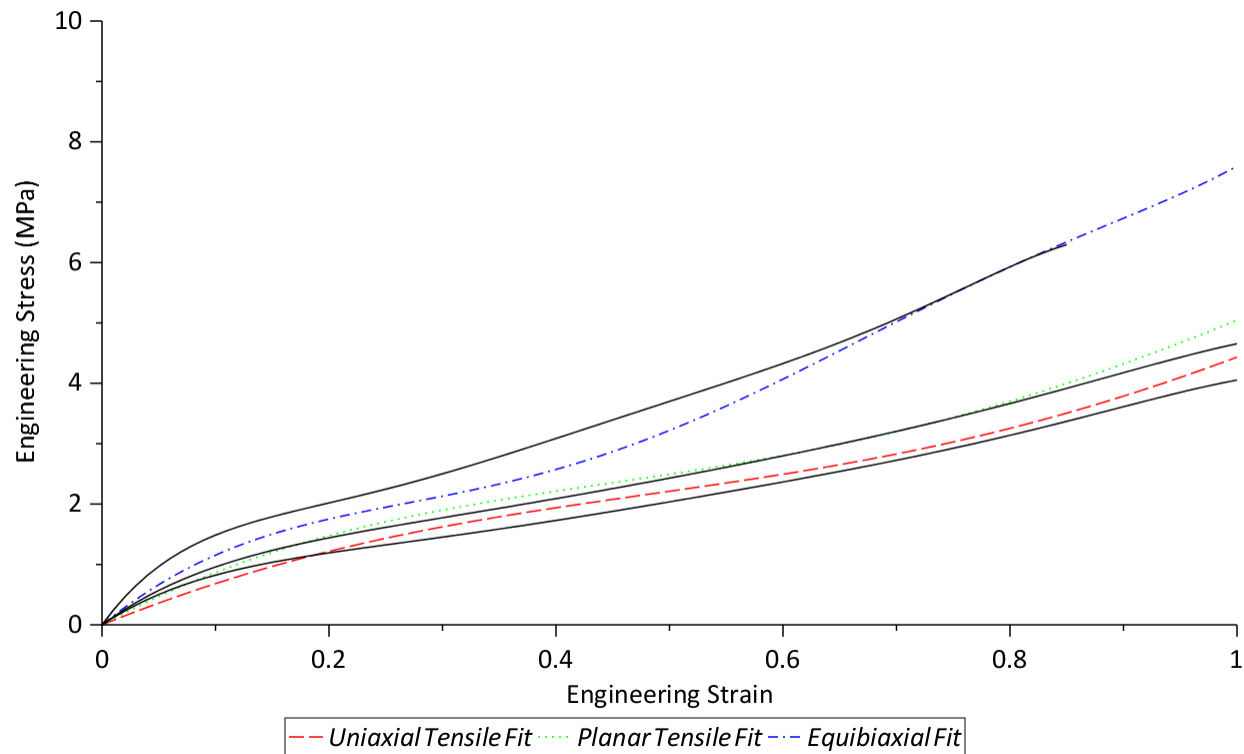


Figure B2: Curve-Fit for Superimposed Material Testing Dataset for 0.00264 s^{-1}

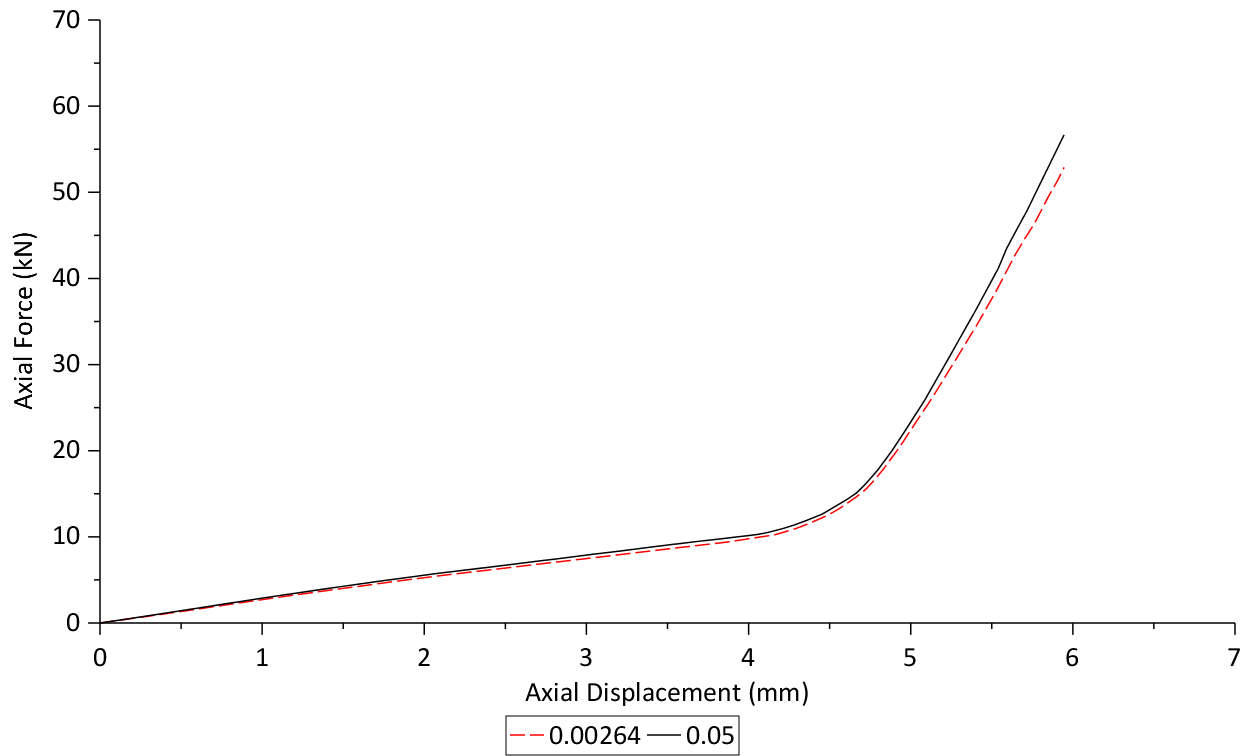


Figure B3: Force-Displacement Comparison of Strain Rates

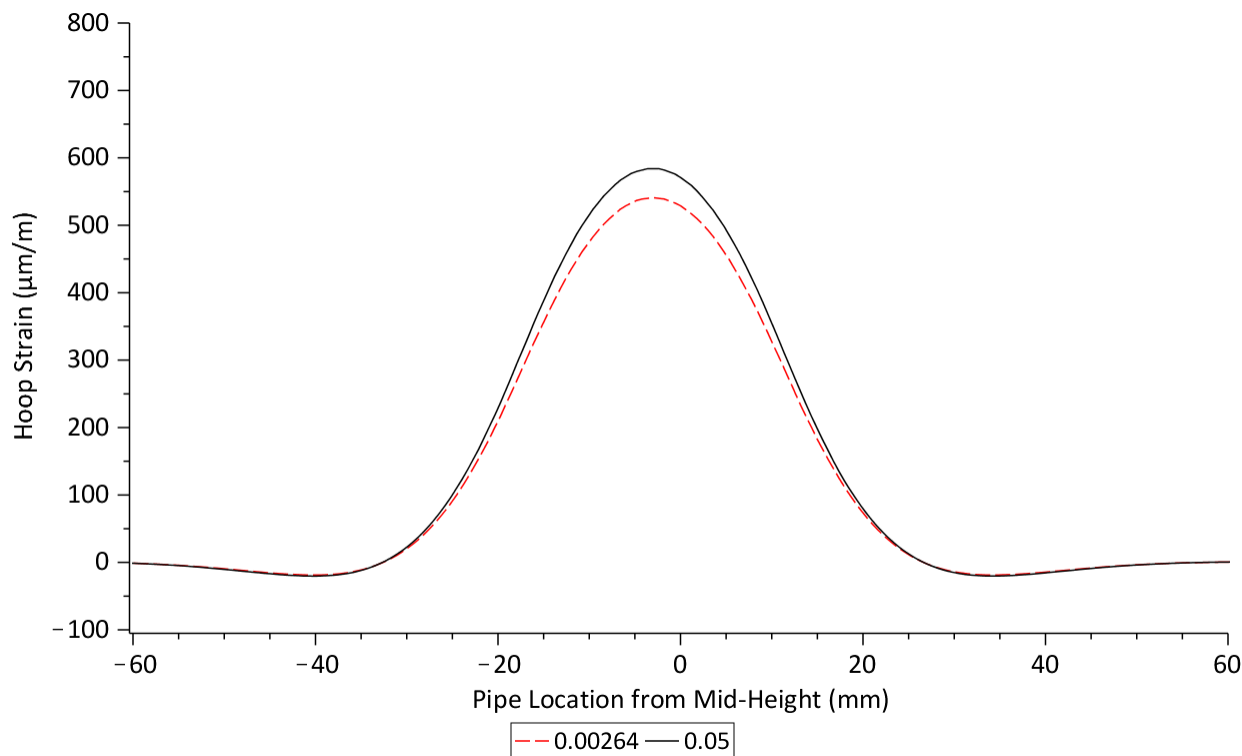


Figure B4: Strain Gradient Comparison of Strain Rates